UNIVERSITY OF SOUTHAMPTON

Heating the Atmospheres of Galaxy Clusters with AGNs

Edward Charles David Pope

Submitted for the degree of Doctor of Philosophy

SCHOOL OF PHYSICS AND ASTRONOMY
FACULTY OF ENGINEERING, SCIENCE & MATHEMATICS

February 20, 2007

UNIVERSITY OF SOUTHAMPTON

ABSTRACT

FACULTY OF ENGINEERING, SCIENCE & MATHEMATICS

SCHOOL OF PHYSICS AND ASTRONOMY

Doctor of Philosophy

Heating the Atmospheres of Galaxy Clusters with AGNs

by Edward Charles David Pope

Numerical simulations are used to study the effect of two heating mechanisms proposed to operate in galaxy clusters: AGNs and thermal conduction. The main results of this work are that thermal conduction cannot reproduce the observed characteristics of the temperature and density profiles of galaxy clusters. As a result it must be drastically reduced and so probably is not a significant source of heating. However, even low-power AGNs activity can exert a significant influence over their surroundings. In addition, low-power sources can inflate cavities of the type that are observed in real galaxy clusters. The heating effect of these cavities can also balance the radiative losses. Theoretical work based on the fraction of galaxies which are detectable in the radio waveband suggests that the low-end of AGN power output is a function of its environment and the mass of the black hole. The effect of accretion and galaxy-galaxy mergers on the $M_{\rm bh} - \sigma_{\rm v}$ relation is also considered. The results suggests that the observed relation can be maintained, regardless of the environment, if significant gravitational radiation is released during the merger of the black holes.

Contents

Chapter 1

Introduction

1.1 The Intra Cluster and Inter Galactic Medium

The visible matter in galaxies, groups and clusters is thought to originate from gas clouds accreting into dark matter haloes. The clouds were heated by the energy released by their initial gravitational collapse after which some of the gas cooled to form the objects that populate the Universe. Initially, these gas clouds formed relatively small proto-galaxies which merged with each other thus forming larger structures ranging from massive galaxies, to galaxy groups and up to clusters of galaxies: the largest organised structures in the Universe (Sarazin, 1986).

Around massive galaxies and in galaxy clusters the gas cooled slowly, forming a quasi-hydrostatic atmosphere (Fabian, 1994). The temperature of this atmosphere is close to the Virial temperature (typically several million K and greater) and is directly observable by X-radiation. Early observations (e.g. Davidsen et al., 1975; Scheepmaker et al., 1976) showed that the spectrum of the X-ray emission is consistent with thermal bremsstrahlung from hot gas (3 - 10 keV) with electron number densities around $10^{-3} - 10^{-1}\mathrm{cm}^{-3}$. The gas is naturally densest near the centre, as a consequence of the approximate hydrostatic equilibrium. As a result, the radiative losses are also greatest here and the weight of the overlying gas will cause a slow inflow of gas towards the centre, establishing a cooling flow.

1.1.1 Galaxy clusters

Regular galaxy clusters are the largest organised structures in the Universe (Sarazin, 1986). They can contain hundreds of galaxies within a region of roughly 10^{25}cm (few $\times$ 10^{4}kpc) across. Using the Virial theorem, the total gravitating mass of a typical cluster can be estimated as $\sim 10^{15}$ $M_{\odot}$ while the mass of the luminous material constitutes only about 10 % of this. Dark matter is generally assumed to account for the missing 90 % of the implied gravitational mass. In this paradigm the visible matter is the tip of the iceberg that sits in the gravitational potential well of a dark matter halo. Since they are so large, galaxy clusters are prominent emitters of X-rays, with typical bolometric X-ray luminosities of $10^{43} - 10^{45}$erg s^{-1} (e.g. Sarazin, 1986).

1.1.2 Elliptical galaxies

The galaxy content of clusters also appears to depend on the cluster properties. For example, Bahcall (1977) showed that the proportion of spiral galaxies decreases as the cluster X-ray luminosity increases. In addition, Melnick & Sargent (1977) showed that the fraction of spiral galaxies also increases with radial distance from the cluster centre. These correlations are consistent with the idea that spirals accreting into clusters are stripped of their gas content through interactions with the cluster gas. As a result, at least the centres of galaxy clusters seem to be primarily the domain of elliptical galaxies.Most galaxies reside in groups or clusters.

Elliptical galaxies are so named because of their smooth and regular appearance. They lack the bright clumps of young blue stars and regions of obscuring dust that are obvious features of spirals and are almost devoid of cool gas, except at the very centre (e.g. Sparke & Gallagher, 2000).

Elliptical galaxies also display a very wide range in physical properties such as size, shape and mass. The largest and the smallest galaxies in the Universe are elliptical galaxies. Dwarf ellipticals are rather common and contain so few stars (only a few million) that they are transparent (Sparke & Gallagher, 2000). In contrast giant ellipticals are

comparatively rare since they exist at the centres of galaxy clusters where they grow by various processes such as mergers and accretion of material from the cooling flow. Due to their immense size these galaxies are often the most luminous object in their group or cluster and are therefore referred to as Brightest Cluster Galaxies (BCGs). A subset of these are the cD galaxies which often possess multiple nuclei and extended envelopes of stars which can reach out to hundreds of kiloparsecs, hinting at formation by multiple mergers. Powerful Active Galactic Nuclei are often located in giant ellipticals (e.g McLure et al., 2004).

1.2 Active Galactic Nuclei

The term Active Galactic Nucleus (AGN) refers to energetic phenomema near the central regions of galaxies from which the emission is particularly strong and cannot be attributed to stars (e.g. Peterson, 1997).

Observationally, the two largest subclasses of AGNs are Seyfert galaxies and quasars (sometimes referred to as QSO's) although the distinction is somewhat arbitrary. The main difference between these subclasses is in the luminosity of the compact central source. In the case of a typical Seyfert galaxy, the total energy emitted by the nuclear source at visible wavelengths is comparable to the energy emitted by all of the stars in the galaxy ($\sim 10^{11} L_{\odot}$). However, for a typical quasar the nuclear source can be brighter than the stars of the host galaxy by a factor of 100 or more. High luminosity quasars are very rare and consequently only found at large distances.

There are also certain observable properties of AGNs which appear to be related to the host galaxy. Many imaging studies suggest that radio-quiet quasars and Seyfert galaxies tend to be found in disk systems (spiral galaxies) while radio-loud quasars and broad-line region galaxies (BLRGs) tend to be found in elliptical galaxies. Other common findings suggest that AGNs are more likely than other galaxies to have close companions and brighter AGNs are typically found in more luminous galaxies (Peterson, 1997).

1.2.1 Unification of AGNs

There is a vast array of different classifications of AGNs. For example, galaxies can be classed as Seyfert 1s and 2s, optically violent variables (OVV), low-ionisation nuclear emission-line region galaxies (LINERS) and BL Lacs, to name but a few. The unified model of AGNs attempts to explain these many types as facets of the same, or a similar, phenomenon (Peterson, 1997). Then most, if not all, of the differences could be due to the viewing angle with respect to the plane of the accretion disk and an obscuring medium. The unified model of an AGN can be summarised as this: a central engine that consists of a hot accretion disk surrounding a supermassive black hole. Energy output is generated by the gravitational infall of material which is heated to high temperatures in a dissipative accretion disk. The detailed structure of the accretion disk depends upon a host of parameters, many of which are not well understood. Moving outwards from the centre lies the Broad Line Region (BLR); a region of rapidly moving and highly ionised clouds. Surrounding the entire central region described so far is a molecular structure, often assumed to be a torus, which is opaque to the AGN emission. Further out lies the Narrow Line Region (NLR) which is the abode of slower moving clouds that are less ionised than those which populate the BLR.

A dipiction of the unified model of AGNs is shown in figure 1.1. This figure demonstrates that the presence of an obscuring medium around the central engine can lead to many different observable characteristics of the same fundamental phenomenon. For example, looking side-on through the obscuring medium towards the central engine means that emission from the BLR is absorbed. Therefore, the line emission will only come from the slower moving clouds in the NLR that are prevalent further away from the central engine.

Figure 1.1 shows the objects observed, as a function of viewing angle, for two classes of object: radio-loud objects (above the white line) and radio-quiet objects (below the white line). Radio-loud objects are traditionally defined as having a ratio of radio to optical power ratio of greater than 10.

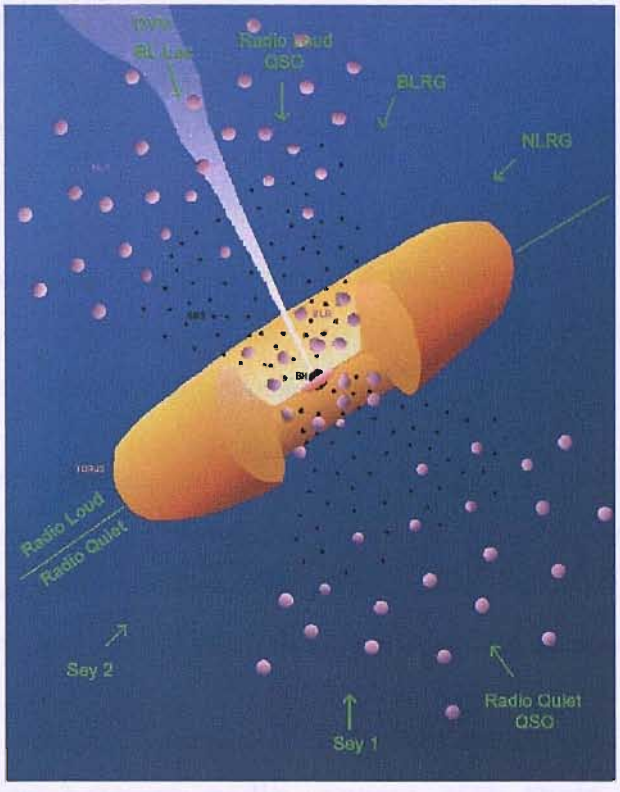

Figure 1.1: Unification of AGN: the different classes are observed because of different viewing angles. Sey refers to Seyfert galaxies, BLRG - Broad Line Region Galaxy, NLRG - Narrow Line Region Galaxy. Taken from the BeppoSAX calender, adapted from Urry & Padovani (1996).

1.3 Radio sources

Normal stars and normal galaxies are not powerful radio sources. For example, the Milky Way has a radio output of roughly $10^{37}\mathrm{erg\,s^{-1}}$ while Seyfert galaxies are roughly 100 to 1000 times more luminous in the radio band. Galaxies with radio power greater than $10^{41}\mathrm{erg\,s^{-1}}$ are called radio galaxies, the most powerful of which radiate up to $10^{45}\mathrm{erg\,s^{-1}}$ of highly polarised radio synchrotron radiation (Sparke & Gallagher, 2000). Synchrotron radiation is emitted when relativistic, charged particles circulate, and therefore accelerate, around a magnetic field line (e.g. Rybicki & Lightman, 1979).

Radio sources often reveal themselves because of their interaction with the surrounding medium. Linear jets, originating from the compact source at the centre of the galaxy lead out to extended lobes which the jets have apparently inflated. The jet velocities are often

a significant fraction of the speed of light. Energy can be transferred to the environment by the PdV work required to expand the radio lobe against the external atmosphere and also by shocks, since at least the early stages of the expansion must have been supersonic, with respect to the ambient gas.

It is possible to construct analytical models for radio sources (e.g. Kaiser & Alexander, 1997). However, when considering the interactions with their environment it is necessary to perform numerical hydrodynamic simulations.

Extended radio structures can be divided into two luminosity categories: FR I and FR II. FR I sources are weaker radio sources which are brightest in the centre, with decreasing surface brightness towards the edges. FR IIs are more luminous, limb-brightened and terminate in hotspots (Fanaroff & Riley, 1974). Quasars are examples of FR II sources.

1.3.1 Interactions between radio sources with their environment and AGN feedback

It is evident that radio sources both affect and are affected by their surroundings. For example, giant elliptical galaxies often produce large radio lobes. In addition, observations of galaxy clusters show an ever-increasing incidence of depressions in the X-ray surface brightness maps, which are often coincident with radio emission (e.g. Bîrzan et al., 2004, and references therein). It is now generally accepted that these are bubbles which have been inflated by the radio lobes of the AGN at the centre of the cluster, see figure 1.2. These bubbles are under-dense, but hot compared to their surroundings and are in pressure equilibrium. Because of their low density they rise buoyantly through the intracluster medium and will therefore be subjected to fluid instabilities such as Rayleigh-Taylor and Kelvin-Helmholtz. If uninhibited, the effect of these instabilities would completely disrupt the bubble and mix its material with its surroundings (e.g. Churazov et al., 2001). However, observational evidence seems to suggest that these X-ray cavities remain intact (see figure 1.2 again), although, presumeably it would be difficult to observe a shredded bubble! One possible explanation is that the same magnetic fields that are responsible to the synchrotron emission could also provide an effective surface tension that could prevent

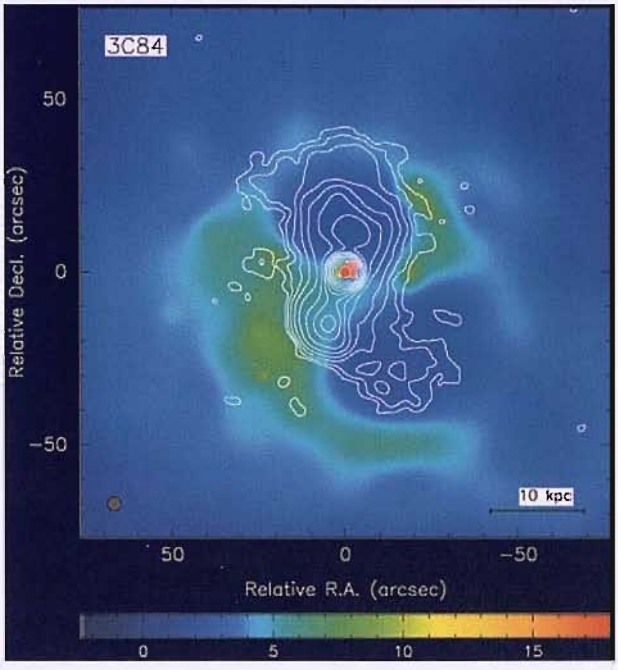

Figure 1.2: The X-ray image of the Perseus cluster taken by the Chandra X-ray Observatory (Fabian et al. 2000). The radio contours were derived from VLA observations and are coicident with depressions in the X-rays.

the bubbles from being disrupted, see figure 1.4. Another possibility is that the growth of the instabilities is slowed by the effect of viscosity, see figure 1.3.

There have been numerous studies of this topic using hydrodynamic simulations. Some of this work has been centred on the passive evolution of bubbles (e.g. Churazov et al., 2001; Dalla Vecchia et al., 2004) or including the effect of magnetic fields (e.g. Robinson et al., 2004), or including viscosity (Reynolds et al., 2002) and the effect on their surroundings. Other work has taken advantage of advances in computational power to investigate the effect of outflows and jets themselves, (e.g. Brüggen & Kaiser, 2002; Basson & Alexander, 2003; Omma et al., 2004; Vernaleo & Reynolds, 2005). Recent work by Heinz et al. (2006) also takes into account precession of the jet and the dynamic state of the cluster environment by using initial conditions cut out from a simulation of cosmological structure formation, see figure 1.6.

The presence of radio lobes indicates that significant quantities of energy are supplied to the atmosphere that surrounds the elliptical galaxy, or permeates the galaxy cluster. It is quite possible that this AGN activity is an example of negative feedback. Negative

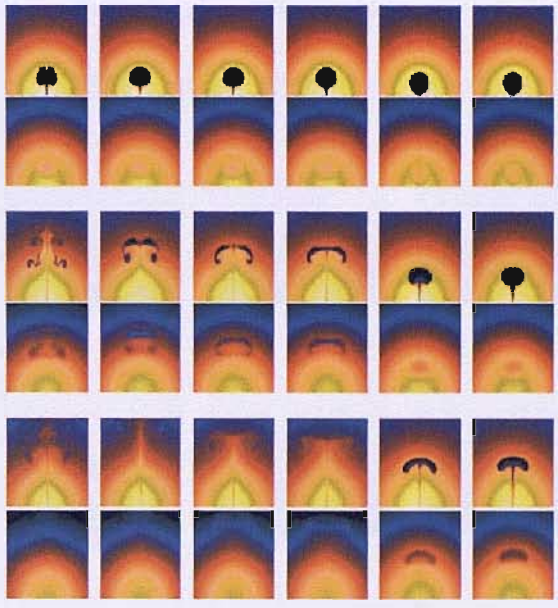

Figure 1.3: Simulations showing the effect of increasing viscosity of the morphology of a buoyant bubble. Each column shows the temporal evolution of a bubble. On the left the evolution in the absence of viscosity is shown. Panels further right show that viscosity slows the growth of the instabilities. The first row shows the density while each second row shows the X-ray surface brightness. Taken from Reynolds, et al. (2005).

feedback occurs when a reaction occurs to oppose the action that first caused it. When applied to elliptical galaxies and galaxy clusters this means that the accretion of material that radiatively cools out of the atmosphere stimulates a response in the form of AGN activity which heats the gas and therefore reduces the accretion rate. There have been several simple studies of feedback processes, for example Churazov et al. (2002). There are also other more detailed studies such as the 1-d numerical simulations of Ruszkowski & Begelman (2002); Brüggen (2003); Hoeft & Brüggen (2004) who found that the combined heating effect of an AGN power output which is proportional to the mass inflow rate, along with thermal conduction could balance the radiative losses. Despite the fact that these models were able to maintain a steady-state there is an obvious problem: the AGN power output tends to a constant in these models. If this were really the case, it would mean that the AGN would be either always detectable or always undetectable, depending on the detection threshold. This is probably not the case since recent work by Best et al. (2005) actually suggests that the probability of detecting the radio output from an

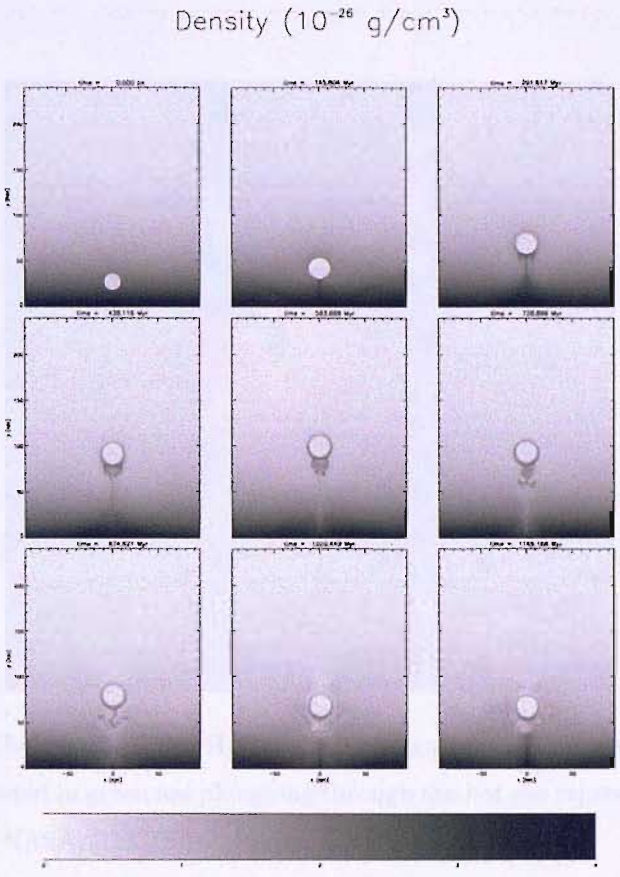

Figure 1.4: 2-d simulations showing the evolution of a magnetically supported bubble. Taken from Robinson, et al. (2004).

elliptical galaxy depends on the mass of the supermassive black hole at its centre. Another problem with these simulations is due to the fact that they are performed in 1-dimension and the heating is unavoidably isotropic. In reality, the influence of the AGN outflow would be highly directional, at least to begin with. However, as time passes shocks, sound waves, gravity waves and also interference between the back flows of the jets could easily result in a much more isotropic distribution of the energy injected by the AGN.

1.4 Aims

To date, only the impact of high power jets, on the cluster environment, has been studied to any great extent. A relatively under-explored area is the effect of lower power outflows, which are likely to display quite different signatures. As a result, the effect and morphology

Figure 1.5: The centre of the Hydra cluster of galaxies. Two radio-emitting gas outflows represented in green are ploughing through the hot gas represented in purple. Credits: X-ray: NASA/CXC/SAO; Radio: Greg Taylor (NRAO).

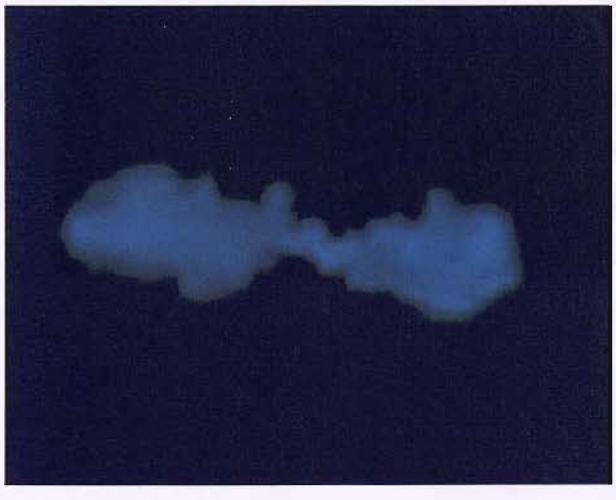

Figure 1.6: Image from the simulations of Heinz, et al. (2006) in which the cluster atmosphere is dynamic and the jets precess. Note the apparent similarity with the Hydra cluster in figure 1.5.

of such lower power outflows will be investigated, in realistic simulated clusters.

A long-standing problem when considering AGN feedback is the power and frequency of the outbursts and the dominant accretion rate that drives the AGN energy output. For example, is the energy required to inflate the cavities in the X-ray maps sufficient to offset the radiative cooling, or is there assistance from an additional mechanism? For example, is the accretion rate onto the AGN dominated by the environment alone, or is the mass of the black hole also influential? Is the time-averaged AGN power output sufficient to offset the radiative cooling, or is there assistance from an additional mechanism? This is investigated using observations of galaxy clusters and results of work on the fraction of galaxies that are detected at radio wavelengths.

AGNs are not the only method by which the gas in galaxy clusters is heated. Another plausible mechanism is the transfer of thermal energy from the cluster outskirts to the inner regions by thermal condution. Part of the aim of this thesis is to address the effect of thermal conduction using 3-dimensional simulations based on data from real clusters such as Virgo and Perseus.

Observations are limited by angular and spectral resolution. As a result, many parameters of distant galaxy cluster, such as the central stellar velocity dispersion of the BCG, are unknown or poorly constrained. Knowing parameters such as these is important for estimating the mass of the black hole at the centre of the galaxy, or studying the Faber-Jackson relation, for example. This can be addressed using observations of the ICM and the atmospheres of elliptical galaxies. The twin effects of galaxy-galaxy mergers and accretion history on the masses of black holes at the centres of galaxies are also important and must be considered.

1.5 Outline

The introduction presented above is intended to briefly cover all of the necessary topics presented in this thesis. More specific introductions will be given at the beginning of each chapter as well as a conclusion at the end of each chapter.

Chapter 2 provides an overview of many of the thermal properties of the intracluster gas as well as some results for AGN-blown bubbles. This includes topics such as radiative cooling times of the ICM and possible energy transfer mechanisms associated with the AGN.

Chapter 3 describes the code and associated techniques used in the simulations of galaxy clusters.

Chapter 4 gives a comparison of the effect of thermal conduction on the evolution of two different galaxy clusters: Virgo and Perseus.

Chapter 5 compares the heating rates required to maintain a steady state, for a sample of galaxy clusters, using a simple analytical model. These are compared to an instantaneous estimate of the energy transport rate by thermal conduction, and an estimate of the power output of the AGN from the radio observations.

Chapter 6 is concerned with the phenomenon of AGN variability. This is addressed using observations of the fraction of galaxies, as a function of black hole mass, that can be detected at radio wavelengths.

Chapter 7 provides a study of the impact of AGN outflows on their surroundings using 3-d hydrodynamic simulations. This includes the effect of different jet powers and duty cycles on their heating capabilities.

Chapter 8 investigates a new method that can be used to calculate the central stellar velocity dispersion of galaxies. This could be particularly useful for extremely distant clusters for which the standard methods are unable to resolve these small regions. Also included in this study is a simple estimate of the effect of galaxy-galaxy mergers and accretion history on the $M_{\rm bh} - \sigma_{\rm v}$ relation.

Chapter 9 summarises the most important results presented in this thesis.

Chapter 2

Thermal Properties of the ICM

2.1 Introduction

The sizes of galaxy clusters were estimated from early X-ray observations by assuming the simplest possible model: that the gas density followed a King approximation to a self-gravitating isothermal sphere (e.g. Lea et al., 1973). However, subequent comparisons of the mass of the ICM with the Virial mass showed that this assumption is physically inconsistent since the gas masses are generally less than 20% of the Virial mass. Dark matter is generally assumed to account for the portion of the Virial mass that is not visible but is implied by observations. Despite this, the King profile does seem to provide a good approximation for the distribution of the galaxies within a cluster (e.g. Sarazin, 1986) and references therein. Furthermore, the β-profile, which is a variation of the King approximation, provides a reasonable fit to the gas distribution (e.g. Mohr et al., 1999).

A slightly more complex, but physically consistent, model would describe the ICM as a spherically symmetric medium with a unique temperature and density at each radius. The gas is initially in hydrostatic equilibrium with a gravitational potential composed of dark matter, galaxies and the self-gravity of the gas itself. Theoretically speaking, the gravitational potentials of clusters can be described as arising from a mass density distribution following a NFW profile (Navarro et al., 1995, 1996, 1997). In reality, the

situation is not so idealised and the gas temperature is not uniform. Some observations also suggest that the ICM is rather a multiphase medium being composed of gas at different temperatures at the same radii (e.g. Edge, 2001).

The origin of the cool gas in galaxy clusters is largely due to the effect of significant cooling. This occurs because of radiative losses, which are dominated by thermal bremsstrahlung at typical cluster temperatures. One of the most noticeable consequences of cooling is the developement of an appreciable drop in temperature towards the cluster centre. Furthermore, as the gas temperature drops, the pressure also falls. As a result, the weight of the overlying gas causes a slow, subsonic inflow of gas known as a cooling flow (Fabian, 1994). Since the cooling time of the ICM, in these regions, is less than a Hubble time, many clusters are expected to contain cooling flows.

Finally, this simplisitic model of the ICM is also altered by the presence of AGNs. The basic properties of plasma bubbles inflated by AGNs can be investigated analytically to some extent; from inflation, to the buoyant rise velocity, to the isoentropy radius.

2.2 Hydrostatic equilibrium

When considering the initial conditions for the temperature and density of the ICM it is usual to assume hydrostatic equilibrium, with the temperature being constant. Indeed, the uniform initial temperature must be a reasonable assumption since for clusters the temperature profile flattens to become uniform at large radii, hinting at the possible initial conditions. The gas temperature is also generally close to the Virial temperature. This is to be expected on theoretical grounds if the gas is shock-heated when it falls into the dark matter gravitational potential (Kaiser, 1991).

A consequence of a uniform temperature is that the density profile is much easier to calculate than for a variable temperature. The hydrostatic assumption also means that no assumptions about the velocity profile of the gas need be made, except that all bulk velocities are initially zero, and that the atmosphere can evolve self-consistently.

2.2.1 Derivation of the King profile

The main use of the King profile is as an analytical approximation to a numerical solution of the non-singular isothermal sphere as determined from the Lane-Emden equation. It is often used to describe the spatial distribution of galaxies in a cluster.

The Lane-Emden equation can be obtained by considering a self-gravitating gas. The denser gas at the centre would be held there, against the pressure gradient, by a gravitational force due to the same gas. This can be written,

$$-\nabla P = \frac{GM\rho}{r^2}. \tag{2.1}$$

For simplicity, spherical symmetry is assumed so it is only necessary to consider the radially dependent components of equation (2.1). After some simple algebra (e.g. Binney & Tremaine, 1987) the Lane-Emden equation is obtained,

$$\frac{\mathrm{d}}{\mathrm{d}r}\left(r^2\frac{\mathrm{d}\ln\rho}{\mathrm{d}r}\right) = -\frac{4\pi G}{\sigma_\mathrm{v}^2}r^2\rho, \tag{2.2}$$

where $\sigma_\mathrm{v} = \frac{k_\mathrm{b}T}{\mu m_\mathrm{p}}$. One of the solutions of this 2nd order differential equation is the singular isothermal sphere (SIS)

$$\rho(r) = \frac{\sigma_\mathrm{v}^2}{2\pi G r^2}, \tag{2.3}$$

The self-gravitating isothermal sphere is often used to approximate the gravitational potential of an elliptical galaxy, (e.g. Binney & Tabor, 1995).

Since the Lane-Emden equation is second order it has another independent solution, although it cannot be expressed analytically. It can be calculated numerically using the condition that the density profile is flat at the origin. A common approximation to this is the King profile: $\rho(r) = \rho_0/[1 + (r/r_0)^2]^{-3/2}$, King (1962).

2.2.2 The β profile

The Lane-Emden equation only considers self-gravity and does not consider the effect of the dark matter halo nor the galaxies. Therefore, to construct a more realistic density profile, the effect of the dark matter, at least, must be included. If the gas and the galaxies

move under the influence of the same, spherically symmetric, gravitational potential ϕ, using the ideal gas law and assuming that the gas is isothermal, the gas density is

$$\frac{1}{\rho}\frac{\mathrm{d}P}{\mathrm{d}r} = -\frac{\mathrm{d}\Phi}{\mathrm{d}r}, \tag{2.4}$$

$$\frac{1}{\rho}\frac{\mathrm{d}\rho}{\mathrm{d}r} = -\frac{\mu m_\mathrm{p}}{k_\mathrm{b}T}\frac{\mathrm{d}\Phi}{\mathrm{d}r}, \tag{2.5}$$

$$\rho_\mathrm{gas} = \rho_\mathrm{gas}(0)\exp\left(\frac{-\mu m_\mathrm{p}\Phi}{k_\mathrm{b}T}\right). \tag{2.6}$$

The pressure, P_gal of the galaxy 'gas' depends on the velocity dispersion σ_v of the particles such that, $P_\mathrm{gal} \propto \sigma_\mathrm{v}^2\rho_\mathrm{gal}$, where ρ_gal is the density of the galaxy 'gas'. Therefore,

$$\sigma_\mathrm{v}^2\frac{\mathrm{d}\rho_\mathrm{gal}}{\mathrm{d}r} = -\rho\frac{\mathrm{d}\Phi}{\mathrm{d}r}, \tag{2.7}$$

$$\rho_\mathrm{gal} = \rho_\mathrm{gal}(0)\exp\left(-\frac{\Phi}{\sigma_\mathrm{v}^2}\right), \tag{2.8}$$

Therefore $\rho_\mathrm{gas} \propto \rho_\mathrm{gal}^\beta$ where

$$\beta = \frac{\mu m_\mathrm{p}\sigma_\mathrm{v}^2}{k_\mathrm{b}T}. \tag{2.9}$$

Consequently, if it is assumed that a King profile adequately describes the galaxy distribution, then the density of the gas is given by

$$\rho_\mathrm{gas} \propto [1 + (r/r_0)^2]^{-3\beta/2}. \tag{2.10}$$

Equation (2.10) describes the so-called β profile. In a study of 45 clusters by Mohr et al. (1999) β was found to be $\sim 2/3$. This value gives the non-singular isothermal sphere profile which falls off as r^{-2}, just like the isothermal sphere, but which also has a core. However, at some point the density profile must steepen further so that $\rho \propto r^{-3}$ otherwise the mass of the cluster will diverge for $r \to \infty$.

2.2.3 NFW profiles

An alternative density profile for the matter that dominates the gravitational potential was introduced by Navarro, Frenk and White, hereafter NFW, (Navarro et al., 1995, 1996, 1997). NFW used high resolution N-body simulations to study the equilibrium density profiles of dark matter haloes in hierarchically clustering Universes and found that all such profiles had the same shape, independent of the halo mass, the initial density fluctuation spectrum, and the values of the cosmological parameters. They found that spherically averaged equilibrium profiles were well fitted, over two decades in radius, by a simple formula originally used to describe the structure of galaxy clusters in a cold dark matter Universe (Navarro et al., 1997). The NFW profile is,

$$\frac{\rho_{\rm DM}(r)}{\rho_{\rm crit}} = \frac{\delta_{\rm c}}{(r/r_{\rm s})(1+r/r_{\rm s})^2} \tag{2.11}$$

where $\rho_{\rm DM}(r)$ is the dark matter density a function of radius, $\rho_{\rm crit}$ is the critical density for closure given by $\frac{3H^2}{8\pi G}$ (where H is the current value of the Hubble constant and G is the Universal gravitational constant), $\delta_{\rm c}$ is the characteristic density parameter and $r_{\rm s}$ is the scaling radius.

The gravitational acceleration, $-\frac{{\rm d}\phi}{{\rm d}r}$, due to the mass of the cluster for a spherically symmetric halo can be calculated from the Poisson equation. For spherical symmetry, the Poisson equation can be written as,

$$\frac{1}{r^2}\frac{\rm d}{{\rm d}r}\left(r^2\frac{{\rm d}\phi}{{\rm d}r}\right) = 4\pi G(\rho_{\rm DM}+\rho) \tag{2.12}$$

where ρ is the baryonic matter distribution which is assumed to be insignificant compared to the effect of the dark matter.

The NFW gravitational potential is,

$$\phi = -4\pi G\frac{{r_{\rm s}}^3}{r}\rho_{\rm crit}\delta_{\rm c}\ln\left(1+\frac{r}{r_{\rm s}}\right) \tag{2.13}$$

The NFW dark matter density profile also has the property that at large radii $\rho \propto r^{-3}$ which means that the total mass is logarithically infinite. The same is also true for the King profile.

2.3 Composition of the ICM

The ionisation energy for Hydrogen is 13.6 eV, the first ionisation energy for Helium is 24.5 eV and the second is 54.4 eV (Zombeck, 1990). These energies correspond to temperatures of 1.57×10^5K, 2.85×10^5K, 6.3×10^5K respectively, which are much lower than the typical ICM temperatures. As a result it is expected that all the Hydrogen and Helium is almost completely ionised.

The mean mass per particle $\mu m_{\rm p}$, in the ICM, for any given abundance, is calculated in the following way, assuming each of the species is completely ionised,

$$\frac{1}{\mu} = 2X + \frac{3}{4}Y + \frac{1}{2}Z \tag{2.14}$$

where X is the mass fraction of hydrogen, Y is the mass fraction of Helium and Z is the mass fraction of all the more massive elements.

The assumed mass abundances are 75% hydrogen and 25% helium. Using equation (2.14), this means that $1/\mu = 27/16 = 1.6875$ and so $\rho = \frac{16}{27} m_{\rm p} n$. The electron number density is then, $n = \frac{27}{14} n_{\rm e}$ so that $\rho = \frac{8}{7} m_{\rm p} n_{\rm e}$. It is useful to have the gas density in terms of electron number density because the electrons are responsible for the X-ray emission.

As already stated, the mass fraction of heavy elements is denoted by Z; the Sun's abundance $Z_\odot \approx 0.02$ (Sparke & Gallagher, 2000), while the most metal poor stars in our Galaxy have less than 1/10000 of this amount. To specify the fraction of a particular element, such as oxygen, in a star or particular medium, it is standard to give the abundance relative to the Sun (e.g. Sparke & Gallagher, 2000),

$$[A/B] \equiv \log_{10} \left[\frac{(\text{number of A atoms/number of B atoms})_*}{(\text{number of A atoms/number of B atoms})_\odot} \right] \tag{2.15}$$

where $_*$ refers to the star, or in this case the ICM, and $_\odot$ to the Sun.

Thus, in a system where [Fe/H] = -2, iron is 1% as abundant as in the Sun. In practice [Fe/H] is more frequently used to describe a system's average heavy element abundance relative to the Sun, rather than only applying to the iron abundance. The typical values for galaxy clusters are [Fe/H] = -0.5, which means that the relative abundance of the metals in galaxy cluster atmospheres is $\approx$ 32% of that present in the Sun.

2.4 Cooling and Cooling flows

2.4.1 Cooling functions

The rate of energy lost to radiation per unit volume, C is $n^2\Lambda(T,\rho)$, where n is the number of particles per unit volume. Λ is called the cooling function and has units of erg cm^3 s^{-1}.

The number of particle collisions per second in a gas is $\propto n^2$ where n is the number density of particles. For the hot intracluster gas, the gas is thermally ionised and the emission is mainly thermal bremsstrahlung, $C \equiv 1.4\times10^{-27}T^{1/2}n_{\rm e}n_{+}Z^2g_{\rm B}$ where Z is the atomic number of positively charged ions in the gas, and $g_{\rm B}$ is the Gaunt factor (Rybicki & Lightman, 1979). Therefore, the cooling losses can be written as $C = n_{\rm e}n_{+}\Lambda(T)$ and the cooling function can be approximated by $\Lambda(T,\rho) \approx \Lambda(T)$.

The cooling function constitutes an important part of a numerical model of the ICM. For analytical models a power-law cooling function could be sufficient. However, with numerical models it is possible to use more realistic cooling rates.

For temperatures in the range of 10^4K - $10^{8.5}$K the tabulated cooling rates of Sutherland & Dopita (1993) are used, see figure 2.1. These take into account both continuum and line cooling mechanisms. Above $10^{8.5}$K thermal bremsstrahlung is assumed to dominate, while the cooling is switched off below 10^4K. Since the rates given by Sutherland & Dopita (1993) are tabulated the cooling rates must be interpolated for given temperatures. The method used for this is given in Chapter 3.

2.4.2 Cooling time and Cooling radius

Gas at a temperature T will have a thermal energy per unit volume of $\frac{5}{2}nk_{\rm b}T$. The cooling time for a monatomic gas is defined as

$$\tau_{\rm cool} = \frac{5}{2}\frac{nk_{\rm b}T}{|C|} = \frac{5}{2}\frac{k_{\rm b}T}{n|\Lambda|}\,{\rm s}, \tag{2.16}$$

this includes the effect of PdV which increases the cooling time.

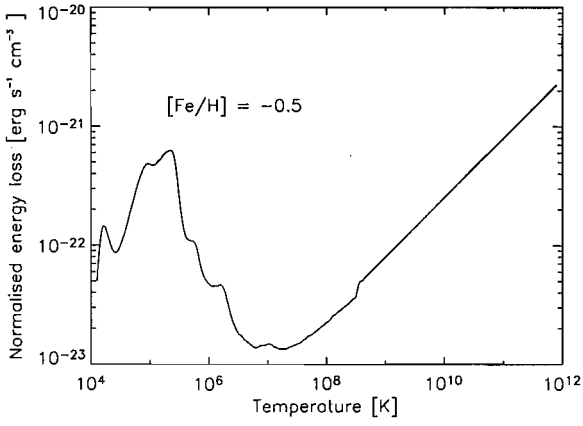

Figure 2.1: Cooling function as a function of plasma temperature. Note that the effects of line cooling at lower temperatures mean that the gas cools much more rapidly at lower temperatures than if we just assume bremsstrahlung. At high temperatures the cooling is dominated by bremsstrahlung.

Typical cooling times can be estimated by scaling the variables to suitable values,

$$\tau_{\rm cool} = 3.3 \times 10^{10} \left(\frac{T}{5 \times 10^7 {\rm K}} \right) \left(\frac{n}{10^{-3} {\rm cm}^{-3}} \right)^{-1} \left(\frac{\Lambda}{10^{-23} {\rm erg\,cm^3\,s^{-1}}} \right) {\rm yr} \qquad (2.17)$$

which is of order the Hubble time.

The cooling time is also a function of radius from the cluster centre. If the cluster is initially isothermal, the radial dependence of the cooling time comes only from the density,

$$\tau_{\rm cool} \propto \frac{1}{n(r)} \qquad (2.18)$$

where $n(r)$ is the initial density of the gas which is usually well described by a β-profile.

Since the density falls with increasing radius, this causes the cooling time to increase. As a consequence there will be a radius beyond which the cooling time will exceed the Hubble time. This radius is called the cooling radius. The cooling radius is often used to calculate the volume of the cluster that requires heating to balance radiative cooling.

Substituting parameters suitable for the Virgo cluster into equation (2.17) demonstrates the radial dependence of the cooling time shown in figure 2.2. According to equation (2.16) the radiative cooling time-scale at the centre of the Virgo cluster is of order 10^8yrs.

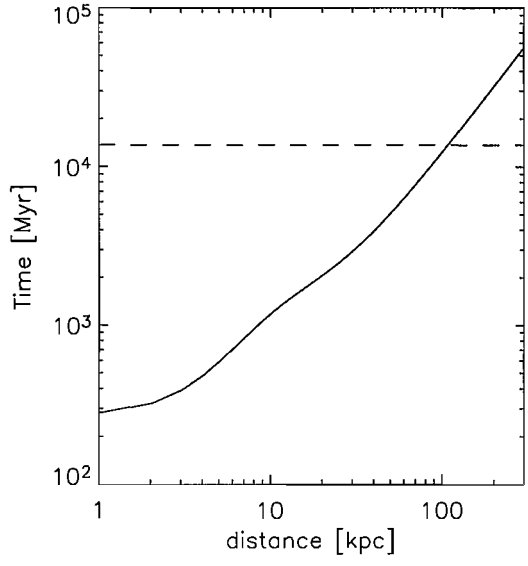

Figure 2.2: The radial dependence of the cooling time for the Virgo cluster. The temperature is assumed to be 3×10^7K and independent of radius and the density profile given by current observations (Ghizzardi et al., 2004). The dotted line shows the Hubble time (13.7 billion years), the point where this line intersects with the cooling time gives the cooling radius which, as can be seen, is roughly 100 kpc for the Virgo cluster

2.4.3 Time taken to cool

Equation (2.17) gives what should more appropriately be referred to as the cooling time-scale for the radiative losses. This is because it is only a rough estimate since it assumes that the radiative losses are constant in time. The actual time taken for a gas to cool from temperature T_0 to T_1 requires a slightly more complex calculation which takes into account the effect of the changing temperature and density on the radiative losses. This can be done using the following method: the rate of change of internal energy per unit volume is is related to the rate of change of the temperature by,

$$\dot{e} = \frac{3}{2} k_{\rm b} n \dot{T} = -n^2 \Lambda(T), \tag{2.19}$$

in this case, $P\mathrm{d}V$ work is neglected. If the effect was included it would increase the cooling time.

It is possible to estimate the temporal evolution of the gas temperature if a couple of

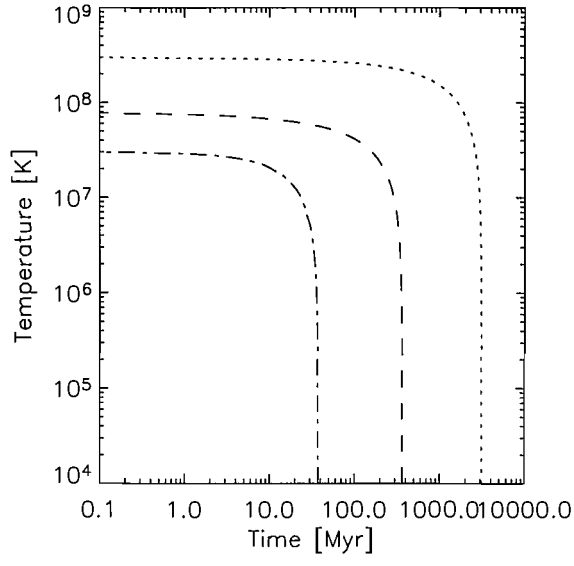

Figure 2.3: The temporal evolution of the ICM gas. The dashed-dotted line represents the centre of the Virgo cluster with $T = 3 \times 10^7$ K, $n = 0.11\text{cm}^{-3}$ as its initial state, the dashed and dotted lines represent gas with $T = 8 \times 10^7$ K and $T = 3 \times 10^8$K respectively and the same density as for the Virgo cluster.

simple assumptions are made. Firstly, if the cooling is isobaric then $n_0 T_0 = nT$. This means that, as the temperature falls, the density increases by the same factor. Since the radiative losses are proportional to the square of the density this effect will dramatically reduce the cooling time. Then, if the heating rate is negligible, the time taken to cool becomes,

$$t_{\text{cool}} = \frac{3}{2} \frac{k_{\text{b}}}{n_0 T_0} \int_{T_0}^{T_1} \frac{T \mathrm{d}T}{\Lambda(T)}. \tag{2.20}$$

Since the cooling function cannot be described analytically, equation (2.20) must be integrated numerically. The results are shown in figure 2.3.

The dash-dotted line in figure 2.3 shows that the time taken for the gas to cool to a low temperature at the centre of the Virgo cluster is roughly 40 Myrs. This should be compared to the the cooling time-scale estimate in figure 2.2 again at the centre of the Virgo cluster. The latter erroneously suggests that the gas will take roughly 300 Myrs to cool which is roughly an order of magnitude more than predicted by equation (2.3).

Figure 2.3 also demonstrates the phenomenon that is commonly known as a cooling

catastrophe. Essentially, the gas temperature falls by a small fraction over the first few 10's of Myrs but thereafter drops catastrophically down towards zero in only a few Myrs. This occurs because the radiative losses are a positive feedback process: the gas density increases because of the radiative losses, causing the density to increase, and so on.

2.4.4 Observations of Cooling flows

Equation (2.17) forms the basis for the postulated existence of a cooling flow. In terms of observations, the strong central peak of the X-ray surface brightness profiles of many clusters of galaxies is generally interpreted as the signature of a cooling flow (Cowie & McKee, 1977; Fabian, 1994). As stated above, standard cooling flow theory suggests that this peak should coincide with the deposition of large amounts of cold gas and significant excess of star formation at the centre of the cooling flow. However, the XMM-Newton and Chandra satellites have demonstrated both the lack of the expected cold gas, at temperatures below roughly 1 keV (e.g. Edge, 2001), and that spectroscopically measured mass-deposition rates are roughly one tenth of the value inferred from the peaks of cluster X-ray surface brightness maps (Voigt & Fabian, 2004). These findings suggest that the gas in the cluster cores is reheated. This heating can be either continuous or periodic but must produce the observed minimum central temperature (or entropy) and the lack of significant excess star formation.

2.5 Heating by AGNs

The evidence of the previous subsection suggests that the ICM is being heated somehow by a non-gravitational source of energy. One of the possibilities is heating by AGNs.

2.5.1 Photoionisation

Gas that lies within the radiation cone of an AGN will be heated by photoionisation from the AGN photons (e.g. Ciotti & Ostriker, 2001). To calculate this heating rate requires

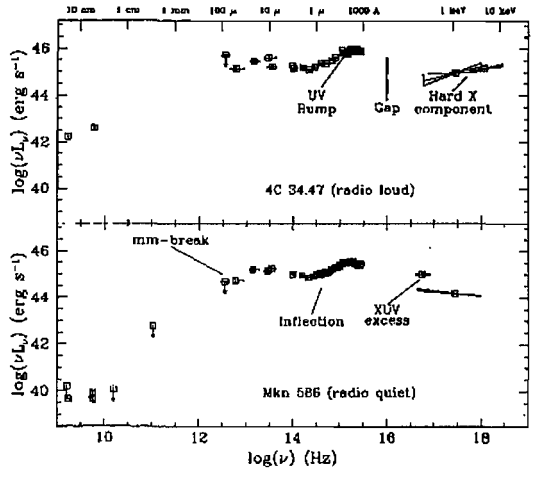

Figure 2.4: Broadband AGN luminosity. Top panel: 4C 34.47 - radio-loud; Bottom panel: Mrk 586 - radio-quiet (Elvis et al., 1994).

the spectrum of emitted photons to be known. The classical spectral energy distributions are given in Elvis et al. (1994), these are shown in figure 2.4. AGNs can also heat their surroundings by a variety of different methods some of which are introduced below.

2.5.2 Generating waves

As an AGN outflow ploughs through the ICM it will create pressure fluctuations which would be expected to generate acoustic waves. Sound, or acoustic, waves owe their existence to the fact that the medium is compressible. Very often, the movements of foreign bodies placed in a gas happen to be the source of acoustic waves (Choudhuri, 1998). For example, the production of sound by a tuning fork. In addition, the motion of the gas itself may also act as a source of sound in certain circumstances; the noise produced by a jet engine being an example.

The sound speed is defined as

$$c_s = \sqrt{\left(\frac{dP}{d\rho}\right)}. \tag{2.21}$$

If the perturbations evolve in times short compared to the time for heat conduction, it is possible to assume adiabatic conditions (P/ρ^γ = constant). In this case the sound

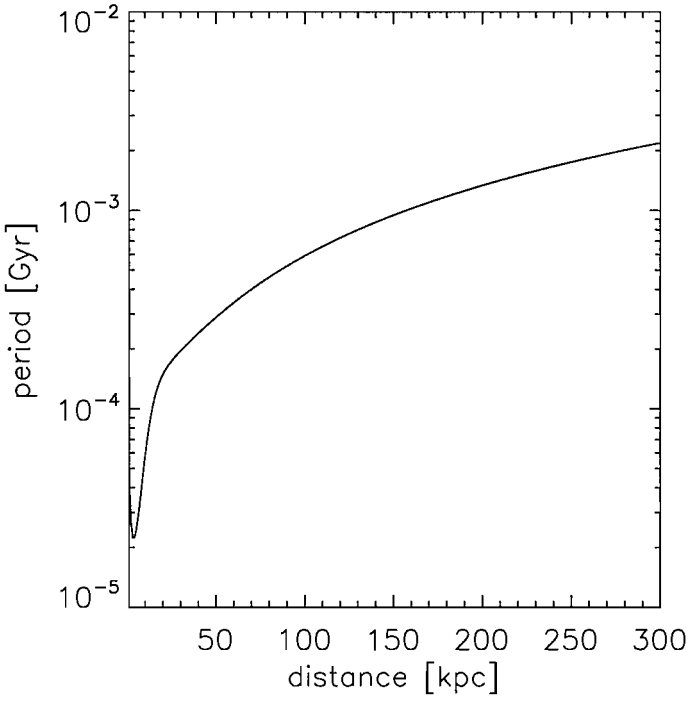

Figure 2.5: Period of buoyant oscillations in the Virgo cluster.

speed is,

$$c_s = \sqrt{\left(\frac{\gamma P_0}{\rho_0}\right)}, \tag{2.22}$$

where P_0 and ρ_0 are the unperturbed pressure and density and γ is the ratio of the specific heats.

Using the Schwarzschild stability criterion it is possible to show that cluster atmospheres are not convectively stable. If this criterion is satisfied then a blob of gas that is adiabatically displaced in a stably stratified atmosphere will exhibit oscillatory motion at the Brunt-Väisälä frequency (e.g. Choudhuri, 1998),

$$\omega^2 = \frac{\mathrm{d}\phi}{\mathrm{d}r}\frac{\mathrm{d}\ln(P/\rho^\gamma)}{\mathrm{d}r}. \tag{2.23}$$

The period associated with this frequency is plotted as a function of radius for the Virgo cluster in figure (2.5). The period rises from roughly 20,000 yr near the origin to approximately 2 Myr at 300 kpc.

The disturbances caused by these oscillations lead to internal gravity waves within the

fluid. They are called internal because they happen within the fluid rather than on its surface. Gravity waves are so-called because they owe their existence to the restoring force of gravity. In atmospheric physics gravity waves can be important for transporting energy from the ground into the upper atmosphere.

Sound waves are non-dispersive, meaning that the phase velocity does not depend on the wave frequency and is equal to the group velocity. In contrast, gravity waves *are* dispersive and the energy can propagate in a completely different direction to the waves themselves. The properties of different types of waves suggest that they could be important when considering how the energy of an outflow is distributed. The heating properties of sound waves have been investigated at some length (e.g. Ruszkowski et al., 2004; Fujita et al., 2004; Fabian et al., 2005; Mathews et al., 2006). Despite the significant body of work on this subject it is not clear whether sound waves can successfully heat the centres of galaxy clusters.

2.6 AGN-blown bubbles

When AGN outflows interact with the ambient material, provided they are over-pressured compared to their surroundings they will excavate a cavity in this medium and fill it with radio-emitting plasma. Consequently, the radio emission from these cavities corresponds to 'holes' when viewed in X-rays (e.g. Bîrzan et al., 2004). The shape of the bubble depends on several factors of which the jet power is one. If the jet is relatively slow the resulting bubble will be roughly spherical. However, as the jet velocity increases the bubble will become progressively less spherical, being elongated as the head of the jet continues to plough through the ambient medium (Soker, 2004).

Once inflated, a bubble will begin to rise buoyantly, being much less dense than its surroundings. As the bubble rises its surface is subject to Rayleigh-Taylor and Kelvin Helmholtz fluid instabilities (e.g. Churazov et al., 2001; Kaiser et al., 2005). These instabilities are due to the less dense bubble supporting the geater density of the ambient medium against a gravitational field and shear motions between the bubble and the exter-

nal medium, respectively. The effect of these instabilities would be to shred the bubbles within a comparatively short period before the bubble has had a chance to rise beyond the inner most regions of the cluster. While this is permissible for some bubbles, others survive, apparently intact, out to comparatively large radii $\sim$ 50kpc, although at such large radii they are also more difficult to spot. Consequently, there appears to be some mechanism, or mechanisms, which help the bubble maintain its structure against the action of the fluid instabilities. The main possibilities for this are viscosity or magnetic fields. However, the recent analytical work of Pizzolato & Soker (2006) suggests that deceleration of the rising bubble could also slow the rate at which the instabilities shred the bubbles. However, this seems unlikely in the light of significant evidence from numerical simulations.

Kaiser et al. (2005) demonstrated analytically that viscous effects can delay the growth of the fluid instabilities, although cannot completely stop them. This effect was verified by numerical simulations by Reynolds et al. (2005) who found that mixing is prevented even if the kinematic viscosity is as little as 1% of the canonical Spitzer value. The analytical work of De Young (2003) and Kaiser et al. (2005) and numerical studies by Robinson et al. (2004) have also demonstrated that magnetic fields can provide an effective surface tension. In the case of magnetised cluster gas, a field strength of a few μG is sufficient to stabilise the bubble surface.

Both observational and theoretical work suggests that thermal conduction and viscosity could play an important role in determining the properties of the intracluster gas. Therefore, it is of interest to investigate some of these effects.

2.6.1 Bubble Inflation

One measure of the amount of energy required to create an X-ray cavity is the PdV work, i.e. the ambient pressure multplied by the volume of the cavity (e.g. Bîrzan et al., 2004). However, the effect of viscosity during the inflation of the bubble is ignored in this case. In principle a sufficiently large shear viscosity could dramatically increase the energy required to inflate bubbles of the volume observed. Using the following, this is shown to

be unlikely.

A full description of the bubble inflation can be obtained from the Rayleigh-Plesset equation which takes into account all of the relevant physical processes. However, a simple analytical estimate suffices to show the effect of viscosity. Consider the following: during a particular time interval a quantity of energy E_0 is injected into a cluster atmosphere and inflates a bubble by PdV work. The total energy in the bubble is given by Churazov et al. (2002) as the sum of the internal energy, $\gamma PV/(\gamma-1)$, and the PdV work. Therefore,

$$E_0 = \frac{\gamma}{\gamma-1} P_0 \Delta V_0 = P_0 \frac{4\pi}{3}\left(r_{\mathrm{max},1}^3 - r_0^3\right) \tag{2.24}$$

where P_0 is the pressure of the cluster gas, $r_{\mathrm{max},1}$ is the final radius of the bubble and r_0 is the initial radius.

For the case where energy is also dissipated by viscosity during the expansion,

$$E_0 - E_{\mathrm{diss}} = \frac{\gamma}{\gamma-1} P_0 \frac{4\pi}{3}\left(r_{\mathrm{max},2}^3 - r_0^3\right) \tag{2.25}$$

where E_{diss} is the energy dissipated by viscosity during the same time interval as energy was supplied and $r_{\mathrm{max},2}$ is the final radius of the bubble for this dissipation process.

Since the final bubble radii are much larger than the initial radii, they can be related to the energy input and dissipated energy by,

$$\frac{E_0 - E_{\mathrm{diss}}}{E_0} = \left(\frac{r_{\mathrm{max},2}}{r_{\mathrm{max},1}}\right)^3. \tag{2.26}$$

Thus, it should be clear that only if the dissipated energy is a significant fraction of the energy input will the final size of the bubbles be drastically different. This suggests that bubbles formed in viscous environments should be indistinguishable from others formed in invsicid, but otherwise identical, conditions.

2.6.2 Bubble rims

Standard theory of plasma bubble inflation suggests that the inflation should be supersonic otherwise Rayleigh-Taylor instabilities on their surface would destroy them before they

fully form (e.g. Reynolds et al., 2005). This is commonly thought to imply that hot shells of compressed ambient gas should be observed around the cavities in constrast to the cool, but bright shell which are actually observed (e.g. Blanton, 2004). That is, the observed shells are both cooler and denser than their surroundings.

Supersonic Rankine-Hugoniot jump conditions (Landau & Lifschitz, 1995) can be used to estimate what sort of conditions one would expect in these shells. The density upstream (subscript 1) and downstream (subscript 2) of the shock around the expanding bubble are related by

$$\frac{\rho_2}{\rho_1} = \frac{(1+\gamma)M_1^2}{2+(\gamma-1)M_1^2}, \tag{2.27}$$

where M, the Mach number, is the ratio of the shock speed to the sound speed.

For a strong shock the downstream to upstream density ratio is always equal to $(\gamma+1)/(\gamma-1) = 4$ for $\gamma = 5/3$, i.e. the density of the shell is 4 times greater than the ambient gas. Thus, since the radiative emission from the shell is proportional to the square of the density, it is understandable that a bubble which has been inflated supersonically should have a bright rim.

The temperature upstream (subscript 1) and downstream (subscript 2) are related by

$$\frac{T_2}{T_1} = \frac{1-\gamma+2\gamma M_1^2}{2+(\gamma+1)}\frac{\rho_2}{\rho_1}, \tag{2.28}$$

where the parameters are as previously specified.

For a strong shock equation (2.28) can be simplified to

$$\frac{T_2}{T_1} = \frac{5}{16}M_1^2. \tag{2.29}$$

Thus, for a strong shock with Mach number equal to 10, the downstream:upstream temperature ratio is roughly 30. From equation (2.29) it is apparent that, unlike the density of shocked material which can be at most a factor of 4 greater than the unshocked gas, the temperature of the shocked gas increases proportionally to the square of the Mach number.

The ratio of the radiated energy per unit volume per unit time in the rim compared to

the ambient material is

$$\frac{\epsilon_2}{\epsilon_1} = \left(\frac{\rho_2}{\rho_1}\right)^2 \left(\frac{T_2}{T_1}\right)^{0.5} \approx 8.9 M_1, \tag{2.30}$$

For $M_1 = 10$ the shocked material radiates roughly 89 times more powerfully, per unit volume, than the ambient material. Consequently, the shells would be expected to be very much brighter than the surrounding material.

Using equations (2.27) and (2.29) for the shell temperature and density it is possible to calculate radiative cooling time-scale for both the ambient gas and the shell gas. As before, the radiative cooling time-scale is defined by equation (2.16) as the internal energy divided by the rate of energy loss.

Assuming that thermal bremsstrahlung is the main radiative process, the ratio of the cooling times is

$$\frac{\tau_{\mathrm{cool2}}}{\tau_{\mathrm{cool1}}} = \frac{n_1}{n_2}\left(\frac{T_2}{T_1}\right)^{0.5} = M_1 \frac{\sqrt{5}}{16}. \tag{2.31}$$

Therefore, the radiative cooling time of the shocked material will be less than that of the ambient material if the Mach number is not too large. The specific requirement is $M_1 < 7.16$, which for a $10^8 K$ cluster atmosphere suggests that the speed of the inflation must be less than roughly 4% of the speed of light. This means that bright, cold rims can only occur if the shock is not too strong.

2.6.3 Bubble rise velocity

Due to the large density difference between the bubble and ambient materials the buoyancy force acting on the bubble is large. As a consequence the rise velocities are also large and the drag force on the bubble is dominated by the effects of turbulence rather than viscosity, if viscosity is low.

The equation of motion for a spherical bubble of radius r_{b} is

$$M_{\mathrm{b}}\ddot{x} = \frac{4\pi}{3} r_{\mathrm{b}}^3 g(\rho_{\mathrm{ext}} - \rho_{\mathrm{b}}) - \frac{1}{2}\rho_{\mathrm{ext}}\dot{x}^2 C_{\mathrm{D}} \pi r_{\mathrm{b}}^2, \tag{2.32}$$

where x is the radial coordinate, g is the gravitational acceleration, ρ_{b} is the density of the bubble, ρ_{ext} is the density of the external medium. r_{b} is the bubble radius and C_{D}

is the drag coefficient, which is usually assumed to be roughly 0.5 (e.g. Churazov et al., 2001).

The simplest way to solve equation (2.32) is to assume that the bubble radius and density and the gravitational acceleration are all constant. In reality, the ambient pressure of the cluster gas falls with increasing radius which would cause the bubble to expand and the bubble density to fall. The gravitational acceleration also falls with increasing distance from the cluster centre (Kaiser, 2003). However, in the simple case outlined, the velocity is,

$$\dot{x}^2 = \frac{2Vg}{C_{\rm D}A}\left[1 - \exp\left(-x^2\frac{V\rho_b}{A\rho_{\rm ext}C_{\rm D}}\right)\right], \tag{2.33}$$

where V is the volume of the bubble, A is the projected surface area.

Therefore, the terminal velocity is,

$$\dot{x} = \left(\frac{2Vg}{C_{\rm D}A}\right)^{1/2} \tag{2.34}$$

Substituting appropriate values for the bubble radius, 10^{22}cm, gravitational acceleration, $g \sim 10^{-7}\mathrm{cm\,s^{-2}}$ and drag coefficient, $C_{\rm D} \sim 0.5$, gives $\dot{x} \sim 7 \times 10^7\ \mathrm{cm\,s^{-1}}$, which is roughly equal to, but less than, the sound speed of the cluster gas.

As the bubble rises the pressure of the external medium continues to drop. This causes the bubble to expand so as to maintain pressure equilibrium which causes the density to fall. Eventually the bubble reaches a radius at which the densities of the bubble material and the external medium are very similar. At this point the buoyancy force becomes negligible and the bubble begins to spread out forming a 'pancake'(Churazov et al., 2001). Of course, the bubble density at formation was significantly lower than that of the ambient medium. Therefore, for this stagnation of the bubble rise to occur means that the density of the cluster atmosphere must decline more rapidly than that of the bubble. For reasons that will become clear, the radius at which the rise of the bubble stagnates is called the 'isoentropy radius'.

2.6.4 Isoentropy radius

Despite the assumption of fixed bubble size in the derivation of the buoyant rise velocity, a more realistic view is that as the bubble rises it expands adiabatically to maintain pressure equilibrium with its surroundings. This means that the bubble pressure and density at any radius can be related to their values at formation by

$$\frac{P}{\rho_{\rm b}^{\gamma}} = \frac{P_0}{\rho_{\rm b,0}^{\gamma}}, \tag{2.35}$$

where the subscript 0 denotes the values at formation.

The central regions of cluster atmospheres are approximately isothermal. This means that the radial dependence of the pressure can be expressed in terms of the density of the cluster gas, $\rho_{\rm ext}$. Using this argument and substituting into equation (2.35) suggests that $\rho_{\rm ext} \propto \rho_{\rm b}^{\gamma}$. Since γ is generally greater than unity (5/3 for an ideal monatomic gas) this means that the bubble density must fall less quickly than the ambient density, thus it is possible for the buoyancy force to dissappear and the bubbles can stagnate at a particular radius.

Substituting temperature and density for pressure in equation (2.35) gives the entropy index $\sigma_{\rm ent}$ which, for a monatomic, ideal gas, is,

$$\sigma_{\rm ent} = \frac{T}{n^{\gamma-1}} = \frac{T}{n^{2/3}}, \tag{2.36}$$

where T is the temperature and n is the number density of the gas.

If the assumption that the bubbles are in pressure equilibrium with the surroundings is true, then this means that at the radius where the bubble density equals the ambient density, the temperatures must be equal as well. Following from this, equation (2.36) implies that the entropy indices of the ambient and bubble material must also be equal. Hence the term 'isoentropy radius' may be applied to this location.

For adiabatic processes the entropy index of a gas will not change, therefore if the entropy index of a bubble is known (or calculated) it is trivial to extrapolate the radius at which the entropy index of the ICM becomes comparable with the entropy index of the

bubble material. However, calculations show that the radii at which these entropy indicies occur are several hundreds of kiloparsecs.

The fact that bubbles are never observed at such large radii could be due to three possibilities: i) hydrodynamic instabilities shred the bubble before it can reach these distances ii) the bubbles do not behave adiabatically and never reach such large radii or iii) The bubbles do reach such radii but we cannot observe them. The first of these suggestions seems less likely than the second since it seems that fluid instabilities must be suppressed in order for the bubble to rise out from the central regions at all. However, the second suggestion could be more plausible and could occur as a result of radiative processes, or energy dissipation by thermal conduction or viscosity. In fact non-adiabatic process are required to increase the entropy of the ambient gas that is radiatively cooling. Consequently, it seems likely that the adiabatic assumption overestimates the isoentropy radii and that a more accuate calculation is required to better estimate this radius.

2.7 Summary

The observed density profiles of the ICM are generally well matched by β-profiles, but are not considerably different from that of a self-gravitating isothermal sphere. This provides a useful starting point for analytical and numerical work on galaxy clusters.

Cooling is clearly an important part of any model of the ICM. The fact that cooling is more rapid near the cluster centre leads to a drop in temperature near the centre and the formation of a cooling flow. If cooling continued unabated a cooling catastrophe would inevitably occur. Heating by AGNs is a possible mechanism by which radiative cooling can be controlled. AGNs can heat their surroundings by a variety of methods: photoionisation, the effects of sound and gravity waves and PdV work done performed by the expanding plasma bubbles as they rise buoyantly through the ICM.

Many of the properties of AGN-blown buoyant bubbles can be estimated analytically, however, to study them in greater detail requires the use of numerical simulations.

Chapter 3

Numerical Simulations of Galaxy Clusters

3.1 Introduction

Simplified initial conditions of galaxy clusters can be obtained relatively easily. However, the subsequent evolution becomes rather complex and requires the equations of hydrodynamics to be solved.

The complexity of the task is increased further by the inclusion of AGNs as heating sources. Self-similar models of radio sources can be derived (e.g. Falle, 1991; Kaiser & Alexander, 1997) but when the interaction with the ICM is taken into consideration the problem becomes 3-dimensional rather 1-dimensional. The best way to study this interaction in sufficient detail is to use numerical simulations.

The code that has been chosen to investigate these phenomena is the FLASH code (Fryxell et al., 2000). FLASH is an adaptive-mesh refinement (AMR) hydrodynamical code developed and made public by the ASC Center at the University of Chicago. It is a modular block structured AMR code, parallelized using the Message Passing Interface (MPI) library.

FLASH has been well tested on a wide range of standard fluid and gravitational test problems with great success (Fryxell et al., 2000). It has also been updated regularly and can be used with confidence. This chapter provides an introduction to the computational techniques used in FLASH and the alterations that were made to tailor the code to the specific purposes of AGN heating and galaxy clusters. Also included are the methods used for setting up the initial conditions of the simulations.

3.2 Finite Difference Methods

Partial differential equations (PDEs) are used to formulate and solve problems that involve unknown functions of several variables, for example fluid flow. They comprise an unknown set of functions of several independent variables and partial derivatives with respect to those variables. FLASH solves the relavent PDEs using the finite difference method.

The finite difference method essentially amounts to discretising derivatives which appear in the PDEs in both time and space. This results in a system of algebraic relations between approximate values at all spatial grid points. The set of equations can then be solved for the discrete grid-point values on the computer. For example, if $q(\mathbf{x}, t)$ is a known analytical function, then, on a finite grid, the approximate value of this function at a location x_i and at time t_n is $Q_\mathrm{i}^\mathrm{n} \approx q(x_\mathrm{i}, t_\mathrm{n})$.

As an example of the finite difference method, consider the advection equation,

$$\frac{\partial q}{\partial t} + v\frac{\partial q}{\partial x} = 0 \tag{3.1}$$

.

The simplest way to discretise the derivatives is to use the one-sided approximation to both $\partial q/\partial t$ and $\partial q/\partial x$. If the grid points are uniformly separated by a distance h, then during a timestep of Δt equation (3.1) can be written,

$$\frac{Q_\mathrm{i}^{\mathrm{n}+1} - Q_\mathrm{i}^\mathrm{n}}{\Delta t} + v\left(\frac{Q_\mathrm{i}^\mathrm{n} - Q_{\mathrm{i}-1}^\mathrm{n}}{h}\right) = 0, \tag{3.2}$$

or

$$\frac{Q_\mathrm{i}^{\mathrm{n}+1} - Q_\mathrm{i}^\mathrm{n}}{\Delta t} + v\left(\frac{Q_{\mathrm{i}+1}^\mathrm{n} - Q_\mathrm{i}^\mathrm{n}}{h}\right) = 0. \tag{3.3}$$

Which of these is appropriate to use depends on the direction of the velocity, v. If the fluid flows from left to right then equation (3.2) should be used since it updates Q_i^n using the value to the left, in the upstream direction. If the fluid flows in the opposite direction, equation (3.3) should be preferred.

Equation (3.2) can be re-written to give an explicit formula for Q_i^{n+1}, in terms of data at the previous timestep,

$$Q_i^{n+1} = Q_i^n - \frac{\Delta t}{h} v(Q_i^n - Q_{i-1}^n). \tag{3.4}$$

Centred approximations to the derivatives can be used to achieve an increase in the accuracy of the estimate to second order,

$$\frac{Q_i^{n+1} - Q_i^{n-1}}{2\Delta t} + \nu\left(\frac{Q_{i+1}^n - Q_{i-1}^n}{2h}\right) = 0, \tag{3.5}$$

which gives,

$$Q_i^{n+1} = Q_i^{n-1} - \frac{\Delta t}{h} v(Q_{i+1}^n - Q_{i-1}^n). \tag{3.6}$$

There are numerous other ways of discretising derivatives but the examples above provide a sufficient introduction to the principles of the theory to understand the subsequent sections.

3.3 The FLASH code

3.3.1 The Hydrodynamic equations

The hydrodynamical equations can be formulated with respect to two classes of reference frames. This results in two distinct methods of implementation of the equations in numerical techniques. In the Lagrangian frame, a frame of reference that is co-moving with the fluid element is used. The fluid density and velocity can be defined for the fluid element. This approach is the basis of smoothed particle hydrodynamics numerical methods.

In the Eulerian frame, a fixed system of reference is used, measuring the properties of the fluid at each point in space and determining how these properties change with time.

Thus, in the Eulerian formulation characteristics of the flow are functions of space and time: $\mathbf{v}(\mathbf{r},t)$, $\rho(\mathbf{r},t)$, where $\mathbf{v}$ is the velocity, ρ the density and $\mathbf{r}$ is the position vector and t is the time.

The FLASH hydro module solves Euler's equations for compressible gas dynamics in one, two, or three spatial dimensions. These equations can be written in conservative form as,

$$\frac{\partial \rho}{\partial t} + \nabla.(\rho \mathbf{v}) = 0 \tag{3.7}$$

$$\frac{\partial \rho \mathbf{v}}{\partial t} + \nabla.(\rho \mathbf{v}\mathbf{v}) + \nabla P = \rho \mathbf{g} \tag{3.8}$$

$$\frac{\partial \rho E}{\partial t} + \nabla[(\rho E + P)\mathbf{v}] = \rho \mathbf{v}.\mathbf{g} \tag{3.9}$$

where ρ is the fluid density, $\mathbf{v}$ is the fluid velocity, P is the pressure, E is the sum of the internal energy ϵ and kinetic energy per unit mass,

$$E = \epsilon + \frac{1}{2}|\mathbf{v}|^2, \tag{3.10}$$

$\mathbf{g}$ is the acceleration due to gravity, and t is the time coordinate. The pressure is obtained from the energy and density using the equation of state. For an ideal gas equation of state, the pressure is given by

$$P = (\gamma - 1)\rho\epsilon, \tag{3.11}$$

γ is the ratio of the specfic heats.

For non-adiabatic flows it is necessary to account for possible losses and gains of heat from external and internal sources. For example, a cooling function can be added to the right hand side of equation (3.9)

$$\frac{\partial \rho E}{\partial t} + \nabla[(\rho E + P)\mathbf{v}] = \rho \mathbf{v}.\mathbf{g} - \left(\frac{\rho}{\mu m_{\rm p}}\right)^2 \Lambda(T,\rho) \tag{3.12}$$

where $\Lambda(T,\rho)$ is the cooling function as a function of temperature and density.

3.3.2 Solving the Energy Equation

The simplest way to temporally advance the fluid equations (equation (3.7) and (3.9)) is the first-order explicit Euler scheme,

$$U_{n+1} = U_n + \Delta t L(U_n) \tag{3.13}$$

where $L(U)$ represents an operator on the state U_n. In terms of the FLASH code, $L(U)$ represents the physics modules.

3.3.3 Thermal Conduction and Viscosity

Diffusive processes can be added to the Euler equations. For example, when taking in to account thermal conductivity and viscosity, FLASH diffuses the quantities of temperature and momentum using the standard diffusion equation,

$$\frac{\partial X}{\partial t} = \nabla(D\nabla X) \tag{3.14}$$

where X is the quantity to be diffused, and D is the diffusion coefficient. The coefficient of thermal diffusion (χ) is related to the coefficient of thermal conductivity (κ) by $\chi = \frac{\kappa}{\rho c_p}$, where c_p is the specific heat at constant pressure.

For the high temperatures of cluster atmospheres the coefficients of thermal conductivity and viscosity are given by the value calculated by Spitzer (1962). In the absence of magnetic fields the coefficients of Spitzer thermal conductivity and viscosity are

$$\kappa_s = \frac{1.84 \times 10^{-5}}{\ln \Lambda_c} T^{5/2} \text{ [erg s}^{-1}\text{cm}^{-1}\text{K}^{-1}\text{]}, \tag{3.15}$$

$$\mu_s = \frac{2.5 \times 10^{-15}}{\ln \Lambda_c} T^{5/2} \text{ [g s}^{-1}\text{cm}^{-1}\text{]}, \tag{3.16}$$

where $\ln \Lambda_c$ is the Coulomb logarithm, defined by equation (3.17).

The standard issue of FLASH provides a module for calculating the Spitzer thermal conductivity and viscosity for typical coronal values of the Coulomb logarithm, $\ln \Lambda_c = 20$.

However, due to the large variation in density over cluster-scale distances it is necessary to take into account the variation of the Coulomb logarithm given by (e.g. Choudhuri, 1998)

$$\Lambda_{\rm c} = 24\pi n_{\rm e}\left(\frac{8\pi e^2 n_{\rm e}}{k_{\rm B}T}\right)^{-3/2}. \tag{3.17}$$

3.3.4 The Piecewise-Parabolic Method

The hydrodynamic equations are solved by FLASH using a modified version of the Piecewise-Parabolic Method (PPM) descended from the PROMETHEUS code (Fryxell et al., 1989). It is a higher-order version of the method developed by Godunov (1959).

In Godunov's method, the flow is divided into a series of slabs, each of which occupies a single zone of the computational grid. The discontinuities between these slabs are treated by solving Riemann's shock tube problem at each zone interface. This treatment has the effect of introducing explicit nonlinearity into the difference equations and permits the calculation of sharp shock fronts and contact discontinuities without introducing significant nonphysical oscillations into the flow. Since the value of each variable in each slab is assumed to be constant, this method is limited to first-order accuracy in both space and time. The conserved quantities are advanced in time by solving conservative finite-difference equations with fluxes computed using the values obtained from the Riemann problem solution (Fryxell et al., 2000).

A formalism for extending Godunov's method to higher order was developed with the MUSCL scheme of van Leer (1979), in which second-order accuracy in both space and time is achieved by representing the flow variables as piecewise linear instead of piecewise constant functions. This is analogous to switching from the rectangle rule to the trapezoidal rule for numerical integration of a function. Another major advance of MUSCL was the incorporation of monotonicity constraints instead of artificial viscosity to eliminate oscillations in the flow. PPM takes the next logical step by representing the flow variables as piecewise parabolic functions. This corresponds to switching to Simpson's rule for numerical integration.

PPM can be characterized as a finite-volume method, rather than as a finite-difference method, since the initial conditions for a problem are specified as the average of each variable in each computational element rather than as values at particular points in space, such as zone centers or zone interfaces. Typically, the variables that are specified include the gas density, the three components of the fluid velocity, the specific internal energy, and the mass fraction of each nuclear species. Additional variables that are required, such as the zone average values of the pressure, temperature, and adiabatic indices, can be obtained from these using the equation of state.

FLASH also uses a second-order operator splitting method to solve the PDEs. Essentially this means that a set of simple sub-problems is solved rather than a single complex problem. Typically, each sub-problem accounts for one term in a system of PDEs. A key feature of this method is that the output of one sub-problem is the input to the next. This can lead to some errors which are reduced by tackling the simplest sub-problem and the next most difficult next, and so on. If all the sub-problems are computed to second-order accuracy, the basic operator splitting method is accurate to first order. However, the Strang (1968) splitting scheme achieves second-order accuracy over two timesteps by solving each of the problems in a given sequence in the first timestep and in reverse order in the next timestep. For the three-dimensional case, the one-dimensional sweeps of the variables are performed in the order $xyz - zyx$.

3.3.5 The Courant-Friedrich-Levy Condition

FLASH calculates three limiting timesteps based on the requirements for consistency in the hydrodynamics, radiative cooling and diffusive processes (thermal conduction and viscosity) of the solution in the entire computational grid. In each timestep the partial differential equations are solved and the system of coupled ordinary differential equations are time-integrated using the minimum of these timesteps.

The hydro timestep is derived from the Courant, Friedrichs and Levy (CFL) condition which essentially requires that material cannot move across more than one cell during a

timestep. This requires that $\Delta t(|v_x| + c_s) < \Delta x$ therefore,

$$\Delta t^{\rm CFL} = C\min\left(\frac{\Delta x}{|v_x| + c_s}, \frac{\Delta y}{|v_y| + c_s}, \frac{\Delta z}{|v_z| + c_s}\right) \tag{3.18}$$

where Δx is the cell dimension, c_s is the sound speed in that cell and C is the CFL coeffient which is set to 0.8 in these simulations.

The cooling timestep is given by

$$\Delta t^{\rm cool} = \frac{e_i}{({\rm d}e_i/{\rm d}t)} \tag{3.19}$$

where e_i is the internal energy per unit volume and ${\rm d}e_i/{\rm d}t$ is the rate of change of internal energy. This timestep is usually very large except for very high cooling rates which correspond to catastrophic cooling, so it is largely unimportant. The diffusion timestep is given by

$$\Delta t^{\rm diff} = 0.5\frac{\min(\Delta x^2)}{\max(\chi)} \tag{3.20}$$

where $\min(\Delta x^2)$ is the smallest cell dimension, χ is the diffusivity and $\max(\chi)$ is the largest diffusivity in the computational zone. This timestep is smaller for larger values of thermal conduction and viscosity.

3.3.6 Adaptive Mesh Refinement

One of the benefits of FLASH is that the numerical resolution can change in response to particular circumstances. This is advantageous compared to a uniform grid because it allows regions of high resolution where they are required and low resolution elsewhere. This can significantly reduce the memory requirements compared to a uniform grid with high resolution everywhere, and consequently improve the running speed dramatically.

FLASH uses a criterion based on the dimensionless second derivative,

$$D^2 \equiv |(F{\rm d}^2F/{\rm d}x^2)/({\rm d}F/{\rm d}x)^2|, \tag{3.21}$$

of a fluid variable F to increase the resolution adaptively whenever $D^2 > c_2$ and de-refine the grid when $D^2 < c_1$, where $c_{1,2}$ are user-defined tolerance parameters. When a region requires refining ($D^2 < c_1$), $2^{\rm d}$ child grids with cell size half that of the parent grid are

placed over the offending region, and the coarse solution is interpolated, where d is the number of spatial dimensions. Each time a given cell refines an extra level of refinement is added, the initial level of refinement is one. For example, if a cell refines once, the level of refinement is two.

3.3.7 Hardware

The simulations were performed on two of the University of Southampton's Beowulf clusters. The first of these, Iridis 1, was used initially and has then been superceded by Iridis 2 with improved speed and memory.

Iridis currently comprises 814 processors, consisting of 600 2.2GHz AMD Opterons and 214 1.8 GHz Intel Xeons. It is an example of a distributed memory computer. These are supercomputers made of individual processor nodes with local memory, where the individual CPUs (nodes) are connected via low latency, high bandwidth connections. The main advantage of the architecture is its low cost. Beowulf clusters can be built from commodity PCs and communicate via Ethernet or Myrinet switchers.

3.3.8 Software

The hydrodynamics code used was FLASH 2.3 and MPICH libraries were used to pass messages. The simulations were performed using code compiled with Portland group compilers. The data were rendered using IDL.

3.4 Initialisation

The density, pressure and gravitiational potential must all be set to specify the intial configuration of the gas. As already stated, the pressure and gravitational potential were set such that the gas was initially in hydrostatic equilibrium. The gravitational potential is assumed to be dominated by non-baryonic dark matter that does not evolve with time.

This means that it is not necessary to calculate the gravitational potential at each timestep and so leads to a dramatic reduction in CPU time.

3.4.1 Boundary conditions

The boundary conditions need to be set at the edges of all grid coordinates. The specific type of boundary depends on the requirements of the simulation. For simulations using 3-d cartesian coordinates periodic boundary conditions do not always make sense, so outflow or hydrostatic boundary conditions were used.

3.4.2 Gravitational Potential

The gravitational potentials for the simulations performed here are derived from observations of real clusters. To do this it is necessary to assume that the cluster atmospheres are in hydrostatic equilibrium, since there is no method to determine the inflow velocity of the gas. Reassuringly, the hydrostatic approximation is good provided that the inflow of gas is subsonic. If the gas is assumed to be initially in hydrostatic equilibrium, then,

$$\nabla P_{\rm obs} = -\rho_{\rm obs} \nabla \phi, \tag{3.22}$$

where $P_{\rm obs}$ is the observed gas pressure, $\rho_{\rm obs}$ is the observed gas density and ϕ is the gravitational potential.

For simplicity, the gravitational potential is assumed to be spherically symmetric. Using the ideal gas equation, which relates the gas pressure to temperature and density, the gravitational acceleration, g, can be determined from the observed temperature and density profiles,

$$g \equiv -\nabla\phi = \frac{k_{\rm b}}{\mu m_{\rm p}} \left(\frac{{\rm d}T_{\rm obs}}{{\rm d}r} + \frac{T_{\rm obs}}{n_{\rm obs}} \frac{{\rm d}n_{\rm obs}}{{\rm d}r} \right), \tag{3.23}$$

In the simulations, the gas is initially assumed to be isothermal. Using this assumption, along with the gravitational acceleration already calculated, allows the initial density

profile to be calculated. Re-writing equation (3.22) for an isothermal gas gives,

$$\nabla\left(\frac{k_{\rm b}T_{\rm iso}}{\mu m_{\rm p}}\ln\rho\right) = \nabla\phi, \tag{3.24}$$

where $T_{\rm iso}$ is the isothermal temperature and ρ is the corresponding gas density profile .

Integrating both sides of equation (3.24) and rearranging for ρ gives,

$$\rho = \exp\left(\frac{-\mu m_{\rm p}\phi}{k_{\rm b}T_{\rm iso}} + C\right), \tag{3.25}$$

where C is a constant of integration and ϕ is the gravitational potential calculated from equation (3.24).

Taking $\phi = 0$ at $r = 0$ means $\rho = \exp(C) =$ constant at the origin. Therefore, we can write

$$\rho = \rho_0 \exp\left(\frac{-\mu m_{\rm p}\phi}{k_{\rm b}T_{\rm iso}}\right). \tag{3.26}$$

Of course, ρ_0 is not entirely a free parameter and must be chosen with care to ensure that the initial density profile is consistent with observations. Since the gas density at large radii does not change much over time, ρ_0 should be chosen so that at large radii the isothermal density profile approximately matches the observed density profile. The value of ρ_0, or the corresponding concentration n_0, required for the isothermal density profile to match the observed density profile is,

$$n_0 = n_{\rm obs}\exp\left(\frac{-\mu m_{\rm p}\phi}{k_{\rm b}T_{\rm iso}}\right). \tag{3.27}$$

Clearly, n_0 is sensitive to the value of the isothermal temperature: for larger temperatures it is smaller and vice versa. Because of this there is an element of trial and error to finding appropriate initial conditions. For example, the initial temperature should be slightly higher than the observed temperature, at large radii, so that it can cool towards the lower observed temperatures as time passes. The temperature at large radii, in the simulation, should not fall below the currently observed temperature within the age of the Universe. If the initial conditions are appropriate and the simulations work as planned, the temperature and density profile of the simulation should pass through a phase that is

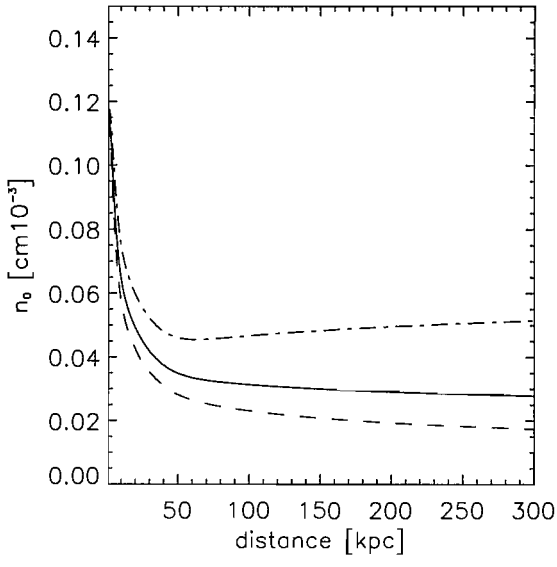

Figure 3.1: Value of n_0 for which the isothermal density profile matches the observations of the Virgo cluster, for three different isothermal temperatures. The solid line gives the results for $T_{\rm iso} = 3 \times 10^7$K, the dashed line is for $T_{\rm iso} = 2.6 \times 10^7$K and the dot-dashed line is for $T_{\rm iso} = 3.6 \times 10^7$K.

reminiscent of the observations. With this in mind, isothermal temperatures for a simulation mimixking the Virgo cluster are chosen and suitable values of n_0 are chosen using figure 3.1 outside 50 kpc where the curves flatten off.

3.5 Customising FLASH

3.5.1 Cooling Module

The original cooling routine in FLASH implements radiative losses from an optically thin plasma (Raymond & Smith, 1977) adopting a piecewise-power-law approximation that provides a reasonable fit to $\Lambda(T)$. As with many modules in FLASH, the cooling module was originally designed with stellar atmospheres in mind, rather than galaxy clusters. This necessitates the implementation of a cooling function that is more suitable to requirements of a galaxy cluster.

To speed up the computation of the radiative losses, the exponents of the cooling function are tabulated for a wide range of temperatures. In the temperature range 10^4K to $10^{8.5}$K the tabulated values of the cooling function given by Sutherland & Dopita (1993) are used. Above $10^{8.5}$K pure bremsstahlung emission is assumed while the cooling rate is set to zero for temperatures below 10^4K. For any value of temperature, a value for the cooling function is interpolated from the tables using the cubic spline method taken from Press et al. (1992).

3.6 Testing Flash

3.6.1 Speedup

Speed-up measures how much the run-time of a program is reduced by running it in parallel on a multiple CPU cluster. However, rather than time, speedup is normally the parameter that is studied. t_1 is the time required by a sequential algorithm to solve a particular problem. Similarly, t_N is the time required to solve the same problem on N processors. Then, the speedup, S, for the problem is defined as

$$S = \frac{t_1}{t_N}, \tag{3.28}$$

and efficiency is defined as,

$$E = \frac{S}{N}. \tag{3.29}$$

The potential speed-up is limited by the fraction of the code that can be parallelised,

$$S = \frac{1}{(p/N + (1-p)} \tag{3.30}$$

where p is the parallel fraction of the code. Equation (3.30) is known as Amdahl's Law.

Consider an example: a program is 99% parallelised and 1% serial. It takes 100 s to execute on a single CPU. Therefore, if it runs on 100 CPUs, the parallel section of the program will excecute in 0.99s, and the total run time will be 1.99s. The speedup in this case is $100/1.99 = 50.25$, and the efficiency $\approx 50\%$. However, in practise the parallelised

fraction is not always well known. Furthermore, Amdahl's Law does not take into account the time required for the nodes to communicate with each other. From equations (3.28) and (3.30) the minimum possible time for a job which is partially paralleliseable is,

$$t_{\rm N} = t_1 \left[\frac{p}{N} + (1-p) \right] \tag{3.31}$$

However, as the number of processors increases so does the time they spend communicating with each other. For example, running a small job on many processors need not run more quickly than on fewer processors because of this overhead. This effect is likely to lead to an extra term which is proportional to the number of processors such that,

$$t_{\rm N} = t_1 \left[\frac{p}{N} + (1-p) \right] + BN, \tag{3.32}$$

where B is a constant which is probably related to the average communication time required by 2 processors.

The optimum number of processors is calculated by differentiating equation (3.32) and setting the result equal to zero,

$$N_{\rm opt} = \sqrt{\frac{t_1 p}{B}} \tag{3.33}$$

If $B = 5\,{\rm s}$ is equal to the average communication time between processors, then for the parameters above, the optimum number of processors is, 4.

In reality, B, as with p, is not easy to determine and there are likely to be other important factors which will slightly alter this predicted optimum. In addition, for some of the jobs t_1 is likely to be of the order of months and since $N_{\rm opt} \propto \sqrt{t_1}$ the optimum number of processors would reach several hundred. Clearly this is not realistic and the practical limit is in the region of 30 or so processors.

An investigation of the speed-up properties of FLASH was conducted using a 2-d passive cooling flow simulation of the Virgo cluster. The cluster was allowed to evolve for 10^9 yrs on a cubic, uniform grid of dimension 5×10^{23} cm (or 162.1 kpc), with minimum and maximum refinement levels 2 and 5, respectively.

Using the definition of the potential speed-up, in equation (3.30), it is possible to calculate the maximum fraction of the code (P) that is parallelised. This assumes that

Number of processors	time taken	Speed up	Efficiency	$P_{\max}$
1	507	1	1	-
2	277	1.83	0.92	0.91
4	145	3.50	0.88	0.95
6	114	4.45	0.74	0.93
8	98	5.17	0.65	0.92
16	95	8.58	0.54	0.94

Table 3.1: Speed up parameters for a simulation run on dual CPU machines.

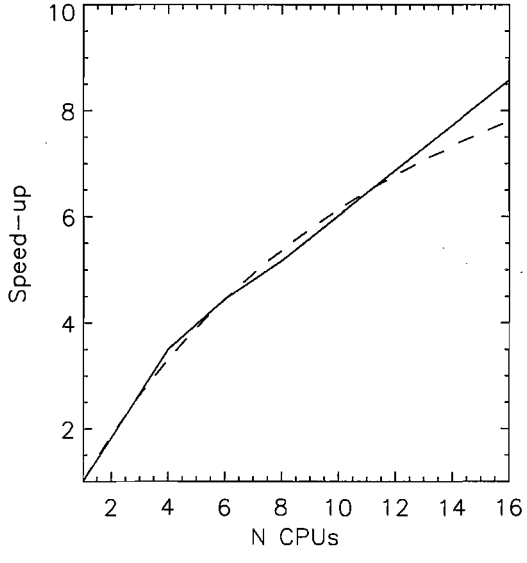

Figure 3.2: The speed-up of Southampton's version of FLASH (solid line) and a comparison with the expected speed-up for P=0.93 (dashed line).

the time taken for the nodes to communicate with each other is a negligible contribution to total time taken to complete the job. In reality this contribution becomes more significant as the number of processors increases, but ignoring it provides a firm upper limit on the parallel fraction of the code,

$$P_{\max} = \frac{(1/S) - 1}{(1/N) - 1}. \tag{3.34}$$

The individual $P_{\max}$ values are all very close to each other, suggesting that this is indeed a good estimate of the parallel fraction of the code. The mean value for running this is $P_{\max} = 0.93$, see table 3.2. Substituting this into equation (3.30) suggests that the

maximum possible speed-up for this code is $S_{\max} = 1/(1-P) \approx 14.3$. This means that on a sufficiently large number of processors the code can only run a maximum of roughly 14 times faster than on a single processor.

3.7 Summary

The most notable alteration to the FLASH code has been the updating of the cooling module. However, the thermal conduction and viscosity modules have also been altered to make them appropriate for galaxy clusters.

In the next chapters the routines described here will be used to study the effects of viscosity and thermal conduction on the developement of a cooling flow, and the interaction of an AGN with the ICM.

Chapter 4

The Effect of Thermal Conductivity on the Virgo and Perseus Clusters

4.1 Introduction

The presence of large temperature gradients in the centres of many relaxed clusters allows the possibility that thermal conduction may play a role in reducing the radiative energy losses in the cluster centre. Indeed, Zakamska & Narayan (2003) have shown that for several galaxy clusters the inward heatflow from the outer regions due to thermal conduction may be sufficient to balance the radiative losses although, in a different sample Voigt et al. (2002) showed that thermal conduction is only able to balance radiative losses in the outer regions of the cluster core. However, though it is possible to achieve an energy balance for these clusters in their present state, this requires the thermal conductivity to vary as a function of radius. Furthermore, it is unclear what effect thermal conduction would have on the ICM if it constitutes a significant process throughout the lifetime of the cluster. Since thermal conduction acts to oppose the formation of the temperature gradient that causes it, one might expect that the temperature and density profiles for those clusters in

which thermal conduction plays a significant role to appear different compared to those clusters in which thermal conduction is less effective. In particular, the temperature profiles in such clusters could be much flatter than in clusters where thermal condcution is heavily suppressed. In addition, temperature gradients also occur outwards towards the edge of clusters. Therefore, it is possible that the high thermal conductivities required to balance the radiative losses may also have a cooling effect by transporting energy away from the cluster centre and out into intercluster space (Loeb, 2002).

One of the primary problems for studying the effects of thermal conduction in plasmas is the unknown value of the thermal conductivity. The theoretical value for the thermal conductivity of a fully ionized, unmagnetized plasma was originally calculated by Spitzer (1962). However, observations indicate the existence of a magnetic field in the ICM ($B < 10\ \mu G$; e.g. Carilli & Taylor, 2002) which can affect this value dramatically. For magnetic fields of these strengths the electron and proton gyro-radii are much smaller than their mean free paths along the field lines. The precise effect that magnetic fields have on thermal conductivity is unclear, although for magnetic fields of the observed strengths the effective thermal conductivity is determined by the topology of the field (Markevitch et al., 2003). A magnetic field tangled on scales much longer than the electron mean free path will suppress thermal conduction perpendicular to the field lines reducing the thermal conductivity to at most one third of the full Spitzer value (if transport along the field line is unaltered) (Sarazin, 1986). For a magnetic field tangled on scales shorter than the electron mean free path the conductivity is suppressed by a factor of up to 100 as the electrons have to travel further to diffuse a given distance perpendicular to the field (Tribble, 1989). In addition, for tangling lengths that are comparable to the electron mean free path, conduction along the magnetic field line can be reduced by a factor of roughly 10 by the effect of magnetic mirrors (Malyshkin & Kulsrud, 2001). Alternatively, recent theoretical work by Narayan & Medvedev (2001) and Cho et al. (2003) has shown that for certain spectra of field fluctuations, turbulent magnetic fields are less efficient at suppressing thermal conduction than previously thought. The highly tangled, turbulent magnetic field may allow significant cross field diffusion such that the thermal conductivity remains of the order of the Spitzer value. In any case the collisional thermal conductivity on 100 kpc scales is likely to be reduced by a factor of 3-100 (Markevitch et al., 2003).

The suppression factor, f, is defined by $\kappa = f\kappa_S$, where κ is the actual thermal conductivity and κ_S is the Spitzer thermal conductivity. To date this factor has been very difficult to constrain from observations: Voigt et al. (2002) and Zakamska & Narayan (2003) find that suppression factors of > 0.3 are sufficient to balance radiative losses in some cluster while other clusters require unphysically high values ($f > 1$). In other cases, the temperature drops across cold fronts in A2142 (Ettori & Fabian, 2000) implies a suppression factor of < 0.004. At the boundaries between the ICM and galaxy-size dense gas clouds in Coma (Vikhlinin et al., 2001) the thermal conductivity is found to be suppressed by a factor of order one hundred. However, one might reasonably expect both of these cases not to be characteristic of the bulk ICM, since they contain boundaries between different gas phases and disjointed magnetic fields. Another estimate uses the existence of cold filaments in galaxy clusters (Nipoti & Binney, 2004) to put constraints on the value of the suppression factor. Although not all of the values of the required quantities are well known, they find that for the Perseus cluster the suppresion factor is < 0.04, which result they consider to be compatible with the results of Markevitch et al. (2003) based on observations of temperature gradients present in A754.

The aim of these simulations is to investigate whether thermal conduction can prevent the catastrophic radiative cooling of the gas at the centres of galaxy clusters by transporting thermal energy from the cluster outskirts to the centre. The temperature and density profiles which occur with this heating process are compared with those derived from X-ray observations.

4.2 Heating by Thermal Conduction

As previously stated, thermal conduction transfers heat so as to oppose the temperature gradient which causes the transfer. In this respect it is a negative feedback process, like AGN heating in response to significant cooling. Therefore, if thermal conduction occurs at all in galaxy clusters it will certainly result in some heating of the cluster centre, but to what extent? If thermal conduction is to provide a solution to the cooling flow problem it must fulfill the following conditions:

1. temperature and density profiles must be simultaneously comparable with observations and stable for cosmologically significant timescales (e.g. Allen et al., 2001).

2. the deposition of large amount of cold gas in the centre of the cluster must be suppressed (e.g. Edge, 2001).

In order to assess the likelyhood that thermal conduction is capable of satisfying the above requirements it is instructive to make analytical predictions based on the relevant hydrodynamic equations. The opposing energy fluxes of radiative cooling, $\epsilon_{\rm rad}$, and thermal conduction, $\epsilon_{\rm cond}$, determine the behaviour of the cluster gas. For a spherically symmetric cooling flow, in which the effect of viscous heating and gravitational effects are ignored, the energy equation is

$$\frac{\mathrm{d}}{\mathrm{d}t}\left(\frac{5k_{\rm B}n_{\rm e}T}{2}\right) = -\epsilon_{\rm rad} + \epsilon_{\rm cond}\ [\mathrm{erg\ s^{-1}cm^{-3}}], \tag{4.1}$$

where the symbols have the definitions given above. The rate of heating due to thermal conduction is given by the divergence of the thermal flux

$$\epsilon_{\rm cond} = \frac{1}{r^2}\frac{\mathrm{d}}{\mathrm{d}r}\left(r^2\kappa\frac{\mathrm{d}T}{\mathrm{d}r}\right)\ [\mathrm{erg\ s^{-1}cm^{-3}}], \tag{4.2}$$

Given the form of equation (2.16), the central cooling time for a radiatively cooling and thermally conducting ICM is given by

$$t_{\rm cool} \approx \frac{n_{\rm e}k_{\rm b}T}{|\epsilon_{\rm rad} - \epsilon_{\rm cond}|}\ [\mathrm{s}]. \tag{4.3}$$

Using equation (4.3), with the initial conditions near the centre of the Virgo cluster (see section 4.3.1), the central cooling time is approximately 200 Myr. This is comparable to the results of the simulation without thermal conduction. The cooling time at $\sim$ 100 kpc is $\sim 10^{12}$ yrs. Thus, if thermal conductivity is the sole process by which the radiative cooling is opposed, then the predicted cooling time of 200 Myr must be extended by at least an order of magnitude. From equation (4.3) this requires the energy flux due to thermal conduction to be equal to the radiative energy flux to within better than 1 %. Such a situation may be possible for exceptional clusters, e.g. those with very low density and high temperatures. This would ensure that the radiative losses are low and the

thermal conductivity is large. However, due to the independent nature of the competing processes it seems unfeasible to expect this to be the case in every galaxy cluster. In addition, although thermal conductivity probably increases the cooling time of the gas at the cluster centre by a factor of a few, in doing so it also reduces the cooling time at larger radii introducing a secondary cooling problem.

The above analysis is based only on estimates since it is impossible to solve the full hydrodynamic equations analytically. Therefore, in order to better understand the effect of thermal conduction on the ICM we perform 3-d simulations in which the hydrodynamic equations are solved numerically.

4.3 Numerical Model

4.3.1 Initial Conditions

From the assumption that the Virgo and Perseus clusters are currently approximately in hydrostatic equilibrium it is possible to derive the gravitational acceleration within the clusters, if both the temperature and the density distributions of the gas are well defined. These are given by Ghizzardi et al. (2004) who combine the data from Chandra, XMM-Newton and Beppo-SAX, for the Virgo cluster, and Sanders et al. (2004a) for the Perseus cluster.

This method for calculating the gravitational potential is considerd to be more accurate than estimating the appropriate parameters for a Navarro, Frenk & White potential (Navarro et al., 1997), since the gravitational potential in the central regions of a real galaxy cluster will be dominated by the central galaxy.

For the Virgo cluster, the deprojected temperature is fitted with a Gaussian (see equation 4.4) and the electron number density by a double beta profile (see equation 4.5). The best-fit temperature profile for the Virgo cluster is

$$T = T_0 - T_1 \exp\left(-\frac{1}{2}\frac{r^2}{\sigma_t^2}\right)[\text{ K}], \tag{4.4}$$

the best fit values are T_0= 2.78 $\times 10^7$ K , T_1 = 8.997 $\times$ 10^6 K and σ_t = 7.39$\times 10^{22}$ cm.

The Virgo electron density is given by:

$$n_e = \frac{n_0}{(1+(r/r_0)^2)^{\alpha_0}} + \frac{n_1}{(1+(r/r_1)^2)^{\alpha_1}} [\text{ cm}^{-3}], \tag{4.5}$$

the best fit values for the Virgo cluster are given by n_0 = 0.089 cm^{-3} , n_1 = 0.019 cm^{-3}, r_0 = 1.6 $\times 10^{22}$cm, r_1 = 7.39 $\times 10^{22}$ cm, α_0 = 1.52, α_1 = 0.705.

For the Perseus cluster, the temperature is well described by the function given in Churazov et al. (2003),

$$T = T_0 \left(\frac{1+(r/\sigma_t)^3}{2.7+(r/\sigma_t)^3} \right) \tag{4.6}$$

the best fit values are T_0= 1.01 $\times 10^8$K and σ_t = 1.94$\times 10^{23}$ cm.

The best-fit values for the density, described by a single β-profile are n_0 = 0.071 cm^{-3}, r_0 = 8.79 $\times 10^{22}$cm, α_0 = 0.81, taken from Pope et al. (2006).

The double β-profile for the gas density found by Ghizzardi et al. (2004) is interesting given the observation that although in general cluster temperature profiles are consistent with a single phase gas, the X-ray surface brightness is less centrally peaked than expected. This is taken as evidence for distributed mass deposition throughout the flow, caused by a multiphase gas (Fabian et al., 2002, and references therein).

The assumption of a precisely uniform initial temperature is adequate for the purposes of this work since the simulation is concerned with only the central few hundred kiloparsecs of each cluster. However, note that it is simplisitic with regard to residual temperature and density perturbations arising from the formation of the cluster which should be taken in to account for a complete study of ICM evolution.

The initial temperature is chosen to be close to the Virial temperature (T_{vir}) which can be estimated using

$$T_{vir} \approx \frac{GM_{vir}\mu m_p}{k_B R_{vir}} [K], \tag{4.7}$$

where M_{vir} is the Virial mass, R_{vir} is the Virial radius, G is the Universal gravitational constant, and μm_p is the mean molecular mass of the gas.

Name	$T_{\rm iso}$/K	ρ_0/g cm^{-3}
Virgo	3×10^7	5.15×10^{-26}
Perseus	9.5×10^7	8×10^{-27}

Table 4.1: Initial temperatures and central densities for the Virgo and Perseus simulations, respectively.

For the Virgo cluster, the Virial mass and radius can be estimated using the gravitational mass profile given by Ghizzardi et al. (2004) which shows a Virial mass of 10^{13}M$_\odot$ with a Virial radius of 100 kpc. The Virial temperature of the Virgo cluster is then $\sim 3.1 \times 10^7$ K and 10^8 K ($M_{\rm vir} = 3.1 \times 10^{14} M_\odot$ at a radius of 300 kpc) for the Perseus cluster.

The actual initial value for the uniform temperature was determined by finding a temperature near to the Virial temperature, for which the simulated temperature profile, after a period of 10^8 yrs of evolution of the ICM, was comparable to current observations. For the Virgo cluster, an initial temperature of 3×10^7 K resulted in an adequate temperature profile. While for the Perseus cluster the initial temperature was 9.5×10^7 K.

The initial density profile required for hydrostatic equilibrium is determined by the derived gravitational potential and the initially uniform temperature up to a multiplicative constant. This constant can be defined as the initial density at the cluster centre. The initial temperatures and densities are given in table 4.1.

In order to implement the plasma thermal conductivity correctly it is essential to know whether the electron mean free path is less than the scale length of the temperature gradient. The scale length of the temperature gradient can be defined as $l_{\rm T} \equiv T/\nabla T$ (Sarazin, 1986). For electron mean free paths which are greater than the scale length of the temperature gradient the thermal conduction is said to 'saturate' and the heat flux approaches a limiting value (Cowie & McKee, 1977). For electron mean free paths much less than the temperature gradient the heat flux depends on the coefficient of thermal conductivity and the temperature gradient.

The mean free path of an electron ($\lambda_{\rm e}$) in an unmagnetized plasma is given by (Sarazin,

1986)

$$\lambda_{\rm e} = \frac{3^{3/2}\left(k_{\rm B}T_{\rm e}\right)^2}{4\pi^{1/2}n_{\rm e}e^4\ln\Lambda_{\rm c}}\ [{\rm cm}] \tag{4.8}$$

Substituting typical values for near the centre of the Virgo cluster ($n_{\rm e} \sim 0.1{\rm cm}^{-3}, {\rm T_e} \sim 10^7{\rm K}$) gives an electron mean free path of roughly 10 pc. For the Perseus cluster the mean free path near the centre is roughly 60 pc. The length of the temperature gradient is of the order of kiloparsecs. For the outer regions of the Virgo cluster ($n_{\rm e} \sim 10^{-4}{\rm cm}^{-3}, {\rm T_e} \sim 3\times10^7{\rm K}$) the mean free path is $\sim$ 20 kpc. For Perseus, the mean free path is roughly 150 kpc. In both cases the scale length of the temperature gradient is of the order of hundreds of kpc. This means that the usual, 'non-saturated' form for the thermal conductivity is suitable at all radii for both the Virgo and Perseus clusters.

Using the above result, the thermal conduction and viscosity are implemented but suppressed by the factor, f. The same suppression factor is used for both conductivity and viscosity as the two processes are intimately linked (e.g. Kaiser et al., 2005). For comparison, there is also a control run in which thermal conduction and viscosity are absent. For the cases in which the effects of suppressed thermal conductivity and viscosity are considered, the suppression factor is constant throughout the ICM. In reality the suppression factor is unlikely to be uniform due to varying magnetic field strength and tangling length. Note that unless the central regions of galaxy clusters are turbulent such that the thermal conductivity is suppressed only by a factor of a few (Zakamska & Narayan, 2003), then it is likely that the tangling length of the magnetic field is shorter in the central regions (due to compression). Therefore the thermal conductivity may be smaller in the centre compared to the outer regions. The effect of this would be to reduce thermal conduction where it is required most.

When taking into account thermal conductivity as a source of heat for balancing radiative losses, i.e. $\epsilon_{\rm cond} \sim \epsilon_{\rm rad}$, it is necessary to have sufficient energy in the outer regions of the cluster to achieve this. The outer regions of a cluster can be considered to be an infinite heat bath if large enough, however, larger volumes take longer to simulate. Simulating smaller volumes is quicker, but it may starve the simulated cluster of the energy that thermal conduction requires. The size of the computational box was fixed as a cube

of dimension 648 kpc, with the cluster centre situated at the box centre. For a computational box of this size the regions outside 5 kpc (inside which the cooling catastrophe was observed to occur in preliminary simulations) contains roughly 10,000 times more energy than can be supplied to the central 5 kpc over the lifetime of a simulation (roughly 2-5 Gyr).

It is also worth pointing out that a problem noted by Dolag et al. (2004) in which simulations involving radiatve cooling and star formation found an increase in temperature at the cluster centre was also observed in our preliminary simulations. This effect is attributed to limited numerical resolution, since this effect of compressional heating was eliminated by increasing the number of computational blocks in the central region of this cluster (see Appendix).

4.3.2 The Simulations

The nature of the problem considered here is 1-dimensional in many respects; this includes the initial conditions and the non-evolving gravitational potential. In general the physical mechanisms operating in this setup will result in mainly radial flow of the gas. It is possible to achieve much higher spatial resolution in a 1-d compared to a 3-d simulation. However, by employing a 3-d geometry non-radial processes may occur, for example: the growth of non-spherical modes of the thermal instability or non-radial mass flow which is likely to occur near the cluster centre.

In order to determine any differences between employing 3-d or 1-d coordinate systems, 1-d spherically symmetric simulations have been performed for two cases of the Virgo cluster: i) the absence of thermal conduction and viscosity and ii) the limit of full Spitzer thermal conductivity and viscosity. The results of these simulations are similar to those performed using a 3-d coordinate system, and are given more completely in Appendix 10.2. The main observable difference is that the evolution of 1-d spherically symmetric clusters is slightly more rapid than in the 3-d case. This behaviour is consistent with the inherent differences between the hydrodynamic equations in 1-d and 3-d. For example, there are extra dissipation terms both including and excluding the viscosity in the 3-d case

Name	Supression factor	Simulated time of Virgo (yrs)	Simulated time of Perseus (yrs)
0κ	0	1.29×10^9	7.7×10^9
0.01κ	1/100	1.35×10^9	9×10^9
0.1κ	1/10	1.89×10^9	12×10^9
1κ	1	4.72×10^9	27.8×10^9

Table 4.2: Summary of the four main simulations

which are absent in the 1-d case (see Appendix 10.2) thus any non-spherically symmetric processes will never be allowed to develop in 1-d.

The main subject of study in this chapter is the Virgo cluster therefore, it is studied with 3-d simulations. Of secondary importance is the Perseus cluster, which is studied using 1-d simulations which are reasonably accurate but have the advantage of running an order of magnitude faster than the full 3-d simulations.

Four simulations have been performed for each cluster. Each simulation is assigned a label such that the number preceeding κ is the suppression factor, f. Table 4.2 provides a summary of the simulations.

1. radiative cooling alone (zero thermal conduction and viscosity) (0κ).

2. radiative and thermal conductivity at one hundredth of the full Spitzer value (0.01κ).

3. radiative and thermal conductivity at one tenth of the full Spitzer value (0.1κ).

4. radiative and thermal conductivity at the full Spitzer value (1κ).

Each simulation was stopped after the onset of a cooling catastrophe in the cluster centre which is characterised by a rapid reduction in the temperature and timestep. This occured for central temperatures of less than $\sim 10^7$ K in all simulations. In the case of the Perseus cluster, the 0.1 and 1 κ simulations were stopped when the temperature at large radii was significantly below the observed temperature at the same location.

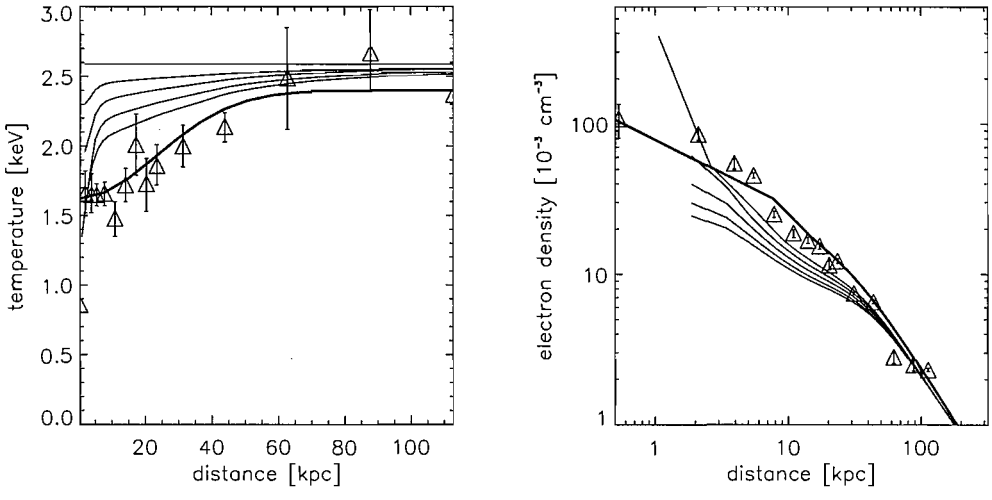

Figure 4.1: Temperature and density profiles evolving with time for simulation 0κ (see table 4.2). The thick lines for both temperature and density are the functions fitted to the data points (triangles) by Ghizzardi et al. (2004). The top line in the temperature plot shows the temperature profile after 3.17×10^8 yr and the bottom line at time of the end of the simulation. These times are given in table 4.2 for each simulation. The intermediate lines represent the temperatures at intervals of 3.17×10^8 yr after the top temperature profile. The temporal sequence of the lines is reversed (bottom to top) in the density plot.

4.4 Results

4.4.1 Temperature and Electron Number Density Profiles

VIRGO

For the Virgo cluster, the temperature and density are presented as spherically averaged profiles, rather than 1-d slices through the cluster. This is done by defining a number of spherical concentric shells at a number of radii, in this case 200, from the cluster centre and averaging the temperature and density between adjacent shells. The temperatures and densities are compared to observations in figures 4.1 to 4.4.

The temperature and electron number density profiles are plotted at intervals of 3.17×10^8 yrs for all, except simulation 1κ which is plotted for every 6.34×10^8

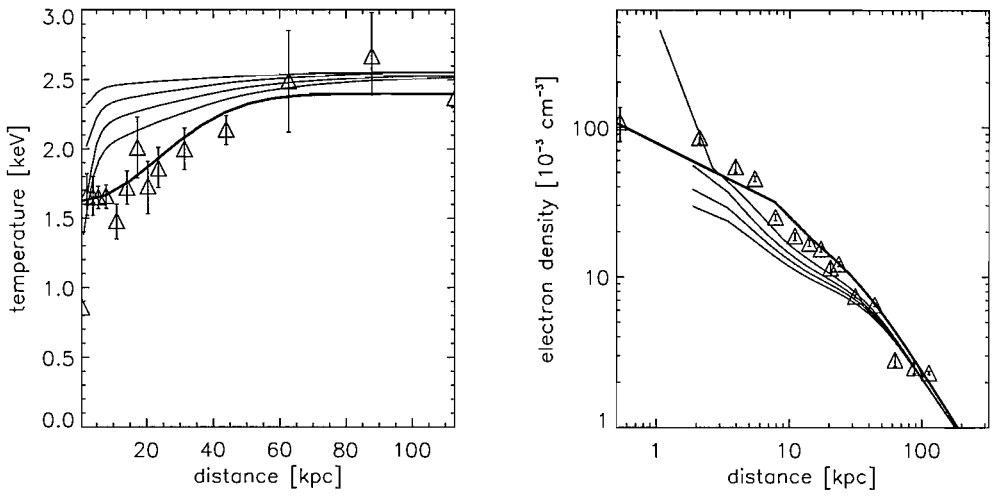

Figure 4.2: Temperature and density profiles evolving with time for simulation 0.01κ.

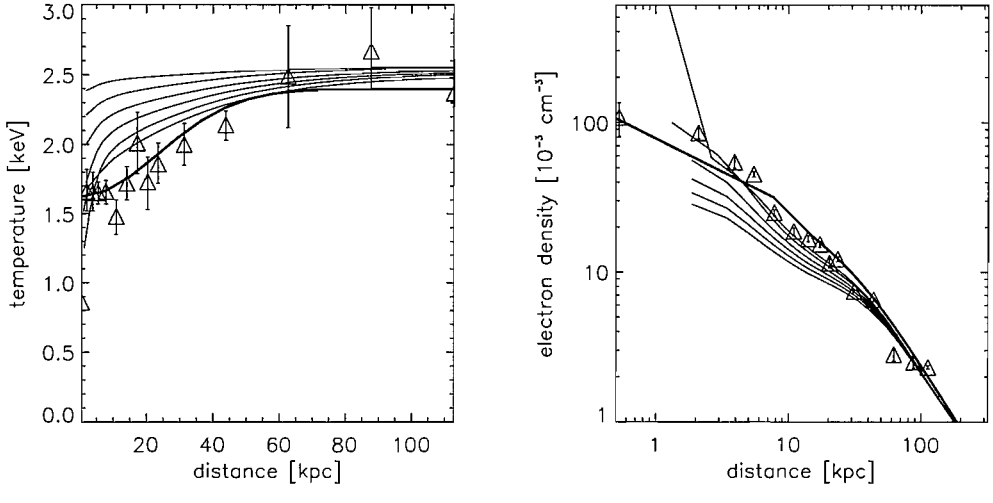

Figure 4.3: Temperature and density profiles evolving with time for simulation 0.1κ.

yrs, and for the final time of the simulation (see table 4.2). The common initial conditions are also shown, for simulation 0κ only. For each simulation the central density increases at all times during the ICM evolution. However, the behaviour of the gas temperature is rather more complex: during the early phases of evolution of the ICM the temperature falls, but appears to rise after the onset of the cooling catastrophe.

The cooling catastrophe is characterised by the relatively sudden and dramatic

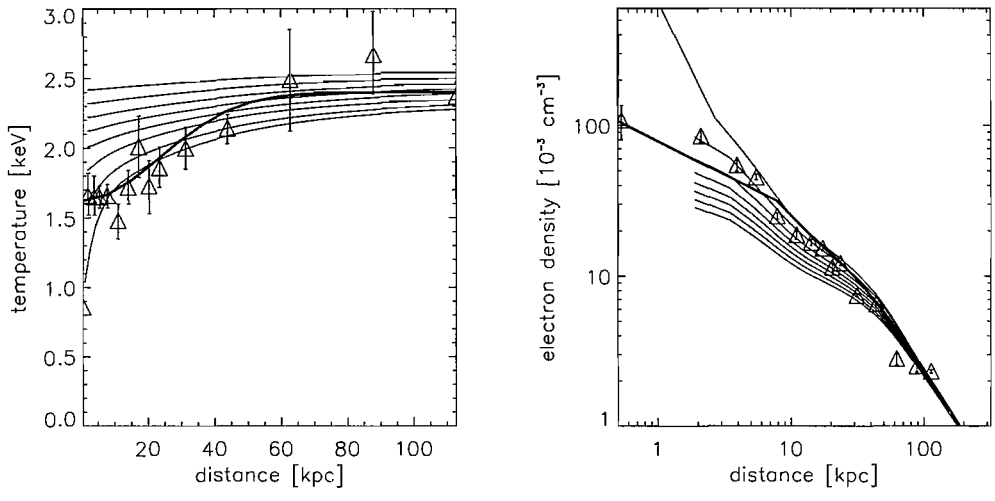

Figure 4.4: Temperature and density profiles evolving with time for simulation 1κ. Note that in this figure the temperature and density are plotted at intervals of 6.34×10^8 yrs.

increase in the central density over a short period of time (few $\times 10^8$ yrs). It should be noted that no physical value of thermal conductivity can prevent the occurance of a cooling catastrophe in the Virgo cluster.

One result from these simulations is that, regardless of whether thermal conductivity and viscosity are present, both the temperature and density profiles eventually approach generic profiles. After 2×10^9 yrs even the simulation with full Spitzer thermal conductivity develops into a cooling catastrophe with temperature and density profiles similar to the other simulations.

The temperature profiles are characterised by a narrow, but deep central dip which deepens with time such that the central temperatures fall below the observed approximate minimum of $T_{vir}/3$ (e.g. Allen et al., 2001). Qualitatively, the main effect of thermal conduction is an increase of the width of the central temperature dip. This is due to thermal conduction tranporting energy down the temperature gradient towards the cluster centre. This reduces the rate at which the temperature falls in the cluster centre, but also increases the effective rate at which the gas cools at larger radii. The time taken to evolve into this profile is roughly inversely

proportional to the magnitude of the thermal conductivity.

The broader temperature dip associated with larger thermal conductivities is accompanied by larger densities in the same region of the cluster. This has the same physical explanation as above. Due to thermal conductivity, the gas at larger radii loses more energy than it would otherwise do due to radiative losses. This prompts the inflow of gas at larger radii creating a build-up of material in a larger region of the cluster centre than for lower values of the thermal conductivity.

The density profiles can be adequately described by a strongly centrally peaked distribution in which the peak grows with time. As energy is radiated away most rapidly in the densest regions, the pressure support is lost from these central regions and the weight of the overlying layers compresses the central gas thus increasing the density dramatically. The fall in central temperature and rise in central density that one observes are both the obvious signs of a strong cooling flow and eventually a cooling catastrophe in which large quantities of gas are being deposited into the central regions of the cluster.

It is evident from figures 4.1 to 4.4 that for increasing thermal conductivity the fit of the simulated density profiles to the observational data improves at larger radii. However, the profiles are not stable over sufficiently long timescales, e.g. the Hubble time. Thus, thermal conduction only delays the occurance of a cooling catastrophe and cannot simulataneously reproduce temperature and density profiles that are consistent with observations.

PERSEUS

Since the simulations of the Perseus cluster are 1-d spherically symmetric they require no azimuthal averaging.

Qualitatively, the results are similar to those for the Virgo cluster. This is particularly true in the absence of the thermal conduction where the central temperature continues to fall and the central density rises, eventually allowing a cooling catas-

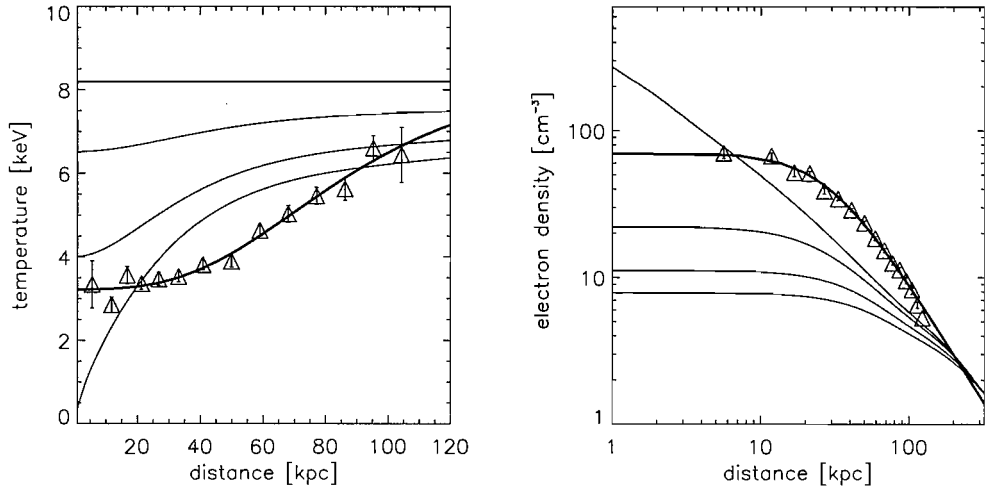

Figure 4.5: Temperature and density profiles evolving with time for simulation 0κ (see table 4.2). The thick lines for both temperature and density are the functions fitted to the data points (triangles) by Sanders et al. (2004a). The top line in the temperature plot shows the temperature profile after 6×10^9 yr and the bottom line at time of the end of the simulation. These times are given in table 4.2 for each simulation. The intermediate lines represent the temperatures at intervals of $3. \times 10^9$ yrs after the top temperature profile. The temporal sequence of the lines is reversed (bottom to top) in the density plot.

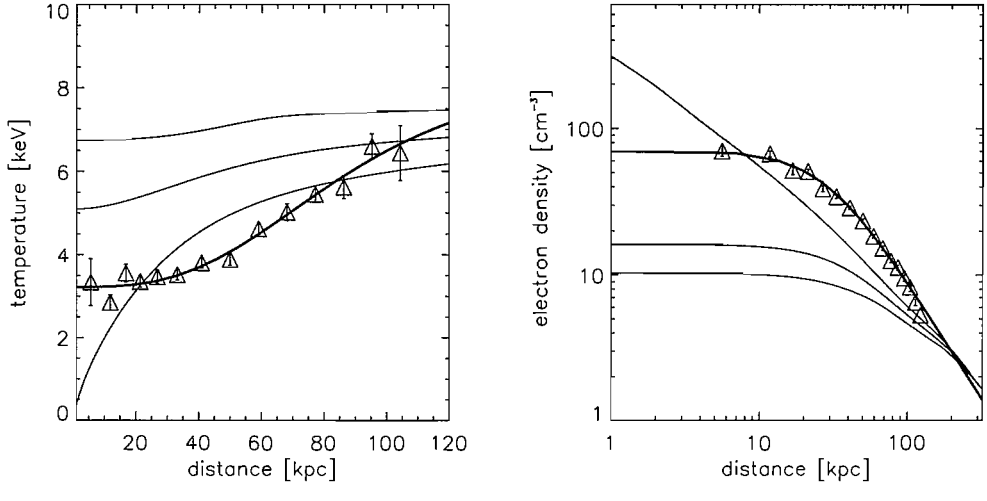

Figure 4.6: Temperature and density profiles evolving with time for simulation 0.01κ

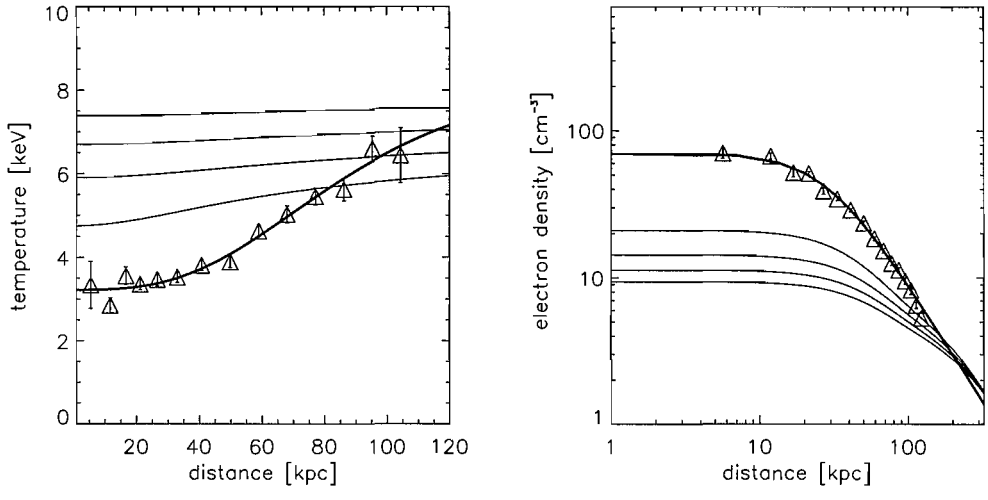

Figure 4.7: Temperature and density profiles evolving with time for simulation 0.1κ

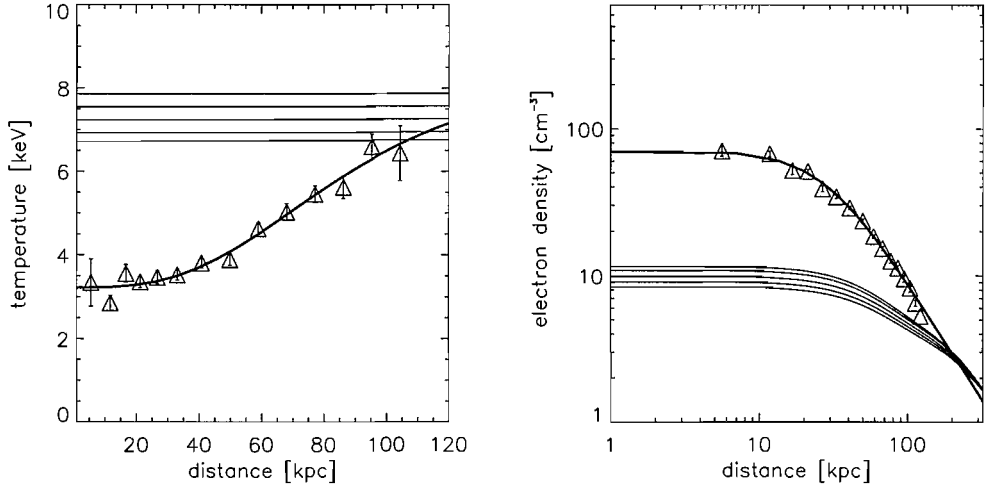

Figure 4.8: Temperature and density profiles evolving with time for simulation 1κ

trophe to occur. However, the timescale for these changes is longer than for the Virgo cluster but still within a Hubble time.

The most obvious difference between the two clusters is that for the full Spitzer value of thermal conduction the temperature profile for the Perseus cluster stays extremely flat. This is an indication that, as expected, thermal conduction can exert a greater influence in the Perseus cluster than the Virgo cluster and balance the radiative losses.

As a result of the balance between thermal conduction and the radiative losses, the central density does not grow as quickly as in the absence of thermal conduction. However, while thermal conduction may be able to balance the radiative losses, it does not seem that any value of thermal conduction can reproduce the observed temperature and density profiles, without the presence of an additional heating mechanism. The main problem is that the width of the temperature dip is comparatively large in the observational data. In the absence of the thermal conduction, the width of the central temperature dip in the simulations is always small. However, the width does increase as the thermal conductivity increases but for the values of thermal conductivity where the dip is wide enough the central temperature does not fall low enough within a Hubble time.

4.4.2 Emissivity Profiles

From the simulated density and temperature data it is possible to derive X-ray surface brightness maps for the radiative cooling function. In the previous subsection the density and temperature distributions of the simulated clusters with were compared with those derived from observations of the X-ray surface brightness of the gas, since these are the fundmental variables used by FLASH. However, calculating the surface brightness from these simulations allows a more direct comparison with the observational data. In practice the surface brightness along a given line of sight is dominated by emission from gas at the smallest radii from the cluster centre along that particular line of sight. Thus it is possible to calculate the emissivity of the gas (ϵ), i.e. the rate of energy loss per unit volume, and plot this as a function of radius. The bolometric emissivity is given by

$$\epsilon = n_e n_p \Lambda_{\rm rad}(T, Z) \ [\text{erg s}^{-1}\text{cm}^{-3}] \tag{4.9}$$

VIRGO

Figures 4.9 to 4.10 show the emissivity after 6.34×10^8 yrs and at the final point in the simulation compared to the currently observed emissivity calculated from the

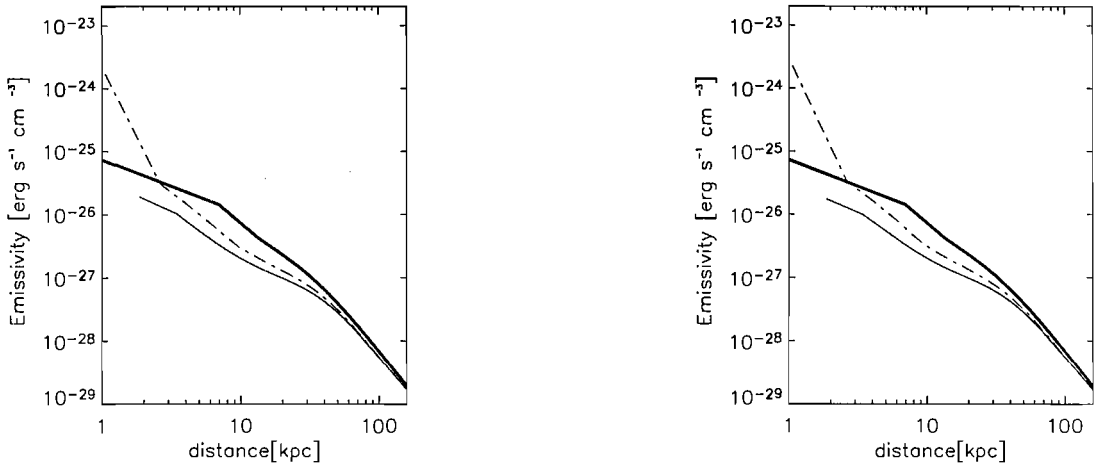

Figure 4.9: Emissivity profiles for (from left to right) simulation 0κ and 100κ. The thick line shows the observed emissivity given by Ghizzardi et al. (2004), the thin solid line shows the emissivity after 6.34×10^8 yrs; the thin dashed line shows the emssivity at the end point of each simulation as given by table 1.

work of Ghizzardi et al. (2004).

XMM-Newton observations revealed that the X-ray surface brightness was less centrally peaked than expected (e.g. Fabian et al., 2002). From figures 4.9 to 4.10 it is evident that the simulated Virgo clusters always develop a strong central peak in the surface brightness distribution, whether or not thermal conduction is taken into account. Such a peak is to be expected given the density profiles in section 4.4.1, but is not present in the observational data. This again indicates that an extra heating mechanism is required in the central few kpc to prevent excessive central cooling.

The general fit to the observational data, at large radii, seems to improve as the value of the thermal conductivity is increased. In addition, the emissivity profiles show more excess emission out to larger radii for the simulations with a larger thermal conductivity. Thus, the emissivity plots re-iterate the previous observation from the density profiles that for higher thermal conductivities there is more mass in the central 20-50 kpc than for lower values of thermal conductivity. This is consistent with the mass flow rates which are larger at all radii for later times in

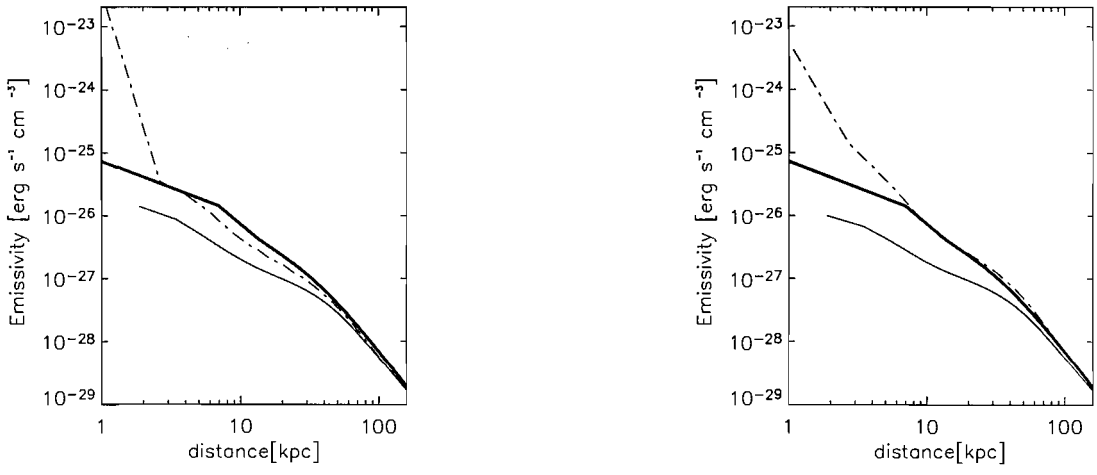

Figure 4.10: Emissivity profiles for (from left to right) simulation 0.1κ and 1κ. The definitions for each line are as in figure 4.9.

the presence of high thermal conductivity than those for lower thermal conductivity (see section 4.4.4). Hence, in order to better match the observations by preventing a cooling catastrophe it appears that the presence of a larger thermal conductivity actually requires the input of more thermal energy. In addition, this heat source would need to distribute its energy out to larger radii for the cases of larger thermal conductvity. The extra energy input required is roughly proportional to the extra volume which requires heating, and so an ICM with large thermal conductivity could require 100-1000 times more energy than for smaller thermal conductivities.

PERSEUS

The fit between the observations and the simulations never seems to be very good for the Perseus cluster. In the absence of thermal conduction, the emissivity does develope a strong central peak. This is in contrast to the observations. The agreement at larger radii is also not particularly good since the observations show excess emission at around 30-100 kpc, compared to the simulations. For increasing values of thermal conductivity, the central emissivity is smaller because it is dominated by the gas density which does not grow much in the presence of significant thermal conductivity.

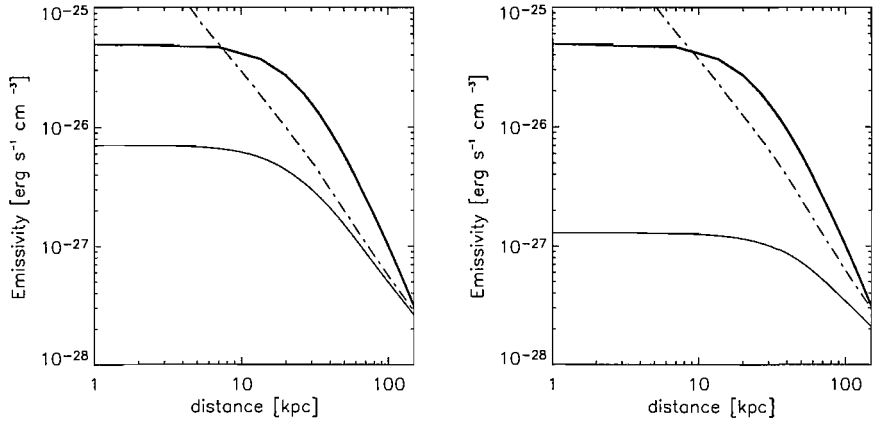

Figure 4.11: Emissivity profiles for (from left to right) simulation 0κ and 0.01κ. The thick line shows the observed emissivity, the thin solid line shows the emissivity after 6×10^9 yrs; the thin dashed line shows the emssivity at the end point of each simulation as given by table 4.2.

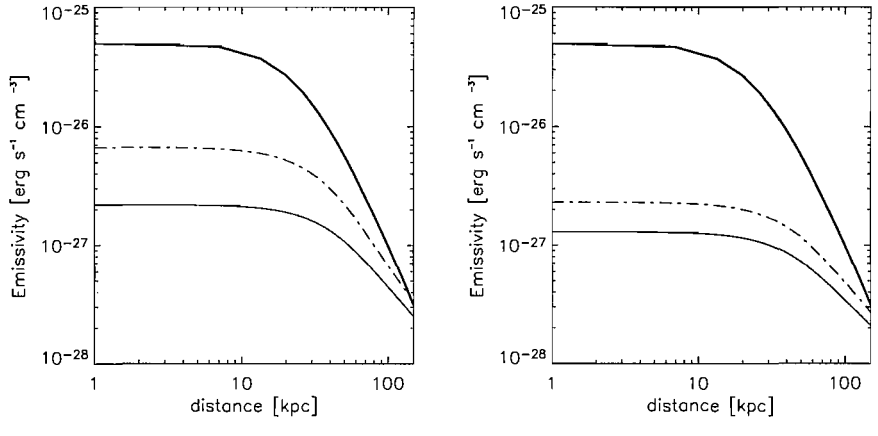

Figure 4.12: Emissivity profiles for (from left to right) simulation 0.1κ and 1κ. The definitions for each line are as in figure 4.11.

In contrast to the Virgo cluster, the agreement between the observations and simulations does not seem to improve with increasing thermal conduction. However, this does not preclude thermal conduction operating in either, or both, of these clusters. It simply implies that there must be additional processes which contribute to the evolution of the ICMs and that thermal conduction is significantly reduced in the Perseus cluster.

4.4.3 Effective Adiabatic Index

The effective adiabatic index can be utilised as an additional diagnostic for the behaviour of the cluster gas. It is defined by $\gamma_{\rm eff} \equiv {\rm d}\ln P/{\rm d}\ln\rho$ where P is the gas pressure, and ρ is the gas density. Following the method of Birnboim & Dekel (2003) $\gamma_{\rm eff}$ is derived for a situation in which the volume of gas is constant, but is subjected to heating and cooling. The pressure in terms of the internal energy per unit mass, e, is given by

$$P = (\gamma - 1)e\rho \ [\text{erg cm}^{-3}], \tag{4.10}$$

where γ is the true adiabatic index (e.g. 5/3 for a monatomic gas)

The rate of change of gas pressure with time is given by

$$\dot{P} = (\gamma - 1)(\dot{e}\rho + e\dot{\rho}) \ [\text{erg cm}^{-3}\ \text{s}^{-1}]. \tag{4.11}$$

The rate of change of internal energy per unit mass for a constant volume of gas subjected to heating and cooling is given by

$$\dot{e} = h - q \ [\text{erg g}^{-1}], \tag{4.12}$$

where h and q are the heating and cooling functions per unit mass respectively.

By converting all the relevant quantities to be compatible with those defined previously and using the definition of the effective adiabatic index we find $\gamma_{\rm eff}$ to be given by

$$\gamma_{\rm eff} = 1 + (\gamma - 1)\left(\frac{n^2 H - n^2 \Lambda_{\rm rad}}{\dot{n} k_{\rm B} T}\right), \tag{4.13}$$

where H is the heating function (the heating analogue of the cooling function, $\Lambda_{\rm rad}$), $\dot{n}$ is the rate of change of number density with time and the other symbols have their usual definitions.

In this derivation the nature of the heating and cooling mechanisms is not important, however, it is sensible to represent them in terms of quantities that have

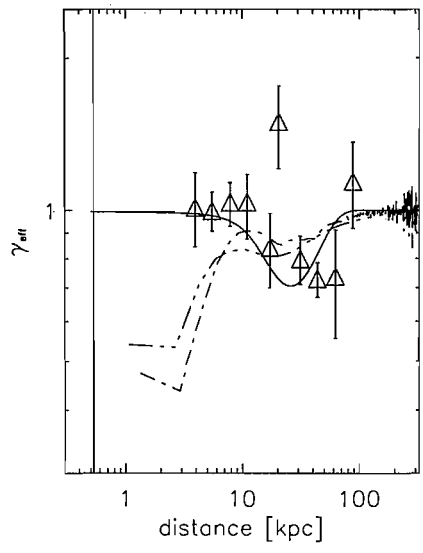

Figure 4.13: Comparison of the effective adiabatic index for simulation 1κ (triple dot dash), 0κ (dot dash) and the effective index from the fits to the observational data (solid line) and the data points. The triangles show the observational data that the fits are based on. At no point in time does the simulation data, within the central 15 kpc, approximate to the observational data. Therefore, for clarity, the $\gamma_{\rm eff}$ profiles for the simulation data are calculated for times where the central temperature is near its lowest point. The vertical line near the left of the figure is the error bar from the data point closest to the cluster centre.

already been defined. From equation (4.13), in the limit where either there is no heating or cooling or these competing effects balance, the effective index is 1, which corresponds to an isothermal equation of state. Furthermore, in the cases where no heating occurs, $\gamma_{\rm eff}$ is always less than one and for extreme cases will tend to zero as $\dot{n}$ tends to $n/t_{\rm cool}$ (where $t_{\rm cool}$ is the radiative cooling time). In the cases where heating occurs, this will have the effect of increasing $\gamma_{\rm eff}$. Using this equation one would predict that the effect of increasing thermal conductivity would increase $\gamma_{\rm eff}$.

VIRGO

Figure 4.13 shows the comparison between the effective adiabatic index obtained from the results of Ghizzardi et al. (2004) with $\gamma_{\rm eff}$ for simulations 0κ and 1κ. In the absence of thermal conductivity $\gamma_{\rm eff}$ is roughly equal to 1 in the outer regions

of the cluster, but falls steeply inside the central 10 kpc towards the central value. The upturn at roughly 3 kpc is probably due to compressional heating towards the end of the simulated time. There is a minimum at roughly 25 kpc and a peak at roughly 15 kpc. For the full Spitzer value of thermal conductivity, $\gamma_{\rm eff}$ follows roughly a similar pattern to the above except that the variation is smoother. In addition, the central effective adiabatic index is higher due to the heating effect of thermal conductivity. In comparison, it is evident that for the functions fitted to the observational data $\gamma_{\rm eff}$ is isothermal throughout the cluster except for around 30 kpc where there is a minimum similar to that noted in the simulation data. Of particular interest is the fact that there are 4 data points between the radii of 4-12 kpc with an effective adiabatic index of roughly 1 that are not consistent with either of the two simulations. By equation (4.13) this value of the observed $\gamma_{\rm eff}$ must be due to heating balancing cooling. Based on these simulations is seems that such a profile for $\gamma_{\rm eff}$ is unattainable with thermal conductivity alone. Therefore, this is strong evidence that the Virgo cluster is being heated in the central regions by a mechanism other than thermal conduction.

Despite the evidence for heating it is impossible to make any strict quantitative predictions about the level of thermal conduction in Virgo. However, according to the observational data $\gamma_{\rm eff}$ appears to vary significantly throughout the cluster. These results suggest that large values of the thermal conductvity tend to smooth out variations of $\gamma_{\rm eff}$. In addition, since thermal conductivity acts to reduce the temperature gradient, any heating source located near the centre of a cluster in which thermal conduction operates at near the Spitzer value is likely to result in a much flatter temperature profile than is currently observed. In the case where thermal conduction is heavily suppressed, it is possible that an additional heat source could maintain the temperature in the cluster centre at the observed level while allowing the region outside to continue to cool radiatively and thus produce the observed wide bowl shape. Thus although it is not possible to put strict constraints on the value of thermal conductivity in Virgo, these results suggest that it is probably suppressed by a factor of at least 10 or more. Recent work by Brüggen (2003) and Ruszkowski

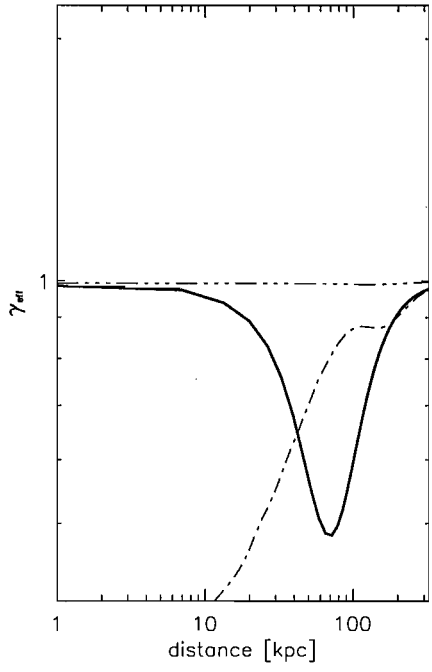

Figure 4.14: Comparison of the effective adiabatic index for simulation 1κ (triple dot dash), 0κ (dot dash) and the effective index from the fits to the observational data (solid line).

& Begelman (2002) suggests that, in 1-d at least, it is possible to achieve a steady state between radiative cooling and simultaneous heating from an AGN and thermal conduction suppressed by factor similar to the suggestion above.

PERSEUS

For full thermal conductivity, the temperature profile is always very flat. This means that the temperature is nearly independent of radius and that the effective adiabatic index is very close to unity. This should also be expected from equation (4.13) because the flat temperature profile indicates that there is a close balance between heating and cooling. As a result, full thermal conductivity provides good agreement with the observations in the inner regions but cannot explain the dip at around 80 kpc.

For zero thermal conductivity, the effective adiabatic index falls towards zero near

the centre and does not provide a good comparison to the observational data except at large radii.

4.4.4 Mass Flow rates

In this Section mass flow rates are calculated, as a function of radius. Thus it is possible to directly estimate the rate at which gas flows in to the cluster centre for different thermal conductivities. In addition, theoretical mass flow rates are also calculated and compared to the results from the simulations.

The mass flow rate is given by the mass flux through a spherical surface

$$\frac{\mathrm{d}M}{\mathrm{d}t} = \int \rho v.\mathrm{d}A = 4\pi r^2 \rho v_\mathrm{r} \ [\mathrm{g\ s^{-1}}], \tag{4.14}$$

where v_r is the projection of the velocity vector on to the radial vector.

VIRGO

Figures 4.15 to 4.16 show the mass flow rates for two different times. The first line (solid) is the mass deposition rate profile after 6.34×10^8 yrs, the second line (dashed) is the profile for the final point in the simulation given in table 4.2.

For the mass flow rate profiles after 6.34×10^8 yrs the flow rate tends to zero in the cluster centre in all simulations. There is also a point near 150 kpc at which the flow rate reaches a maximum. From here on this point is referred to as the break-radius (Edge et al., 1992; Allen et al., 2001). The increase outside the break-radius (at roughly 200 kpc) is probably not realistic, but is due to edge effects in which the initial velocities are large, but dissipate over the duration of the simulation.

For the later profiles, when the cooling flow is well established, the central mass flow rate increases up to several solar masses per year in all cases. The break-radius also moves further away from the cluster centre. The peak mass flow, at the break radius, is smaller for larger values of thermal conductivity. This is possibly a consequence of the action of shear viscosity which slows the inflow of the gas. In

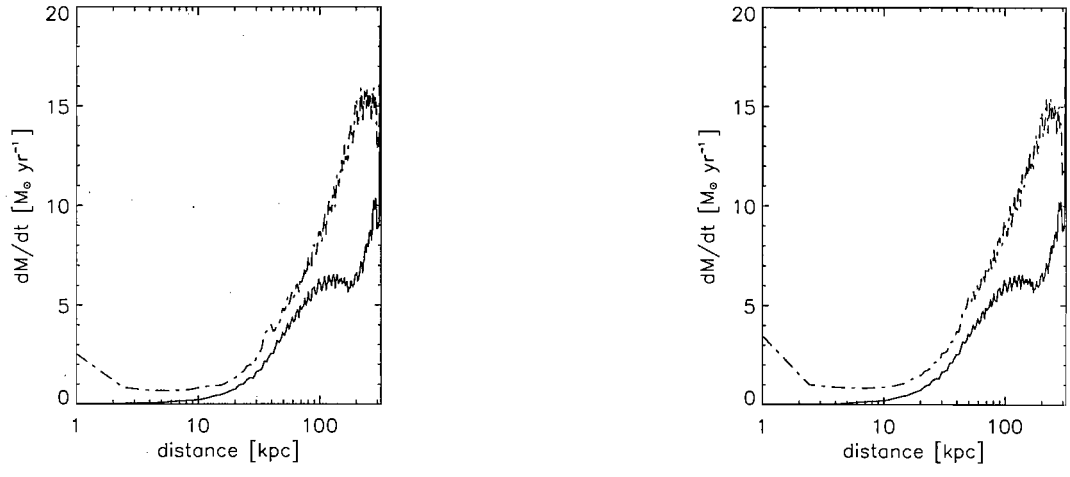

Figure 4.15: Mass flow rates for (from left to right) simulations 0κ and 0.01κ. In all plots the solid line shows the mass flow rate at 6.34×10^8 yrs; the dashed line refers to the end point in the simulation. The times of the end points are given in table 4.2.

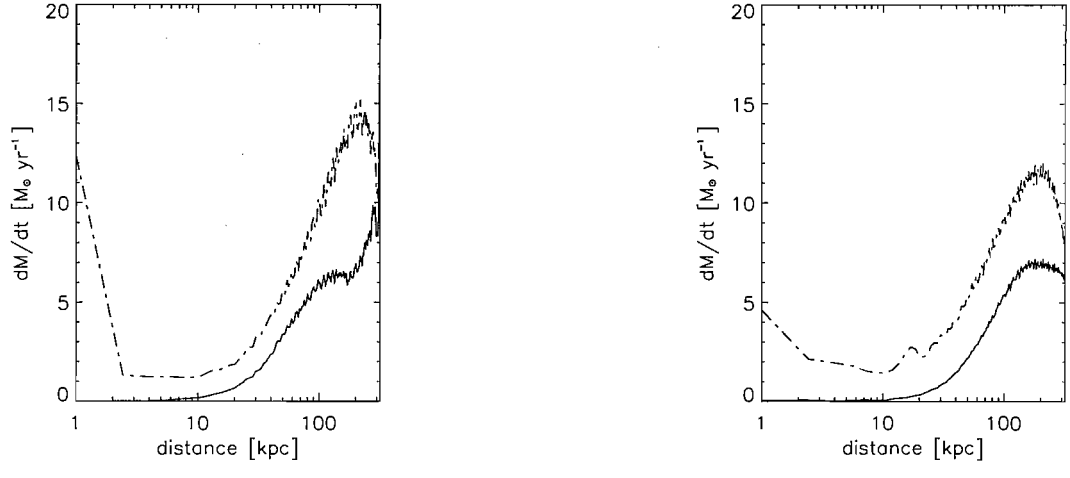

Figure 4.16: Mass flow rates for (from left to right) simulations 0.1κ and 1κ. The dashed and solid lines are defined as in figure 4.15.

addition, the width of the mass flow rate peak increases with increasing thermal conductivity and viscosity, indicating that in such cases there is more mass flowing towards the centre and that the inflow velocity falls off less quickly with radius. Thus it is possible that the central galaxies in clusters, which are thermally conducting, may be more massive, by a factor of a few, than those in cluster in which thermal conduction does not occur.

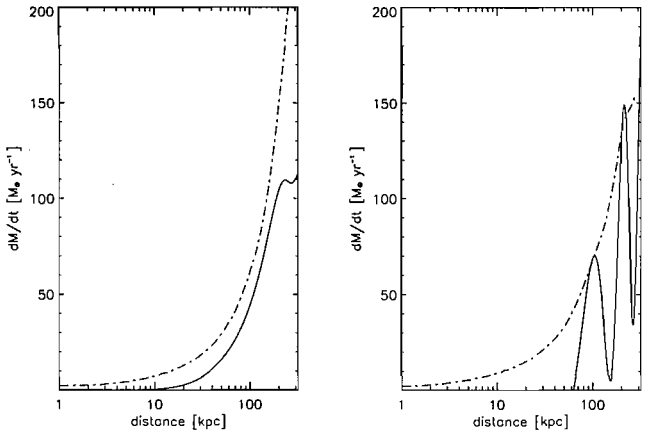

Figure 4.17: Mass flow rates for (from left to right) simulations 0κ and 0.01κ. In all plots the solid line shows the mass flow rate at 6×10^9 yrs; the dashed line refers to the end point in the simulation. The times of the end points are given in table 4.2.

The calculated mass flow rates are important for comparison with observational results. Edge (2001) finds the mass of molcular gas around M87 to be less than $1.3 \times 10^8 M_\odot$. If the Virgo cluster has been cooling for roughly 10 Gyr then the average mass deposition rate over this period cannot be greater than 0.013 $M_\odot$ yr^{-1}. We find that for a thermal conductivity at the Spitzer value the mass deposition rate in the centre of the cluster is negligible for the first $\sim 10^9$ years, but rises to several $M_\odot$ yr^{-1} thereafter. In addition, the rate of mass deposition will continue to increase after this time as the cooling catastrophe accelerates. For the cases with suppressed thermal conductivity the central mass deposition rate is significant from earlier times meaning that more gas is deposited in the cluster centre for these simulations. Therefore, although the central mass flow rates of a few $M_\odot yr^{-1}$ appear at first rather modest, it is worth noting that the mass flow rates in the centre will quickly exceed the observations' upper limit.

PERSEUS

Figures 4.17 to 4.18 show the mass flow rates as a function of radius for two different times. The first line (solid) is the mass flow rate after 6×10^9 yrs, the second line (dashed) is the profile for the final point in the simulation given in table 4.2.

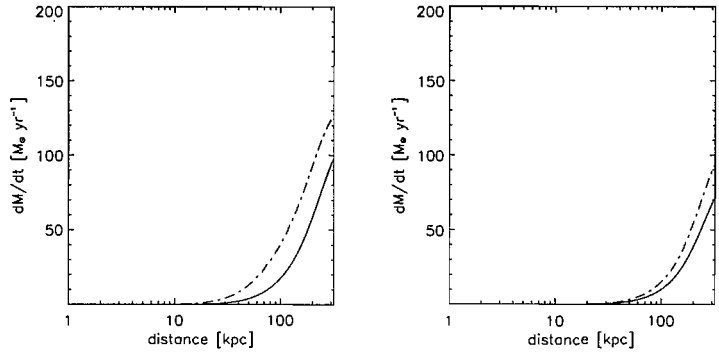

Figure 4.18: Mass flow rates for (from left to right) simulations 0.1κ and 1κ. The dashed and solid lines are defined as in figure 4.17.

In these simulations, the mass flow rate always tends to zero in the centre of the cluster. It is possible that this is a consequence of the 1-d geometry of these simulations. Furthermore, unlike the 3-d cartesian simulations of the Virgo cluster, there does not seem to be a peak in the mass flow rate at larger. This may be because of numerical effects or a peculiarity of the Perseus cluster, however it is not clear which of these dominates.

Despite the lack of similarity at late times between the results for the Virgo and Perseus simulations, it should be noted that the initial evolution of the mass flow rate is similar to that of the Virgo cluster. As an example of this, see figure 4.20. At early times, there is a peak in the mass flow rate that moves radially outwards with passing time. Eventually, the peak disappears, which is probably due to the particular velocity profile in the Perseus simulations.

PREDICTIONS

It is possible to compare the calculated mass flow rates from these simulations with analytical predictions. In order to do this, both the density and velocity profiles are required. However, it is not possible to solve the full hydrodynamic equations analytically for the velocity profile as a function of time due to the complexity of the problem. Instead it is possible to use both observational and simulation data to constrain the functional form of the velocity profile at any given time.

Figures 4.15 and 4.16 show that there is clearly a break radius in the mass flow rate profiles which agrees with the observations of Edge et al. (1992) and Allen et al. (2001). However, unlike these authors the mass flow rate is plotted at each radius, and not the cumulative mass flow rate. Since the radiative cooling rate is greatest near the cluster centre, gas in the central regions will lose its pressure support. This means that not only would one expect the gas infall velocity to tend asymptotically to zero for large radii, but that the scale height of the velocity profile will increase as a function of time as the less dense gas at larger radii has time to cool. The radiative cooling time as a function of radius is given by equation (2.16). The cluster gas is assumed to be isothermal and the density to follow a generalised β-profile. Rearranging for the radius, gives the cooling radius as a function of time

$$\frac{r_{\rm cool}}{r_0} = \left[\left(\frac{2t\Lambda_{\rm rad0}n_0}{3k_{\rm B}T^{0.5}}\right)^{\frac{2}{3\beta}} - 1\right]^{\frac{1}{2}}, \tag{4.15}$$

where r_0 is the scale height of the density distribution. For the Virgo cluster the value of β is roughly 0.47 for radii greater than roughly 30 kpc.

Equation (4.15) implies that after times of order 0.3 Gyrs the velocity scale height grows proportionally to $t^{1/(3\beta)}$.

Further constraints on the velocity profile can be determined using equation (4.14) and what is already known about the gas density of the Virgo cluster. The electron number density given by equation (4.5) implies that at large radii the density scales as $r^{1.4}$. Substituting this into equation (4.14) implies that in order for there to be a break radius the infall velocity of the gas must fall off more quickly than approximately $r^{-0.6}$. Furthermore, by the observation that the mass flow rate tends asymptotically to zero in the cluster centre (before the cooling catastrophe occurs) it follows that, at least, in the central region the velocity cannot fall off faster than r^{-2}. However, it should be noted that after the occurance of the cooling catastrophe the central mass flow rate becomes finite. This suggests that the velocity profile steepens at least in the central few kiloparsecs and may be an indication that the gas is in free-fall after the onset of the cooling catastrophe. Thus, for the Virgo cluster, if the infall velocity follows a power-law ($v \sim r^{-\alpha}$) then α may be constrained to lie

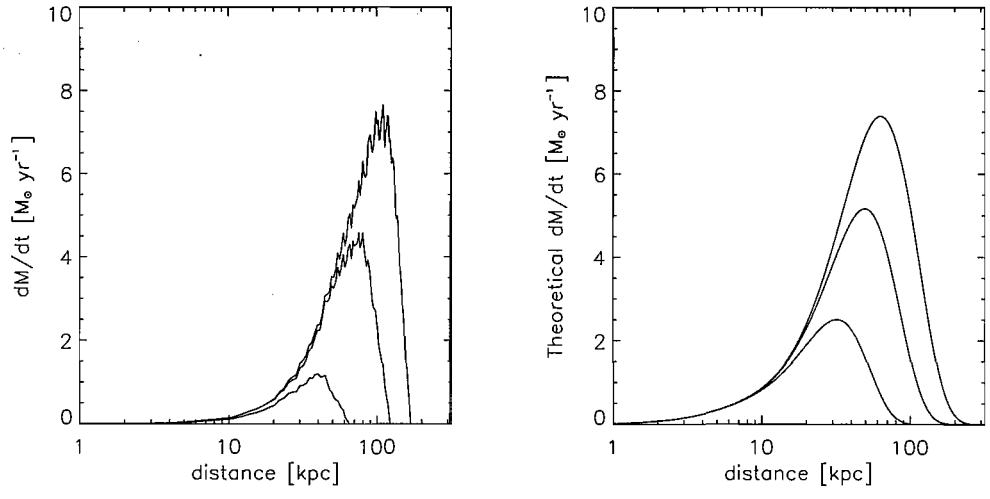

Figure 4.19: Virgo cluster: Comparison of the mass flow rates for increasing time for simulation 0.01κ data (left) and from simple theoretical predictions at the same times.

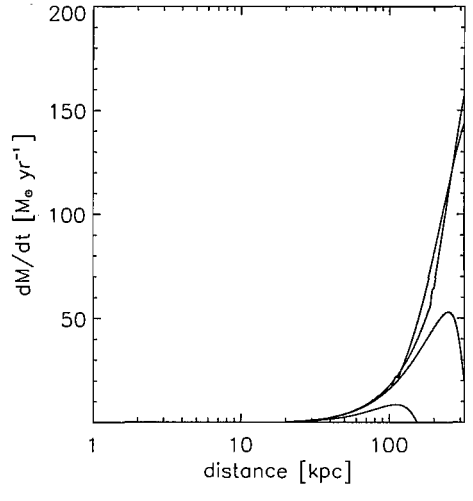

Figure 4.20: Perseus cluster: mass flow rates after 1,2,3 and 4 $\times 10^8$ yrs for simulation the 0κ simulation data.

between 0.6 and 2. In general, for any cluster in which the gas density may be described by a β-profile the constraints on α are $(2 - 3\ \beta) \leq \alpha \leq 2$.

In the absence of an analytical expression for the velocity profile $v \sim \exp(-r^2/{r_s}^2)$ is adopted, which satifies the condition above, where r_s is the scale height of the velocity profile which is equivalent to the cooling radius described in equation (4.15).

In order to understand the dependence of the mass flow rate on velocity it is sensible use the density profile that was calculated for the initial conditions of these simulations, and the velocity profile described above and vary only the velocity scale height with time. The peak mass flow rate is determined by the velocity in the cluster centre, which by comparison with the simulations was chosen to be of order 10^5cm s^{-1}. The density profile can be assumed to remain fixed since the density should not change significantly until a cooling catastrophe occurs. However, a gradual increase in the central density will inevitably occur due to the inflow of gas towards the cluster centre. The results of this basic analysis are compared to the simulation data in figure 4.19. It is obvious that despite the simplistic nature of the analysis its predictions match the simulation results reasonably well. In addition, the analysis should hold for clusters in general and not just the Virgo cluster. Thus the inflow velocity profile, $v \sim \exp(-r^2/{r_s}^2)$, can be taken as a generic approximation for the gas velocity in radiatively cooling clusters.

4.5 Summary

These results suggest that the effect of thermal conduction varies from cluster to cluster. In the Virgo cluster thermal conduction is unable to prevent the occurance of a cooling catastrophe and can only increase the cooling time in the cluster centre by a factor of a few. Tests using different coordinate systems and spatial resolutions show that the developement of a cooling catastrophe is inevitable in this cluster. This should not be a consequence of the chosen initial conditions since the cluster is allowed to evolve self-consistently, taking into account all relevant physics, using standard intial conditions used in cluster formation theory.

The effect of thermal conduction on the Perseus cluster is rather different. Because the intracluster gas is so much hotter than the Virgo cluster, thermal conduction occurs at a much higher rate. Consequently, close to the Spitzer value, heat transport by thermal conduction closely balances the radiative losses and prevents

the formation of a strong temperature gradient. However, for low values of thermal conductivity, the temperature profile does resemble the same case for the Virgo cluster.

For both clusters, the simulated temperature and density profiles fail to simultaneously converge to the observational constraints. For the Virgo cluster, the mass flow rates also suggest that significantly more mass is deposited in the cluster centre than is observed. Somewhat contrary to expectations it seems that for the Virgo cluster, the mass flow rates are also greatest for the simulations in which thermal conduction is most important. The extra central concentration of mass causes emissivities with broader peaks than for lower thermal conductivities. A consequence of this is that more energy would have to be injected by a central AGN, for example, than for more weakly conducting cases to avert a cooling catastrophe.

These results are in agreement with Voigt et al. (2002) who found that in their sample thermal conduction could only balance radiative losses in the outer regions of cluster cores. There is a slight contradiction with the findings of Zakamska & Narayan (2003) who found that the temperature and density profiles of several galaxy clusters were consistent with a steady state maintained by physically meaningful values of thermal conduction. However, since Zakamska & Narayan (2003) do not take into account the effect of line cooling, which is more significant at the lower temperatures near cluster centres, and only look for the temperature and density profiles which will ensure a steady state, it is unclear whether their study and this work are comparable. Furthermore, neither of Voigt et al. (2002) nor Zakamska & Narayan (2003) have made predictions about the Virgo cluster.

For the case of the Perseus cluster, thermal conduction is so effective at balancing the radiative losses that the central mass flow rate never becomes very large. This also means that the emissivity never becomes strongly peaked in the centre for large values of the thermal conductivity. However, after a sufficiently long time it is possible, if not probable, that the larger values of thermal conductivity would eventually result in a broader peak in the emissivity.

The simulated and observed effective adiabatic indices indicate that there must be a heat source at the centres of the Virgo and Perseus clusters. This is because the observed effective adiabatic index is close to unity in the centre, but falls further out before rising back to unity at large radii and incompatible with the simulation data. The dip is presumeably a sign of cooling dominating over heating at these radii.

In the absence of thermal conduction, the effective adiabatic indices derived from the simulation data drop towards the centre. For the Perseus cluster where thermal conduction operates at the full Spitzer value, the effective adiabatic index stays very close to unity at all radii. This agrees with the observations at small radii but not at larger radii where the observations suggest a dip in the index.

Given the comparison between the observed and simulated effective adiabatic indices and the temperature and density profiles it seems that thermal conduction is suppressed to at most 1/100 to 1/10 of the full Spitzer value, for both clusters. However, even if thermal conductivity and viscosity are suppressed by a factor of 100, the thermal conduction and viscous dissipation of sound waves generated in the ICM could still be significant.

For the overall energy budget it seems that thermal conduction could be able to suppress radiative cooling in hotter clusters while it might be quite ineffective in cooler clusters, such as Virgo. Therefore, thermal conductivity cannot be responsible for the universal temperature profiles of clusters as observed by Allen et al. (2001).

Since thermal conduction seems to be an unreliable heating source for the central regions of clusters, it is necessary to investigate alternatives. The main contender is heating by outflows from AGNs.

As a prelude to simulations of jets heating the ICM, it is necessary to gain some intuition for the sort of energy injection rates that are required in real clusters. To do this, one can construct a simple model of the ICM and compare the observed energy injected by AGNs with the required heating rates. Matching the observed

injected energy with the required heating rates also allows the AGN duty cycle to be estimated. The required heating rates also imply values for the thermal conductivity. These can be compared to the simulations of the Virgo and Perseus clusters to see if the results are compatible.

Chapter 5

Heating Rate Profiles in galaxy clusters

5.1 Introduction

There is certain observational evidence that the temperature profiles of galaxy cluster atmospheres are well described by the same mathematical function across a range in redshift (e.g. Allen et al., 2001). Given such similarity it is possible that the atmospheres of galaxy clusters are in a quasi-steady state and that observable parameters such as the radial temperature profile do not vary signicantly over the lifetime of a cluster. This universal temperature profile would be difficult to sustain if the density profiles varied significantly with time. In addition, if large quantities of gas were deposited in the central regions one might expect that the density profiles would be much more centrally peaked than observations suggest. The culmination of this argument is that, at least in the central regions, the inward flow rate of mass must be roughly independent of radius to ensure that mass is not deposited at any particular location which would significantly alter the density profile. Of course, if material cools out of the flow, then the density distribution determined from X-rays could be unchanged. This cool material would then presumably go on to form stars.

One particular problem a constant mass flow rate near the centre is that all of the mass flowing in this region must be deposited at the cluster centre. Therefore, unless the mass flow rate is small this would result in large quantities of gas at the cluster centre.

In contrast, spectroscopically determined mass deposition rates suggests that mass *is* deposited at a roughly constant rate throughout the cluster, at resolved radii (Voigt & Fabian, 2004). However, a roughly constant mass deposition rate is indicative of a mass flow rate that is roughly proportional to radius, rather than constant as the density profiles suggest. Yet, if such a flow were persistent this proportionality would result in density profiles which contradict the observational evidence by being more centrally peaked. Again, if material the material deposited at each radius cooled out of the flow, then the density distribution determined from X-rays could be unchanged.

In order reconcile the implications of the density profiles and mass deposition rates then one possible explanation is that the mass flow rate exhibits two different asymptotic properties. That is, near the cluster centre or within the central galaxy the mass flow rate should be roughly constant so that the density profiles are essentially left unchanged, while the mass deposited at the cluster centre is sufficiently small to agree with observations. At larger radii the mass flow rate should still be proportional to radius and satisfy the observations on resolvable scales which imply a constant mass deposition rate.

The two main candidates for heating cluster atmospheres discussed here AGNs (e.g. Tabor & Binney, 1993; Churazov et al., 2001; Brüggen & Kaiser, 2002; Brüggen, 2003) and thermal conduction (e.g. Gaetz, 1989; Zakamska & Narayan, 2003; Voigt et al., 2002; Voigt & Fabian, 2004). Deep in the central galaxy other processes such as supernovae and stellar winds will also have some impact on the ambient gas.

However, AGN are only periodically active which could result in similarly periodic heating rates, thus making the possibility of a totally steady state unlikely. In this

case one could imagine a scenario in which a quasi steady-state is possible where temperature and density profiles oscillate around their average values. However, it is also possible that dissipation of the plasma bubbles may occur over timescales longer than the period of AGN activity thus providing almost continous heating (e.g. Reynolds et al., 2005).

Thermal conduction may also play a significant role in transferring energy towards central regions of galaxy clusters given the large temperature gradients which are observed in many clusters, as discussed in the previous chapter.

To answer the questions regarding the necessary heating rates and mechanisms involved in galaxy clusters I construct a simple model based on two main assumptions: galaxy clusters are in approximate steady state, and the mass flow rates fulfill the constraints provided by observations at both large and small radii. To ensure this, the radial behaviour of the mass flow rates is modelled using an observationally motivated, but empirical function consistent with the observations. Mathematical functions fitted to the temperature and density data of seven galaxy clusters can be used to derive the required heating rates within regions which are consistent with those for which the mass flow rates were determined. I will also compare the observed energy currently available in the form of plasma bubbles with the heating requirements for each cluster. From the heating rate profiles I calculate the thermal conduction suppression factor as a radial function for each cluster in order that one may determine which clusters could be heated by this process.

The results are given for a cosmology with $H_0 = 70 \mathrm{kms}^{-1}\mathrm{Mpc}^{-1}$, $\Omega_M = 0.3$ and $\Omega_\Lambda = 0.7$.

5.2 Functions fitted to observational data

In this section details of the functions used to derive the mass deposition and heating rate profiles are given, as are the references to the observational data, and a com-

parison with the data in figure 5.1. However, first the observational data must all be directly comparable. This means converting, where necessary between different cosmological model that were used, by the original authors, to process the data.

The density and temperature profiles for all of the clusters except for A2199 and A1795 were obtained assuming $H_0 = 70\text{kms}^{-1}\text{Mpc}^{-1}$. In addition, since the observations of Bîrzan et al. (2004) also assume that $H_0 = 70\text{kms}^{-1}\text{Mpc}^{-1}$ it is sensible to re-scale both the length scales and densities of A2199 and A1795 to this case, so as to make the comparisons simpler. Length scales transform linearly with the Hubble constant

$$\frac{l(2)}{l(1)} = \frac{H_0(1)}{H_0(2)}, \tag{5.1}$$

where $H_0(1)$ is the Hubble constant used to determine length $l(1)$. Therefore, for $H_0(1) = 50\text{kms}^{-1}\text{Mpc}^{-1}$ and $H_0(2) = 70\text{kms}^{-1}\text{Mpc}^{-1}$ the ratio $l(2)/l(1) = 50/70 \approx 0.714$.

The densities are derived by deconvolving the surface brightnesses to obtain the density-dependent emissivity. Cowie et al. (1987) show that the central density, n_0, is proportional to $(S_0/a)^{1/2}$, where S_0 is the central surface brightness and a is the scale-height which describes the surface brightness β-profile. Therefore, since the central densities depend on the scale-height, as shown, they must also depend on the Hubble parameter in the following way

$$\frac{n_0(2)}{n_0(1)} = \left[\frac{H_0(2)}{H_0(1)}\right]^{1/2}. \tag{5.2}$$

Consequently, for $H_0(1) = 50\text{kms}^{-1}\text{Mpc}^{-1}$ and $H_0(2) = 70\text{kms}^{-1}\text{Mpc}^{-1}$ the ratio $n_0(2)/n_0(1) = (70/50)^{1/2} \approx 1.18$.

Temperatures are unchanged by changes in the Hubble parameter.

Since the density and temperature profiles for A2199 are described without a particular scale-height one must include the change of the Hubble parameter in both the central density and the radial distance. This means that the density must be scaled as follows

Name	$n_0(\mathrm{cm}^{-3})$	$n_1(\mathrm{cm}^{-3})$	β_0	β_1	r_0(kpc)	r_1(kpc)
Virgo	0.089±0.011	0.019 ± 0.002	1.52±0.32	0.705	5±1	23.3±4.3
Perseus	0.071±0.003		0.81±0.04		28.5±2.7	
Hydra	0.07±0.02		0.72±0.004		18.6±0.5	
A2597	0.13±0.07		0.15±0.10	0.79±0.06	1.0±2.6	43±14
A2199	0.19		0.75		1	
A1795	0.066±0.067		0.24±0.11	0.41±0.13	57±37	12±4.9
A478	0.153±0.019		0.55±0.05	0.41±0.34	145±32	6.6±1.9

Table 5.1: Summary of best fit parameters for density profiles with 1-sigma errors obtained from the least-squares fitting procedure. We do not give errors the model function parameters for A2199 since we were unable to obtain the observational data. See table 5.2 for references.

$$n = n_0(r^{-\beta_0}) = 1.18 n_0((r/0.71)^{-\beta_0}), \tag{5.3}$$

since $\beta_0 = 0.75$ this means that overall the density can just be multiplied by a constant, 0.91, in order to convert from a Universe where $H_0(1) = 50\mathrm{kms}^{-1}\mathrm{Mpc}^{-1}$ to one where $H_0(1) = 70\mathrm{kms}^{-1}\mathrm{Mpc}^{-1}$. The same principle is applied to the temperature profile of A2199, where the change of the Hubble parameter enters becuase of the unscaled radial profile, for which the multiplicative constant is 0.905.

The functions used to fit the data are given below and the values of the fitted parameters are given in tables 5.1 and 5.2.

The Virgo cluster's electron number density data was fitted by Ghizzardi et al.

(2004) using a double β-profile,

$$n = \frac{n_0}{[1+(r/r_0)^2]^{\beta_0}} + \frac{n_1}{[1+(r/r_1)^2]^{\beta_1}}. \tag{5.4}$$

For simplicity, the Perseus (see Sanders et al., 2004b) and Hydra (David et al., 2001) density data were fitted with single β-profiles,

$$n = \frac{n_0}{[1+(r/r_0)^2]^{\beta_0}}. \tag{5.5}$$

The observational data for A2199 proved impossible to obtain so the fits presented by the original authors (Johnstone et al., 2002) were used,

$$n = n_0 \left(\frac{r}{r_0}\right)^{-\beta_0}. \tag{5.6}$$

For A2597, A1795 and A478 (see McNamara et al., 2001; Ettori et al., 2002; Sun et al., 2003, respectively) the function given by Dennis & Chandran (2005) are used to fit the density distributions,

$$n = \frac{n_0}{[1+(r/r_0)^2]^{\beta_0}} \frac{1}{[1+(r/r_1)^2]^{\beta_1}}. \tag{5.7}$$

As above, functions have only been fitted to the temperature data when the original authors had not included confidence intervals.

Ghizzardi et al. (2004) found that the Virgo temperature data is best described by a Gaussian curve,

$$T = T_0 - T_1 \exp\left(-\frac{1}{2}\frac{r^2}{{r_{ct}}^2}\right). \tag{5.8}$$

Churazov et al. (2003) fitted the Perseus temperature data with the function,

$$T = T_0 \left[\frac{1+\left(r/r_{ct}\right)^3}{\delta+\left(r/r_{ct}\right)^3}\right]. \tag{5.9}$$

The temperature data for A2597, A1795 and A478 were fitted using the same function as Dennis & Chandran (2005),

$$T = T_0 - \frac{T_1}{\left[1+(r/r_{ct})^2\right]^{\delta}}. \tag{5.10}$$

Name	T_0(keV)	T_1(keV)	r_{ct}(kpc)	δ	Reference
Virgo	2.4±0.1	0.77±0.10	23±4		1
Perseus	8.7±1.1		63±5	2.7±0.3	2
Hydra	2.73±0.07		10	0.12±0.01	3
A2597	4.1±0.1	2.0±0.2	16±10	0.7±0.4	4,5
A2199	1.0		1	0.29	6
A1795	7.2±1.9	5.1±2.2	40±34	0.5±0.7	7,5
A478	9.7±1.5	7.6±1.7	16±5	0.3±0.2	8,5

Table 5.2: Summary of temperature parameters fitted to the data with 1-sigma errors obtained from the least-squares fitting procedure. References:-(1) Ghizzardi et al. (2004); (2) Sanders et al. (2004); (3) David et al. (2001); (4) McNamara et al. (2001) and Rafferty et al. (2005), in preparation; (5) Dennis & Chandran (2005); (6) Johnstone et al. (2002); (7) Ettori et al. (2002); (8) Sun et al. (2003). Errors are not given errors for A2199 since the observational data was not available. No error for the Hydra temperature scale-height is given since none was given in the original publication, David et al. (2001).

The best-fit temperature profile for the Hydra cluster is given by David et al. (2001) as a power-law,

$$T = T_0 \left(\frac{r}{r_{\rm ct}} \right)^{\delta}. \tag{5.11}$$

The A2199 temperature data was found by the original authors (Johnstone et al., 2002) to be described by a power-law without a characteristic length-scale. For consistency equation (5.11) is used to represent the temperature distribution in this cluster.

Although 1-sigma errors are provided for the fitted parameters that describe the

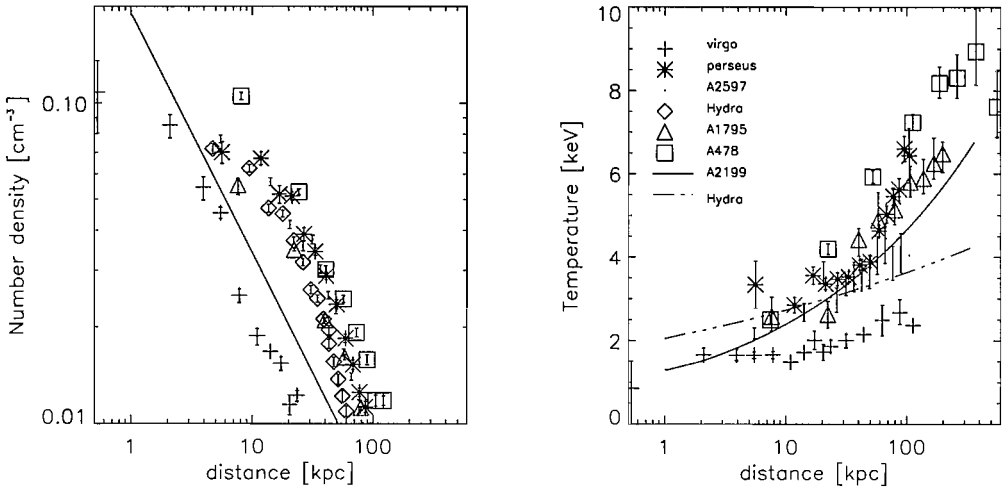

Figure 5.1: Left: density data for all clusters except A2199 for which the best-fit is shown, since the observational data was not available. Right: temperature data except for A2199 and Hydra for which the fitted functions are shown, since the observational data was unavailable. The key in the right-hand panel applies to both temperature and density data.

temperature and density distribution of the gas in galaxy clusters, they will not give errors for any quantities derived from these parameters. The reason for this is that the errors and gradients of the temperature and density are all model dependent. In addition, the calculations are complex, making the standard propagation of errors impractical and error estimates themselves very uncertain. In addition, very conservative estimates of the confidence limits can be made although they are too vague to be of importance.

5.3 The Model

5.3.1 General heating rates

Starting from the assumption that the atmospheres of galaxy clusters are spherically symmetric, and in a quasi steady-state, it is possible to derive what the time averaged heating rate, as a function of radius, must be in order to maintain the observed

temperature and density profiles,

$$h = n^2 \Lambda_{\rm rad} + \frac{1}{r^2}\frac{\rm d}{{\rm d}r}\left[\frac{\dot{M}}{4\pi}\left(\frac{5k_{\rm b}T}{2\mu m_{\rm p}} + \phi\right)\right], \tag{5.12}$$

where $\dot{M}$ is the mass flow rate, T is the gas temperature, n is the gas number density, $\Lambda_{\rm rad}$ is the cooling function and ϕ is the gravitational potential. The flow of the gas is assumed to be subsonic.

The difference between the rate at which mass enters and leaves a spherical shell, of thickness Δr, is called the mass deposition rate, $\Delta\dot{M}$. In terms of the mass flow rate, the mass deposition rate is

$$\Delta\dot{M} \approx \left(\frac{{\rm d}\dot{M}}{{\rm d}r}\right)\Delta r \tag{5.13}$$

Consequently, the mass flow rate, at a particular radius, can be recovered by summing the contributions of the mass deposition rate in each shell up to that radius. Henceforth, the mass flow rate is referred to as the integrated mass deposition rate.

For subsonic gas flow the cluster atmosphere can be assumed to be in approximate hydrostatic equilibrium allowing the gravitational acceleration to be calculated.

To avoid anomalies when calculating spatial derivatives, contniuous analytical functions are fited through the density and temperature data in the previous section. This ensures that there are not any large discontinuities which may result in extreme heating rates.

The only unknowns in equation (5.12) are then the integrated mass deposition rate, $\dot{M}$, and the heating rate, h.

5.3.2 Calculating Mass Deposition rates

In the classical cooling flow picture, which assumes that the heating is zero everywhere, and ignoring the effect of the gravitational potential, the bolometric X-ray

luminosity, integrated mass deposition rate and gas temperature are related by integrating equation (5.12) (e.g. Fabian, 1994) over a spherical volume. Analytically, the bolometric X-ray luminosity within a given radius is simply the volume integral of the radiative cooling rate per unit volume,

$$L_{\rm X}(<r) = 4\pi \int_0^r n^2 \Lambda_{\rm rad} r^2 {\rm d}r. \tag{5.14}$$

Integrating the second term in equation (5.12) gives the reationship between bolometric luminosity, integrated classical mass deposition rate and temperature,

$$L_{\rm X}(<r) = \frac{5k_{\rm b}}{2\mu m_{\rm p}} \dot{M}_{\rm clas}(r) T(r). \tag{5.15}$$

For observational data the luminosity and classical mass deposition rates at each radius are estimated by dividing the observed 2-d projection of the cluster into concentric shells. Using this method one is able to reconstruct the 3-d properties of a cluster. The contribution, to the total X-ray luminosity, of the jth spherical shell, of thickness Δr, is then calculated by discretizing equation (5.15),

$$\Delta L_{\rm Xj} = \frac{5k_{\rm b}}{2\mu m_{\rm p}} \left(\dot{M}_{\rm clasj} \Delta T_{\rm j} + \Delta \dot{M}_{\rm clasj} T_{\rm j} \right). \tag{5.16}$$

In any given shell, the term involving $\Delta T_{\rm j}$ is assumed to be small compared to the term involving $\Delta \dot{M}_{clasj}$. By ignoring the $\Delta T_{\rm j}$ term the resulting mass deposition rate is larger than it would be if the change in temperature across the shell was taken into account. Therefore, the classical value is the absolute maximum possible mass deposition rate. The luminosity of a given shell is then assumed to be (e.g. Voigt & Fabian, 2004),

$$\Delta L_{\rm Xj} = 4\pi r^2 \Delta r n^2 \Lambda_{\rm rad} = \frac{5k_{\rm b} T_{\rm j}}{2\mu m_{\rm p}} \Delta \dot{M}_{\rm clasj}. \tag{5.17}$$

The rate at which mass is deposited within the jth shell is

$$\Delta \dot{M}_{\rm clas,j} = \frac{4\pi {r_{\rm j}}^2 \Delta r {n_{\rm j}}^2 \Lambda_{\rm rad}}{\frac{5k_{\rm b} T_j}{2\mu m_p}}. \tag{5.18}$$

The total X-ray luminosity emitted by the gas within a particular radius is calculated by summing the contributions from all of the shells within this radius

$$L_{\rm X}(<r) = \frac{5k_{\rm b}}{2\mu m_{\rm p}}\dot{M}_{\rm clas}(<r)T(r), \tag{5.19}$$

where $\dot{M}_{\rm clas}(<r)$ is the integrated mass deposition rate obtained by sumning the contribution from each shell within the radius, r.

If a heating term is included, the expression equivalent to equation (5.15) becomes,

$$L_{\rm X}(<r) - H(<r) = \frac{5k_{\rm b}}{2\mu m_{\rm p}}\dot{M}_{\rm cool}T(r), \tag{5.20}$$

where $\dot{M}_{\rm cool}$ is the integrated mass deposition rate, resulting from the excess of cooling over heating. This integrated mass deposition rate is distinct from the integrated classical mass deposition rate which is only used to describe the situation in the absence of heating.

With equation (5.16) becomes,

$$\Delta\big(L_{\rm X,j} - H_{\rm j}\big) = \frac{5k_{\rm b}}{2\mu m_{\rm p}}\big(\dot{M}_{\rm cool,j}\Delta T_{\rm j} + \Delta\dot{M}_{\rm cool,j}T_{\rm j}\big). \tag{5.21}$$

In practice, a realistic estimate of the mass deposited into each shell, which takes into account heating, can be obtained by fitting models to the X-ray spectrum of each shell or a larger region if desired. The spectroscopic mass deposition rate is just a fitting parameter in this case and an integrated value can be obtained in exactly the same way as for the classical case above.

Generalising equation(5.19) to allow for heating shows that if the spectroscopically determined mass deposition rate, $\dot{M}_{\rm obs}$, is representative of the actual mass deposition rate, $\dot{M}_{\rm cool}$, then one can determine the heating rate from,

$$L_{\rm X}(<r) - H(<r) = \frac{5k_{\rm b}}{2\mu m_{\rm p}}\dot{M}_{\rm obs}(<r)T(r) = \frac{5k_{\rm b}}{2\mu m_{\rm p}}\dot{M}_{\rm cool}T(r). \tag{5.22}$$

If the spectroscopically determined value for the mass deposition rate is a true representative of the real mass deposition rate, then the integral within the cooling radius is simply the integrated mass deposition rate within the cooling radius,

irrespective of the radial distribution. Therefore, it would seem a sensible starting point for any calculations of the heating rates in galaxy clusters. To ensure consistency between theory and observations, the same mass flow rate (integrated mass deposition rate) must be employed, over the same region, in our heating models. Consequently, if the observed spectroscopic mass deposition rate integrated up to the cooling radius are used, then to be strictly accurate, the derived heating rates are only valid up to this radius.

5.3.3 Model Integrated Mass Deposition Rates

It is now possible to construct a model for the integrated mass deposition rate in galaxy clusters on the basis of the observational evidence. Although the model function is essentially empirical there are three main constraints to which it must adhere. These are: firstly, the fact that the observed spectroscopic mass deposition rate in each shell is approximately constant up to the cooling radius suggests linear dependence of flow rate on radius. Secondly, the observed density profiles also suggest that the mass deposition rate is negligible near the cluster centre. Otherwise a pronounced peak would be observed in the density profiles. Thirdly, the integrated mass deposition rate at the cooling radius must be equal to the observed integrated mass deposition rate at that location. A simple empirical form for the integrated mass deposition rate which is, in some way, consistent with the above is

$$\dot{M}(r) = \dot{M}_{\rm obs}(< r_{\rm cool})\left[K + \left(\frac{r}{r_{\rm cool}}\right)^2\right]^{0.5}, \qquad (5.23)$$

where $\dot{M}_{\rm obs}(< r_{\rm cool})$ is the integrated spectroscopic mass deposition rate at the cooling radius, K is a constant and $r_{\rm cool}$ is the cooling radius.

To estimate K we express it the following way, $K = (r_{\rm K}/r_{\rm cool})^2$, where $r_{\rm K}$ is a length scale corresponding to K. A suitable value for $r_{\rm K}$ is the radius of the central galaxy, roughly 30 kpc, since the effect of the interstellar medium is likely to significantly alter the inflow of material. This leads to values for K ranging from 0.73, for Virgo, to 0.04, for A478.

Note that equation (5.23) implies that $d\dot{M}/dr = 0$ for small radii, meaning that no material is deposited. However, at or near $r = 0$ the material must be deposited since it cannot flow to negative radii. This can account for the excess star formation which is observed to occur in these regions. For reasonable gradients of the temperature distribution, the second term on the right hand side of equation (5.12) then tends to infinity as r tends to zero. This implies that the model predicts negative heating rates, h, for small radii. In otherwords, the model is only valid outside the region at the very centres of clusters. To indicate the range over which this model can provide physically meaningful predictions, the minimum radius for each cluster at which h=0 is listed in table 5.3,. This minimum radius is taken as the lower integration limit in the calculation of the total heating rates.

For each cluster the observations are inevitably limited by spatial resolution and in some cases the lower integration limits, explained above, occur at radii which are closer to the cluster centre than the spatial resolution limits. In principle, the spatial resolution presents a limit beyond which one is unable to accurately describe the temperature and density of the cluster gas. However, because the temperature and density data for each cluster are fitted with analytical function their behaviour on sub-resolution scales can be extrapolated.

5.3.4 Thermal conduction

Thermal conduction of heat from the cluster outskirts to their centres may provide the required heating of the central regions without an additional energy source, like an AGN (e.g. Gaetz, 1989; Zakamska & Narayan, 2003; Voigt & Fabian, 2004). Of course, thermal conduction only transports energy from one region to another and does not lead to net heating. However, consider the case for which there is an infinite heat bath at large radii, then any drop in temperature at large radii, due to the inward transfer of thermal energy, is negligible.

Several 1-d models have been able to achieve a steady-state using thermal con-

duction alone (e.g. Zakamska & Narayan, 2003) and the combined effects of thermal conduction and AGNs (e.g. Brüggen, 2003; Ruszkowski & Begelman, 2002). Therefore, it seems sensible to compare the required heating rates with an estimate of the energy transport supplied by thermal conduction given the current state of each galaxy cluster.

As usual, the thermal conductivity is assumed to be given by Spitzer (1962), but includes a suppression factor, $f(r)$, defined in the previous chapter, to take into account the effect of magnetic fields,

For a steady-state to exist, the heating by thermal conduction must be equal to the heating rate,

$$\epsilon_{cond} = -h, \tag{5.24}$$

where h is the required heating rate per unit volume, given by equation (5.12).

This is essentially the same energy equation as solved by (e.g. Zakamska & Narayan, 2003), although mass deposition, line-cooling and variations in the Coulomb logarithm are allowed in this model. Equation (5.24) is then solved, using the observed temperature and density profiles, to determine the radial dependence of the suppression factor. This is different to the approach of (Zakamska & Narayan, 2003). In their paper they use the same equations to calculate temperature and density profiles that are consistent with a constant suppression factor. These derived profiles are only constrained by observations at the minimum and maximum radii accessible to observations. In this model the density and temperature profiles are taken from the observed data and the suppression factor is allowed to vary with radius.

The suppression factor is obtained by integrating both sides of equation (5.24) over a spherical surface and then rearranging for f,

$$f(r) = \frac{\int_{r_{\rm min}}^{r} r^2 h(r) \mathrm{d}r}{1.84 \times 10^{-5} r^2 \mathrm{d}T/\mathrm{d}r T^{5/2} / \ln \Lambda_{\rm c}}. \tag{5.25}$$

Note that the energy flux due to thermal conduction, $\kappa \mathrm{d}T/\mathrm{d}r$, increases with radius so that, for an infinite heat bath at large radii, energy must always be deposited

Name	$L_X(r_{\rm cool})/10^{42}{\rm ergs}^{-1}$	$L_X(r_{\rm cool})/10^{42}{\rm ergs}^{-1}$	$r_{\rm cool}/kpc$	$r_{\rm min}/kpc$
Virgo	10.7	$9.8^{+0.8}_{-0.7}$	35	1
Perseus	550	670^{+40}_{-30}	102	3
Hydra	243	250^{+15}_{-15}	100	3
A2597	470	430^{+40}_{-30}	129	4
A2199	156	150^{+10}_{-10}	113	1
A1795	493	490^{+30}_{-30}	137	1
A478	1494	1220^{+60}_{-60}	150	3

Table 5.3: Comparison of bolometric luminosities derived from our functions fitted to the data (column 2) with those given in Bîrzan et al. (2004) (column 3), the cooling radius (column 4) and the lower integration limits (column 5).

at each smaller radius, rather than taken away.

5.4 Results:1

5.4.1 Comparison of Luminosities

To ensure that the model estimates are compatible with observations, the bolometric X-ray luminosities, within the cooling radius, are determined from the functions fitted to the data and compared to the observed luminosities presented in Bîrzan et al. (2004). The metallicity for the cooling function is assumed to be half-solar.

Table 5.3 demonstrates reasonable agreement between the results obtained using the fitted functions and those presented in Bîrzan et al. (2004).

Name	$\dot{M}_{\rm spec}(< r_{\rm cool})$	$\dot{M}_{\rm clas}(< r_{\rm cool})$	$\dot{M}_{\rm spec}(< r_{\rm cool})\frac{r_{\rm K}}{r_{\rm cool}}$
Virgo	$1.8^{+1.2}_{-0.16}$	10	1.3
Perseus	$54^{+48.}_{-18}$	183	4.7
Hydra	14^{+9}_{-7}	315	1.3
A2597	59^{+40}_{-40}	480	3.2
A2199	$2^{+7}_{-1.9}$	150	0.1
A1795	18^{+12}_{-10}	478	0.9
A478	150^{+60}_{-68}	570	6

Table 5.4: Mass deposition rate parameters (all quantities in solar masses per year). The integrated spectral mass deposition rates are taken from Bîrzan et al. (2004) and the classically determined values are from Fabian (1994) and references therein. The central mass flow rates calculated using equation (5.23) are also shown for comparison.

5.4.2 Integrated Mass Deposition rates

Since the values of the integrated mass deposition rates that are used is critical to determining the heating rates, they are presented first. In table 4 compares the integrated spectroscopic mass deposition rate, $\dot{M}_{\rm spec}(< r_{\rm cool})$ (Bîrzan et al., 2004), with the integrated classical mass deposition rate, $\dot{M}_{\rm clas}(< r_{\rm cool})$ (Fabian, 1994) at the cooling radius, and the central integrated mass deposition rate predicted by equation (5.23).

From equation (5.20) it is clear that the spectroscopic mass deposition rates are indicative of the energy injected into the cluster. Because of this, the spectroscopic mass deposition rate should be less than the classical value,depending upon the

relative magnitudes of the heating and cooling, as is the case. However, because of the time taken to dissipate this injected energy into the ambient gas this implies that the current spectroscopic mass deposition rates are a function of the heating which has taken place over the last few times 10^8 yrs.

The central integrated mass deposition rates predicted by equation (5.23) are sufficiently low that the total mass deposited in the cluster centre, over a Gyr, will not significantly alter the total central mass. It should be noted that a smaller value of the constant, K, in equation (5.23), would result in still smaller central integrated mass deposition rates.

5.4.3 Required Heating rates and Thermal Conduction Suppression factors

The heating rates are shown in figure 5.2, for the form of integrated mass deposition rates given in equation (5.23). For comparison, we also show the volume heating rate profiles for unsuppressed thermal conduction.

Figure 5.2 shows that the heating rates for the entire sample of clusters exhibit similar profiles. This is because the radiative losses most strongly depend upon the density, therefore so must the required heating rate. Since the majority of the density profiles are described by β-profiles, this similarity is expected.

In comparison, it is clear that the volume heating rates for unsuppressed thermal conduction vary from cluster to cluster and do not share the same profile as the required heating rates. Even for the clusters in which thermal conduction can supply the necessary energy, the different radial dependences require that the suppression factor is fine-tuned to provide the correct heating rate for all radii. This demonstrates the different nature of the physical processes involved in radiative cooling and thermal conduction, making a balance between the two hard to achieve.

The radial dependence of the thermal conduction suppression factor required for

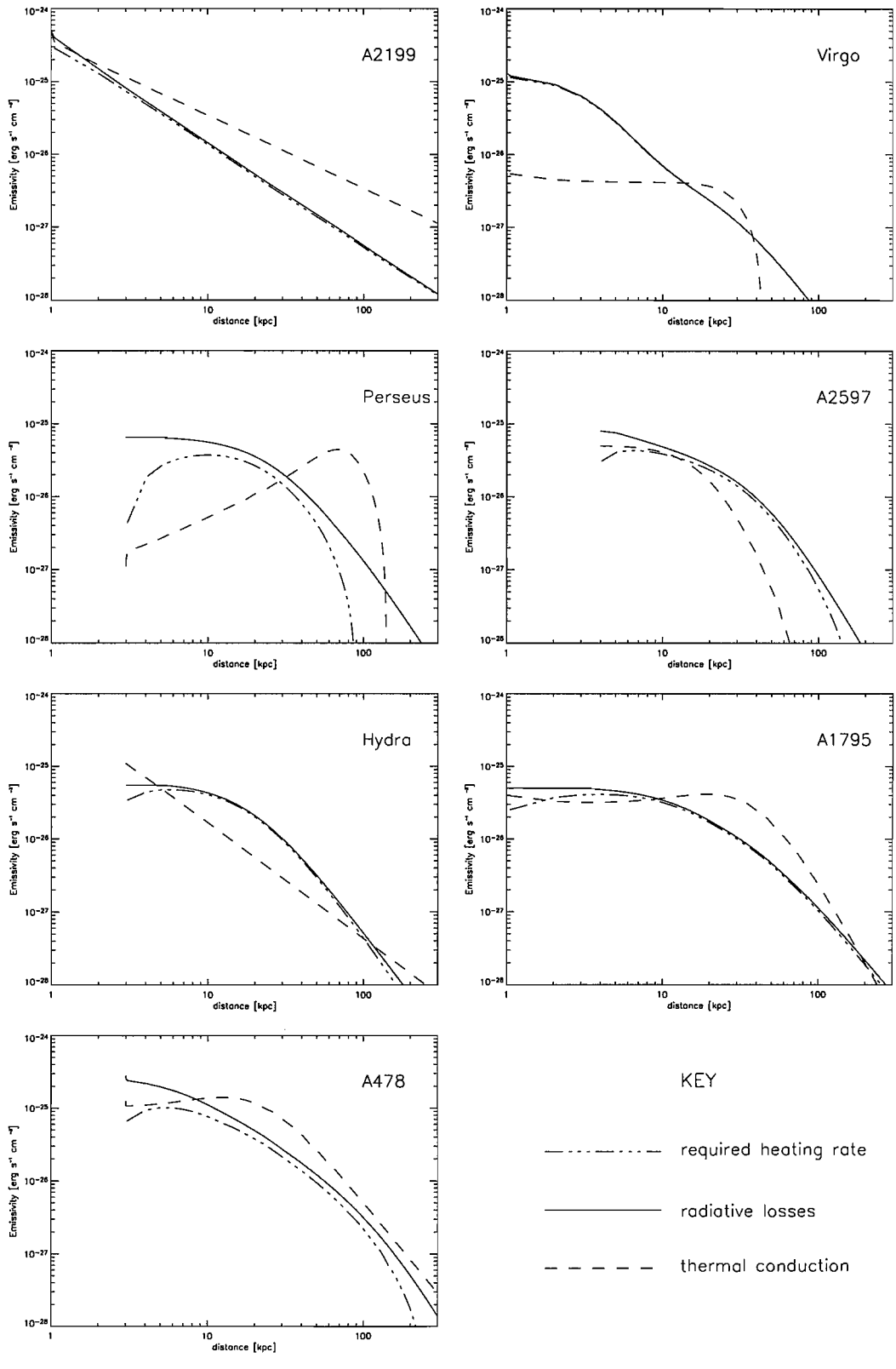

Figure 5.2: Comparison of cooling and heating rate profiles for each cluster. The heating rates fall to zero at a radius which depends upon the mass deposition rate. At the point at which this occurs, we also terminate each of the other curves since we cannot determine the gas properties within this radius.

thermal equilibrium is given by equation (5.25). The results, plotted in figure 5.3, suggest that thermal conduction could provide the required heating rates in A2199, A478, Perseus and very nearly A1795. It seems impossible that thermal conduction would be able to transport sufficient energy towards the central regions for the remainder of the sample.

It is evident that the suppression factor profiles are different in almost every case, although A1795 and A478 appear to have certain features in common. The only commen trait is that the required suppression factor tends to be largest near the centre, except for A2597 and Hydra. This suggests that even in the regions where the suppression factor takes physically meaningful values ($f < 1$), in order for thermal conduction to provide the necessary heating, the parameters which determine the suppression factor require unique fine tuning in each cluster. Note that suppression factors of greater than unity are unphysical for laminar flows but are possible in mixing layers (e.g. Cho et al., 2003).

These suppression factors can be compared with those found by Zakamska & Narayan (2003) who studied four of the clusters in our sample. They find suppression factors or 1.5, 2.4, 0.4 and 0.2 for Hydra, A2597, A2199 and A1795 respectively. Their values agree with these results in that this work also finds that thermal conduction must take unphysically large values for Hydra and A2597 and realistic value for the remaining two clusters. Voigt & Fabian (2004) also provide a suppression factor, roughly 0.2-0.3, for A478 which is consistent with, albeit lower than, the possible values found here for the same cluster.

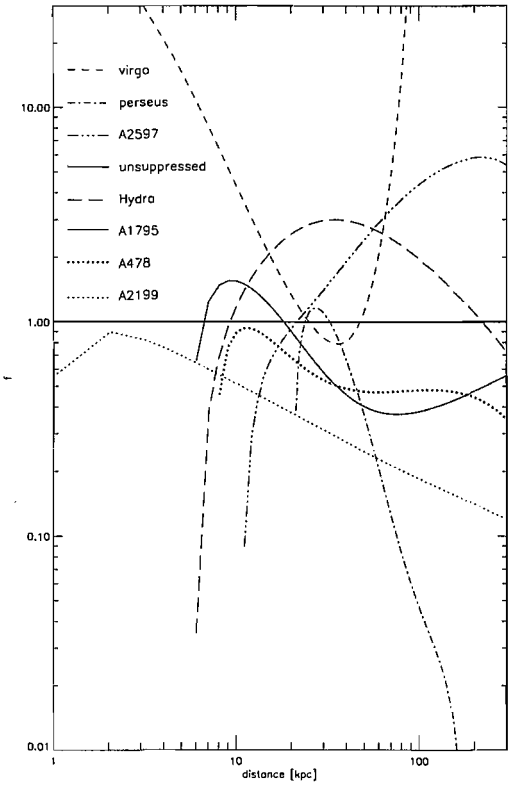

Figure 5.3: Thermal conduction suppression factors for the sample of seven clusters. The thick, solid line shows the maximum physically meaningful suppression factor (f=1) for comparison.

5.5 Comparison of Required Heating Rates with Observations

5.5.1 Comparison with AGN

The time-averaged mechanical luminosity of a central AGN in each cluster is estimated using

$$\langle L_{\rm mech} \rangle = \frac{\alpha PV}{t}, \tag{5.26}$$

where α=16. P is the ambient cluster gas pressure, V is the bubble volume and t is the estimated period for recurrent AGN activity. It is initially assumed that the period of activity for each AGN is 10^8 yrs. The factor 16 arises from 2 bubbles per outburst, a factor of 2 for the energy dissipated in the shock expansion of the

bubble and 4 for $\gamma/(\gamma-1)$ where $\gamma = 4/3$ for relativistic gas.

This is simply an estimate of the rate at which energy is injected into the cluster, by the central AGN, and is not related to any particular physical process by which this energy is dissipated e.g. the viscous dissipation of sound waves or effervescent heating.

The estimated AGN power injection rates are given in column 2 of Table 5. To compare the required heating rates with the observational estimates of AGN heating in equation (5.26) the volume integral of equation (5.12) must be calculated. This provides an estimate of the heating luminosity required within a given volume to satisfy the requirements of the assumed steady-state. Comparing this value with that of the power output from AGNs at the centres of galaxy clusters provieds an estimate of the frequency with which buoyant plasma bubbles, identical to those currently observed, must be produced in order to provide sufficient heating within the cooling radius. This is defined as the AGN period, which may be calculated using

$$\frac{4\pi \int_{r_{\rm min}}^{r_{\rm cool}} r^2 h \mathrm{d}r}{\langle L_{\rm mech} \rangle} = \frac{t}{\tau}, \tag{5.27}$$

where $r_{\rm cool}$, the upper integration limit, is the cooling radius and $r_{\rm min}$ is the radius at which the heating rate tends to zero for our chosen descriptions of the mass flow rate, τ is the calculated period and t is the time defined in equation (5.26).

5.5.2 The Combined Heating by Thermal Conduction and AGN

To estimate the total rate of energy injection by AGNs into the cluster gas within the cooling radius we assume that all of the energy available in the bubbles is dissipated within the cooling radius. Over a spherical surface the rate at which thermal conduction transfers heat across a radius, r, is

$$L_{\rm cond}(r) = 4\pi r^2 \kappa \frac{\mathrm{d}T}{\mathrm{d}r}. \tag{5.28}$$

The maximum total rate at which energy can be injected into this region is the

sum of these two processes. This sum is compared with the heating rate required for steady-state and allowing for mass deposition. This gives the thermal conduction suppression factor required to maintain a steady-state given the current AGN heating rate. This suppression factor is calculated using

$$f = \frac{L_{\rm heat}(< r) - \langle L_{\rm mech} \rangle}{L_{\rm cond}(r)}, \tag{5.29}$$

where $L_{\rm heat}(< r)$ is the required heating rate for the spherical volume within r, $\langle L_{\rm mech} \rangle$ is the current mechanical power of the AGN assuming a period of 10^8yrs.

5.6 Results:2

5.6.1 AGN Duty Cycles

The AGN periods (see table 5.5) for Virgo and A478 are of the order of 10^6 yrs which is very short compared to the predicted lifetimes of AGN (e.g. Nipoti & Binney, 2005, and references therein). In contrast, the Hydra cluster requires recurrent outbursts of magnitude similar to the currently observed one only every 10^8 yrs, or so. The required periods for the remaining AGNs are of the order of 10^7 yrs. From this, the obvious conclusion is that if thermal conduction is negligible and if this sample is representative of galaxy clusters in general, then many if not all clusters will probably be heated, at certain points in time, by extremely powerful AGN outbursts. However, it is worthwhile pointing out that roughly 71% of cD galaxies at the centres of clusters are radio-loud (Burns, 1990) which is larger than for galaxies not at the centres of clusters. This may suggest that the galaxies at the centres of clusters are indeed active more frequently than other galaxies. It is possible that a combination of these two effects satisfies the heating requirements we have identified.

In contrast to the spectroscopically derived mass deposition rates, the plasma bubbles, that still exhibit radio emission and are currently observable, are probably more indicative of the current heating rate rather than the heating rate over the

previous 10^9 years, or so. If this is true, only Hydra is currently being excessively heated in this small sample.

These results also show that the gas outside the cooling radius requires significant amounts of energy to allow a steady-state. Given the large heating requirements for the regions outside the cooling radii of Virgo, A2199 and A478, it is reasonable to ask whether it is possible for the observed plasma bubbles in these clusters to deliver energy at such large radii. The observational evidence (e.g. Bîrzan et al., 2004) seems to show that bubbles rarely rise to beyond 40 kpc from the cluster centre and in general tend to reach only a few tens of kiloparsecs. This may be because beyond these radii, hydrodynamic instabilities have shredded the bubbles (e.g. Kaiser et al., 2005; Reynolds et al., 2005; Robinson et al., 2004; Churazov et al., 2001), or alternatively the isoentropy radius at which the bubbles spread out and form pancakes is generally at radii of these magnitudes (e.g. Churazov et al., 2001). Alternatively, the apparent absence of bubbles at larger radii may be a selection effect since they are harder to detect against the rapidly declining X-ray surface brightness profiles. In any case, it is possible that extremely powerful outbursts with highly extended jets such as Hydra-A or Cygnus-A type events are the best mechanism by which energy is supplied to such large radii, since they cannot be reached by smaller scale outbursts.

5.6.2 The Combined Heating by Thermal Conduction and AGNs

From table 5.5 it is clear that A2597 is currently being heated insufficiently by the combined effects of AGN and thermal conduction. Thus, it seems that the only way that A2597 can avoid a cooling catastrophe is by an exceptionally large AGN outburst which will have to be roughly 100 times more powerful than the current outburst in order to provide sufficient heating. Of the other clusters in this sample, the suppression factors are all physically acceptable except for Hydra. The reason for this and the negative value of the suppression factor for Hydra is that the energy of the current AGN outburst exceeds the heating requirements within the cooling

Name	$L_{\rm mech}/\alpha(10^{42}{\rm ergs}^{-1})$	$\tau/(10^8{\rm yr})$	$L_{\rm cond}/(10^{42}{\rm ergs}^{-1})$	$L_{\rm heat}/(10^{42}{\rm ergs}^{-1})$	f
Virgo	$0.052^{+0.028}_{-0.032}$	0.078	13.7	10.7	0.72
Perseus	$5.9^{+3.8}_{-1.2}$	0.28	4360	236	0.05
Hydra	$27.1^{+1.5}_{-2.9}$	1.9	112.8	231	−1.8
A2597	$5.6^{+5.2}_{-1.6}$	0.21	71.0	427	4.8
A2199	$1.3^{+1.9}_{-1.2}$	0.14	797	149	0.16
A1795	$12.5^{+16.8}_{-1.3}$	0.43	1280	465	0.2
A478	$1.9^{+1.0}_{-0.3}$	0.026	2720	1169	0.4

Table 5.5: Assumed average mechanical luminosity per bubble in each cluster based on the observations summarized in Bîrzan et al. (2004) and assuming a period of 10^8 yrs in (column 2), period of each AGN in units of 10^8 yrs evaluated at the cooling radius (column 3), rate at which energy is supplied to the region within the cooling radius by thermal conduction (column 4), the total required heating rate within the cooling radius (column 5) and the suppression factor for combined heating by AGNs and thermal conduction (column 6). All quantities are evaluated at the cooling radius.

radius. However, the errors associated are relatively large so it is difficult to say with any certainty if a combination of heating by thermal conduction and AGN can achieve a steady-state.

Although the global suppression factor for thermal conduction is physically acceptable, it still requires fine-tuning inside each cluster to allow a steady-state.

5.7 Summary

In the heating of intracluster gas, the energy input required from AGNs is likely to depend on the strength of any other heating processes. For example, if thermal conduction is present and can reduce the integrated mass deposition rate towards the cluster centre, it is likely that in this case the AGN outbursts will have to be less powerful than in an otherwise identical cluster in which thermal conduction does not occur. There may also be additional heating processes such as stirring by galaxy motions or the gas motion resulting from past cluster-cluster mergers.

The heating rates required to maintain a steady state, for a sample of seven galaxy clusters, have been calculated, with the assumption that the mass flow rates are radially dependent. This model uses the spectroscopically determined integrated mass deposition rates. Below is a summary of the main findings for each cluster, in terms of the mass deposition rates, thermal conduction and required AGN period.

A2199: It appears that, without AGN heating, thermal conduction is sufficient for the steady-state heating requirements. In the absence of thermal conduction, the required AGN period of roughly 10^7 yrs is short, but still compatible with predicted AGN lifetimes. When simultaneous heating by both AGN, based on the current outburst, and thermal conduction are considered, the suppression factor necessary to satisfy the heating requirements within the cooling radius is roughly 0.16 which is acceptable.

Virgo: Even allowing for mass deposition, thermal conduction alone is insufficient for providing the heating requirements at all radii. This agrees with the simulations performed in the previous Chapter. The required AGN period, in the absence of thermal conduction, of roughly 10^6 yrs is very short compared with predicted AGN lifetimes suggesting that significantly larger AGN outflows are required at certain intervals to prevent a cooling catastrophe. This is interesting since Virgo has the smallest heating requirement in our sample. Within the cooling radius, the combined effect of the current AGN outburst and thermal conduction can achieve the required

heating with a suppression factor of 0.7.

Perseus: It seems that in the absence of an AGN, thermal conduction may be insufficient compared to heating requirements at roughly roughly the central 30 kpc, but may be sufficient outside this radius. However, the results of the simulations in the previous Chapter suggest that the observed temperature profile could not form if thermal conduction was efficient. This result highlights the inadequacies of energy budget calculations compared to complete hydrodynamic calculations. Without thermal conduction, the required AGN period of roughly 3×10^7 yrs is also compatible with predicted AGN lifetimes. The suppression factor for the combined effect of AGN and thermal conduction to provide the required heating is 0.05.

Hydra: Thermal conduction alone cannot provide the necessary heating for maintaining a steady-state. The required AGN period in the absence of thermal conduction is long compared with predicted AGN lifetimes which reflects the powerful nature of the current outburst. This is the most powerful central AGN outflow in this small sample. Since the current AGN outburst in Hydra is so powerful, it more than satisfies the heating requirements within the cooling radius. This inevitably leads to a negative value for the suppression factor.

A2597: It appears that thermal conduction on its own cannot provide sufficient heating except between roughly 4-10 kpc. Without thermal conduction, the required AGN period is also compatible with predicted AGN lifetimes. A2597 has the largest heating requirements in this sample, followed by A478. Both require more than two orders of magnitude more heating power within the cooling radius than Virgo. It is interesting to note that even a combination of the current AGN heating rate and full Spitzer thermal conduction provide roughly only one fiftieth of the required heating rate within the cooling radius. It therefore seems as if the only means by which a cooling catastrophe can be averted in this system is by an extremely powerful AGN outburst, or a cluster-scale merger.

A1795: On its own, thermal conduction is sufficient to match the heating re-

quirements throughout most of the cluster, although not near 5 kpc. The required AGN period, in the absence of thermal conduction, of roughly 4.3×10^7 yrs is also compatible with predicted AGN lifetimes. For a combination of heating by AGN and thermal conduction a suppression factor of roughly 0.2 is required to achieve the necessary heating.

A478: Thermal conduction alone should be sufficient for matching the heating requirements. In addition, the required AGN period in the absence of thermal conduction is very short compared with predicted AGN lifetimes. The central AGN outburst in this system is the least powerful in our sample.

These results suggest that heating from AGN, with periods of 10^8 yrs, alone is unable to maintain a steady-state, but may result in a quasi steady-state if more powerful outbursts are interspersed with the more common lower power outbursts. Alternatively, it may be that a combination of AGN heating and thermal conduction could provide the necessary heating, at least within the cooling radius, in all but one cluster of our sample: A2597. However, although thermal conduction is a possible heating mechanism of the central regions of galaxy clusters it is still not clear whether thermal conduction actually is an efficient heating mechanism in galaxy clusters. For example, from numerical simulations of the Virgo cluster by Pope et al. (2005), taking in to account thermal conduction with different suppression factors, the observed temperature profiles are most consistent with a suppression factor of between 0-0.1. This is at odds with the value of the suppression factor we have derived for most clusters in this sample. In all cases the effectiveness of thermal conduction must be fine-tuned as a function of radius in order to allow a steady-state of the cluster gas.

It is worth noting that galaxy clusters also need to be heated at radii outside the cooling radius if a time-averaged steady-state is to be maintained. Two possible mechanisms for this are sound waves excited by buoyantly rises bubbles and comparatively rare, but very powerful, AGN outbursts.

It may also be possible to predict which clusters are more likely to experience more powerful AGN outbursts in the near future. For example, if a cooling flow has formed, the fractional decrement in gas temperature between the cooling radius and the cluster centre is likely to be larger than in a cluster which has recently been heated by a large AGN outburst. Then, if the period required to maintain a steady state is much less than 10^8yrs, the implication may be that a powerful outburst is iminent.

Based on the above criteria it seems that in this sample A478 and A2597 are the clusters most likely to experience a powerful AGN outburst in the near future. Virgo appears also to be a candidate for an iminent ouburst, however, the relatively small temperature difference between the cluster center and the cooling radius indicates that it may recently have experienced sufficient heating.

The results for the required heating rates indicate that, if buoyant plasma bubbles are the only heating mechanism by which clusters are heated and assuming the original period, then, of this small sample, only the AGN at the centre of Hydra is currently injecting sufficient energy to heat the gas within several multiples of the cooling radius. For the remaining six clusters, the energy available in the form of plasma bubbles is only sufficient to provide the required heating within a relatively small fraction (roughly 0.1-0.5) of the cooling radius. This significant energy deficit implies that these clusters may not be in a steady-state, or that the AGNS are active far more frequently at the centres of clusters than outside.

A possible scenario which is consistent with these results is that AGNs in general produce only relatively small or moderately powerful outbursts, such as we observe in the majority of clusters, which delay the occurence of a cooling catastrophe by a small amount each time. These small heating events may occur too infrequently to prevent the formation of a cooling flow and the temperature gradient grows with time. Eventually sufficient material is accreted by the central galaxy to initiate an extremely energetic outburst such as those seen in Cygnus-A and Hydra-A. This would also allow the heating of material at radii which are hard to reach with lower

power outbursts. In this way the moderately powerful AGN outflows observed in most clusters only delay more energetic events. Such a scenario for clusters, small-scale AGN heating interpersed occasionally with more energetic events, evolution is complex and would have to be modelled numerically.

One difficulty with observations of galaxy clusters is that the timescales are incredibly long. Consequently, it is almost impossible to observe the evolution of any part of these systems during a human lifetime. As a result, many of the current interpretations of certain observed features may not be entirely correct. This is not a criticism of the current techniques, many of them are ingenious, but simply means numerical simulations can be used to help refine these techniques.

Using simulations, it is possible to 'observe' the evolution of various properties within a comparatively short time. These simulations can be used to investigate the properties of AGN heating, for example. In principle, the spatial resolution of a simulation can be significantly greater than is possible for real observations. Therefore, using simulations it may be possible to attribute certain observational signatures to particular events and physical processes. Of course, there must be a word of caution here: the results of simulations often correspond somewhat to the initial assumptions.

Chapter 6

Heating the ICM with Jets from AGNs

6.1 Introduction

Collimated outflows or jets are ubiquitous throughout the Universe. They are observed in star forming regions, X-ray binary systems and in AGNs. Yet despite many years of study it is still not clear how these outflows or jets are produced. Regardless of this, it is becoming increasingly clear is that outflows of all types influence their surroundings, whether this is the ICM (e.g. Fabian et al., 2002; Forman et al., 2005; Nulsen et al., 2005; Zanni et al., 2005; Croton et al., 2006; Sijacki & Springel, 2006; Vernaleo & Reynolds, 2005), the atmospheres of elliptical galaxies (e.g. Binney & Tabor, 1995; Best et al., 2006) or the interstellar medium (e.g. Fender et al., 2005). In galaxy clusters, the interaction between AGN jets and their environment is immediately apparent from the giant radio lobes that are inflated in the cluster gas by the outflow. Estimates of the enthalpy required to inflate these regions, divided by a relevant timescale, can then be used to estimate the jet power, (e.g. Bîrzan et al., 2004). In contrast, the interaction of X-ray binary jets with their surroundings is only recently beginning to become clear, with only the Cygnus X-1 jet having been

observed to produce a bow shock similar to those seen with AGN jets (Gallo et al., 2005).

6.2 Jet Setups

Despite an increasing number of recent studies being conducted in this area (e.g. Basson & Alexander, 2003; Omma et al., 2004; Zanni et al., 2005; Vernaleo & Reynolds, 2005; Heinz et al., 2006), setting up jet simulations is still not trivial. The approach must be tailored to the specific requirements of each hydrodynamics code. For example, it is possible to conceive of numerous ways of introducing jets, with the most common being introduction on a boundary. Boundary injection works well for codes, such as ZEUS, which support 3-d polar coordinates. In this case, a spherical boundary near the centre of the grid can be created and material injected in the form of two anti-parallel jets. This method also provides a natural solution to the problem of the jet opening angle: the injected jet material will automatically move in a radial direction with the specified opening angle. In contrast, codes such as FLASH do not support 3-d polar coordinates. This makes an inner boundary at the centre of the grid diffult to create. As a consequence of this the simplest way forward is to restrict the volume of the simulation to one half of the entire volume, thereby placing one of the cartesian boundaries at the centre of the simulated clusters, and inject material via a single jet. The cartesian coordinate system also makes the jet opening angle difficult to determine.

For a cartesian grid there are also two main alternatives to boundary injection. These are i) creating two perturbation regions which are the sources of the jets, and ii) adding energy and momentum to two regions which act as the sources of the jets. Each of these alternatives is described below, but due to conceptual and numerical problems, I do not discuss them in great detail.

In this Chapter, the definitions and usage of 'bubble', 'cavity' and 'remnant' is essentially interchangable.

6.2.1 Perturbation jets

In this method each jet is generated by perturbing the temperature and density, while maintaining pressure equilibrium, and the velocity of a spherical region which is close to the cluster centre. To create the typical characteristics of a jet, the temperature is raised by a typical factor of 100 compared to the ambient gas, while the density is reduced by a factor of 100. This approach, along with specifying the initial velocity, can be taken for the first timestep, but after this the ambient temperature will have been affected by the jet. Consequently it is necessary to have a prescription for the jet temperature and velocity as a function of the ambient parameters at each timestep. This can be achieved by assuming that the jet power and mass flow rate are constant in time, as described below.

The mass flow rate of the jet material out of the perturbation region is,

$$\dot{m} = A\rho v \tag{6.1}$$

where A is the area over which the jet injection occurs, ρ is the jet material density and v is the bulk velocity of the jet.

The jet power is the sum of the internal and kinetic parts,

$$\dot{E} = \dot{m}\left(\frac{5k_{\rm b}T}{2\mu m_{\rm p}} + \frac{1}{2}v^2\right). \tag{6.2}$$

Assuming the power and mass flow rate are constant and substituting P/ρ for $k_{\rm b}T/\mu m_{\rm p}$ and using $\rho = \dot{m}/(Av)$, gives a quadratic equation in terms of jet velocity,

$$\dot{E} = \dot{m}\left(\frac{5}{2}\frac{PAv}{\dot{m}} + \frac{1}{2}v^2\right). \tag{6.3}$$

Since the jet is assumed to be in pressure equilibrium with the ambient gas, solving equation (6.3) gives the jet velocity for a given value of the ambient pressure,

$$v = \left(\frac{25}{4}P^2A^2 + \frac{2\dot{E}}{\dot{m}}\right)^{1/2} - \frac{5}{2}PA. \tag{6.4}$$

The temperature of the jet can then be determined by substituting for the density using equation (6.1),

$$T = \frac{\mu m_{\rm p}PAv}{\dot{m}k_{\rm b}}. \tag{6.5}$$

During the phase when the jet is active, all cooling in the immediate vicinity of the injection regions is turned off to ensure numerical stability. After the injection phase is completed, and during the subsequent phase of passive evolution of the jet, the radiative losses are restarted [1]. This does not significantly alter the results as the duration of the jet injection phase is short compared to the cooling time.

In this method energy is not added to the grid at each timestep as well because equation (6.3) provides a prescription for how the temperature and velocity should behave. This means that the information about the material contained in the perturbation region at the beginning of the timestep is lost. Essentially, the energy of the material in the perturbation region is thrown away and assigned new values. This means that energy is also lost from the system during this process. As a result it is not possible to determine the exact amount of energy added or subtracted from the grid in each timestep.

6.2.2 Perturbation jets: results

In this section I show plots for several 2-d simulations that investigate the evolution of high and low speed jets (8×10^9 and 8×10^9 cm s^{-1} respectively) and a simulation in which there were multiple outbursts. The high-speed jet was active for 2×10^6 yrs and the low speed jet for 5×10^6 yrs.

Figure 6.1 shows the early evolution of an energetic outflow in terms of the density. In this particular example, there is no counter jet. Despite this it is still interesting to note the features of this outflow. After sufficient time there are pressure enhancements at the leading end of the jet. These are often observed in real AGNs, for example Hercules, as hotspots. The jet channel also displays the characteristic X shape which is a signature of self-collimation.

[1]Note that, in the limit where the jet is highly supersonic, the internal energy of the jet material is negligible and the jet velocity tends to a constant given by the energy and mass injection rates only, as expected from equation (6.2), $v = 2\dot{E}/\dot{M}$.

It is of particular interest that the lower velocity jet produces quasi-spherical bubbles which seem to be quite stable to the action of Rayleigh-Taylor and Kelvin-Helmoltz instabilities. The evolution of these bubbles is shown in figure 6.2. Bubbles can be defined more generally to not only include true bubbles, but also tori or "rings" seen in projection. This result is quite different to the behaviour of simulated bubbles that are produced *adhoc* rather than inflated by jets. It seems that the stability of the bubbles may be enhanced by the velocity field around the bubble surface.

Another point of interest is that the back flows of the jets interact to produce plumes of material expanding perpendicular to the jet axis, that are warmer than the ambient gas. Effectively, this means that outflows not only heat in the direction of the jet propagation but also perpendicularly to it as well, see particularly figure 6.3.

The very long term evolution of the lower velocity jets is shown in figure 6.4 which is a snapshot of a simulation in which jets were 'switched on' every 10^8yrs. It is difficult to discern many of the bubbles except for the one to the far left. This is because the first injection leads to turbulence in the cluster gas which still sufficiently disturbs the ICM at the time of the next injection so that the jets are completely disrupted. The remnants of the later injections are visible as low density vortices which reside near the cluster centre. Perhaps higher velocity jets would have penetrated the turbulent medium better and led to more coherent bubbles. However, this is difficult to tell since the higher velocity jets, in this method, did not really produce structures that could qualitatively be described as bubbles.

Interestingly, the morphology of the bubble on the left of figure 6.4 is reminiscent of the 'spherical cap' bubble that is pointed out in the Perseus cluster (e.g Fabian et al., 2002). In the case of the Perseus cluster, the shape of the bubble is sometimes thought to be an indication that the ICM is viscous. The results of these 2-d simulations seem to suggest that viscosity is not a requirement for AGN-blown bubbles to remain intact out to large distances.

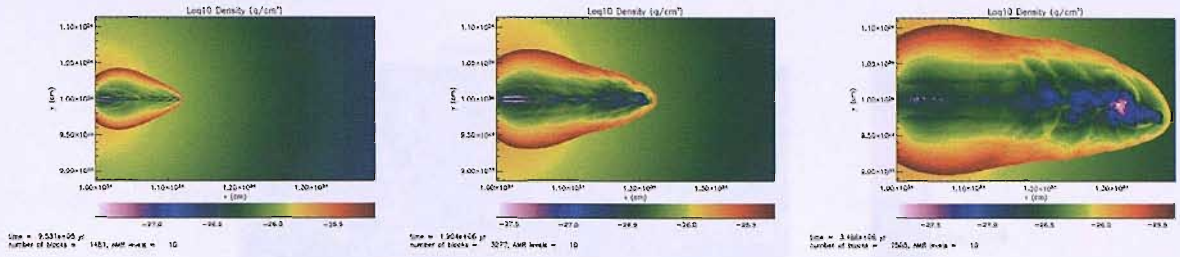

Figure 6.1: Density plots of a high velocity jet ($v \sim 7 \times 10^9 \mathrm{cm\,s^{-1}}$).

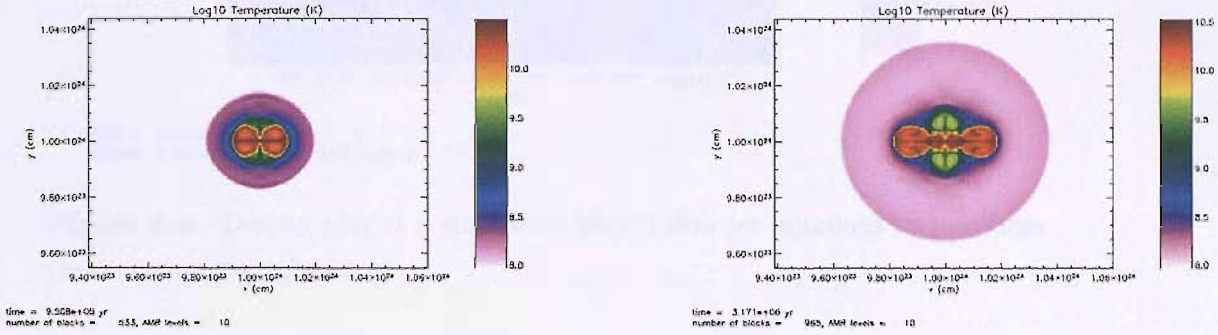

Figure 6.2: Temperature plots of a low-velocity jet in a simulated version of the Perseus cluster ($v \sim 1.7 \times 10^9 \mathrm{cm\,s^{-1}}$)

Originally, this jet injection mechanism appeared to work satisfactorally for a wide range of jet parameters and was computationally stable. However, an update of the Beowulf cluster, Iridis 2, seemed to alter the way that the code ran and this method subsequently became unstable. As a result, an alternative method was required with the different attempts being discussed below.

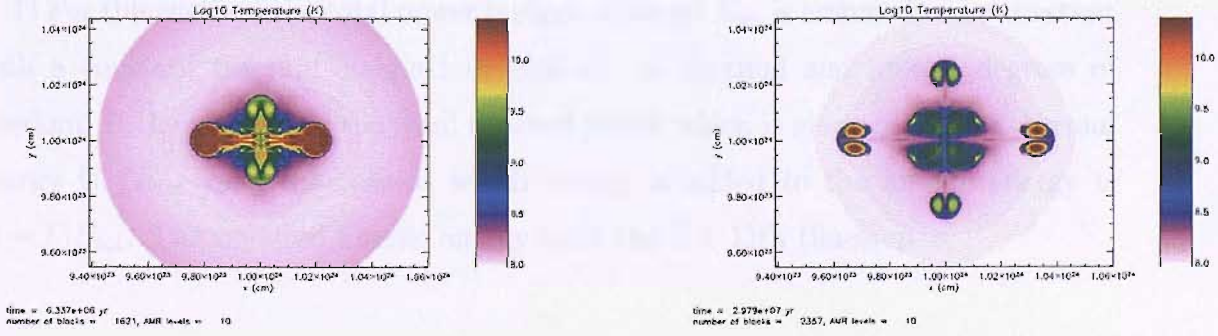

Figure 6.3: Temperature plots of the same low-velocity jet in the Perseus cluster.

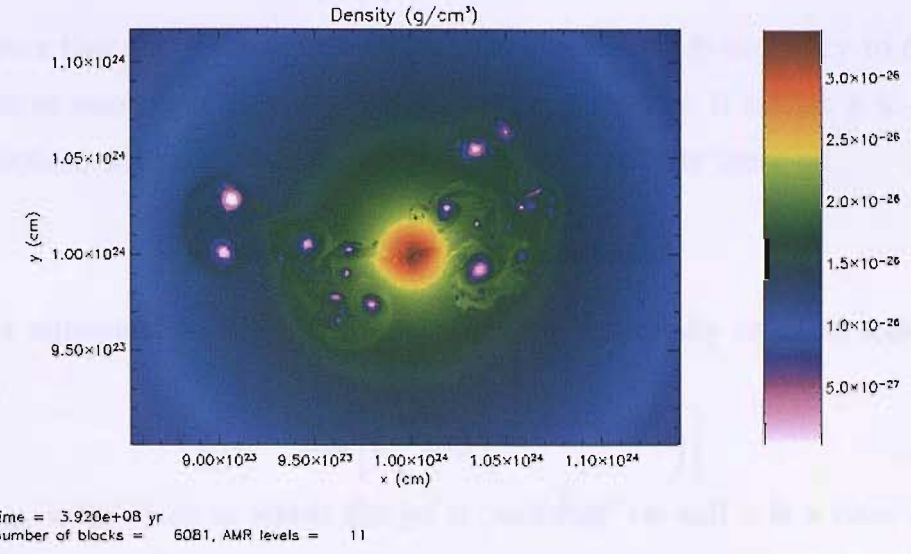

Figure 6.4: Density plot of a simulation after 3 slow jet injections in the Virgo cluster ($v \sim 1.7 \times 10^9 \mathrm{cm\,s^{-1}}$).

6.2.3 Energy injection jets: constant fractions

An alternative method of jet production is to inject energy at a specific location and at a particular rate, this is the method employed by Omma et al. (2004). Since jets have both kinetic and and thermal energy, the injected energy must be divided between these two degrees of freedom. There are numerous ways of doing this, but the two most obvious choices are: 1) giving a constant fraction to each of the degrees of freedom and 2) supplying thermal energy at a rate to maintain the jet temperature at a constant value and supplying the remainder as kinetic energy.

1) For this method the total power budget of the jet $\dot{E}_{\mathrm{jet}}$ is assumed to be constant with a constant fraction assigned to each of the thermal and kinetic degrees of freedom. If the fraction of the total injected power which is given to the jet thermal energy is $f\dot{E}_{\mathrm{tot}}$ then the rate at which energy is added to the kinetic energy is $(1-f)\dot{E}_{\mathrm{tot}}$. The updated kinetic energy after the $(i+1)$th timestep is,

$$E_{\mathrm{kin,i+1}} = E_{\mathrm{kin,i}} + \dot{E}_{\mathrm{i}}\Delta t \tag{6.6}$$

where $\dot{E}_{\rm i} = (1-f)\dot{E}_{\rm tot}$.

To ensure that the jet moves in a particular direction it is necessary to calculate the velocities associated with the kinetic energy. Therefore, if the jet is to move in the x-direction, with zero opening angle, then the x-velocity must be,

$$v_{\rm x,i+1} = \sqrt{2[E_{\rm kin,i+1} - (v_{\rm y,i}^2 + v_{\rm z,i}^2)]}. \tag{6.7}$$

To ensure numerical stability, the energy is added gradually using an exponential function,

$$\dot{E}(t) = \dot{E}_{\rm tot}\left[1 - \exp\left(\frac{-(t-t_{\rm start})}{\tau}\right)\right] \tag{6.8}$$

where $t_{\rm start}$ is the time at which the jet is 'switched' on and τ is a time constant which was set to 10^6yrs.

An exponential decay was also used when the jet is switched off.

$$\dot{E}(t) = \dot{E}_{\rm tot}\left[\exp\left(\frac{-(t-t_{\rm end})}{\tau}\right)\right] \tag{6.9}$$

where $t_{\rm end}$ is the time at which the jet is 'switched' off and the value of the time constant is the same as for equation (6.8).

The energy is spatially injected according to a Gaussian distribution around a central point, r_0,

$$\dot{E}(r) = \dot{E}(0)\exp\left(-\frac{1}{2}\frac{(r-r_0)^2}{r_{\rm jet}^2}\right) \tag{6.10}$$

where $\dot{E}(0)$ is the amplitude of the energy injection rate, r is the radial coordinate and $r_{\rm jet}$ is the approximate radius of the jet.

An important part of this particular process is that the injection region must stay in pressure equilibrium with the surroundings. If this is not ensured, the pressure in the vicinity of the heat source will exceed the ambient pressure. Consequently, the heated fluid will expand to reduce the pressure excess and the density of this expanding parcel of gas will drop. Such a situation is more reminiscent of an explosion rather than a collimated outflow. How to maintain pressure equilibrium is not quite as clear as first thoughts would suggest. For example, once energy is injected,

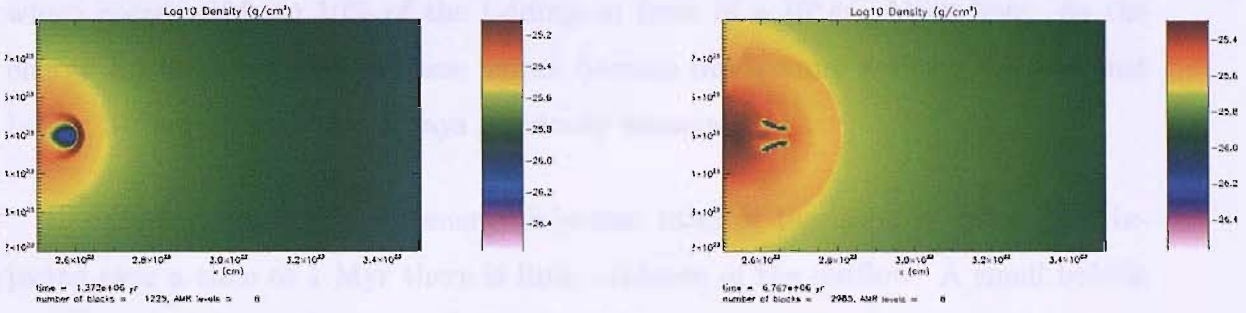

Figure 6.5: Density plot for an energy injection rate of $10^{42}\mathrm{erg\,s^{-1}}$ at the time shown. The internal and kinetic energy are injected in equipartition.

the pressure outside the injection region will no longer hold its original value. As a result it was decided to ensure that the injection region must maintain equilibrium with the value of the pressure before the energy was injected. Using the fact that $P = (\gamma - 1)\rho\epsilon$, the density required to maintain pressure equilibrium can be calculated using,

$$\rho_{i+1} = \frac{P_0}{(\gamma - 1)\epsilon_{i+1}}. \tag{6.11}$$

where P_0 is the initial pressure before the jet was activated.

6.2.4 Energy injection jets: results

This mechanism results in the formation of bubbles which are visibly different to the previous injection process. As expected, when the fraction of internal energy increases (and the fraction kinetic energy decreases) the resulting bubble becomes fatter in the direction perpendicular to the outflow velocity. Conversely, for a small fraction of internal energy, the outflow becomes elongated in the direction of propagation. As each of these type of bubble rises, they evolve through a spherical cap phase and eventually form a hollow tube that flares out towards the base, see figure 6.5.

Preliminary 2-d tests showed that for very high energy injection rates the outflow velocity was unphysically high ($v > c$), in addition the temperatures were also un-

physically large (10^{12} K). This was the case for an energy injection rate of 10^{46}erg s^{-1} which corresponds to 10% of the Eddington limit of a $10^8 M_\odot$ black hole. As the energy injection rate drops these values become much more realistic until at just below 10^{45}erg s^{-1} they are always physically meaningful.

Results suggested that for energy injection rates of the order of 10^{40}erg s^{-1} injected over a time of 1 Myr there is little evidence of the outflow. A small bubble of warm gas is formed that is of slightly higher temperature than the ambient gas in addition to a shock front which propagates through the gas. When inflated for a much longer time the result is basically the same. The shock/sound front is roughly 10^6 K hotter than the ambient gas.

While this mechanism is useful for investigating the morphological properties of bubbles for different fractions of thermal and kinetic energy the properties of the jet introduced at the boundary are more desirable.

6.2.5 Energy injection jets: constant temperature

2) A feasible alternative to the constant-fraction injection described above is one in which the fraction of energy that goes towards the internal energy is calculated by the requirement that a constant jet temperature must be maintained. The remainder of the energy goes towards the kinetic energy. Again, the energy is injected while maintaining pressure equilibrium.

The energy required to maintain a constant temperature $T_{\rm jet}$ is calculated from the difference between that temperature and the current temperature of the material $T_{\rm i}$,

$$\Delta\epsilon_{\rm th,i} = \frac{1}{\gamma - 1}\frac{k_{\rm b}}{\mu m_{\rm p}}(T_{\rm jet} - T_{\rm i}) \tag{6.12}$$

As usual, the internal energy is updated by $\epsilon_{\rm th,i+1} = \epsilon_{\rm th,i} + \Delta\epsilon_{\rm th,i}$.

For simplicity the effect of mass injection is ignored. This is not unreasonable since the injection region is small (roughly 10^{21} cm) and the total mass injected is

insignificant.

While this method is a feasible option it seems which rather contrived compared to injecting a constant fraction of energy into the kinetic and thermal degrees of freedom.

6.2.6 Results

The results applying to this mechanism are qualitatively indistinguishable from the above method. For example, specifying a higher jet temperature is the analogue of increasing the fraction of internal energy compared to the kinetic energy.

6.3 Boundary introduced jets

An obvious alternative to the above methods, that also allows for mass injection, is to introduce the jets on one of the boundaries. However, as already stated, FLASH does not support 3-d polar coordinates. This means that it is necessary to either create a cubic boundary at the centre of the grid or to simulate only half of the original grid with a single jet. Since the former possibility is extremely difficult and time consuming it was decided that the latter would be the more profitable choice. Given this choice, the volume of the simulation should also be restricted in the direction of the jet. This was taken to be the x-axis, $5 \times 10^{23}\text{cm} < x < 10^{24}\text{cm}$ $0 < y < 10^{24}\text{cm}$ $0 < z < 10^{24}\text{cm}$, where the gravitational potential is centred at $x_0 = y_0 = z_0 = 5 \times 10^{23}\text{cm}$ and $r_0^2 = x_0^2 + y_0^2 + z_0^2$.

As with each of the above jet introduction methods, the jet is assumed to be in pressure equilibrium with its surroundings. The gas density is modified on the x-boundary using the following function which ensures that outside the region the

gas density is unaltered, but is reduced to $\rho_0 - \rho_1$ at r_0,

$$\rho_{\rm jet}(r) = \rho_0 - \rho_1 \exp\left[-\frac{1}{2}\left(\frac{r - r_0}{r_{\rm jet}}\right)^2\right] \tag{6.13}$$

for $|r - r_0| < 2r_{\rm jet}$, where $r = \sqrt{(y^2 + z^2)}$, ρ_0 is the density of the ambient material into which the jet is injected. $\rho_0 - \rho_1$ is chosen to be $\rho_0/100 \approx 5. \times 10^{-28}{\rm g\,cm^{-3}}$.

The jet temperature is calculated from the criterion of pressure equilibrium with the ambient gas, using $T_{\rm jet}(r) = P_0/\rho_{\rm jet}(r)$, where $P = 2.2 \times 10^{-10}$ at the centre of the Virgo cluster at the start of the simulations.

The velocity of the jet material is distributed along the inner x-boundary as,

$$v_{\rm x}(r) = v_{\rm jet} \exp\left[-\frac{1}{2}\left(\frac{r - r_0}{r_{\rm jet}}\right)^2\right] \tag{6.14}$$

for $|r - r_0| < 2r_{\rm jet}$.

Across the rest of the boundary, reflective boundary condition are used so as to replicate the effect of the missing half of the simulation.

6.4 Boundary introduced jets: results (1)

The results of preliminary simulations using this method, suggest that the morphology and subsequent evolution of the structures formed by energetic outflows depends strongly upon the jet velocity.

When considering the jet velocity, it is useful to compare it with the respective sound speeds of the ambient medium and the jet material itself. This can be done using two different Mach numbers. $M_{\rm a}$ is defined as the ratio of the jet bulk velocity to the sound speed, $c_{\rm s,a}$, of the ambient gas: $M_{\rm a} \equiv v_{\rm jet}/c_{\rm s,a}$. $M_{\rm j}$ is the ratio of the bulk velocity to the sound speed of the jet material itself: $M_2 = v_{\rm jet}/c_{\rm s,j}$. For simulations of the Virgo cluster the initial adiabatic sound speed of the ambient gas is $8.31 \times 10^7{\rm cm\,s^{-1}}$.

The rate at which mass is added to the cluster by the jet is calculated from the integral of the mass flux over the area of the injection region,

$$\dot{M} = \int \rho \boldsymbol{v}.\mathrm{d}\boldsymbol{A}. \tag{6.15}$$

The region within which the material is injected gives the automatic integration limits which are required when calculating the mass flow rate of the jet using equation (6.15),

$$\dot{m} = 2\pi v_{\mathrm{jet}} \int_{r_0}^{r_0+2r_{\mathrm{jet}}} \exp\left[-\frac{1}{2}\left(\frac{r-r_0}{r_{\mathrm{jet}}}\right)^2\right]\left(\rho_0 - \rho_1 \exp\left[-\frac{1}{2}\left(\frac{r-r_0}{r_{\mathrm{j}}}\right)^2\right]\right)(r-r_0)^2\mathrm{d}r. \tag{6.16}$$

The energy injection rate is given by equation (6.2), however, because both T and v are radial functions it is more informative to calculate the area averages of these quantities to give the energy injection rate. The area-averaged jet velocity is,

$$\langle v \rangle = \frac{v_{\mathrm{j}}}{2r_{\mathrm{j}}} \int_{r_0}^{r_0+2r_{\mathrm{j}}} \exp\left[-\frac{1}{2}\left(\frac{r-r_0}{r_{\mathrm{j}}}\right)^2\right](r-r_0)^2\mathrm{d}r. \tag{6.17}$$

Remembering that the jets are created so that they are in pressure equilibrium with their surroundings, it is possible to determine the area averaged jet temperature,

$$\langle T \rangle = \frac{\mu m_{\mathrm{p}} P_{\mathrm{amb}}}{2k_{\mathrm{b}} r_{\mathrm{j}}} \int_{r_0}^{r_0+2r_{\mathrm{j}}} \left(\rho_0 - \rho_1 \exp\left[-\frac{1}{2}\left(\frac{r-r_0}{r_{\mathrm{j}}}\right)^2\right]\right)^{-1}(r-r_0)\mathrm{d}r. \tag{6.18}$$

The values of the mass flow rate, area-averaged jet velocity and jet power are given for several different values of the velocity amplitude, in table 6.1. The other parameters, ρ_0, ρ_1, r_{jet} and P_{amb} are unchanged. For the given input parameters the mean jet density is $2.93 \times 10^{-26}\mathrm{g\,cm^{-3}}$ and the mean jet temperature is $1.32 \times 10^{8}\mathrm{K}$.

The jet powers given in table 6.1 should be compared with the current jet power of M87 which is roughly $3 \times 10^{42}\mathrm{erg\,s^{-1}}$ (Owen et al., 1998).

6.4.1 Effect of jet velocity on bubble morphology

The different outflow velocities, listed in table 6.1, are used to investigate the effect of jet velocity and power, on the morphology of the inflated bubble. The slowest jets in

$v_0\,(\mathrm{cm\,s^{-1}})$	$\dot{M}\,(\mathrm{M_\odot yr^{-1}})$	$\langle v\rangle\,(\mathrm{cm\,s^{-1}})$	$\dot{E}\,(\mathrm{erg\,s^{-1}})$
2.6875×10^8	2.05	1.16×10^8	6.79×10^{42}
3.34×10^8	2.55	1.44×10^8	9.04×10^{42}
4.08×10^8	3.12	1.76×10^8	1.2×10^{43}
5.375×10^8	4.11	2.32×10^8	1.89×10^{43}
1.075×10^9	8.21	4.65×10^8	7.99×10^{43}
2.15×10^9	16.41	9.29×10^8	4.97×10^{44}

Table 6.1: Jet parameters

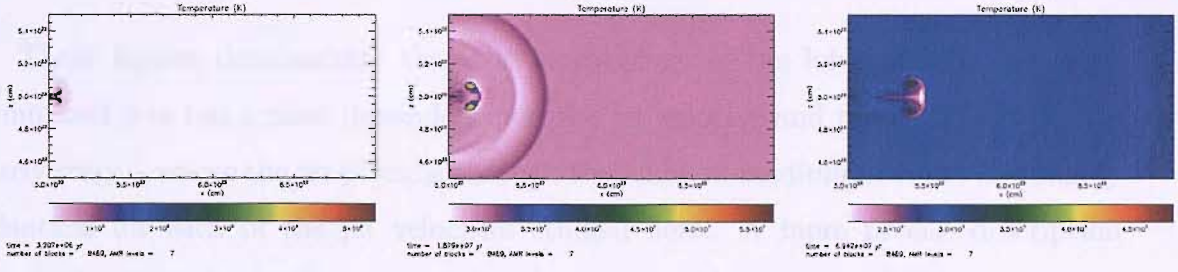

Figure 6.6: Temperature plots for a jet velocity of $3.34 \times 10^8 \mathrm{cm\,s^{-1}}$ at the time shown.

this set of simulations are supersonic with respect to the surroundings ($M_\mathrm{a} = 3.23$), but is subsonic with respect to the jet material ($M_\mathrm{j} = 0.72$). In contrast the fastest of the jets are supersonic with respect to both the ambient medium and the jet material, $M_\mathrm{a} = 25.9$ and $M_\mathrm{j} = 5.8$. The other jet velocities were chosen to investigate the intermediate Mach numbers between these extremes, in particular the velocities which are transonic with respect to the jet material,$0.8 < M_\mathrm{j} < 1.3$. The different morphologies are shown for a few velocities in figures 6.6 to 6.8. In these simulations the jet was active for 10^{14}s (3.17×10^6yrs).

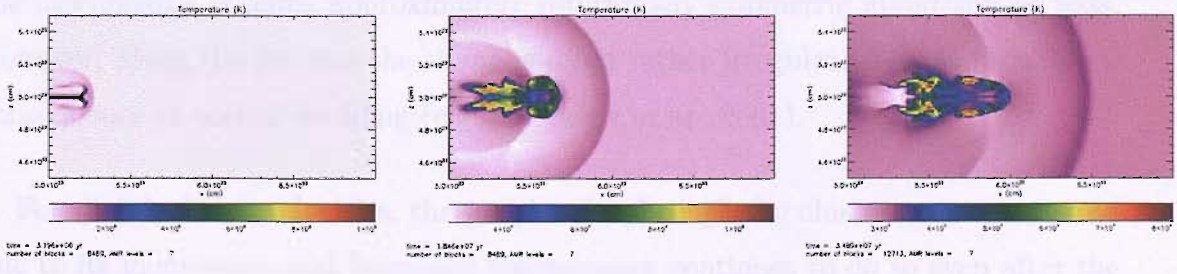

Figure 6.7: Temperature plots for a jet velocity of $1.075 \times 10^9 \mathrm{cm\,s^{-1}}$ at the time shown.

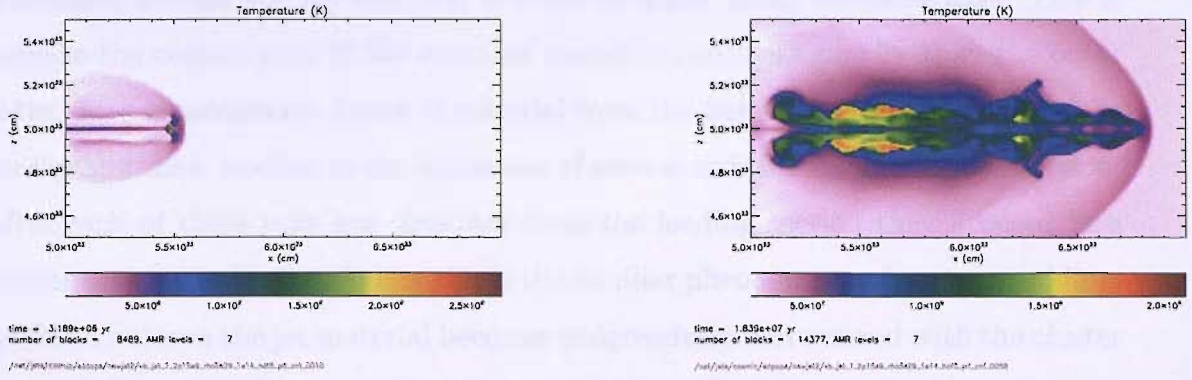

Figure 6.8: Temperature plots for a jet velocity of $2.15 \times 10^9 \mathrm{cm\,s^{-1}}$ at the time shown.

These figures demonstrate that the morphology of the lobes inflated by these simulated jets has a clear dependence on the jet velocity and power. However, the early stages, where the jet ploughs through the ambient medium, seem to be roughly identical for each of the jet velocities studied here. A more precise description would be that the jet flows out from the origin and is surrounded by a coccoon of jet material which flows back from the hotspot, at the leading surface of the jet, towards the centre. A bow shock moves ahead of this structure with shocked intracluster gas lying between the bow shock and the contact surface.

For the largest jet velocity investigated here ($v_\mathrm{j} = 2.15 \times 10^9 \mathrm{cm\,s^{-1}}$), the jet travels almost ballistically and so ploughs a significant distance through the cluster atmosphere. This structure is shown in figure 6.8, which is reminiscent of powerful radio sources.

When the energy injection has been switched off, the injected material is described as a remnant. This remnant continues to rise along its original trajectory and the morphology remains approximately rotationally symmetric about the jet axis. However, along the jet axis the shape is often rather irregular. This is probably a consequence of vortex shedding (e.g. Churazov et al., 2001).

For slightly lower velocities, the jet ploughs through the cluster atmosphere and due to its momentum and buoyancy the remnant continues to do so even after the jet has been switched off. As with the previous case, the remnant is rotationally

symmetric around the jet axis, but is often irregular along the same axis. This is because the central part of the remnant seems to rise more rapidly than the outer parts. As a consequence, layers of material from the outer regions of the bubble are continually shed, leading to the formation of several tails behind the leading section. After each of these tails has detached from the leading section they proceed in a similar way to the leader. Again, this is the familiar phenomenon of vortex shedding. As this continues the jet material becomes progressively more mixed with the cluster gas and the contrast between the jet material and the ambient gas lessens. Since the X-ray brightness is proportional to the square of the density a lessening density contrast means that the remnant becomes less conspicuous.

The typical morphology of lower velocity jets is markedly different to those with higher velocities described above. This is evident when comparing figure 6.6 to figures 6.7 and 6.8. Again, the early stages of the jet evolution are more or less indistinguishable from the higher velocities. However, once the jet has been switched off the evolution begins to differ and there is no general description of the subsequent behaviour that applies across the entire range of jet velocities. Instead a non-spherical remnant forms. The best description of the shape of this remnant is that it very roughly resembles a tear-drop shape aligned along the jet axis, with the blunt end at the head. As it rises, due to buoyancy and the momentum of the jet, the tear-drop becomes compressed at both ends and begins to resemble the cap of a mushroom. The rise continues with a speed comparable to the local buoyancy velocity and the remnant further resemble a spherical air bubble cap in water. Eventually, due to the effect of fluid instabilities, a torus is formed with clearly visible vortices. These vortices are the location of both the hottest and lowest density gas that remains from the original jet material. Vortex shedding again leads to the formation of a tail. Interestingly, cool and dense material is also lifted out from the cluster centre in the wake of the rising remnant. This means that these bubbles are capable of reducing the quantity of cold material at the centres of clusters. This phenomenon is also observed in the wake of the south western bubble of the Virgo cluster, (Forman et al., 2005).

At this point it is worth discussing the differences between bubbles inflated by jets and non-inflated bubbles which are placed at will into the cluster atmosphere for the purposes of simplying the physics. As the latter bubbles buoyantly rise they quickly disintegrate under the action of fluid instabilities. They are almost completely destroyed after rising little more than their initial diameter, (e.g. Churazov et al., 2001). In the past this type of bubble was the only type that could be produced given computational constraints. The results seemed to suggest that alternative processes had to be invoked to prevent the instabilities shredding the bubbles. Analytical (e.g. De Young, 2003; Kaiser et al., 2005) and numerical studies (e.g. Robinson et al., 2004; Reynolds et al., 2005) have shown that either viscosity or magnetic fields are required to maintain the integrity of a bubble against the action of fluid instabilities. However, neither of these are present in these simulations and yet, contrary to current theoretical work, the bubbles remain intact for significantly longer than non-inflated bubbles. The conclusion must therefore be that something in the process of inflation creates a velocity field which helps to keep the bubbles intact. One possible reason that the growth of instabilities may be reduced on inflated bubbles is that when jets inflate bubbles some material flows back towards the centre from the point of impact with the ambient medium. This reduces the relative velocity between the radio lobe and the ambient material. This could reduce the impact of Kelvin-Helmholtz instabilities which occur as a result of relative motion between two neighbouring fluids.

Another interesting feature of these lower jet velocity simulations is that the bubbles also develop dense, cold fronts, in the cluster gas. It is interesting to note that the same sort of Mach numbers which are required to produce stable bubbles are also of the magnitude that allow cold fronts to form.

6.4.2 Comparison with laboratory jets

It is possible to compare the morphology of the simulated jets, and their remnants, with those studied under controlled conditions in laboratories. In such studies in-

Figure 6.9: Dye visualization of the first moments of the evolution of a vortex ring at t=4s, 8s, 12s and 16s; the Reynolds number is about 1000. The orifice at which the ring is created is located just below the bottom of each image; the height of each image is about 12 cm. Taken from http://www.fluid.tue.nl/WDY/vort/vortrings/vortrings.html.

jected material is often dyed in order to make it visible against the surroundings.

Figure 6.9 shows the injection and evolution of a jet in water. A sheet of the dyed fluid is rolled-up in a spiral as the core of the vortex ring is formed. The spiral form of the dyed fluid can be seen because undyed ambient fluid from outside the vortex generator is entrained in the vortex during its formation. At the final stage shown, the vortex has the shape of an isolated ring with dyed fluid. The ring will propagate further straight upward until it reaches the free surface of the water in the tank.

The morphology of the laboratory jets, shown in figure 6.9, is strikingly similar to the jets inflated by the low-power jets studied in this thesis. For example, see figure 6.6. If the numerical resolution of the simulations was greater it is likely that the results would clearly show the rolled-up nature of the vortex ring.

6.4.3 Comparison with previous studies

It is important to clarify the differences between the simulations performed for this thesis and some of the previous studies of AGN outflows. A common feature of the previous studies is the huge energy injection rates that are often employed. The idea behind this is that an AGN may only be active for 10 % of the time. Therefore to match the radiative losses for all time, each outburst should be roughly 10 times the radiative losses. However, the AGN power output can be roughly continuous,

Authors	Code	Power ($\mathrm{erg\,s^{-1}}$)	v ($\mathrm{cm\,s^{-1}}$)	Method
Omma et al. (2004)	ENZO	6×10^{43}	10^9	Grid
Vernaleo & Reynolds (2005)	ZEUS	10^{46}	1.05×10^9	Boundary
Brüggen & Kaiser (2002)	FLASH	4.1×10^{43}	-	Grid
Basson & Alexander (2003)	ZEUS	–	10^{10}	Boundary
Zanni et al. (2005)	PPM code	10^{46}	10^{10}	Boundary

Table 6.2: Comparison of jets simulated by other groups. The velocity in row 3 is not given since the jet is created by adding only internal energy. The jet power is not given in row 4 because the authors only discuss the ratio of jet power to radiative losses, and do not specify the radiative losses. However, it is probably in the region of $10^{44} - 10^{46}$.

but highly variable. Indeed, if the probability distribution of AGN power output *is* log-normal then one would expect low-power outbursts to be far more numerous than extremely powerful ones. As a result it seems that low-power AGN activity is far more likely to be observed than high power outbursts. This provides a possible explanation for why many AGNs seem to be providing insufficient heating to their host cluster.

Since the AGN output is dominated by low-power activity, at least in terms of the fraction of time, it is likely to exert a strong influence on its surroundings. As a result, it seems that the study of low-power AGN activity in simulations is a vastly under-explored subject.

In this subsection I will compare the morphologies of simulated high-power jets taken from the literature. These jets have been generated using different numerical codes and with a variety of different injection mechanisms. The comparison is not exhaustive but contains a few of the most recent simulations of jets in cluster environments. The chosen simulations ignore relativity physics and magnetohydrodynamics. The authors, hydro code used, jet power, velocity and injection method are summarised in table 6.2.

Boundary injected jets are investigated by Basson & Alexander (2003); Zanni

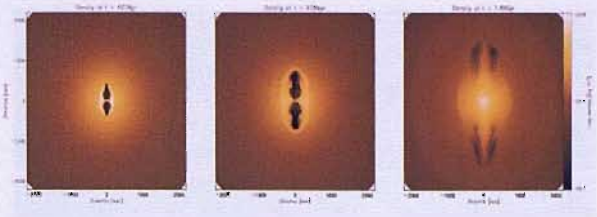

Figure 6.10: Plots of the density at different points in time, taken from Basson & Alexander (2003).

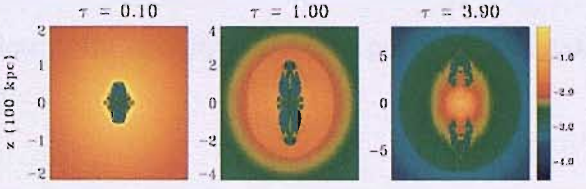

Figure 6.11: Plots of the density at different points in time, taken from Zanni et al. (2005).

et al. (2005); Vernaleo & Reynolds (2005) who use the ZEUS hydrodynamics code, with the exception of Zanni et al. (2005) who employ an unspecified PPM hydro code. It is interesting to compare these results since the jet properties assumed by Basson & Alexander (2003) and Zanni et al. (2005) are probably very similar, but they use different codes. Qualitatively, at least, the morphologies of these jets seem to be similar, which is reassuring. They are elongated in the direction of the jet and as such are reminiscent of extremely powerful FRII sources. However, this morphology is not reminiscent of the X-ray cavities that are prevalent in galaxy clusters. This is probably because the kinetic power dominates the total power of these jets and they propagate roughly ballistically through the ICM. If the kinetic and thermal powers were in equipartition the remnant would probably be less long and thin, but fatter in the direction perpendicular to the jet axis.

The simulations of Vernaleo & Reynolds (2005) employ jets that are similar in power to those already mentioned above, but with a velocity that is an order of magnitude lower. Therefore, it is interesting to note that these jets produce cavities or remnants that are more similar to those observed in real clusters. This is because they are less elongated than those produced by Basson & Alexander (2003) and

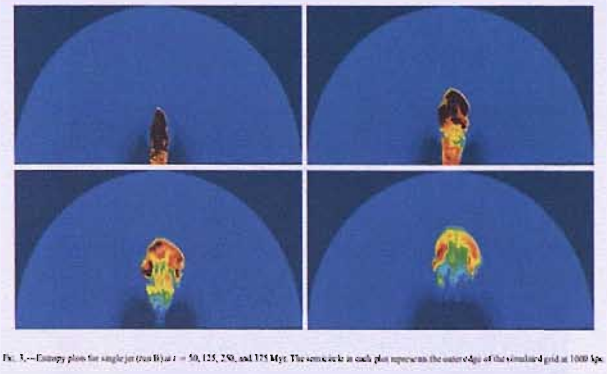

Figure 6.12: Plots of the entropy at different points in time, taken from Vernaleo & Reynolds (2005).

Zanni et al. (2005). It is perhaps a further indication that the morphology of the remnant is a strong function of the ratio of kinetic to thermal powers of the jet. Of course, an extra consideration in predicting the morphology of a remnant is the density of the ICM. It is possible that a jet which forms a roughly spherical cavity in a cluster atmosphere may produce an elongated structure if located in a less dense environment.

Grid-injected jets are represented here by Brüggen & Kaiser (2002) and Omma et al. (2004). In the case of Brüggen & Kaiser (2002), the simulation is actually in 2-dimensions rather than 3. The jet is created by heating the material at a particular location; no kinetic energy or mass is added to the grid. The heated material expands and rises, due to buoyancy, but becomes extremely turbulent. The result of this injection scheme does not seem to produce the collimated jets that are typically observed.

In contrast, the jet introduction mechanism employed by Omma et al. (2004) injects both thermal and kinetic energy. The remnants formed by this process are comparable with observations. Again, this is probably due to the comparatively low jet velocities.

It is clear that various parameters affect the geometry of the jet and its remnant. The above discussion strongly suggests that jet power and the relative fractions of

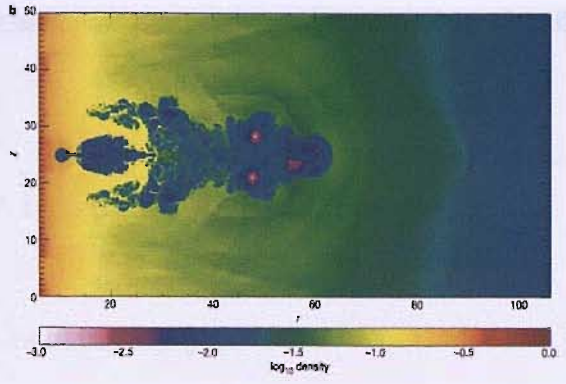

Figure 6.13: Plots of the density after 120 Myr, taken from Brüggen & Kaiser (2002).

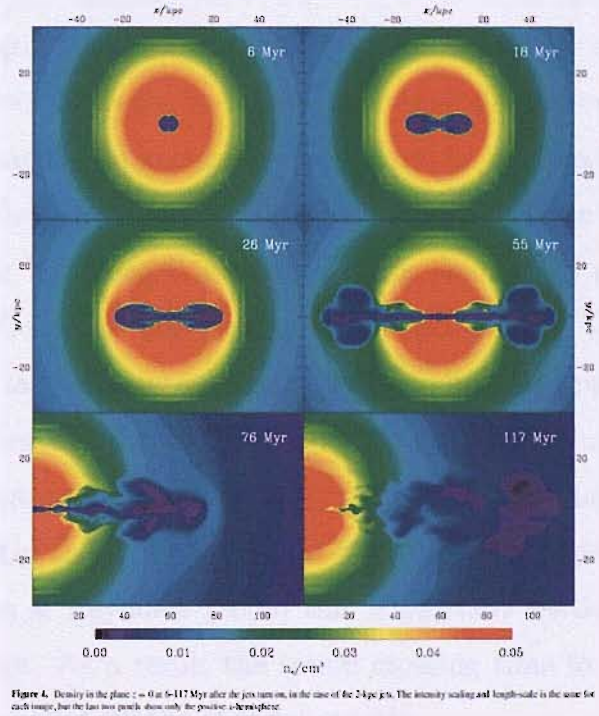

Figure 6.14: Plots of the density at different points in time, taken from Omma et al. (2004).

thermal and kinetic energy are fundamental among these. For example, from the sample above, no high-powered jet is quite able to produce the bubble-like structures that are created by the lower-powered jets simulated in this thesis.

6.5 Boundary introduced jets: results (2)

6.5.1 Long-term heating by jets

Having investigated the effect of jet power and velocity on bubble morphology, the next logical step is to investigate the long-term heating effect of jets. In an ideal simulation there would be some sort of mathematical prescription that would specify the power and duration of each outburst, in response to a stimulus from the ambient medium. For example, the inflow rate of material into the central regions of the simulations grid could be used to determine the power output for a jet that is continuously active. However, in reality, if not the simulations, the inflowing gas would have some angular momentum which must be removed before the gas can be accreted on to the supermassive black hole at the centre of the galaxy. In this case, it is not clear how long it should take for the gas to move from the level of the smallest grid scale to the vicinity of the black hole. Vernaleo & Reynolds (2005) attempt to take this into account by including an appropriate time delay in their models. They also found certain problems; mainly that for a continuously active jet, the jet channel does not close and so the jet material always flows to the hotspot at the head of the jet and does not heat the inner regions of the cluster. In the case of Vernaleo & Reynolds (2005) this is partially because their jet channel is exceptionally large. As a result the sound crossing time for the channel is also significant and gas cannot fill the channel quickly.

A slowly closing jet-channel need not occur, nor be a problem for several reasons. With narrower jets the channel could fill more quickly, in addition the ICM is likely to be 'windy' which could fill the jet channel in a relatively short period of time.

Furthermore, the direction of the jet could precess over time meaning that jet material would not always pass along the same channel. Clearly, including the effects of a 'windy' ICM and jet precession increases the complexity of the simulation although some recent work in this area is presented by Heinz et al. (2006). Also, implementing the latter of these possiblities would not be advisable using the current setup. This is because, for a single jet, the jet should be aligned perpendicularly to the boundary, otherwise reflection from the boundary could result in unphysical flow patterns.

It should be noted that the work on the fraction of galaxies that are radio-loud, presented in Chapter 7, does not necessarily help to determine appropriate jet powers. For example, it was shown that the heating rates for a given AGN could be log-normally distributed. For a simulation, the power of each AGN outburst could then be drawn, at random, from this distribution and would be consistent with the observations. However, this is probably not an accurate way of implementing the result from Chapter 7 because the log-normal distribution probably arises as a response to the behaviour of the ambient medium.

In the absence of any quick and simple prescription for defining the duration and power of jet outbursts, each of these quantities is assumed to be constant. Clearly the parameter space for an investigation of this sort is huge as it would include the possible range of jet velocities, along with the duration of jet activity and the length of time between successive jet outbursts. Henceforth, the duration of jet activity will be referred to as Δt and the length of time between outbursts as τ. This means that the time-averaged power output from the jet will be

$$\langle \dot{E} \rangle = \frac{\Delta t \dot{E}}{\tau}. \tag{6.19}$$

Table 6.3 gives the jet parameter values used in the following simulations. The jet powers should be compared to the initial radiative losses of $6 \times 10^{43} \mathrm{erg\,s^{-1}}$ within the computational domain.

v_0 (cm s^{-1})	Δt (s)	τ (s)	$\langle \dot{E} \rangle$ (erg s^{-1})
5.375×10^8	10^{14}	3.156×10^{15}	5.99×10^{41}
5.375×10^8	10^{14}	1×10^{15}	1.89×10^{42}
5.375×10^8	10^{14}	3.156×10^{14}	5.96×10^{42}

Table 6.3: Jet-activity model parameters

6.5.2 Qualitative descriptions

In each example, the early stages are very similar. The jet ploughs through the ICM, forced onwards by the energy injection. Even after the jet has been switched off, the remnant continues to rise and quickly moves at a rate comparable to the local buoyant velocity. There are several effects that the jet injection has on the surroundings. As the remnant rises, a channel is created in its wake. This channel is of lower density and pressure than the surroundings, which means that material behind the bubble is dragged upwards in the draught. It also means that a subsequent remnant does not suffer the same retardation as the first, since there is less material obstructing its path. Fluid motions induced by the back flow of material from the hotspot and the rise of the remnant will also affect the evolution of a second jet and its remnant. However, if the time between successive outbursts, τ, is sufficiently long, then each jet will have minimal influence on each subsequent injection. This is because the fluid motions induced by the first jet have had a chance to dissipate somewhat, the atmosphere has relaxed and the jet channel will have closed [2].

These two extremes of behaviour are observed in the simulations presented here. As τ falls, the influence of the preceeding jet increases. For example, it is difficult to determine any qualitative difference between the evolution of the remnants produced by jets which are activated at intervals of $\tau = 3.156 \times 10^{15}$s (100 Myr), see figure 6.15. However, for $\tau = 1.0 \times 10^{15}$s (31.7 Myr) the evolution of each individual remnant is

[2]It should be noted that the morphology of the bubbles is slightly different in this set of simulations compared to the previous set, where only single injections were studied. This is because the boundary conditions are different in these two cases. The reason for changing the boundary conditions is described in Chapter 3.

slightly different, see figure 6.16. The second jet injection initially appears to evolve similarly to the first but gradually begins to exhibit the effects of the preceeding remnant. Firstly, it forms a hollow, conical tail, that was absent from the first bubble, which gradually mixes with the ambient material. Secondly, it remains narrower than the first remnant and material is dragged from the central regions in to the remnant above, eventually punching a hole through the middle. The third remnant follows a vaguely similar pattern and again, material is lifted upwards from this remnant through each of the preceeding bubbles.

For $\tau = 3.156 \times 10^{14}$s (10 Myr) similar behaviour is observed, see figure 6.17. Material from the second jet quickly ploughs into material from the first. At a relatively early stage it is impossible to distinguish which material came from which ejection as the remnants are well merged. However, the rapid rise of the second remnant punches a hole through the middle of the first remnant. Material from each subsequent ejection is quickly dragged upwards along the channel and as a result the remnants stay very narrow.

6.5.3 Temperature and Density Profiles

The azimuthally averaged temperature and density profiles can be used to obtain quantitative information about the effect of jets and their remnants on the ambient medium. These are presented in figure 6.18 to 6.20.

A slightly unexpected property of the temperature profiles is that there is not a significant peak in the centre, except while the jet is active. The fact that there is a large peak while the jet is active is largely due to the jet material not being excluded while the temperature profiles are calculated. In this respect, in future simulations it might be advisable to inject the jet material as a second fluid. In this way one could descriminate between material heated by the jet and the hot jet material itself. The lack of a large central temperature increase is interesting in light of a common concern with strong central heating sources that they would

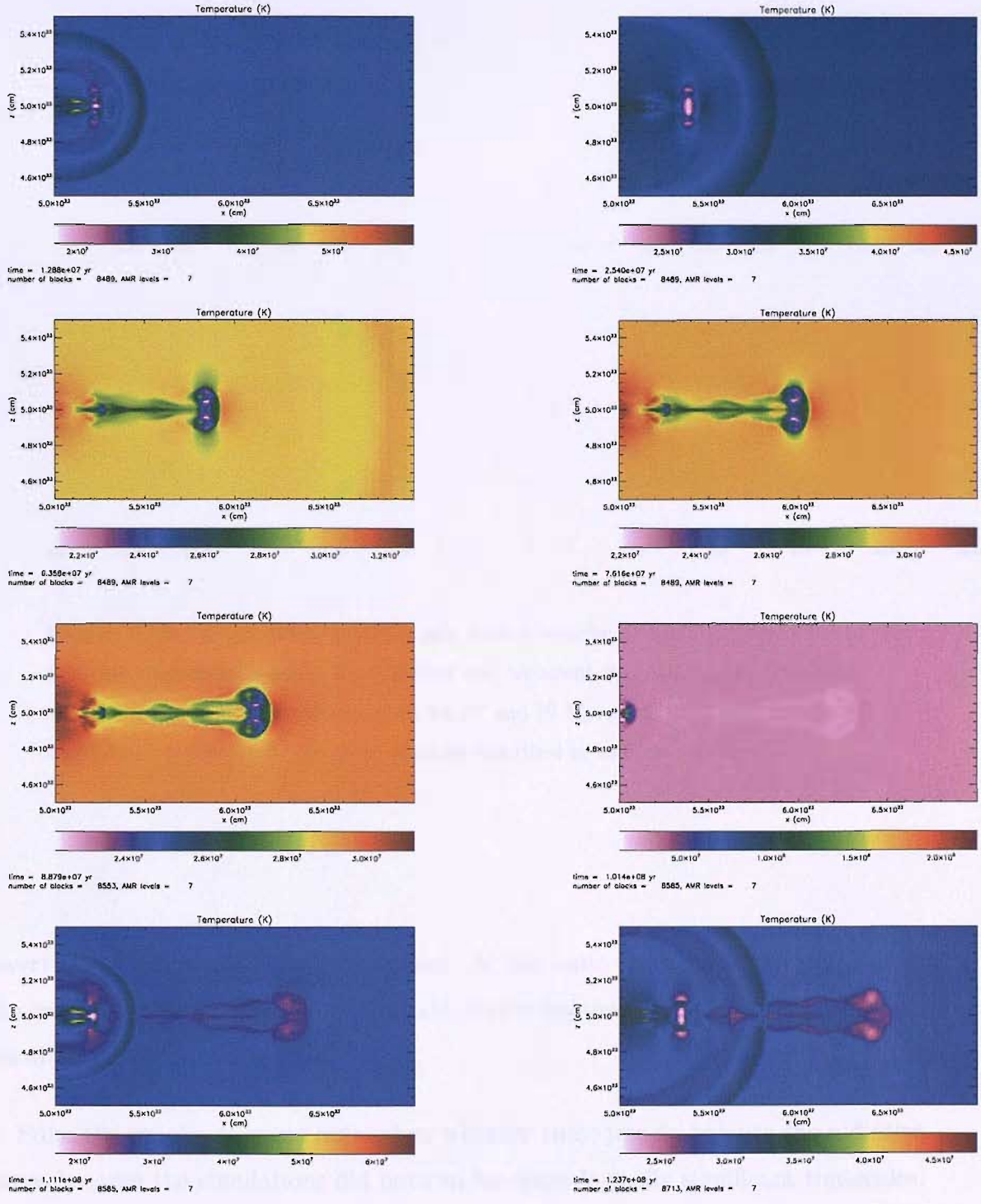

Figure 6.15: Temperature plots for jets with a velocity of $5.375 \times 10^8 \mathrm{cm\,s^{-1}}$. The jets are active for 3.17 Myr and recurrent every 100 Myr. The simulations are shown at approximately 13, 25, 64, 76, 89, 101, 110 and 120 Myr. Note that the leading cavity carves out a channel behind it, allowing subsequent cavities to catch up and merge, thus producing a single large cavity. This cavity is somewhat reminiscent of those observed in real life. The same process could happen in real life - large cavities may be the result of several out bursts, rather than a single large one.

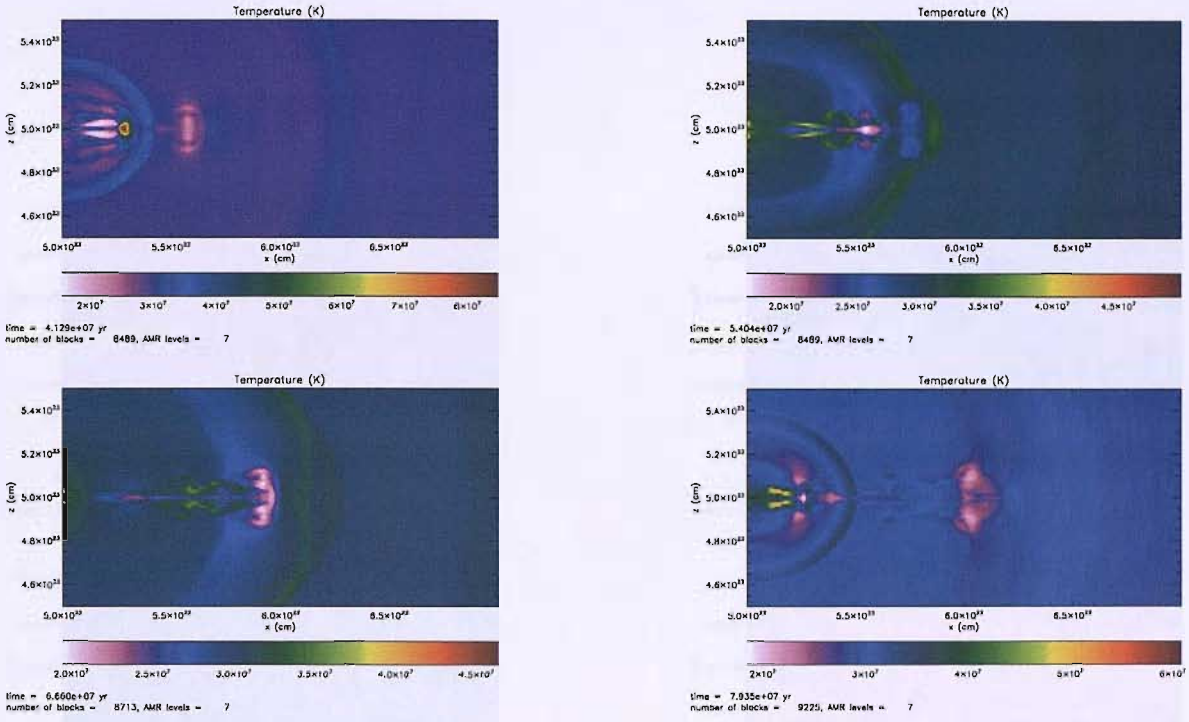

Figure 6.16: Temperature plots for jets with a velocity of $5.375 \times 10^8 \mathrm{cm\,s^{-1}}$. In this case the jets were active for 3.17 Myr and recurrent every 31.7 Myr. The simulations are shown at approximately 41, 54, 67 and 79 Myr. The main features of this simulation are essentially the same as those described in the previous figure.

invert the observed temperature gradient. At the same times when the jet is active the central density is also reduced. Again, this is because of the presence of the hot, low-density jet material.

From the graphs, it is not quite clear whether these jets do balance the radiative losses because the simulations did not run for cosmologically significant timescales. However, this was not necessarily the objective of these simulations - particularly since there was no feedback between the mass inflow rate and the jet power. The main objective of the simulations was to show that low-power jets can produce many of the objects observed in real clusters rather than suggest they are solely responsible for heating the ICM.

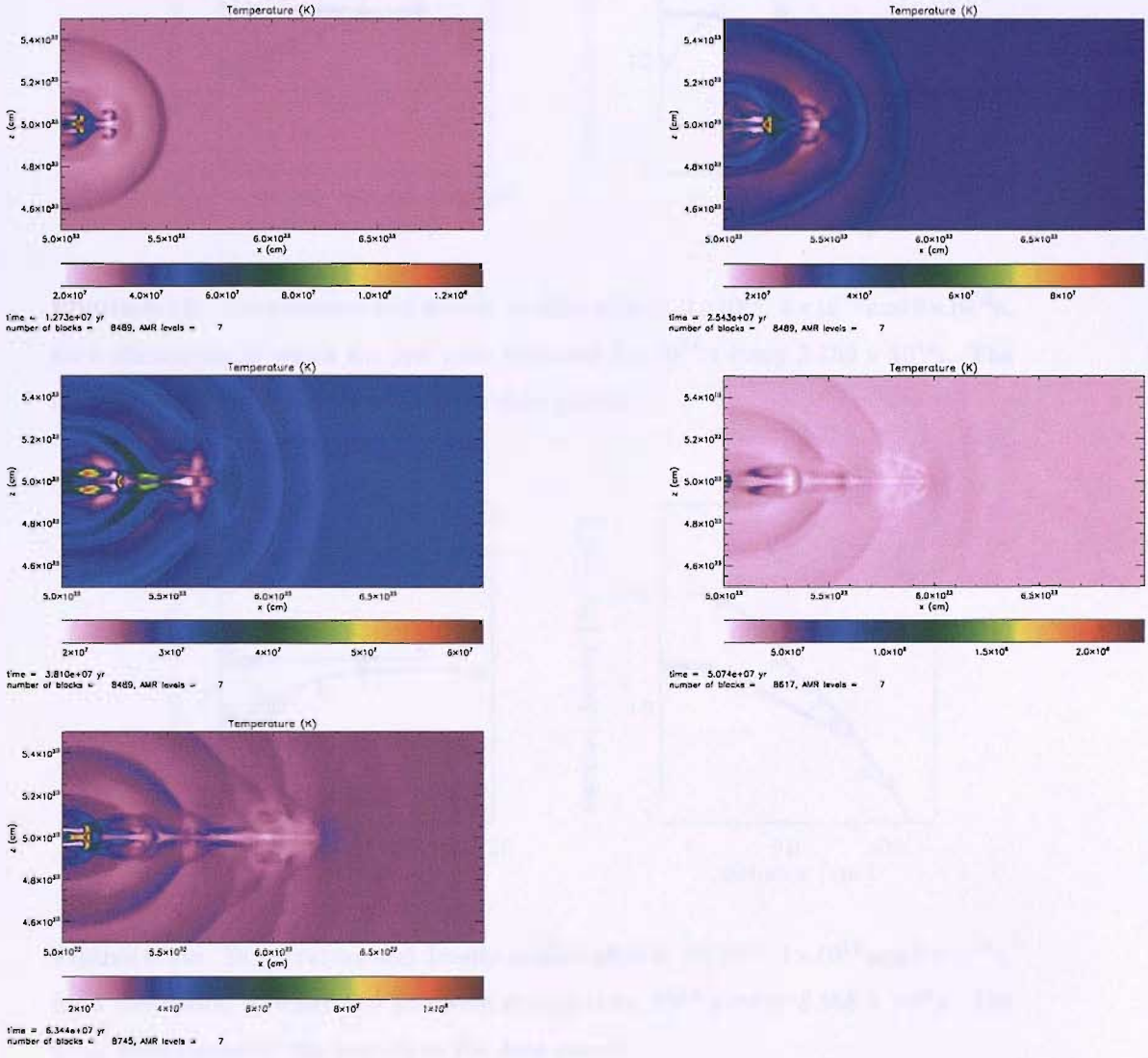

Figure 6.17: Temperature plot for jets with a velocity of $5.375 \times 10^8 \mathrm{cm\,s^{-1}}$. These jets were active for 3.17 Myr and recurrent every 10 Myr and are shown at roughly 13, 25, 38, 51 and 63 Myr. In this example, the waves generated by the jets injections are highly prevalent and close together. Again, subsequent cavities catch up with the leader, but in this case, the result does not appear directly comparable with observations.

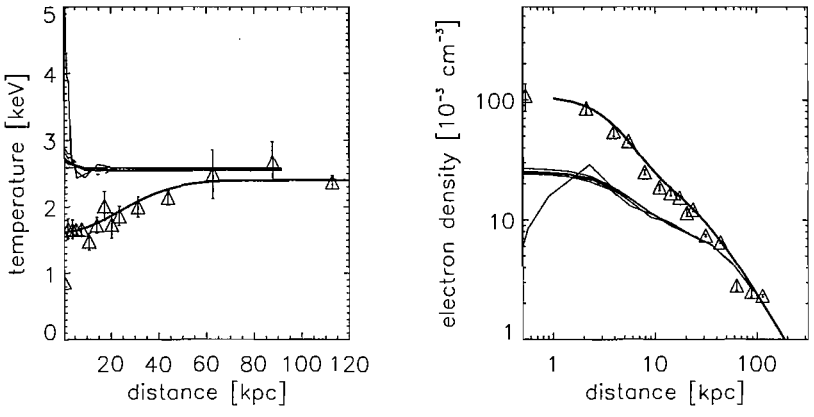

Figure 6.18: Temperature and density profiles after 0, 2×10^{15}, 4×10^{15} and 6×10^{15}s, for a simulation in which the jets were activated for 10^{14} s every 3.156×10^{14}s. The thick lines represent the best-fit to the data points.

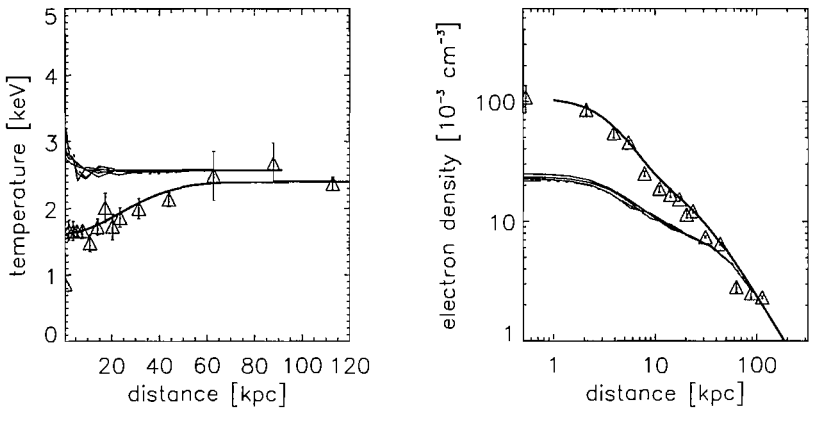

Figure 6.19: Temperature and density profiles after 0, 2×10^{15}, 4×10^{15} and 6×10^{15}s, for a simulation in which the jets were activated for 10^{14} s every 3.156×10^{14}s. The thick lines represent the best-fit to the data points.

6.5.4 Mass flow rate profiles

These plots show the spherically-averaged mass flow rate at each radius. Wherever the figures show that the mass flow rate is positive, the average mass flow at that radius is directed outwards. It is negative where the average mass flow rate at that radius is directed inwards. The mass flow rates are presented at the times shown in the captions of figures 6.21 to 6.23.

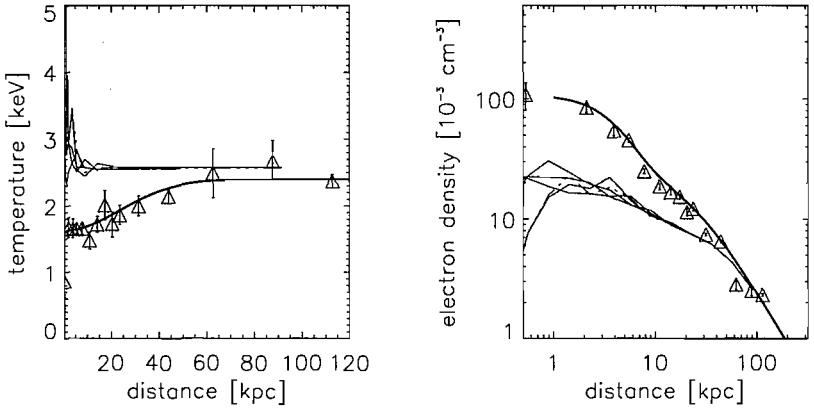

Figure 6.20: Temperature and density profiles after 0, 2×10^{15}, 4×10^{15} and 6×10^{15}s, for a simulation in which the jets were activated for 10^{14} s every 3.156×10^{14}s. The thick lines represent the best-fit to the data points.

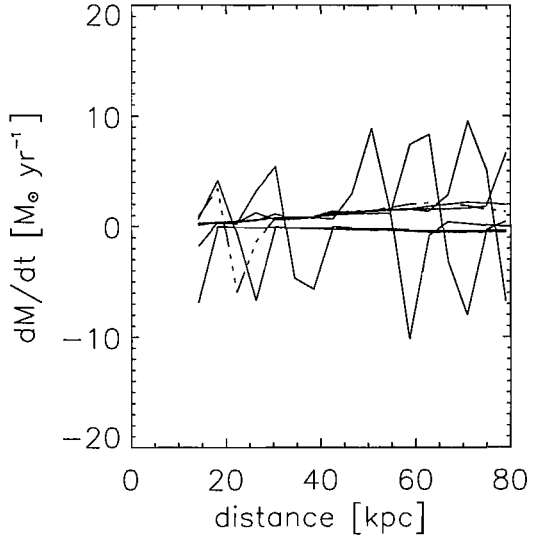

Figure 6.21: Mass flow rate profiles at 4,8,12,16,20,24,28,32,36 and 40 $\times10^{14}$s for an outflow of velocity $5.375 \times 10^{8}\mathrm{cm\,s^{-1}}$ that is active for 10^{14}s every 10^{15}s. The triple dot-dashed line shows the mass flow rate at the latest time.

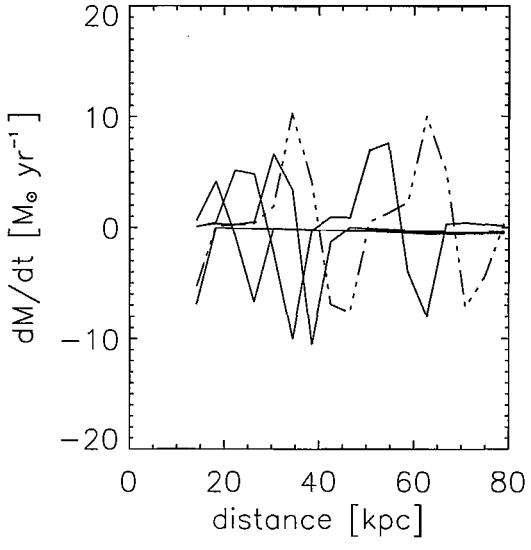

Figure 6.22: Mass flow rate profiles at 4,8,12,16,20 and 24 $\times 10^{14}$s for an outflow of velocity $5.375 \times 10^{8}\mathrm{cm\,s^{-1}}$ that is active for 10^{14}s every 3.156×10^{15}s. The triple dot-dashed line shows the mass flow rate at the latest time.

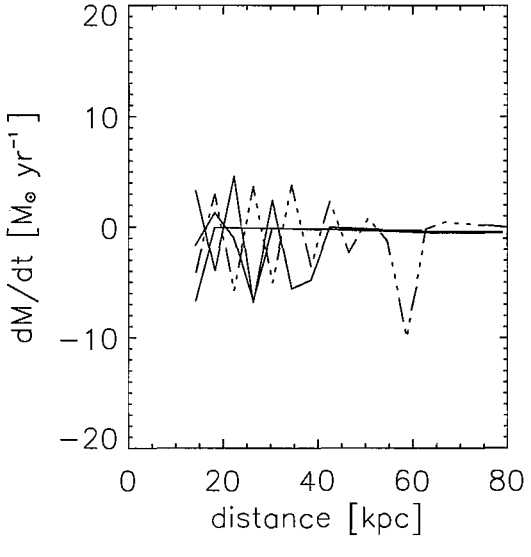

Figure 6.23: Mass flow rate profiles at 4,8,12,16 and 20 $\times 10^{14}$s for an outflow of velocity $5.375 \times 10^{8}\mathrm{cm\,s^{-1}}$ that is active for 10^{14}s every 3.156×10^{14}s. The triple dot-dashed line shows the mass flow rate at the latest time.

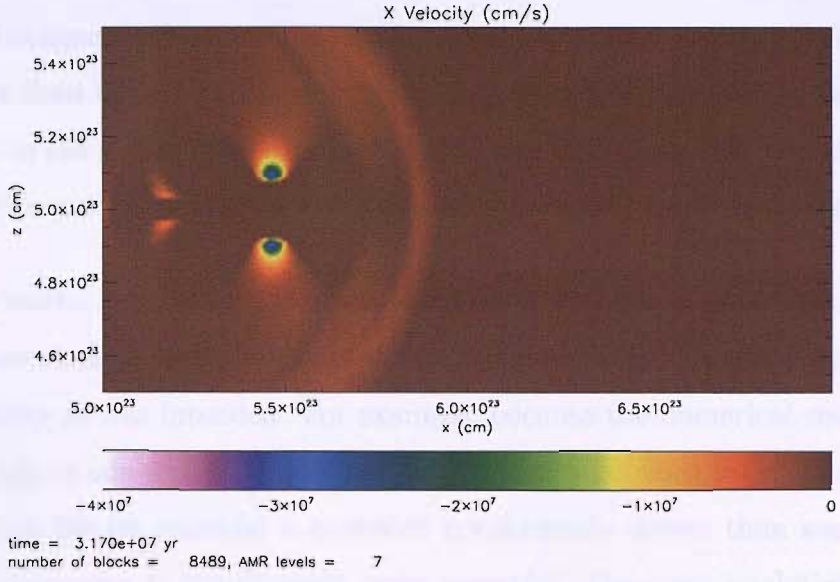

Figure 6.24: A map of the gas velocity in negative X-direction. The material is flowing inwards behind the shock. The dark red colour is where the velocity is zero or positive in the X-direction.

To qualitatively describe the mass flow rate profiles it is sensible to start with simulations for which τ is long. When considering these simulations it is obvious that the shock moves outwards but there is a region behind this where the material flows inwards, see figure 6.24. This structure is reminiscent of an oscillation and will be referred to as such, henceforth. As time passes, the oscillation propagates outwards.

The origin of the inflowing region behind the shock has been discussed by Alexander (2002) and Basson & Alexander (2003) who suggest that it is created by the adiabatic expansion of material swept up by the shock. The mass flow rates associated with this phenomenon are relatively modest, being no greater than roughly 10 $M_{\odot}$. Nevertheless, this still suggests that low-power AGNs can induce large-scale motions within the ICM. Therefore, if successive AGN outbursts are not always aligned along the same axis, this could result in an extremely dynamic environment, even if residual motions from mergers are not considered.

A second mechanism by which material is lifted out of the cluster centre is entrain-

ment of material behind the buoyantly rising remnant. Essentially the entrainment occurs because the buoyantly rising remnant carves out a channel which is at lower pressure than the surroundings. Material is therefore pushed into this channel and will rise in the wake of the buoyantly rising remnant. However, this effect is unlikely to contribute significantly to the spherically averaged mass flow rate profiles.

It is worth highlighting a possible problem with these simulations. Because of the constraints of numerical resolution, it appears that the jets are not as hot and low density as was intended. For example, because the numerical resolution cannot be as high as one would like certain features are smoothed over. This may actually mean that the jet material is probably considerably denser than was intended and as a consequence is significantly more powerful. However, analytical estimates in the next section suggest that the quantity of energy injected is comparable with the intended values.

6.6 Boundary introduced jets: results (3)

One aim of numerical simulations is to find the correct bit of physics that can explain and reproduce certain observations. The results of numerical simulations can also be used to ascertain the accuracy of certain observational techniques, and hopefully help calibrate them. An application of the latter is discussed below.

6.6.1 Comparing with observational methods: cavity enthalpy and energy input

Observational evidence of AGN heating in galaxy clusters relies on estimates made from cavities inflated in the ICM. However, it is not clear how accurately the injected energy can be estimated from observations. This can be addressed to some extent using the simulations described above.

The following analysis of cavities generated by simulated jets is not intended to be exhaustively accurate. For example, a more observationally oriented method would be to create mock X-ray surface brightness maps and then derive the volumes of the cavities. However, this would be rather time consuming, whereas calculating the cavity volumes straight from the data is much simpler.

A further simplification is to assume that the cavity is spherical. This is not so far from the truth, but again makes the algebra simpler. The enthalpy of the cavity, $\gamma PV/(\gamma - 1)$, can be obtained by multiplying the bubble volume by the value of the ambient pressure at the same location. This can be compared with the energy injected by the AGN, $E = \dot{E}\Delta t$.

In the most commonly used observational approach, an estimate of the AGN power is obtained by dividing the enthalpy by a timescale that is assumed to be characteristic of the dissipation timescale. The possible choices for this are the buoyancy timescale, sound travel timescale and the refilling timescale. The shortest of these is the sound travel timescale, i.e. the time taken for a sound wave to travel from the cluster centre to the current location of the bubble,

$$t_{\rm sound} = D\sqrt{\frac{\mu m_{\rm p}}{\gamma k_{\rm b} T}}, \tag{6.20}$$

where D is the distance of the bubble centre from the cluster centre.

The timescale above is the shortest choice and therefore provides an upper limit on the derived AGN power. Calculations of enthalpies for two different cavities taken from the simulation data are summarised in tables 6.4 and 6.5. The first cavity, seen in figure is studied at two different points in time to investigate the effect of evolution on the derived quantities. Clearly, it would be preferable to investigate this method with a larger sample of cavities; a sample of two is insufficient to draw any solid conclusions from. Nevertheless, the results can still be used to gain a tentative understanding of any sources of error in the standard technique.

$\dot{E}$ (erg s^{-1})	Δt (s)	E (erg)	r_b (kpc)	$\frac{\gamma}{\gamma-1}PV$ (erg)	D (kpc)
9×10^{42}	10^{14}	9×10^{56}	3.2	7.3×10^{56}	16
9×10^{42}	10^{14}	9×10^{56}	4.8	2.1×10^{57}	35
1.89×10^{43}	10^{14}	1.9×10^{57}	3.2	1.1×10^{57}	10

Table 6.4: Comparison of energy known to be injected by jets and cavity enthalpies in the simulations. r_b is the radius of the cavity.

$\dot{E}$ (erg s^{-1})	$\langle\dot{E}\rangle$ (erg s^{-1})	$t_{\rm sound}$ (yr)	$\frac{\gamma}{\gamma-1}\frac{PV}{t_{\rm sound}}$ (erg s^{-1})
9×10^{42}	6×10^{41}	1.9×10^{7}	1.2×10^{42}
9×10^{42}	6×10^{41}	4.1×10^{7}	1.8×10^{42}
1.89×10^{43}	1.9×10^{42}	1.1×10^{7}	2.9×10^{42}

Table 6.5: Comparison of the instantaneous and time-averaged jet energy injection rates and jet power determined from the cavity enthalpies divided by the sound travel timescale, $t_{\rm sound}$.

From table 6.4 it seems that the cavity enthalpy is indeed a reasonably good estimate of energy injected by the jet. However, from the first two lines of the table we note that the estimate of the enthalpy has increased by a factor of three as the cavity moves outwards. This is caused by the effect of the aerodynamic forces on the volume of the cavity. As the cavity rises, aerodynamic forces tend to make it expand, this effect is studied in detail in Pavlovski, et al 2006, in prep[3]. The effect is in addition to the expansion which occurs because of the drop in external pressure as the cavity rises. It means that the cavity volume is larger than one would expect from purely adiabatic expansion, causing an over-estimate in the enthalpy and therefore the jet power.

Table 6.5 suggests that the jet power determined from the cavities is not a good estimater of the instanteous jet power, $\dot{E}$. The derived jet powers are roughly an order of magnitude less than the instantaneous jet power. However, the comparison with the time-averaged jet power, $\langle\dot{E}\rangle$, is significantly better. This is unlikely to be a real effect except for line two in the tables. The reason for the exception is

[3]Calculations of the aerodynamic forces can also constrain estimates of the dissipation rate of bubble energy and maximum distance from the cluster cente that a bubble can rise.

described below.

Essentially the enthalpy of any particular cavity only 'knows' the quantity of energy injected. Dividing the cavity enthalpy by a particular timescale only results in an almost arbitrary value for the jet power. Only if the exact time between inflation of two adjacent cavities is known can the time-averaged jet power output be estimated. This is the case for the data in line two of the tables. Applying this rule to observational data means that it would only be possible to estimate the time-averaged jet power for clusters for which at least two pairs of bubbles are observed. One possible candidate for this would be the Perseus cluster.

6.6.2 An estimator of the instantaneous jet power

In principle, it may be possible to not only estimate the time-averaged jet power, but also the instantaneous jet power using observational data. This could allow better determinations of the radio-power/jet-power correlation. It could also be used to put constraints on the duty cycles of AGNs in clusters. Both of these are important parameters that would help to better understand the behaviour of AGNs.

The starting point for this derivation is to speculate that a spherical bubble will detach from the jet that is inflating it, if it's buoyant velocity becomes greater than its expansion velocity (e.g. Churazov et al., 2001). This assumption is somewhat tentative since the jet material moves faster than the buoyant velocity of the bubble and thus could maintain contact with the bubble even for significant buoyant velocities. In addition, more powerful sources will be less -likely to inflate spherical bubbles, as previously discussed. However, the assumption serves as a useful starting point.

The expansion velocity of the bubble is estimated from the rate at which work is done against the ICM by the jet,

$$L = \frac{\gamma}{\gamma - 1} P_0 4\pi r_{\rm b}^2 v_{\rm exp}, \tag{6.21}$$

where L is the jet power, P_0 is the pressure in the ICM at the location where the bubble is inflated, r_b is the radius of the inflated cavity and v_{exp} is the velocity of the expansion.

The buoyant velocity, v_{buoy}, of a spherical bubble is taken to be the terminal value derived in Chapter 2,

$$v_{buoy} \approx \left(\frac{8 r_b g}{3 C_D}\right)^{1/2}, \tag{6.22}$$

where g is the gravitational acceleration where the bubble is inflated and $C_D \approx 0.5$ is the drag coefficient. This is undoubtedly an exaggerated value for the velocity in the early stages of the buoyant rise, but does provide an idea of the correct behaviour.

The radius at which the bubble should have detached from the jet is obtained by equating and $v_{buoy} = v_{exp}$. Rearranging for the jet power gives,

$$L \sim 72 \sqrt{g} P_0 r_b^{5/2} \,\mathrm{erg\,s^{-1}}. \tag{6.23}$$

Equation (6.23) tells us that more powerful jets can inflate large bubbles before they have a chance to detach. Substituting suitable values taken from the simulations of the Virgo cluster, ($g \sim 5 \times 10^{-8} \mathrm{cm\,s^{-2}}$, $P_0 \sim 2 \times 10^{-10} \mathrm{cm\,s^{-3}}$ and $r_b \sim 5\mathrm{kpc}$) gives, $L \sim 1 \times 10^{44} \mathrm{erg\,s^{-1}}$, which is an over-estimate by an order of magnitude. This can be addressed somewhat by taking into account the adiabatic expansion of the bubble as it rises through the ICM. For example, the bubble radius at a location r is related to the initial bubble radius $r_b(0)$, at which it detached from the jet, the pressure at the location where it was inflated and the current ambient pressure, $P(r)$: $r_b = [P_0/P(r)]^{1/(3\gamma)} r_b(0)$. As described in the previous subsection, there is also an additional effect due to aerodynamic forces, however, including these would unecessarily complicate the simple model. The estimate of the jet power now becomes,

$$L \sim 72 \sqrt{g} \left(\frac{P(r)}{P_0}\right)^{1/2} P_0 r_b^{5/2} \,\mathrm{erg\,s^{-1}}. \tag{6.24}$$

Substituting the same values as above, and assuming that the pressure at the current location of the bubble is roughly $P_0/5$ gives $L \sim 6 \times 10^{43} \mathrm{erg\,s^{-1}}$. Clearly, this model

still over-estimates the jet power by a factor of a few. There are several possible reasons for this. One is computational: the effect of finite numerical resolution can lead to errors whereby more energy than was intended could be injected. Another possible reason for this is that the jet was switched-off before the bubble had a chance to detach. An equally likely source of error is the over-estimate of the initial buoyant velocity. If the actual buoyant velocity is a factor K lower than that used above, the estimate of the luminosity will also be reduced by the same factor. So, $K = 0.2$ means that $L \sim 1 \times 10^{43} \mathrm{erg\,s^{-1}}$ which is very close to the actual value used in the simulations.

This model can also be used to estimate the duration of the energy injection phase. This is defined by,

$$\Delta t \equiv \frac{\gamma}{\gamma - 1}\frac{P(r)V}{L} \approx \frac{1}{3}\left[\frac{P(r)}{P_0}\right]^{1/2}\left(\frac{3C_{\rm D}}{8g}\right)^{1/2} r_{\rm b}^{1/2}\,\mathrm{s}. \tag{6.25}$$

Using the usual values gives $\Delta t \sim 6 \times 10^{13}$s; a factor of 2.5 less than the value used in the simulations. However, including the correction factor, K, means $\Delta t \sim 3 \times 10^{14}$s, which is within a factor of three of the value used in the simulations.

Thus, in this method, the AGN power can still be estimated using $L \sim \gamma PV/(\gamma - 1)/\Delta t$. However, the choice for Δt should be that described in equation (6.25), rather than the standard estimates which are based on refilling timescales, sound and buoyancy travel times.

As a final thought, new cavities will be produced after intervals of Δt, if the jet is continuously active. Δt will also remain constant if the jet maintains the same power. Assuming that the detached cavity moves at the buoyant speed, it is possible to estimate how far the first cavity would have moved in the time taken to inflate a second. This distance, Δr, is given by,

$$\Delta r \approx v_{\rm buoy}\Delta t \sim \frac{1}{3}\left[\frac{P(r)}{P_0}\right]^{1/2} r_{\rm b}\,\mathrm{cm}, \tag{6.26}$$

where the symbols are as previously defined.

Equation (6.26) tells us that the first cavity will have moved less than a bubble radius in the time taken to inflate a second cavity. This can imply two things: firstly, if the jet does remain active and produces many cavities in quick succession, the result would be to form a single, large cavity. This cavity would probably become turbulent due to the mixing of several nearby cavities, c.f. the outflow produced by Brüggen & Kaiser (2002). In this case, the method for estimating instantaneous jet powers is probably inaccurate. The most likely scenario in which this could happen is the jets that are dominated by thermal energy. If the jets were momentum driven then the cavity is less likely to be spherical. Secondly, in observations where there is a single, well-defined cavity, this could imply that the jet injects energy in a manner that resembles discrete outbursts. This does not necessarily mean that the jet switches off, but simply that the power output becomes significantly reduced at various times. This is perhaps another hint that the energy input by AGNs is extremely variable. Hence, the above method for determining jet powers can be applied to any cavity that does not appear to turbulent.

6.6.3 An estimator of jet velocity

It is possible to estimate the jet velocity using another simple model. The accuracy of this method can be tested by comparing the results with the values used in the simulations.

The starting point for this model is to calculate the average-density of material within the spherical cavity inflated by a jet. Then, if the initial expansion completely evacuates all of the ambient material from the cavity so that the cavity is only filled by material injected by the jet, the average density of this material within the cavity is,

$$\rho_{\rm b} = \frac{\int \dot{m} {\rm d}t}{V_{\rm b}(t)}, \tag{6.27}$$

where $\dot{m}$ is the mass injection rate by the jet and $V_{\rm b}(t)$ is the cavity volume as a

function of time.

Equation (6.21) can be solved to give the cavity volume as a function of time. This assumes that the cavity expands in approximate pressure equilibrium with the surroundings, and that the jet power remains constant,

$$V_{\rm b} = \frac{4}{3}\pi r_{\rm b}^3 = \frac{\gamma - 1}{\gamma}\frac{Lt}{P_0}, \tag{6.28}$$

where the parameters are as previously defined.

Equation (6.28) is appropriate for relatively low-power jets or high-power jets which are only active for a short period. High-power jets active for longer periods would not inflate bubbles but would travel ballistically through the ICM. The only way that they can inflate bubbles is by precession of the jet.

If the mass injection rate by the jet is also constant, then the average density within the cavity is time-independent and given by,

$$\rho_{\rm b} = \frac{\gamma}{\gamma - 1}\frac{\dot{m}P_0}{L}. \tag{6.29}$$

However, $L/\dot{m}$ is related to the jet power, as in equation (6.2). Since the thermal and kinetic energies of the jets studied in these simulations are roughly in equipartition, equation (6.29) can be re-written to obtain the jet velocity,

$$v_{\rm j}^2 \approx \frac{\gamma}{\gamma - 1}\frac{P_0}{\rho_{\rm b}}. \tag{6.30}$$

Substituting the appropriate values from the simulations ($P_0 = 2\times10^{-10}\mathrm{erg\,cm^{-3}}$, $\rho_{\rm b} = 10^{-26}\mathrm{g\,cm^{-3}}$) gives $v_{\rm j} = 2.35 \times 10^8\mathrm{cm\,s^{-1}}$. This is almost exactly the same as the area-averaged value used in the simulations. If the radius of the bubble as a function of distance from the cluster centre was known this method could be used to estimate the jet velocity for any cavity.

In principle this method could be used to determine the jet velocity from observations of cavities that are currently being inflated. However, constraints on the density of the material within the cavity are not particularly strong. Thus, any estimates based on these constraints will also be highly uncertain.

Equation (6.29) also shows that the bubble density is essentially independent of the jet density but depends on the ambient pressure and jet velocity. Consequently, denser bubbles will be inflated in higher pressure environments and by slower jets. This is easy to understand intuitively: if the bubble expands slowly, for whatever reason, the jet will have chance to pile more material into the bubble. This could have consequences for the type of bubbles which are produced because it means that the bubble density in equation (2.32) is no longer negligible. For denser bubbles the buoyant force would be less and the jet could inflate larger bubbles before they detach from the jet.

6.7 Conclusion

The results of these simulations suggest that while effects such as magnetic fields and viscosity may be important in determining the morphology of remnants of AGN outbursts, other effects such as jet velocity are also significant. It is possible to generate a cavity in the ICM which remains relatively intact compared to bubbles which are not inflated by an outflow. This is probably due to the back flow which occurs as a consequence of the impact of the jet with its surroundings. The back flow reduces the shear velocity between the remnant and the ICM which retards the growth of fluid instabilities.

The jet remnants which best resemble the cavities observed in real clusters are those which are inflated by relatively slow outflows. For example, outflows with velocities of a few $\times 10^8 \mathrm{cm\,s^{-1}}$ readily produce objects that resemble the 'spherical cap' bubble observed in the Perseus cluster (e.g. Fabian et al., 2002) or the eastern torus in the Virgo cluster (e.g. Churazov et al., 2001). In contrast, high velocity jets

produce structures which are much more reminiscent of FR II type radio sources, and cannot be described accurately as a bubble. This hints that many of the bubbles seen in real clusters could have been formed by relatively slow jets. Perhaps this could imply something about the fuelling mechanism, or that the jet velocity is reduced due to the comparatively dense atmospheres which envelope them in galaxy clusters.

The shocks produced by supersonic jets can be an efficient method of heating and redistributing the ICM. Shocks increase the entropy of the gas, which means that any gas that has been lifted out from the cluster centre will not immediately fall back to its original location, but will settle at some intermediate location. The shocks are visible as ripples or oscillations in the mass flow rate profiles. The amplitude of these ripples is no greater than roughly 10 $M_{\odot}\mathrm{yr}^{-1}$.

The simple model of cavity inflation can provide a reasonable estimate of the instantaneous jet power, under particular circumstances, and the time for which the jet was active. However, it has not been tested extensively, and due to the simplifications may not apply equally well to all clusters. As such, a more detailed study is required to better determine the accuracy of the model and calibrate it properly so that it can be used with observations. However, there are obvious inadequacies. One of these is the assumption that of spherical expansion. This is probably not true in the majority of cases, particularly for very powerful jets. Also, it is possible that the jet could switch off before buoyancy makes the bubble separate from it. In this case, the power estimate provides an upper limit, which is useful nevertheless. In addition, the jet could be active for longer than the time required to inflate a single cavity, and may then produce turbulent structures. This would make the estimate inaccurate.

One significant assumption in this set of simulations is that the jet is active periodically. In reality the outbursts are probably triggered by the environment and are probably not exactly periodic. The subject of variability of radio sources is considered in the next Chapter. This includes the effect of the environment and the black hole mass on the power output of the AGN.

Chapter 7

The Fraction of Radio-Loud Galaxies

7.1 Introduction

It is well known that elliptical galaxies are commonly the hosts of powerful radio AGNs (e.g. McLure et al., 2004). These sources give rise to lobes of radio emission embedded in the X-ray emitting gaseous haloes surrounding the host galaxies. There is also growing theoretical evidence that outflows from AGNs play a significant role in the evolution of their surroundings (e.g. Brüggen & Kaiser, 2002; Croton et al., 2006; Sijacki & Springel, 2006).

In theoretical work, outflows from AGNs are commonly used to prevent catastrophic radiative cooling in both elliptical galaxies (e.g. Tabor & Binney, 1993; Binney & Tabor, 1995) and galaxy clusters (e.g. Churazov et al., 2001; Brüggen & Kaiser, 2002; Brüggen, 2003; Basson & Alexander, 2003; Omma et al., 2004; Dalla Vecchia et al., 2004). However, for there to be a long term balance between the heating and cooling processes there must be some sort of feedback mechanism through which the cooling gas triggers AGN outbursts. As yet, it is still unclear

what this precise mechanism is. A great part of the problem is that we are unsure of the dominant accretion mechanism onto supermassive black holes in these environments. Without this it is difficult to make good theoretical predictions, of the AGN activity, that may be compared with observations.

Recent work by Best et al. (2005), studying low luminosity radio sources ($L_{1.4\mathrm{GHz}} \lesssim 10^{25}\mathrm{W\,Hz^{-1}}$), has shown that the fraction, f_{radio}, of radio AGNs hosted mainly by field ellipticals, scales strongly with black hole mass, $f_{\mathrm{radio}} \propto M_{\mathrm{bh}}^{1.6}$. The overall fraction of sources that are radio AGNs brighter than some luminosity L is given by

$$f_{\mathrm{radio}} = f_0 \left(\frac{M_{\mathrm{bh}}}{10^8 M_\odot}\right)^{\alpha} \left[\left(\frac{L}{L_*}\right)^{\beta} + \left(\frac{L}{L_*}\right)^{\gamma}\right]^{-1}, \tag{7.1}$$

where $\alpha = 1.6 \pm 0.1$, $\beta = 0.37 \pm 0.03$, $\gamma = 1.79 \pm 0.14$, $L_* = (3.2 \pm 0.5) \times 10^{24}\mathrm{W\,Hz^{-1}}$.

However, equation (7.1) only applies up to $f_{\mathrm{radio}} \sim 0.25$ above which the trend flattens off in the observational data for more massive black holes.

If the mass accretion rate onto the central black hole is responsible for this scaling, there may be several possibilities for the processes which could produce this. For a classical cooling flow around an elliptical galaxy the mass flow rate should scale as $M_{\mathrm{bh}}^{1.5}$. However, Best et al. (2006) also suggest that Bondi accretion from a cooling flow may be responsible for the AGN controlled gas cooling in elliptical galaxies. Although both of these processes are feasible explanations for the radio fraction of AGNs it is not yet clear how the accretion rate enters into any theoretical description of the phenomenon.

Below is a description of a simple theoretical model for AGN outbursts which is tested using different accretion mechanisms to determine which process can most accurately recreate the observational results.

7.2 The Model

7.2.1 The Basic Model

The power output from the AGN is assumed to be proportional to a systemic accretion rate $\dot{m}$, multiplied by a mediating factor θ. θ is a random variable which is used to simplistically model the variable nature of the accretion process. If θ was not present in this model the power output would be constant and the AGN would be either always detectable or always undetectable. Since AGNs are known to be highly variable, θ provides a simple way of introducing variability into the model. The power output is therefore given by,

$$H = \delta c^2 \dot{m} \theta, \tag{7.2}$$

where c is the speed of light, and δ is some constant conversion efficiency which relates not only to the fraction of the rest mass energy that is released, but also to the fraction of that energy which is deposited into the outflow and is subsequently used for heating the gaseous halo of the galaxy.

In this model the AGN is permanently active, but may not always give rise to an outflow detectable above a given luminosity threshold.

7.2.2 Requirements of the Model

Best et al. (2005) determined the fraction, $f_{\rm radio}$, of AGNs with a radio luminosity greater than some lower cutoff determined by the flux limit of the radio surveys used, at a given black hole mass. In the model described above it is necessary to introduce a similar lower cutoff, $H_{\rm min}$, although in mechanical power rather than radio luminosity.

Best et al. (2006) find the following connection between mechanical power and

$L_{1.4\mathrm{GHz}}/\mathrm{W\,Hz^{-1}}$	$H/\mathrm{erg\,s^{-1}}$
10^{22}	1.9×10^{42}
10^{23}	4.8×10^{42}
10^{24}	1.2×10^{43}

Table 7.1: Values of AGN power output H corresponding to particular values of the radio luminosity $L_{1.4\mathrm{GHz}}$.

radio luminosity,

$$\left(\frac{H}{10^{43}\mathrm{erg\,s^{-1}}}\right) = (3.0 \pm 0.2)\left(\frac{L_{1.4\mathrm{G\,Hz}}}{10^{25}\mathrm{W\,Hz^{-1}}}\right)^{(0.40\pm0.13)}, \tag{7.3}$$

where $L_{1.4\mathrm{G\,Hz}}$ is the observed radio luminosity at 1.4 GHz [1].

Equation (7.3) is used to calculate a value of H_{min} for a given radio luminosity lower cutoff. Consequently, an outburst will only be 'detected' if $H \geq H_{\mathrm{min}}$. Table 7.2.2 gives values of H, the AGN power output that correspond to particular values of the radio luminosity L at 1.4GHz.

The AGN driving the heating will be observable, if the radio luminosity associated with the heating rate H is above the detection threshold. This requirement can be expressed by setting the detectable lower limit of the heating rate to H_{min}. Following the above discussion, only AGNs for which

$$\theta \geq \frac{H_{\mathrm{min}}}{\delta \dot{m} c^2} \equiv x \tag{7.4}$$

may be detected. The probability of a source being detectable is therefore given by

$$P(H \geq H_{\mathrm{min}}) = \int_x^\infty g(\theta)\,\mathrm{d}\theta = f(x). \tag{7.5}$$

where $g(\theta)$ is the probability density function (PDF) of θ.

[1] Note that if the mechanical powers are systematically wrong by some factor f, due to errors in the estimation of either radio bubble energies or ages, this would simply scale the values of H and be equivalent to a change in the value of δ.

7.2.3 Constructing the radio luminosity function

To construct a radio luminosity function analogous to equation (7.1), for a given black hole mass, using equation (7.5) the lower detection limit is allowed to vary. For low luminosities ($L < L_*$) equation (7.1) can be simplified to,

$$f_0\left(\frac{M_{\rm bh}}{10^8 M_\odot}\right)^{\alpha}\left(\frac{L}{L_*}\right)^{-0.37} \approx P(H \geq H_{\rm l}), \tag{7.6}$$

where the parameters are as previously defined.

Equation (7.3) suggests $H \propto L^{0.4}$. Substituting this relation into equation (7.6) gives,

$$P(H \geq H_{\rm min}) \propto \frac{1}{H_{\rm min}}. \tag{7.7}$$

Equation (7.7) can be extended by using equation (7.5) which tells us that the probability of an AGN being detectable is a function of the parameter $x = H_{\rm min}/(\delta \dot{m} c^2)$. This means equation (7.7) must become

$$P(H \geq H_{\rm min}) \propto \frac{\delta \dot{m} c^2}{H_{\rm min}}. \tag{7.8}$$

Any model for $g(\theta)$ that can reproduce this functional form, for $L < L_*$, is essentially equivalent. For example, equation (7.6) tells us that in this luminosity regime different scalings of the luminosity or changes in the normalisation are indistinguishable. It is impossible to discern whether the luminosity is scaled by a value L_* or the normalisation is changed by $L_*^{0.4}$. It should be noted that the scaling of equation (7.8) on $H_{\rm min}$ cannot always follow this form since for sufficiently small values it would result in unphysically large values (> 1) for the probability. However, the main application of equation (7.8) is to provide a simple argument for how the radio-loud fraction will depend on the fundamental parameters in the regime of low radio luminosities, $L < L_*$. Any detailed calculations involving the probability of detecting an AGN will necessarily require a complete and physically motivated probability distribution for θ which avoids the singularity at $H_{\rm min} \rightarrow 0$.

It would be possible to produce a model for which the distribution of θ depends on the black hole mass. With such a model it may be possible to explain the entire radio luminosity function, if this were fine-tuned to produce the correct luminosity scaling. However, the analysis below concentrates on a distribution of θ which is independent of black hole mass and designed to fit only the low-power end of the radio luminosity function. This is a physically motivated model based on the log-normal distribution which, for educated assumptions, satisfies the requirements of the radio luminosity function for $L < L_*$. In this model, some other physical effect is required to explain the steepening of the RLF for $L > L_*$ at the same value of L_* for all black hole masses. It is unclear what this property is, but one possibility is that L_* is a property controlled by the source environment.

7.3 Accretion Modes

It is clear that the fraction of AGN detected at radio wavelengths will depend strongly upon the dominant mode of accretion on to the black hole. The functional forms of several different modes of accretion are given below. Their influence on the behaviour of $P(H \geq H_{\rm min})$ will be studied in the next section.

The five different cases are: i) standard Bondi accretion, ii) Bondi accretion from a maximum cooling flow iii) a phenomenological formula, iv) classical mass flow rate, v) Eddington limited accretion.

i) The standard Bondi accretion rate formula is given in equation (7.9),

$$\dot{M}_{\rm Bondi} = \pi (G M_{\rm bh})^2 \left(\frac{\gamma k T}{\mu m_{\rm p}} \right)^{-3/2} \rho_0, \tag{7.9}$$

where G is the Universal gravitational constant, $M_{\rm bh}$ is the black hole mass, γ is the adiabatic index (5/3), T is the gas temperature in the vicinity of the black hole, k is the Boltzmann constant, and $\mu m_{\rm p}$ is the mean mass per particle where we assume that $\mu = 0.59$, ρ_0 is the gas density in the vicinity of the black hole.

ii) Equation (7.10) for Bondi accretion is taken from Croton et al. (2006) and applies specifically to Bondi accretion from a strong cooling flow, i.e the temperature of the accreted gas depends on its cooling history. Also note that the Bondi accretion rate depends on both the black hole mass and the temperature of the surrounding gas,

$$\dot{M}_{\rm Bondi,cf} \approx G\mu m_{\rm p}\frac{kT}{\Lambda(T)}M_{\rm bh}, \tag{7.10}$$

where T is the gas Virial temeprature, $\Lambda(T)$ is the cooling function as a function of gas temperature. This formula is derived by equating the the sound crossing time at the Bondi radius, to the cooling time at the same location.

iii) A phenomenological accretion rate utilised in a study of semi-analytical galaxy formation by Croton et al. (2006) is also included. It is designed to reproduce the observed low-energy radio activity (e.g. $L_{1.4\rm GHz} \lesssim 10^{25}\rm W\,Hz^{-1}$) and the turnover at the bright end of the galaxy luminosity function,

$$\dot{M}_{\rm radio} = \kappa\left(\frac{M_{\rm bh}}{10^8 M_\odot}\right)\left(\frac{f_{\rm hot}}{0.1}\right)\left(\frac{V_{\rm vir}}{200\rm kms^{-1}}\right)^3, \tag{7.11}$$

where $\kappa = 6\times10^{-6}M_\odot\rm yr^{-1}$ is a constant, $f_{\rm hot}$ is the fraction of halo mass in hot gas and is roughly constant for $V_{\rm vir} \geq 150\rm km\,s^{-1}$ and $V_{\rm vir}$ is the Virial velocity of the halo. Croton et al. (2006) relate the temperature of the halo to the gas Virial velocity by $T = 35.9V_{\rm vir}^2$ K. Substituting into equation (7.11) demonstrates that for cases ii) and iii) the mass accretion rate scales in very similar ways. It has been assumed that $V_{\rm vir} = \sigma_{\rm v}$, the velocity dispersion of the halo.

Mechanisms iv) and v) have been chosen to illustrate the limiting cases of environment dominated and black hole dominated accretion, respectively.

iv) Equation (7.12) gives the mass flow rate predicted from the classical cooling flow model which depends only on X-ray luminosity and temperature of the gas, but not the mass of the central black hole,

$$\dot{M}_{\rm cool} = \frac{2\mu m_{\rm p}L_{\rm X}}{5kT}. \tag{7.12}$$

It is important to note that the cooling flow $\dot{m}$ is expected to exceed that of

Bondi accretion from a cooling flow. This is because the value of the cooling flow $\dot{m}$ refers to the total mass deposited within the cooling radius. As the volume of interest increases, so will $\dot{m}$ (e.g. see Pope et al., 2006, for an explanation). In contrast, Bondi accretion from a cooling flow only applies to a small region near the black hole. Thus, the mass flow rate will necessarilly be smaller. Of course, in some cases, the cooling flow $\dot{m}$ exceeds the Eddington limit, but one would not expect the central AGN to accrete all of this material. The majority of it would, in reality, be deposited at larger radii leaving only a small fraction to reach the central regions. The point of interest is in how the cooling flow $\dot{m}$ scales rather than the absolute value.

v) The Eddington accretion rate depends only on black hole mass. Essentially this mechanism has been chosen to investigate the radio-loud fraction one would expect from an accretion mode that depends linearly on black hole mass, but not the gas properties,

$$H_{\rm Edd} = 1.3 \times 10^{38} \left(\frac{M_{\rm bh}}{M_{\odot}} \right) {\rm ergs}^{-1}. \tag{7.13}$$

7.4 Results and Discussion

Using equation (7.8), the probability that an AGN is detectable is directly proportional to the accretion rate. The right hand side of equation (7.8) must also scale in the same way as equation (7.1). Therefore, the black hole mass dependence in equation (7.1) must come from the black hole mass dependence of the accretion rate. This property can then be used to descrimate which accretion modes could provide a good match to the observed radio-loud fraction. In the regime $L < L_*$ it is possible to discriminate between the accretion models using equation (7.8) without the need for a full and mathematically self-consistent probability function for θ. The derivation of an example for the probability function with the correct behaviour in the regime of interest is deferred to the next sub-section.

For the first accretion mode, Bondi accretion, a sample of 9 galaxies is taken

Accretion mode	A	B
Bondi	-10.88	2.16
Cooling flow Bondi	-4.94	1.52
Phenomenological	-12.24	1.8
cooling flow	-1.61	0.78
Eddington	-1.47	1.0

Table 7.2: Best-fit parameters relating accretion rate to black hole mass.

from Allen et al. (2006). They provide velocity dispersions, from which the black hole masses are calculated (see below), and power released from the Bondi accretion rate for each system. For the subsequent four modes 41 galaxies are selected from Fukazawa et al. (2006), who provide X-ray luminosities and gas temperatures (but not central densities, hence the need for the Allen et al. (2006) sample). The velocity dispersions for these galaxies are taken from McElroy (1994).

The black hole masses are calculated using the well-established correlation between black hole mass and central velocity dispersion commonly referred to as the $M_{\rm bh} - \sigma_{\rm v}$ relation. Gebhardt et al. (2000) give this $M_{\rm bh} - \sigma_{\rm v}$ relation as,

$$M_{\rm bh} = (1.2 \pm 0.2) \times 10^8 M_\odot \left(\frac{\sigma_{\rm v}}{200 {\rm kms}^{-1}} \right)^{(3.75 \pm 0.3)}. \quad (7.14)$$

In elliptical galaxies the environmental properties of the gas halo, the X-ray luminosity and temperature, are linked with the central black hole mass. Therefore, since the Bondi accretion rate from a cooling flow is a function of black hole mass and temperature only, it could be expressed in terms of black hole mass alone. To do this the accretion rate is plotted versus black hole mass to determine the best-fit power-law which describes the $\dot{m} - M_{\rm bh}$ relation for each accretion mode,

$$\ln \left(\frac{\dot{m}}{M_\odot {\rm yr}^{-1}} \right) = A + B \ln \left(\frac{M_{\rm bh}}{10^8 M_\odot} \right). \quad (7.15)$$

The best-fit parameters are given in table 7.2.

The B coefficients describing individual $\dot{m} - M_{\rm bh}$ relations are roughly as expected. For example, the Bondi accretion is proportional to the square of the black hole mass,

while $B = 2.16$. The value of $B \approx 1.5$ is expected for Bondi accretion from a cooling flow, since the cooling function has very weak dependence on temperature at these temperatures. The value of $B = 1.8$ is expected for the phenomenological accretion rate since $\dot{m} \propto M_{\rm bh}\sigma_{\rm v}^3$. In principle one might expect the cooling flow accretion rate to be proportional to $M_{\rm bh}^{1.5}$ (Best et al., 2005) however, there is so much scatter in the $\dot{m} - M_{\rm bh}$ plot that any scaling could apply equally as well as many others. Obviously, the Eddington accretion rate would be expected to scale linearly with black hole mass which agrees with $B = 1$.

From table 7.2 it is clear that only Bondi accretion from a cooling flow can provide the dependence of accretion rate that will match black hole mass dependence of equation (7.1). As a result, all of the subsequent calculations are based around this accretion process.

Having ruled out five of the six accretion modes, it is necessary to find an appropriate and physically motived probability distribution, to use in equation (7.5), and will avoid a singularity for very small values of $H_{\rm min}$.

7.4.1 The Log-normal Distribution of AGN power output

Consider a time-line of heating events, $H(t)$. It is straight forward to define the time-averaged heating rate,

$$H_\tau = \frac{1}{\tau}\int_0^\tau H(t)\mathrm{d}t. \tag{7.16}$$

In each time interval τ the quantity H_τ is considered to be a random variable with a PDF, $g(H_\tau)$. An approximate expression for $g(H_\tau)$ can be obtained by following a procedure similar to that used in the formulation of the log-normal theory of turbulence (e.g. Yaglom, 1966; Monin & Yaglom, 1975). It will be assumed that the heating function, $H(t)$, is self-similar, in the same sense that turbulence is. The function that describes the heating time-line 'looks' the same on all time-scales. This is the same as for a fractal and 'looks' means that the statistical properties are the same on all time-scales.

For the time interval τ_0, the mean heating rate is $\langle H \rangle$, where τ_0 is of the order of the age of the Universe. $\langle H \rangle$ denotes a statistical average,

$$\langle H \rangle = \int g(H) H \mathrm{d}H. \tag{7.17}$$

The time-line is then divided into r smaller pieces of length $\tau_1 = \tau_0 r^{-1}$, each with a time-averaged heating rate H_1. The H_1 are a set of random variables with identical PDFs and mean values $\langle H_1 \rangle = \langle H \rangle$. The τ_1 pieces are further subdivided, each into r pieces of length $\tau_2 = \tau_1 r^{-1} = \tau_0 r^{-2}$. The process can be continued n times. Now, consider a time period τ_n in the range,

$$\tau_0 \geq \tau_\mathrm{n} = \tau_0 r^{-\mathrm{n}} \gg \tau_\mathrm{t}. \tag{7.18}$$

The random variable H_n can be written as the product,

$$H_\mathrm{n} = H_0 \frac{H_1}{H_0} \cdots \frac{H_\mathrm{n}}{H_{\mathrm{n}-1}}, \tag{7.19}$$

where $H_\mathrm{i}/H_{\mathrm{i}-1}$, $1 \leq \mathrm{i} \leq \mathrm{n}$, by construction is a dimensionless random variable. Alternatively,

$$\ln H_\mathrm{n} = \ln H_0 + \ln W_1 + \ldots + \ln W_\mathrm{n}, \tag{7.20}$$

where $\ln H_\mathrm{n}$ is the sum of the random variables $\ln W_\mathrm{i} = \ln H_\mathrm{i}/H_{\mathrm{i}-1}$. The variables $\ln W_\mathrm{i}$ are assumed to be independent, due to the random character of the division process, but need not be identically distributed. Each $\ln W_\mathrm{i}$ has an individual mean M_i and variance S_i.

By the central limit theorem the probability distribution of $\ln(H_\mathrm{n}/H_0)$ becomes Gaussian for $n \gg 1$ if the contribution to the overall sum, of each $\ln W_\mathrm{i}$, is small. Specifically, the last statement requires that no single $\ln W_\mathrm{i}$ should dominate over the others. This is a simplified form of the Lindeberg criterion (e.g. Feller, 1968). The mean of the distribution will then be the sum of the individual means $M_\mathrm{n} = \Sigma M_\mathrm{i}$ and variance the sum of the individual variances $S_\mathrm{n}^2 = \Sigma S_\mathrm{i}^2$. This implies that the PDF of H_n/H_0 tends toward the log-normal distribution,

$$g(H_\mathrm{n}/H_0) = \frac{H_0}{H_\mathrm{n} S_\mathrm{n} \sqrt{2\pi}} \exp\left[-\frac{1}{2} \left(\frac{\ln(H_\mathrm{n}/H_0) - M_\mathrm{n}}{S_\mathrm{n}} \right)^2 \right]. \tag{7.21}$$

The fact that the distributions of the $\ln W_{\rm i}$ need not be identical means that the mean and variance of the $\ln(H_{\rm n}/H_0)$ distribution can be independent of each other. However, to ensure that the means are independent of the duration $\tau_{\rm n}$ over which the average is taken requires that $M_{\rm n} = -S_{\rm n}^2/2$. Note that the cumulative probability for H given in equation (7.21) remains finite and approaches unity for $H_{\rm min} \rightarrow 0$.

7.4.2 Applying the log-normal distribution to the model

The discussion in the previous subsection can be applied to this model of AGN heating. If one considers n cycles such that equation (7.21) applies, then $H_{\rm n} = H = \delta\dot{m}c^2\theta$. For constant δ this implies that θ follows a log-normal distribution of the form,

$$h(\theta/\theta_0) = \frac{\theta_0}{\sqrt{2\pi}\sigma\theta}\exp\left[-\frac{1}{2}\left(\frac{\ln(\theta/\theta_0) - M_{\rm n}}{S_{\rm n}}\right)^2\right]. \tag{7.22}$$

That is, $\ln(\theta/\theta_0)$ is normally distributed with a mean value of $M_{\rm n}$ and standard deviation, $S_{\rm n}$.

As long as individual cycles have a lifetime that is short compared to the age of the Universe, equation (7.22) can be applied to find $P(H \geq H_{\rm min})$. $g(\theta)$ can be determined using the argument that $g(\theta){\rm d}\theta = h(\theta/\theta_0){\rm d}(\theta/\theta_0)$.

Equation (7.22) can be used to find the probability that an AGN is detectable, from equation (7.5),

$$P(H \geq H_{\rm min}) = \frac{1}{2}{\rm erfc}\left(\frac{\ln(H_{\rm min}/H_0) + S_{\rm n}^2/2}{\sqrt{2}S_{\rm n}}\right), \tag{7.23}$$

where erfc is the complimentary error function and $H_0 = \delta\dot{m}c^2\theta_0 \equiv \delta_0\dot{m}c^2$. Note that the cumulative probability for H given in equation (7.23) remains finite and approaches unity for $H_{\rm min} \rightarrow 0$.

Accretion mode	$\delta_{0,1}$	$\delta_{0,2}$	$\delta_{0,3}$	$S_{\rm n,1}$	$S_{\rm n,2}$	$S_{\rm n,3}$
Cooling flow Bondi	8.8×10^{-4}	1.1×10^{-3}	1.0×10^{-3}	2.4	2.68	2.97

Table 7.3: Values of $\delta_{0,i}$ and $S_{\rm n,i}$ in the log-normal model, for each accretion mode and lower detection cutoff, that are consistent with observations. The subscript i=1 - 3 correspond to detection limits of $L_{1.4\rm GHz}$=10^{22}, 10^{23} and 10^{24} W Hz^{-1} respectively.

7.4.3 Results from the Log-normal distribution

Comparing this theoretical estimate with the best-fit to the observed radio-loud fraction in dependence of $M_{\rm bh}$ from Best et al. (2005) constrains the free parameters in our model, δ_0 and $S_{\rm n}$ for Bondi accretion from a cooling flow. These values are assumed to be constant and independent of $M_{\rm bh}$ and the environmental parameters. However, in principle there is no reason why δ_0 or $S_{\rm n}$ could not depend upon the luminosity or the environment of the host galaxy. The task of fitting the $P(H \geq H_{\rm min})$ to equation (7.1) is dramatically simplified by using an analytical expression for the $\dot{m} - M_{\rm bh}$ relationship rather than the data itself.

It is clear from figure 7.1 that a good agreement, between the best-fit from Best et al. (2005) and the theoretical model, can occur for the estimate of the Bondi accretion rate from a cooling flow. This suggests that both black hole mass and the environment play an integral part in determining the observed radio-loud fraction.

It is interesting to note that, in agreement with observations, the radio-loud fraction generated using this model flattens off at large black hole masses. This effect is not taken into account by equation (7.1) but can be estimated using this theoretical model. To do this, equation (7.1) is fitted to $P(H \geq H_{\rm min})$ using a black hole mass dependence with a variable value of the exponent that also depends on black hole mass. A good fit is provided by,

$$\alpha = \frac{16.1}{10.1 + (M_{\rm bh}/10^8 M_\odot)^{1/2}}. \tag{7.24}$$

Figure 7.2 shows the best-fit of equation (7.1) to the model results for Bondi accretion from a cooling flow, using the variable α.

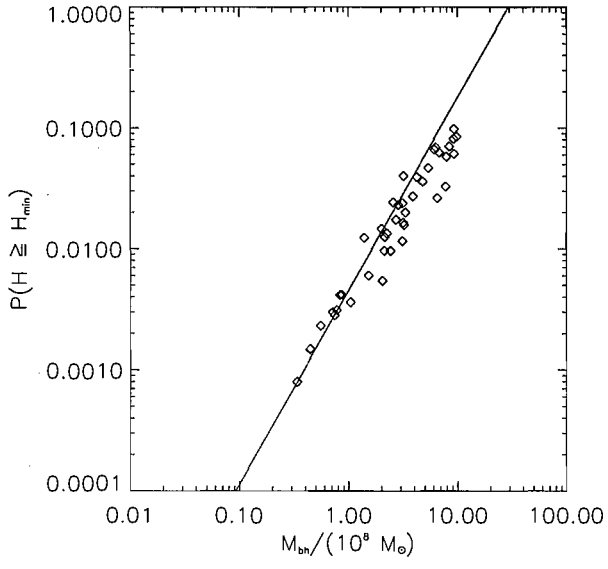

Figure 7.1: Comparing the observed radio-loud fractions of AGN (stars) with that predicted by Bondi accretion from a cooling flow, for the log-normal model, for a minimum radio power of $10^{24}\mathrm{W\,Hz^{-1}}$ corresponding to a minimum heating rate of $H = 1.2 \times 10^{43}\mathrm{erg\,s^{-1}}$. The diamonds represent the predicted radio-loud fraction according to equation (7.23). The solid line shows the prediction derived from observations as given in equation (7.1).

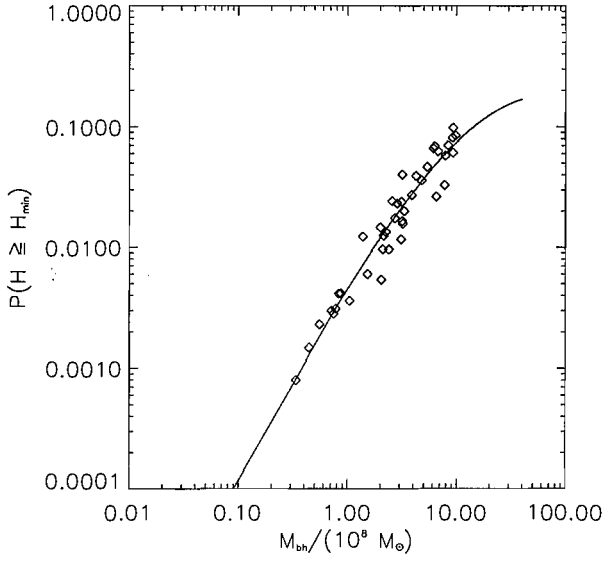

Figure 7.2: Effect of using a variable α in equation (7.1): best-fit of equation (7.1) to $P(H \geq H_{\mathrm{min}})$ for Bondi accretion from a cooling flow for normal ellipticals.

7.4.4 The radio-loud fraction for Brightest Cluster Galaxies

$P(H \geq H_{\rm min})$ can also be evaluated for Brightest cluster galaxies (BCGs). Using equation (7.8) it is possible to make some predictions about how $P(H \geq H_{\rm min})$ might be different for BCGs compared to field elliptical galaxies. For example, intracluster gas is generally hotter than the haloes around elliptical galaxies. This suggests that the $P(H \geq H_{\rm min})$ for BCGs will be larger than for field ellipticals, for the same black hole mass. Interestingly, observational evidence (e.g. Burns, 1990) suggests that a larger fraction of galaxies at the centres of clusters show radio outflows than those not at the centre of clusters. This would not be the case if in AGNs in BCGs were fueled entirely by classical Bondi accretion. In this case, all other things being equal, the Bondi accretion rate from a hotter atmosphere will be lower than from a cooler atmosphere. As a result one might expect the fraction of galaxies detectable in the radio to be lower for BCGs than for field ellipticals.

The temperature of the intracluster medium bears little or no relation to the mass of the black hole in the central galaxy, therefore, one would expect $\dot{m} \propto M_{\rm bh}$ for BCGs.

Using the same values of δ_0 and $S_{\rm n}$ that were determined for normal ellipticals (i.e. those galaxies not at the centres of clusters) one can determine the radio-loud fraction of galaxies at the centres of galaxy clusters. The objects used for this prediction are taken from Kaastra et al. (2004) and Donahue et al. (2005). Furthermore, from these publications the sample was restricted to those objects for which black hole masses could be obtained from Fujita & Reiprich (2004).

Figure 7.3 shows the $P(H \geq H_{\rm min})$ values obtained for BCGs, as a function of black hole mass, compared with the relation determined for ellipticals not located at the centres of clusters. The most obvious feature of figure 7.3 is that $P(H \geq H_{\rm min})$ is greater for BCGs than field ellipticals at all black hole masses.

The values of $P(H \geq H_{\rm min})$ scale with black hole mass although with a slightly

shallower slope than for the normal ellipticals. The slope is also weakly dependent on the detection threshold, for example $P(H \geq H_{\rm min}) \propto M_{\rm bh}^{0.67}$ for $H_{\rm min} = 1.2 \times 10^{43}{\rm erg\,s^{-1}}$, $P(H \geq H_{\rm min}) \propto M_{\rm bh}^{0.58}$ for $H_{\rm min} = 4.8 \times 10^{42}{\rm erg\,s^{-1}}$ and $P(H \geq H_{\rm min}) \propto M_{\rm bh}^{0.48}$ for $H_{\rm min} = 1.9 \times 10^{42}{\rm erg\,s^{-1}}$. In contrast, $P(H \geq H_{\rm min}) \propto M_{\rm bh}^{1.5}$ for normal ellipticals compared to $f_{\rm radio} \propto M_{\rm bh}^{1.6}$ as found by Best et al. (2005). Comparing with equation (7.1), the normalisation of the radio-loud fraction is $f_0 \approx (1.4 - 5) \times 10^{-3}$ for the normal ellipticals (compared to $f_0 = 3.5 \times 10^{-3}$ given by Best et al. (2005)) and $f_0 \approx 0.12 - 0.37$ for AGNs at the centre of clusters. For a $10^8 M_\odot$black hole, the probability that AGNs in BCGs are more powerful than a given lower cutoff is $\sim$ 4-5 times greater than for AGNs not at the centres of clusters.

Best et al. (2006) in prep, find that the fraction of radio-detectable AGNs in BCGs increases with black hole mass less steeply than for normal ellipticals, but has a higher normalisation. Interestingly, the predicted values of $P(H \geq H_{\rm min})$ for the cooling flow Bondi accretion rate seem to agree qualitatively with this result.

The combined results of this study suggest that Bondi accretion from a cooling flow could be responsible for the observed dependence of $f_{\rm radio}$ on $M_{\rm bh}$. This is because Bondi accretion from a cooling flow seems to provide a good fit to the data for both normal galaxies and BCGs. However, while this statement may be correct these results cannot rule out the possiblity that the radio-detected fraction of normal ellipticals is determined by other processes such as the Eddington accretion rate for BCGs, or a different accretion rate but with a varying efficiency δ_0. In addition, Bondi accretion from a cooling flow would certainly not be continuous. For one thing, the accretion rate on to the AGN would surely be reduced as a result of the energy injected by the previous outburst. Instead, a more likely scenario is that Bondi accretion occurs almost continuously but varies in response to the effect of radiative losses and the heating response on the ambient gas. At various points in time the accretion rate is characteristic of Bondi accretion from a cooling flow. Presumeably, the power output during these phases results in more powerful outbursts than from classical Bondi accretion. These outburst are more likely to be observable.

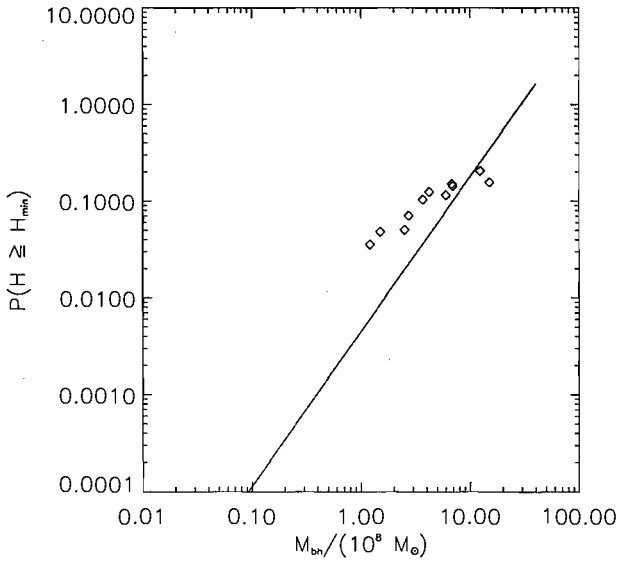

Figure 7.3: Comparison of radio-detected fractions for ellipticals at the centres of clusters for Bondi accretion from a cooling flow, for a minimum radio power of $10^{24}\mathrm{W\,Hz^{-1}}$. Also shown is the radio-detected fraction for normal elliptical galaxies, defined by equation (1).

7.5 Summary

This simple accretion model not only adequately matches the observed radio-detected fraction of AGNs as a function of black hole mass, but also responds correctly to changes of the lower selection limit. According to this model, the accretion mode which best describes the observed radio-detected fraction is Bondi accretion from a cooling flow. This strongly suggests that the environment plays a strong role in setting the level of AGN activity we observe in elliptical galaxies.

Assuming that the AGN activity follows a self-similar pattern in time, it follows that the energy output of the AGN is approximately log-normally distributed. This distribution of AGN activity predicts the correct slope for the fraction of radio-loud AGNs as a function of radio luminosity at low radio luminosities. However, other models for the AGN activity with similar properties may be possible. Nevertheless, it is interesting to note that the X-ray lightcurves of accreting black holes are consistent

with being self-similar as well. Uttley et al. (2005) show that the X-ray fluxes of AGNs and Galactic microquasars follow a log-normal distribution. The accretion rates in these systems are usually assumed to correlate with the X-ray behaviour fluxes. Hence, it is encouraging to note the same behaviour predicted by this model.

Using this model one can also investigate the scaling of the radio-detected fraction for galaxies at the centre of clusters for the accretion processes outlined above. Bondi accretion from a cooling flow provides an estimate of the fraction which compares well with the observational results (Best et al 2006, in prep). This, in particular, may suggest that Bondi accretion from a cooling flow is the main driving force behind the radio-detected fraction of all elliptical galaxies, whether they are located at the centres of clusters or elsewhere. This model suggests that the radio-detected fraction of BCGs will also scale with black hole mass but with a slightly shallower slope than for normal ellipticals. Furthermore, the normalisation of this fraction is roughly a factor of 4-5 higher, for black hole masses at $10^8 M_{\odot}$, than for normal ellipticals. This would not be the case for classical Bondi accretion which would reduce the accretion rate in a hotter atmosphere. However, this does not mean that AGNs do not ever accrete at the classical Bondi rate, rather that the more powerful, and hence observable outbursts, are generated by Bondi accretion from a ccoling flow. Whenever, the AGN is not accreting at this rate it could well be accreting at the classical Bondi rate. Furthermore, since these observations imply that the AGN responds to its environment, Eddington limited accretion is also ruled out as driver for the fraction of galaxies that are detectabel in the radio.

The results of this work suggest that Bondi accretion, in particular from a cooling flow, plays an important role in the properties of observed AGN outflows. This could provide important constraints for theoretical work studying galaxy evolution and AGN activity.

There are numerous properties of distant galaxies which are relatively poorly constrained. The central stellar velocity dispersion is one of these. The limitations of spatial resolution mean that the central regions of very distant clusters are poorly

resolved. The next Chapter focusses on a new method, based on the X-ray emitting atmospheres which allows an independent estimate of the stellar velocity dispersion.

Given the apparent importance of black hole mass in determining the power output of radio AGNs, there is also a discussion of the effect of accretion and mergers on the mass of the black hole and the $M_{\rm bh} - \sigma_{\rm v}$ relation.

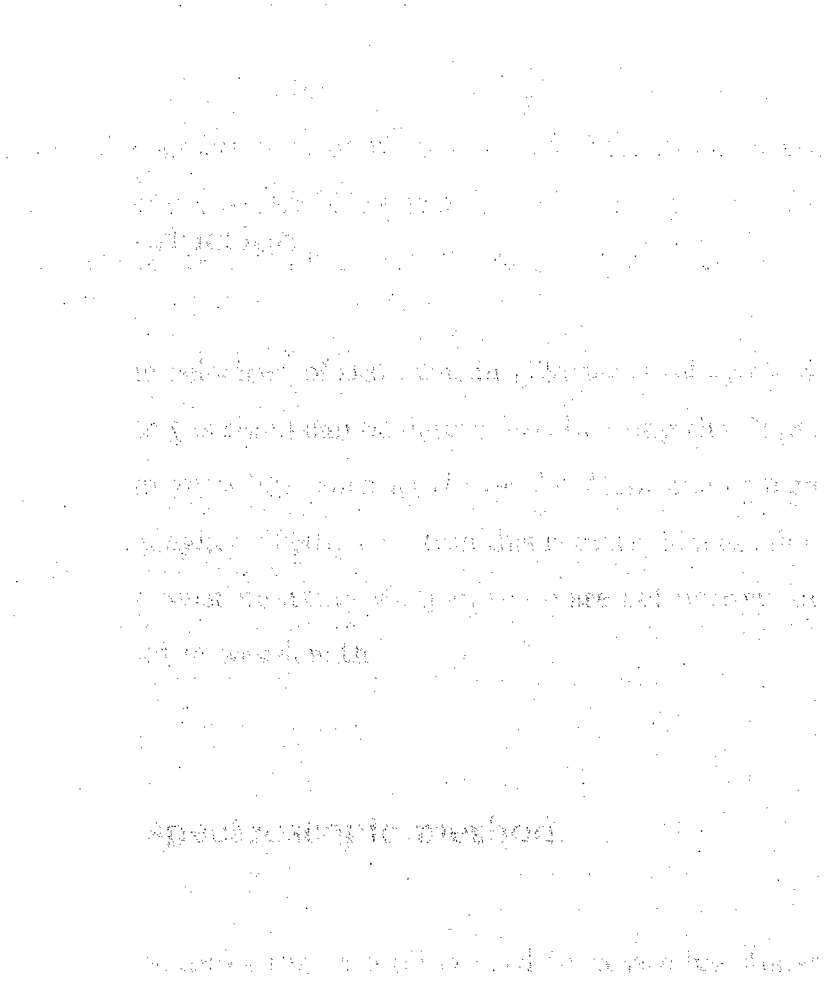

Chapter 8

Using the ICM to estimate the central stellar velocity dispersion

8.1 Introduction

Measuring the velocities of stars within galaxies is relatively difficult. The speed of a cool or warm gas cloud can be determined by using the Doppler shift of at a bright peak of an emission line, such as Hα or the 21cm line of neutral atomic hydrogen (Sparke & Gallagher, 2000). For stars this is more difficult since absorption features in the spectra must be used. Many of these are not narrow, but have an significant intrinsic spread in wavelength.

8.2 The spectroscopic method

The spectral features that are often used to determine stellar velocity dispersions are the Ca II triplet, Mg I *b* triplet, and Ca H + K optical absorption features (Greene & Ho, 2006). The most commonly used are the Ca II triplet (CaT) and Mg I *b* triplet which occur in a region of relatively low AGN contribution with rest

wavelengths of 8498, 8542 and 8662 Å and 5167, 5173 and 5184 Å respectively. For CaT the redshift limit is roughly $z \leq 0.068$ for ground based telescopes, since for longer wavelengths water vapour bands begin to reduce atmospheric tranparency (Onken et al., 2004).

The light of all of the stars in a galaxy is the sum of their individual spectra, each Doppler-shifted in wavelength according to their motion. Their orbital motion causes lines in the summed spectrum to be wider and shallower than those of an individual star. In elliptical galaxies most of the light comes from G and K giant stars. Typically nearby stars of this type are observed with the same spectropgraph and used as spectral templates with which the galaxy spectrum can be deconvolved (Sparke & Gallagher, 2000). In principle, if the distribution in space and velocity for each type of star was known, and their spectra were exactly the same as the template stars, it would be possible to reproduce the galaxy spectrum precisely. A common choice for the spatial and velocity distribution of the stars, integrated along the line of sight (z-axis), is the Gaussian, where $\sigma_{\rm v}(x, y)$ is the velocity dispersion perpendicular to the line of sight.

The central stellar velocity dispersion seems to be related to several properties of the host galaxy. For example plotting the velocity dispersion against the bolometric optical luminosity, $L_{\rm V}$, shows that roughly, $L_{\rm V} \propto \sigma_{\rm v}^4$ (Faber & Jackson, 1976). This is known as the Faber-Jackson relation which tells us that the elliptical galaxies with a large velocity dispersion are also more luminous. The central stellar velocity dispersion is also related to the Virial temperature of the gas in the halo of an elliptical galaxy.

A similar relationship has been shown to exist between the stellar velocity dispersion and the masses of black holes at the centres of galaxies, determined independently (e.g. Tremaine et al., 2002). This is known as the $M_{\rm bh} - \sigma_{\rm v}$ relation.

8.3 The Gravitational Method

8.3.1 Motivation

The spectroscopic method of determining the central stellar velocity dispersion is excellent for nearby galaxies, but becomes less effective for very distant objects since the galaxy cores become harder to resolve. This means that stellar velocity dispersion are hard to obtain for galaxies located in distant clusters which are frequently at redshifts greater than 0.068.

Current results, such as the Faber-Jackson relation, outlined in the preceeding section suggest that there is a strong correspondance between the central stellar velocity dispersion and the graviational potential of the galaxy. Therefore, it seems plausible that the stellar velocity dispersion could be estimated from the gravitational potential of the galaxy, if this was known.

As discussed throughout this thesis, the gravitational acceleration throughout galaxy clusters and elliptical galaxies can be determined from the gas temperature and density measurements of the X-ray emitting atmospheres. Assuming hydrostatic equilibrium, the gravitational acceleration is given by,

$$g(r) = \frac{\nabla P}{\rho} = \frac{k_{\rm b}}{\mu m_{\rm p}} \left(\frac{{\rm d}T}{{\rm d}r} + \frac{T}{n} \frac{{\rm d}n}{{\rm d}r} \right). \tag{8.1}$$

The atmospheres of these clusters and galaxies are also much more spatially extended the core of the galaxy which could potentially make this method valuable at high redshifts. Because of this, the main aim of determining the stellar velocity dispersion from the gravitational acceleration profile of a galaxy, or cluster, is to provide a direct replacement for the spectroscopic method at high redshifts.

8.3.2 The Theory

From experience, the gravitational acceleration peaks at a few tens of kpc from the centre which is attributed to the influence of the central galaxy (for example see figure 1 of Kaiser et al., 2005). The radial location of the maximum of the gravitational acceleration will be referred to as $r_{\rm m}$ and the value of the gravitational acceleration at this point is $g(r_{\rm m})$. The gravitating mass within $r_{\rm m}$ can then be estimated in the usual way using Newton's law of gravitation,

$$g(r_{\rm m}) = -\frac{G\,M(r < r_{\rm m})}{r_{\rm m}^2}, \tag{8.2}$$

where G is Newton's Universal gravitational constant.

Galaxy clusters and the centres of galaxies, especially ellipticals, are generally assumed to be Virialised structures (Sparke & Gallagher, 2000). Very crudely a Virialised system can be described as a structure whose distribution of material is stationary. The Virial theorem relates gravitational mass within the Virial radius to the velocity dispersion (e.g Sarazin, 1986),

$$\frac{G\,M(r < r_{\rm m})}{r_{\rm m}} = \langle \sigma_{\rm v}^2 \rangle, \tag{8.3}$$

where $\langle \sigma_{\rm v}^2 \rangle$ is the mass-weighted velocity dispersion. The velocity dispersion is related to the radial velocity dispersion by $\langle \sigma_{\rm v}^2 \rangle = 3\sigma_{\rm v}(r)^2$.

Substituting for $M(r < r_{\rm m})$ from equation (8.2) gives,

$$g(r_{\rm m})r_{\rm m} = 3\sigma_{\rm v}(r_{\rm m})^2. \tag{8.4}$$

It is now possible to determine $\sigma_{\rm v}(r_{\rm m})$ if the gravitational acceleration is inferred from X-ray observations using equation (8.1). To compare this method with the well-established spectroscopic method, equation (8.4) can be written in terms

of the spectropscopically measured velocity dispersion $\sigma_v(x,y)$. Using cartesian coordinates the total velocity dispersion must be $\sigma_v^2 = \sigma_v(x)^2 + \sigma_v(y)^2 + \sigma_v(z)^2$. If the random motion is isotropic, then each of the components of the velocity dispersion are equal: $\sigma_v(x) = \sigma_v(y) = \sigma_v(z)$, so that $\sigma_v^2 = 3\sigma_v(x)^2$. The spectropscopcally measured velocity dispersion must be composed in a similar way: $\sigma_v(x,y)^2 = \sigma_v(x)^2 + \sigma_v(y)^2 = 2\sigma_v(x)^2$. To accomodate this, equation (8.4) should be re-written as

$$g(r_m)r_m = \frac{3}{2}\sigma_v(x,y)^2. \tag{8.5}$$

8.3.3 The Effect of Inflow on the Derived Gravity

One of the primary assumptions of this method is that the atmospheres of galaxies and clusters are in approximate hydrostatic equilibrium. It is required because the flow velocity of the gas is difficult to observe. Using numerical simulations it has been possible to study the effect of a growing cooling flow on the gravitational acceleration as derived from the temperature and density of the X-ray emitting atmosphere. In these simulations the gravitational field does not change in time. As a result, the derived gravitational field would also be temporally invariant if the velocity terms were not ignored. Fortunately, the results show that ignoring these terms only leads to significant errors when the flow velocity becomes comparable to the sound speed of the atmosphere, as expected. Furthermore, such velocities only arise when a cluster atmosphere is approaching a cooling catastrophe, described in chapter 2. In fact, the derived gravity profile changes negligibly throughout most of the evolution of a cooling flow. Only after a cooling catastrophe has occured does the appearance change noticeably and even then the only significant change is within a small radius of the centre leaving the rest of the profile unaltered. It is clear that full thermal conductivity only delays the time after which the gravity deviates significantly from the true value. Otherwise the profiles are very similar, see figure 8.3.

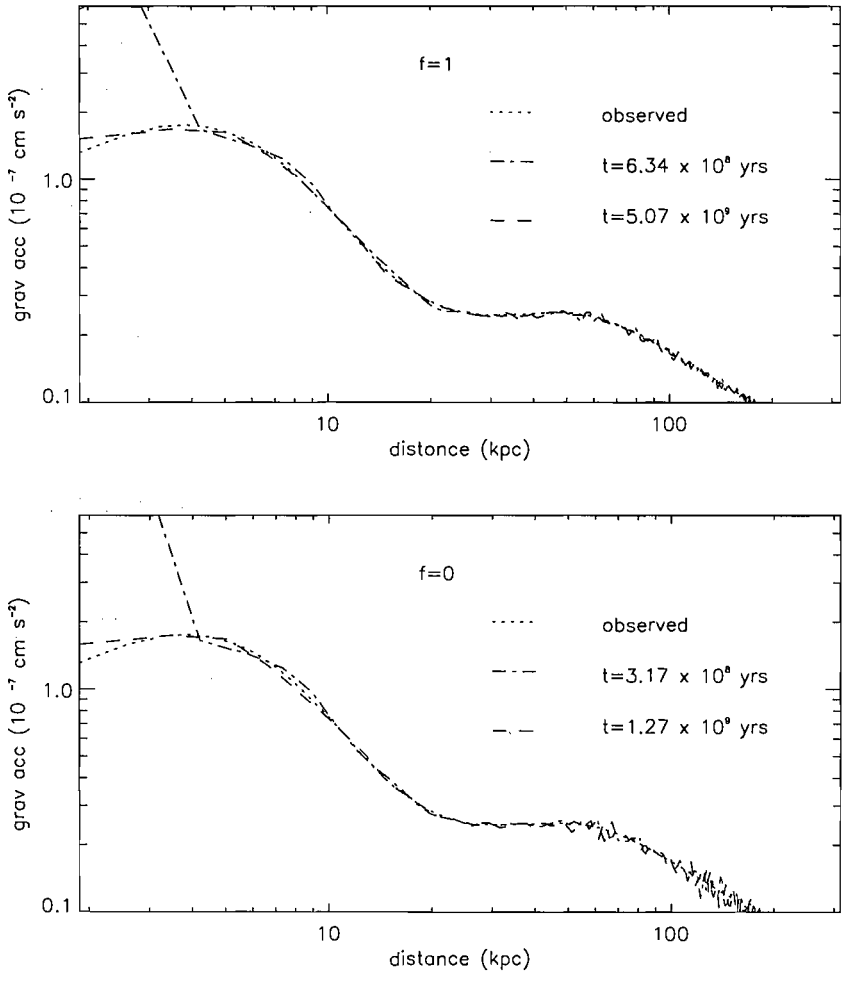

Figure 8.1: The absolute, observed and derived gravitational acceleration profile of the Virgo cluster for simulations which include full thermal conductivity (f=1) and zero thermal conductivity (f=0), where f is the suppression factor previously defined.

8.4 Results and Discussion

8.4.1 Fits to Temperature and Density Data

In the sample used in this section there are 6 objects that were not included in the sample used in chapter 5. These are the galaxy groups: AWM4 and MKW4, and the elliptical galaxies: NGC 4472, NGC 4636, NGC 4649 and NGC 6482. The data for AWM4 and MKW4 were taken from O'Sullivan & Vrtilek (2003), the fits for NGC 4472, NGC 4636 and NGC 4649 were taken from Brighenti & Mathews (1997)

Name	$n_{\rm i}$	$r_{\rm i}$	$\beta_{\rm i}$
AWM4	7.73×10^{-3}, 2.9×10^{-3}	32.1, 128.4	1.5, 1.1
MKW4	0.066	4.71	0.7
NGC 4472	0.095, 0.000597, -0.0004	1.46, 8.14, 85.7	2, 1.14, 1.19
NGC 4636	0.151	1.43	1.57
NGC 4649	0.1, 0.0014	0.91, 18.21	1.8, 3
NGC 6482	0.151, 0.01	0.79, 7.23	0.69, 0.89

Table 8.1: Best-fit parameters of the density profiles for the elliptical galaxies and galaxy groups.

and the fits for NGC 6482 were taken from Khosroshahi et al. (2004).

The density profiles for AWM4, MKW4 and NGC 6482 are described by β-profiles of the form, $\Sigma n_{\rm i}[1+(r/r_{\rm i})^2]^{-\beta}$ while the fits for NGC 4472, NGC 4636 and NGC 4649 are given in terms of slightly different functions $\Sigma n_i[1+(r/r_i)^{\beta}]^{-1}$ where i=0,1,2 etc. The summation sign indicates the the total density is given by the sum of multiple components.

The temperature profile for AWM4 is isothermal and described by $T(r) = T_0$. For MKW4 the temperature profile is given by $T(r) = T_0 - \frac{T_1}{(1+(r/r_{\rm a})^2)^{\alpha}}$. For NGC 4472, NGC 4636 and NGC 4649 the temperature profile is modelled using $T(r) = 2T_0/[1 + (\frac{r_{\rm a}}{r+r_{\rm b}})]$. Finally the temperature profile for NGC 6482 is modelled using $T(r) = T(0)/[1 + (r/r_{\rm a})^2]^{\alpha}$. The values of the density and temperature best-fits are given in table 8.1.

The gravity profiles derived from the fits in table 8.1 are shown in figures 8.2 and 8.3. As an aside, it is interesting to note the different gravitational acceleration profiles for each of the clusters and groups. In some cases the central peak is large and close to the centre while a peak that has a lower magnitude is sometimes further from the centre. In some cases, notably the Perseus cluster, there is a secondary peak at larger radii ($\sim$ 50 kpc) which is probably due to the dark matter gravitational potential of the cluster. However, the maxima which occur at radii between 3 to 30 kpc are assumed to be attributable to the gravity of the central galaxy rather than

Name	T_0	T_1	r_a	r_b	α
AWM4	2.55	-	-	-	-
MKW4	2.76	1.41	53.5	-	-
NGC 4472	0.75	-	4.29	6.43	-
NGC 4636	0.54	-	3.95	4.99	-
NGC 4649	0.9	-	24.3	24.3	-
NGC 6482	0.7	-	3.4	-	0.111

Table 8.2: Best-fit parameters of the temperature profiles for the elliptical galaxies and galaxy groups.

to the cluster.

8.4.2 Velocity dispersion estimates

Using equation (8.5) and figures 8.2 and 8.3 the stellar velocity dispersions can be estimated and are given in table 8.3.

If the gravitational method is to be at all valuable or predictive then r_m should be outside the most central data point derived from the X-ray observations. This is because it is essentially impossible to say, with any certainty, what is happening at locations inside the most central data point. This is always the case, for this sample of 12 objects. The inner most data point are given in table 8.4 along with the redshift of each system.

The results in table 8.3 indicate that for the galaxy clusters, the best agreement between the different velocity dispersion estimates occurs for M87, in the Virgo cluster. The agreement is also within 15% for A2597 while the largest difference occurs for A1795 where there is a 40% difference although Hydra-A is close behind. However, the agreement is within a factor of 2 for all the clusters in this sample.

For the elliptical galaxies, the agreement seems better than for the central cluster galaxies. The largest difference is roughly 30%, for both NGC 4649 and 6482,

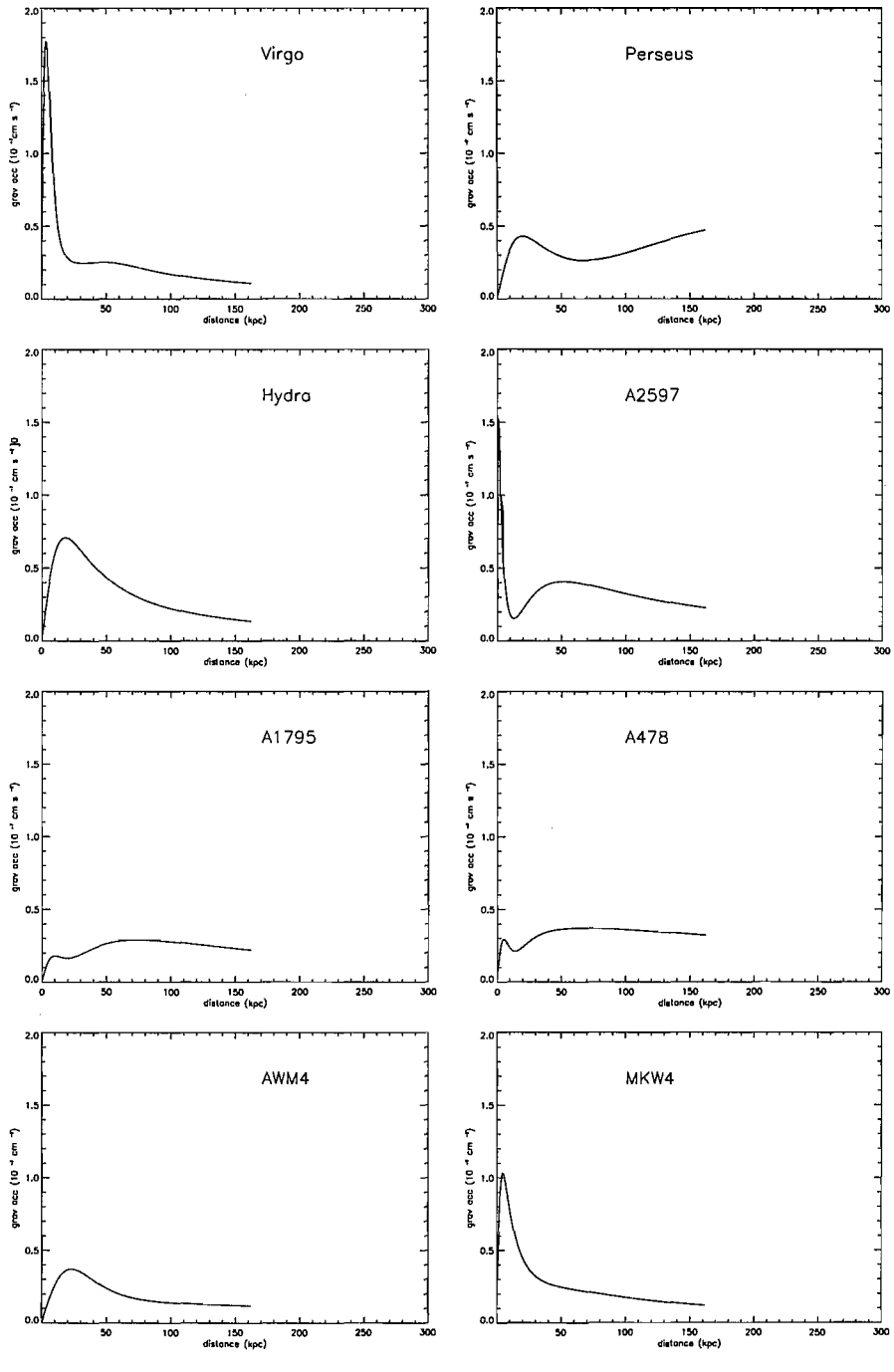

Figure 8.2: Absolute gravitational acceleration profiles for 8 clusters and groups.

Name	$g(\mathrm{m})(10^{-8}\mathrm{cm\,s^{-2}})$	$r_\mathrm{m}/10\mathrm{kpc}$	$\sigma_{\mathrm{v,g}}(\mathrm{km\,s^{-1}})$	$\sigma_\mathrm{v}(\mathrm{km\,s^{-1}})$	$\sigma_\mathrm{v}/\sigma_{\mathrm{v,g}}$
Virgo	17.7	0.36	368	355	0.96
Perseus	4.3	2	419	272	0.65
Hydra	7.1	1.8	514	308	0.60
A2597	15	0.1	178	206	0.86
A1795	1.8	1.0	176	297	1.69
A478	2.95	0.51	175	-	-
AWM4	3.7	2.3	419	264	0.63
MKW4	10	0.4	313	226	0.72
NGC 4472	28.0	0.156	300	303	1.01
NGC 4636	14.9	0.12	192	207	1.08
NGC 4649	39.5	0.081	255	339	1.33
NGC 6482	29.6	0.075	215	286	1.33

Table 8.3: Comparison of spectroscopic and gravitationally determined stellar velocity dispersions. σ_v is the spectroscopic value of the stellar velocity dispersion and $\sigma_{\mathrm{v,g}}$ is the value determined by the gravitational method.

Name	$r_\mathrm{min}/\mathrm{kpc}$	z
Virgo	1	0.0042
Perseus	3	0.0176
Hydra	3	0.2
A2597	4	0.085
A1795	1	0.062
A478	3	0.088
AWM4	3	0.032
MKW4	2.9	0.02
NGC 4472	0.22	0.0033
NGC 4636	0.21	0.00316
NGC 4649	0.19	-
NGC 6482	0.54	0.013

Table 8.4: Location of most central data point and object redshift. The redshifts are taken from the SIMBAD database.

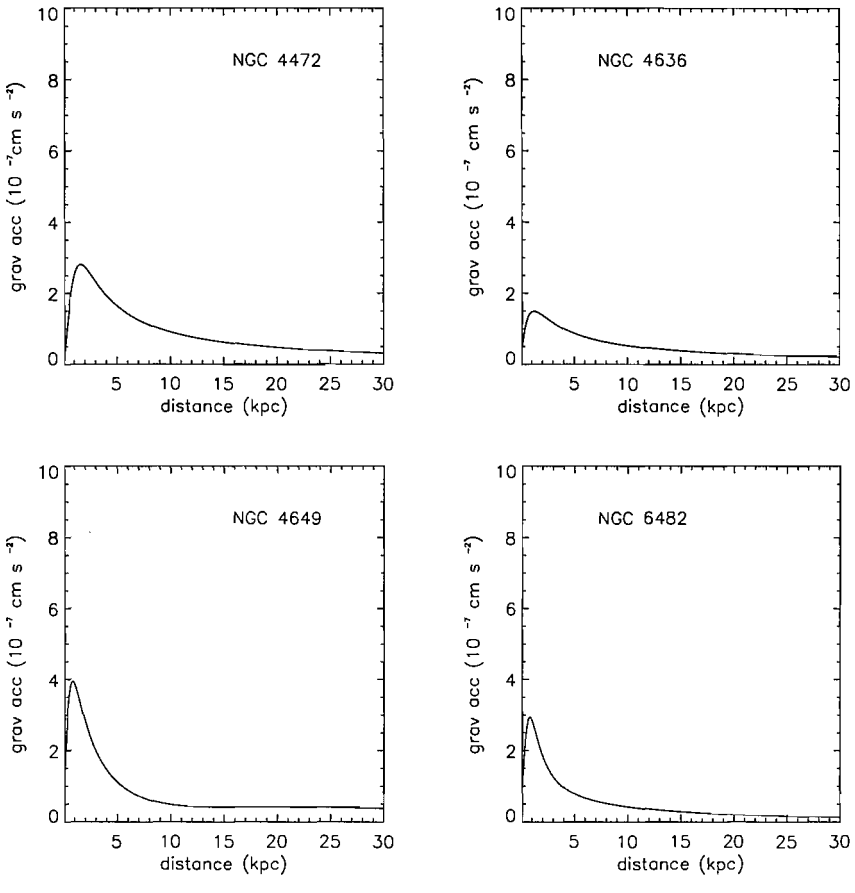

Figure 8.3: Absolute gravitational acceleration profiles for 4 elliptical galaxies.

while for NGC 4472 and NGC 4636 the agreement is better than 10 %. While the agreement is clearly not perfect, especially for the black holes of galaxies located at the centres of clusters, it seems that the gravitational estimate can provide an estimate, in the absence of other methods, of the stellar velocity dispersion at high redshifts.

A possible reason for the lack of good agreement for some of the clusters galaxies could be that some are currently experiencing either extremely powerful outflows from the central AGN or are undergoing mergers or collisions. Such energetic events could render the hydrostatic approximation less meaningful than for a relaxed cluster. For example, the galaxy group AWM4 is currently experiencing an AGN outburst and exhibits the rare characteristic of having an apparently isothermal atmosphere (O'Sullivan & Vrtilek, 2003). Hydra-A is a well known radio source

(David et al., 2001) that appears to be injecting energy at a greater rate than the cooling losses within the cooling radius (Pope et al., 2006). A very powerful outburst is likely to cause the ICM to expand rapidly; effectively the ICM is flowing outwards. In addition, the elongation of the X-ray surface brightness along the jet axis could also result in misleading density and temperature profiles even after being azimuthally averaged.

There is significant evidence that the Perseus cluster is currently experiencing some disturbances near the cluster centre (e.g. Churazov et al., 2003). One possibility is that the central galaxy, NGC 1275, may be oscillating around the centre of the gravitational potential and stirring the gas. This could cause the density and temperature profiles to exhibit larger scale heights than they would if they were in hydrostatic equilibrium.

Each of the possibilities listed above is likely to result in an over-estimate of the stellar velocity dispersion since, although the magnitude of the peak in the gravitational acceleration might not change, elongated temperature or density profiles will cause the location of the gravitational peak to migrate to larger radii. Indeed it is interesting to note that Hydra-A shows nearly the worst agreement between the two methods, but also has the most powerful radio source in the sample.

Alternatively, the effect of a strong cooling flow could cause the scale heights of the density and temperature profiles to appear smaller. This would cause the location of the gravity peak to occur at smaller radii and thus a reduced estimate of the central stellar velocity dispersion. Perhaps this is the reason that the gravitational estimate of the stellar velocity dispersion in A1795 is smaller than expected. It is interesting to note that an observable signature of rapid inflow is likely to be a large difference in temperature, of the ICM, between the centre of the cluster and the maximum temperature. at large radii. The temperature near the centre of A1795 is roughly 2.1 keV, while the maximum temperature, at large radii, is roughly 7 keV. The temperature difference is even larger for A478, being 2.1 keV in the centre and reaching roughly 9 keV at larger radii. This temperature difference is significantly

larger than that in the Virgo cluster where the central temperature is roughly 1.63 keV and the maximum temperature is only 2.4 keV.

Since there is no spectroscopic estimate of the stellar velocity dispersion available, that I am aware of, for A478, the low value cannot be ruled out as inaccurate. However, the gravitational estimate of the stellar velocity dispersion, for A1795, is much lower than the spectroscopic value and could be an indication of the problem highlighted above. On a contradictory note, it is perfectly possible that a large temperature difference between the central and outer regions of a galaxy cluster is not an indication that there is a rapid inflow of material. This configuration could be as stable as any other. The reason for suggesting that it may signify a rapid inflow is based on analytical estimates and numerical simulations in which cooling dominates over heating and leads to a significant drop in the central temperature.

8.4.3 Implied black hole masses

The central stellar velocity dispersion can be used to estimate the mass of the supermassive black hole at the centre of a galaxy using the $M_{\rm bh} - \sigma_{\rm v}$. However, as yet, it is not clear that the $M_{\rm bh} - \sigma_{\rm v}$ relation applies particularly well to black holes located in BCGs. This is largely because clusters are very distant objects, making it almost impossible to directly measure the black hole masses. Where there have been independent estimates, the black holes at the centres of the Virgo and Cygnus clusters seem to be significantly more massive than expected from the $M_{\rm bh} - \sigma_{\rm v}$ relation (Fujita & Reiprich, 2004). After a description of how to estimate black hole masses using the gravitational method, I present an outline of some of the different processes which could affect black hole masses, in different environments.

Currently, black hole masses can be estimated by several different methods. Some of these are empirical, such as the $M_{\rm bh} - \sigma_{\rm v}$ relation while others such as reverberation mapping are more direct. Reverberation mapping is a technique which utilises the time-delay between variations in the continuum output and the response in the line-

emitting regions of AGN. It can be used to estimate the Virial mass within the broad-line region (e.g. Peterson, 1997; Onken et al., 2004; Peterson, 1993) which is assumed to be related to the mass of the black hole at the centre of the galaxy. However, as the redshift of the object increases so do relativistic effects such as time-dilation. This means that variations in the AGN output are slower. Furthermore, AGNs at high redshifts are often extremely luminous, this makes the broad-line region larger further increasing the time required to make time-delay measurements. Despite the fact that reverberation mapping black hole mass estimates can be used for relatively high-redshift object ($z \lesssim 0.4$), there do not seem to be any estimates for black holes in BCGs.

The $M_{\rm bh} - \sigma_{\rm v}$ relation can be applied, under the assumption that it applies sufficiently well to all galaxies, regardless of their environment. The $M_{\rm bh} - \sigma_{\rm v}$ given by Fujita & Reiprich (2004) is,

$$M_{\rm bh} = 1.318 \times 10^8 \left(\frac{\sigma_{\rm v}}{200 {\rm km\,s^{-1}}} \right)^{3.75} M_{\odot}. \tag{8.6}$$

If black holes in BCGs are well described by the $M_{\rm bh} - \sigma_{\rm v}$ relation then the gravitational method could be used to estimate the black hole masses of extremely distant objects, via the $M_{\rm bh} - \sigma_{\rm v}$ relation,

$$M_{\rm bh} = 3.79 \times 10^7 \left(\frac{g_{\rm m}}{10^{-8} {\rm cms^{-2}}} \right)^{1.875} \left(\frac{r_{\rm m}}{10 {\rm kpc}} \right)^{1.875} M_{\odot}. \tag{8.7}$$

Clearly, any errors in the gravitational estimate of the stellar velocity dipsersion will be magnified by equation (8.7). Therefore, the factor of 2 difference between the gravitational method and the spectroscopic method for determining the stellar velocity dispersion could lead to black hole mass estimates that are different by a factor of roughly 10. A comparison of the black hole mass estimates is given in table 8.5. As with the stellar velocity dispersion estimates, the agreement is very good for Virgo, A2597, NGC 4472 and NGC 4636. The worst discrepancy occurs

Name	$M_\sigma(10^8 M_\odot)$	$M_{g,r}(10^8 M_\odot)$
Virgo	$11.4^{+3.2}_{-2.6}$	12.97
Perseus	$4.2^{+5.0}_{-2.6}$	21.1
Hydra	$6.8^{+4.2}_{-2.9}$	45.4
A2597	$1.5^{+3.2}_{-2.6}$	0.9
A1795	$6.0^{+1.7}_{-1.4}$	0.8
A478	-	0.8
AWM4	3.7	21.1
MKW4	2.1	7.1
NGC 4472	6.25	6.0
NGC 4636	1.50	1.1
NGC 4649	9.53	3.3
NGC 6482	5.0	1.7

Table 8.5: Comparison of the black hole mass estimates. M_σ is the mass estimate using the spectropscopc value of the stellar velocity dispersion and $M_{g,r}$ is the mass estimate using the gravitational method.

for A1795 closely followed by Hydra, but the difference between the two methods is never worse than a factor of 7.5. Comparing the results with the redshifts in table 8.4 suggests that the agreement is better for closer objects, as expected.

Interestingly, the gravitational method of determining the stellar velocity dispersion, and hence the black hole mass, may be distantly related to an alternative which proposes that the mass of a black hole can be estimated from the Sersic index that describes the surface brightness profile of a galaxy's bulge (Graham & Driver, 2006). Presumably, the surface brightness of the galaxy reflects the underlying gravitational potential. Therefore, it is possible that the two methods are similar.

8.4.4 The effect of mergers

To determine whether equation (8.6) can be applied to BCGs, it is necessary to consider the effects of galaxy environment on the stellar velocity dispersion and the

black hole mass. The question of the effect of the environment on a galaxy is an important one. For example, galaxies located at the centres of clusters are not only near the centre of a massive cooling flow but also experience comparatively frequent mergers. Clusters grow by the gravitational merging of smaller clusters and groups (Sarazin, 2002). The same is true, on a smaller scale, for galaxies. Chandrasekhar (1942) showed that a massive object moving through a distribution of lighter, collisionless particles suffers a drag force, known as dynamical friction. Dynamical friction slows down the more massive galaxies near the centre of a spherical clusters. Massive galaxies that spiral into the cluster centre will eventually merge to form a single giant galaxy, if they are not tidally disrupted first (Sarazin, 1986). This is thought to be the mechanism by which cD galaxies form since they have several properties which distinguish them from ordinary massive elliptical galaxies. These galaxies are defined by Matthews et al. (1964) as galaxies with the nucleus of a very luminous elliptical galaxies embedded in an extended amorphous halo of low surface brightness.

The effect that mergers could have on the $M_{\rm bh} - \sigma_{\rm v}$ relation can be investigated using a simple model. Following the work of Nipoti et al. (2003), assume that a galaxy of mass M_1 with stellar velocity dispersion $\sigma_{\rm v,1}$ collides and merges with a galaxy of mass M_2 with stellar velocity dispersion $\sigma_{\rm v,2}$. The merger is assumed to be dissipationless, the kinetic energy of the galaxy merger is assumed to be much less than the internal energy and no mass is lost from the system. Conserving energy, the final velocity dispersion must be,

$$\sigma^2_{\rm v,tot} = \frac{M_1\sigma_1^2 + M_2\sigma_2^2}{M_1 + M_2}. \tag{8.8}$$

According to equation (8.8), the final velocity dispersion must be $\sigma^2_{\rm v,tot} \leq \max(\sigma^2_{\rm v,1}, \sigma^2_{\rm v,2})$. Thus, if the kinetic energy of the merger is not taken into account and mass is not lost from the system then the stellar velocity dispersion cannot increase. The classical mass of a black hole formed by the merger of the two others is $M_{\rm bh,tot} = M_{\rm bh,1} + M_{\rm bh,2}$, where no gravitational waves are emitted, or $M^2_{\rm bh,tot} = M^2_{\rm bh,1} + M^2_{\rm bh,2}$ for maximally

efficient radiative merging. In either case the black hole mass will increase, while the stellar velocity dispersion appears not to. This means that black holes at the centres of BCGs could be more massive, for a given stellar velocity dispersion, than the $M_{\rm bh} - \sigma_{\rm v}$ relation would suggest.

The following extends the work of Nipoti et al. (2003). If the kinetic energy of the collision is taken into account the results are slightly different. Consider the example where a static mass M_1 merges with mass M_2 that has a systemic velocity of v. Equation (8.8) becomes,

$$\sigma^2_{\rm v,tot} + v^2_{\rm tot} = \frac{M_1\sigma_1^2 + M_2(v^2 + \sigma_2^2)}{M_1 + M_2}, \tag{8.9}$$

where $v_{\rm tot}$ is the systemic velocity of the final galaxy. Conserving momentum reveals that $v_{\rm tot} = v/2$, for an equal mass merger. Then, if the systemic velocity is assumed to equal the stellar velocity dispersion, $\sigma^2_{\rm v,tot} = 5\sigma^2_{\rm v,1}/4$ while $M_{\rm bh,tot} = 2M_{\rm bh,1} = 2M_{\rm bh,2}$ or $M_{\rm bh,tot} = \sqrt{2}M_{\rm bh,1}$. This means that, for equal mass mergers where the velocity of the collision is important, a black hole can become less massive than the $M_{\rm bh} - \sigma_{\rm v}$ relation predicts.

Note that this simple model assumes the sizes of the galaxies remain the same. An alternative is to estimate the change in size from energy conservation considerations.

It is also instructive to investigate the effect of several non-equal mass mergers where the velocity of the collision is still important. Again, for simplicity it is assumed that the mass of the satellite galaxy, M_2, is the same for every merger, as are its stellar velocity dispersion and the systemic velocity with respect to a fixed frame of reference. In this model it is also necessary to take into account the velocity of both the dominant (more massive) galaxy in the merger and the final galaxy.

This model can be simply described in terms of a sequence. For the Nth merger the total mass of the final galaxy is $(N+1)M_2$, since the accreted galaxies all have the same mass. The mass of the dominant galaxy, in the Nth merger, is NM_2 and

has both systemic velocity and velocity dispersion determined by the $(N-1)$th merger which are written $\sigma_{\mathrm{v,N-1}}$ and $v_{\mathrm{N-1}}$, repsectively. $\sigma_{\mathrm{v,N-1}}$ and $v_{\mathrm{N-1}}$ are the properties of the dominant galaxy after the previous merger.

The satellite galaxies are assumed to alternate their direction of approach to the dominant galaxy with each merger. Since the dominant galaxy is initially stationary, all of the mometum comes from the satellite. Therefore, the effect of bombarding the dominant galaxy on alternate sides with galaxies of identical mass and velocity has the effect of cancelling out the motion induced by the previous collision. Otherwise, after many mergers the final galaxy would be moving with significant velocity in the same direction as the satellites, having effectively been booted out of the cluster! In reality the direction from which each satellite approaches is likely to be more or less random.

Using the above, the Nth final velocity dispersion can be written as a series in terms of the previous value,

$$(N+1)\sigma^2_{\mathrm{v,N}} + v^2_{\mathrm{tot}} = N\left(\sigma^2_{\mathrm{v,N-1}} + v^2_{\mathrm{N-1}}\right) + (\sigma^2_{\mathrm{v,1}} + v^2). \tag{8.10}$$

The velocity of the final galaxy is calculated by conserving linear momentum and can be written as,

$$(N+1)v_{\mathrm{tot,N}} = Nv_{\mathrm{tot,N-1}} - v(-1)^N \tag{8.11}$$

where $(-1)^N$ alternates the direction of the approaching satellite galaxy.

Equations (8.10) and (8.11) can be solved numerically to investigate the effect of mergers on the stellar velocity dipsersion. Deviation away from the $M_{\mathrm{bh}}-\sigma_{\mathrm{v}}$ relation can be deduced by plotting $[M_{\mathrm{bh,N}}/M_{\mathrm{bh,1}}]/[\sigma^4_{\mathrm{v,N}}/\sigma^4_{\mathrm{v,1}}]$. Essentially, this amounts to comparing the coefficients which describe the relation at $M_{\mathrm{bh,1}}$ and $\sigma_{\mathrm{v,1}}$ with that at $M_{\mathrm{bh,N}}$ and $\sigma_{\mathrm{v,N}}$. [1] This was done for both classical and maximally radiative merging

[1] In the limit of no deviation $[M_{\mathrm{bh,N}}/M_{\mathrm{bh,1}}]/[\sigma^4_{\mathrm{v,N}}/\sigma^4_{\mathrm{v,1}}] = 1$.

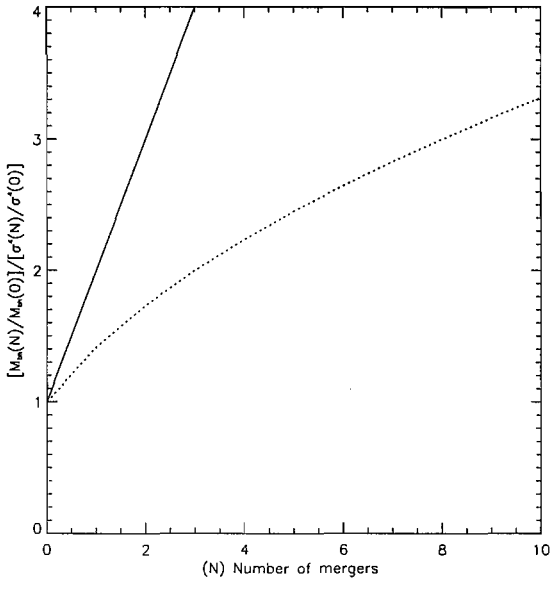

Figure 8.4: Deviation of the $M_{\rm bh} - \sigma_{\rm v}$ relation for mergers where the velocity of the satellite is $v = 0$. Solid line indicates classical black hole mergers and dashed line indicates maximally radiative black hole mergers.

of the black holes. The results are shown in figures 8.4, 8.5 and 8.6 for both black hole merging mechanisms and three different systemic velocities of the satellite. Figure 8.4 shows the results when the satellite's velocity is negligible. Figure 8.5 shows the results when the satellite's velocity is equal to its stellar velocity dispersion and figure 8.6 shows the results when the satellite velocity is equal to $\sqrt{3}$ times the stellar velocity dispersion.

Clearly, the velocity of the collision is important, as is the mechanism by which black holes merge. For maximally radiative merging of black holes, deviation away from the $M_{\rm bh} - \sigma_{\rm v}$ relation is small over a few 10s of non-equal mass mergers. In contrast, for classically merging black holes, the deviation is considerably larger. An interesting property of the maximally radiating black hole mergers is that for equal mass mergers the deviation of the $M_{\rm bh} - \sigma_{\rm v}$ relation results in a less massive black hole than the relation suggests. In contrast, for non-equal mass mergers, the effect is to make the black holes more massive than the $M_{\rm bh} - \sigma_{\rm v}$ relation suggests. Over the course of 10 mergers these effects can roughly cancel each other and lead to minimal deviation away from the usual $M_{\rm bh} - \sigma_{\rm v}$ relation. As a result it seems that

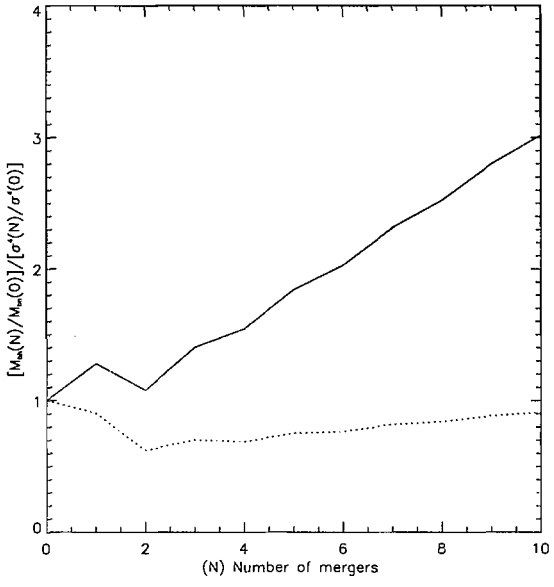

Figure 8.5: Deviation of the $M_{\rm bh} - \sigma_{\rm v}$ relation for mergers where the velocity of the satellite is $v = \sigma_{\rm v,1}$. Solid line indicates classical black hole mergers and dashed lineindicates maximally radiative black hole mergers.

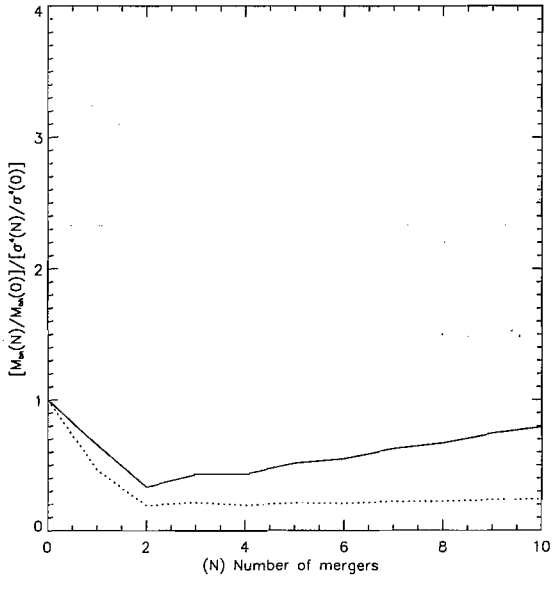

Figure 8.6: Deviation of the $M_{\rm bh} - \sigma_{\rm v}$ relation for mergers where the velocity of the satellite is $v = \sqrt{3}\sigma_{\rm v,1}$. Solid line indicates classical black hole mergers and dashed line indicates maximally radiative black hole mergers.

mergers with maximally radiating black hole merging can preserve the $M_{\rm bh} - \sigma_{\rm v}$ relation to good accuracy.

An important effect that has been neglected here is mass loss through tidal disruption. This can increase the stellar velocity dispersion for equal mass mergers, but was not taken into account because of the difficulty in estimating the mass and kinetic energy lost in tidal disruptions. Another important effect could be accretion on to the black hole induced by the merger. However, to study this in any detail would require detailed numerical simulations.

8.4.5 The effect of accretion

Mergers are not the only mechanism by which black holes can grow; an alternative is accretion. For the accretion process implied by analysis of the radio-loud fraction in chapter 6, it is possible to naively estimate the growth rate of the supermassive black hole. The accretion rate for Bondi accretion from a cooling flow is,

$$\frac{{\rm d}m}{{\rm d}t} = G\mu m_{\rm p}\frac{k_{\rm b}T}{\Lambda(T)}M_{\rm bh}. \tag{8.12}$$

In reality only a fraction, a, of this material will actually be swallowed by the black hole. Solving the differential equation to find the time evolution of the black hole mass gives,

$$M_{\rm bh}(t) = M_{\rm bh,0}\exp\left(aG\mu m_{\rm p}\frac{k_{\rm b}T}{\Lambda(T)}t\right), \tag{8.13}$$

assuming that at $t = 0, M_{\rm bh} = M_{\rm bh,0}$.

The temperatures of galaxy cluster atmospheres can be a factor of a few higher than for elliptical galaxies. Consequently, it is not unreasonable to expect that the mass of a black hole at the centre of a field elliptical to be less than that in an otherwise identical BCG. The ratio of the black hole masses in this case would

be $M_{\rm bh,cluster}/M_{\rm bh,field} = \exp\left(aG\mu m_{\rm p}k_{\rm b}t[T_{\rm cluster}/\Lambda(T_{\rm cluster})] - [T_{\rm field}/\Lambda(T_{\rm field})]\right)$. If $T_{\rm cluster} = 3 \times 10^7$K, $T_{\rm field} = 5 \times 10^6$K, $a = 0.5$, $t = 10^{10}$years and the emission is dominated by thermal bremsstrahlung, $M_{\rm bh,cluster}/M_{\rm bh,field} \approx 9$.

In this scenario it is insufficient to only consider the effect of higher accretion rates on the black hole mass. The accretion rates could also affect the entire core of the galaxy and therefore the stellar velocity dispersion.

The gravitational potentials of elliptical galaxies are often approximated by a self-gravitating isothermal sphere. In this case, the density can be written,

$$\rho(r) = \frac{\sigma_{\rm v}^2}{2\pi G r^2} = \rho_0 \left(\frac{r_0}{r}\right)^2, \tag{8.14}$$

which means,

$$2\pi G \rho_0 r_0^2 = \sigma_{\rm v}^2. \tag{8.15}$$

Within the core radius, r_0, the initial mass is the volume integral of the density within this region $M_0 = 4\pi\rho_0 r_0^3$. As time passes and material is accreted into the core region, the core mass will increase: $M(t) = M_0 + \int \dot{m} dt$. If the core radius remains roughly constant, then the central density, ρ_0, will increase with time, according to $\rho_0(t) = M(t)/(4\pi r_0^3)$. Substituting into equation (8.15) for $\rho_0(t)$ gives the stellar velocity dispersion as a function of time,

$$\sigma_{\rm v}^2(t) = \sigma_{\rm v,0}^2 \left(1 + \frac{\int \dot{m} {\rm d}t}{M_0}\right), \tag{8.16}$$

where $\sigma_{\rm v,0}^2 = GM_0/(2r_0)$ is the initial stellar velocity dispersion before accretion started to alter it.

If $M_{\rm bh,cluster}/M_{\rm bh,field} \approx 9$, then for the cluster black hole to lie exactly on the $M_{\rm bh} - \sigma_{\rm v}$ relation requires that $1 + \frac{\int \dot{m} dt}{M_0} \approx 3$ after $t = 10^{10}$years. This implies that over the specified time, accretion from a cooling flow must increase the mass in the core of the galaxy by a factor of 3 to be consistent with the $M_{\rm bh} - \sigma_{\rm v}$ relation. This

example also requires the stellar velocity dispersions at the centres of these galaxies to increase by a factor of greater than 1.7. In this case, the accretion rate required to cause such an increase is roughly $2M_0/t$, where $t = 10^{10}$years, to agree with the original calculation.

Using $g_m = GM_0/r_m^2$ to estimate M_0 for the elliptical galaxies in table 8.3, it seems that a typical value of M_0 is a few $\times 10^{10} M_\odot$. This implies that the required accretion rates into the galaxy core are a few solar masses per year. Such accretion rates are comparable to, but generally less than, both the classical cooling flow and spectroscopically determined mass flow rates in galaxy clusters. These accretion rates definitely allow the possibility that black holes at the centre of clusters could lie of the same $M_{bh} - \sigma_v$ relation as black holes in field elliptical galaxies.

Despite the fact that maintaining the $M_{bh} - \sigma_v$ relation is physically possible in galaxy clusters, it is very difficult to determine whether this actually does happen. For example, one of the problems in accreting material from a cooling flow is getting rid of the angular momentum in order for the material to penetrate to sufficiently small radii. Alternatively, perhaps this means that it is less of problem for material to reach the galaxy core than to reach the black hole at the very centre of the galaxy. Furthermore, although the mass deposition rates within the cooling radius exceed the required accretion rates it is not clear that sufficient material would necessarily reach the galaxy core. For example, a significant fraction might remain at large radii and never reach the galaxy, while another sizeable fraction could stagnate around the 'edge' of the galaxy where recent star formation is observed.

It should also be noted that it is entirely possible that the effect of the cluster atmosphere on the accretion rate is actually significantly less than estimated here. For example, the fraction of the material swallowed by the black hole could be significantly less than 0.5. Or Bondi accretion from a cooling flow may only apply for a relatively small fraction of the time and is interspersed between long periods of a much lower accretion rate. In all of these cases $M_{bh,cluster}/M_{bh,field}$ would be closer to unity. That said, the suggestion that the black hole mass does not significantly

change because of the environment does not preclude the stellar velocity dispersion from increasing due to increased accretion. Interestingly, this would have the effect of making black holes at the centres of clusters less massive than one would expect from the $M_{\rm bh} - \sigma_{\rm v}$ relation.

8.5 Summary

From the temperature and density profiles of the atmospheres of elliptical galaxies and galaxy clusters it is possible to derive the gravitational acceleration as a function of radius. From these, and using the Virial theorem it is possible to estimate the stellar velocity dispersion near the centre of the galaxy.

Estimates of the stellar velocity dispersion, using this method, are in approximate agreement with those measured spectroscopically. However, the agreement is significantly better for field elliptical galaxies than for those at the centres of clusters and is also better for closer objects. In general the values determined from galaxy clusters seem to over-estimate the stellar velocity dispersion. This could be a consequence of AGN activity deforming the atmosphere. A possible explanation for the lower than expected values of the velocity dispersion could be that these clusters are currently in a strong cooling flow and the gas flow velocity near the cluster centre is not negligible.

The effect of galaxy mergers and the wider galactic environment, on black hole mass, have also been considered. It seems that if the kinetic energy of a merger is insignificant, an equal mass merger would make the resultant black hole mass greater than the $M_{\rm bh} - \sigma_{\rm v}$ relation predicts. In contrast, if the kinetic energy of the collision is significant in a equal mass merger, the resultant black hole would be less massive than the $M_{\rm bh} - \sigma_{\rm v}$ relation predicts. The deviation is less if the black holes are assumed to merge with maximum possible gravitational wave emission. Non-equal mass mergers, where the kinetic energy of the collision is important, will increase the black hole mass compared to the value predicted by the $M_{\rm bh} - \sigma_{\rm v}$ relation.

The combined effect of occasional equal mass mergers and frequent non-equal mass mergers could lead to black holes remaining close to the observed $M_{\rm bh} - \sigma_{\rm v}$ relation.

The larger accretion rates which occur in cluster environments probably lead to more massive black holes than in otherwise identical galaxies. This could make the cluster black holes more massive than the $M_{\rm bh} - \sigma_{\rm v}$ relation predicts unless accretion on to the galaxy core also increases the stellar velocity dispersion. Simple estimates suggest that the required mass flow rates to achieve this are roughly a few solar masses per year. This is within the capability of a galaxy cluster, but it is not clear if this actually happens. Thus, it is not impossible that black holes at the centres of BCGs do lie on the $M_{\rm bh} - \sigma_{\rm v}$ relation, but it need not be the case. However, if black holes in BCGs are relatively well described by the $M_{\rm bh} - \sigma_{\rm v}$ relation, then the gravitational determination of the stellar velocity dispersion could provide a method by which the masses of very distant black holes can be estimated.

Chapter 9

Conclusions

The focus of this thesis has been to investigate the effect of thermal conduction and AGN heating on the ICM and the atmospheres of elliptical galaxies using numerical and analytical work, in comparison with observations.

From both hydrodynamic simulations and simple energy balancing arguments, it seems that thermal conduction can, in principle, balance the radiative losses in certain clusters, e.g. the Perseus cluster. Such systems tend to be hotter and more massive clusters than those in which thermal conduction cannot balance the radiative losses. However, results from the simulations show that the observed temperature gradients never develop in such clusters and the temperature profiles stays remarkably flat. This suggests that thermal conduction must be heavily suppressed, in order to allow the observed temperature profiles to form. The same agreement between simulations and energy arguments also applies to (less massive) clusters, such as Virgo, for which thermal conduction proves to be insufficient to balance the radiative losses. In these cases, a generic temperature profiles forms regardless of the value of the thermal conduction thermal conduction. The time taken to form this profile grows with increasing thermal conduction. As a result it seems that thermal conduction is probably suppressed by a large factor, say 100. This means that alternative heating processes are required to balance the radiative losses.

Evidence continues to accumulate that AGNs exert a significant influence on their surroudings. However, simple analytical estimates based on the energy required to inflate the X-ray cavities observed in the ICM, with a dissipation timescale of 100 Myr, seem to suggest that AGNs may not be providing the required energy injection rate. This theory leads to several possibilities. Firstly, it is possible that the energy required to generate a cavity in the ICM has been underestimated. A second possibility is that these AGN are active more frequently than those not at the centres of clusters. However, there are also other possibilities: the AGN may not need to provide 100 % of the required heating all of the time; the heating is likely to be correlated to the radiative losses and quite possibly periodic to some extent. Therefore, at various points the AGN power output should exceed the radiative losses while at other times the reverse will be true. There are also numerous other heating mechanisms, and it is quite possible that the AGN is the last in a long line of heating mechanisms. For example, star formation, galaxy motions, major cluster-cluster mergers and thermal conduction, to some extent, will all be present in galaxy clusters. If the radiative losses exceed the heating provided by the sum of these mechanisms then gas will be accreted onto the supermassive black hole and stimulate an outburst. The power of this outburst will presumeably be correlated with the accretion rate and NOT the bolometric radiative losses. Therefore, the observation that the AGN is not balancing the radiative losses could be true, and explicable by the fact that the AGN does not have to balance the losses all by itself.

The difficulty with this subject is that all of the possibilities listed above are difficult to rule out and could well be occuring. There is also the problem that the alternative heating mechanism are essentially unobservable, with current telescopes. Until an accurate method is found for estimating the energy dissipation rate of X-ray cavities, the question of what fraction of the required energy input is provided by the AGN will still be unanswered. However, it is possible that at least the effect of mergers and galaxy motions can be assessed using cosmological simulations which study the growth of structure in the Universe.

Work done on the fraction of BCGs which are detectable above a particular radio

luminosity suggests that BCGs are active more frequently than AGNs not at the centre of clusters. This work also suggests that the accretion rate in these systems is dominated by Bondi accretion from a cooling flow. Therefore, the accretion rate is a function of both the black hole mass and the environment. If the energy output of the AGN is, in part, determined by the environment, this can be referred to as negative feedback. Damped oscillations are often a signature of negative feedback. Therefore it may be reasonable to expect the AGN power output to also be periodic.

Using 3-d hydrodymamic simulations, the effect of low-power jets is considered for the case of the Virgo cluster. An intriguing property of structures created by low-power jets is that they resemble the cavities observed in real clusters. For example, the structures remain intact for long periods rather than being shredded by fluid instabilities. This somewhat negates the need for magnetic fields which would provide surface tension, or viscosity, to slow the growth of the instabilities.

The property which is probably responsible for this behaviour is probably the back flow of material from the head of the jet. The back flow of material reduces the relative velocity of the cavity with respect to the ambient gas. This can slow the growth of Kelvin-Helmholtz instabilities, at least.

The jets are also able to dramatically slow down or indefinitely postpone the onset of a cooling catastrophe. Because they are relatively weak and only active for a short period, the jets probably deposit a large amount of energy near the cluster centre. This is in contrast to what one might expect for very powerful jets which travel ballistically near the cluster centre and only deposit their energy at larger radii.

When bubbles are produced in quick succession, the most recently formed bubbles quickly catch up with their predecessors thus creating a larger, more amorphous cavity. This is because following bubbles rise in the low-density channel carved out by the leading bubble. As a result, energy is mostly deposited near the leading bubble and not closer to the cluster centre. Therefore, it seems that there is likely

to be some optimum timescale for recurrent AGN outbursts which maximises the energy deposited near the cluster centre.

Simple analytical models, from which the jet power and velocity can be estimated, show results which agree with the simulations. In principle these techniques could be applied to observations, and in some cases they could be used to improve the accuracy of some of the current estimates.

Using the atmospheres of galaxy clusters, it is possible to constrain certain information about the central galaxy. This is because of the shape of the gravitational acceleration near the cluster centre which is indicative of the central galaxy. For clusters at high redshift, estimates of the central stellar velocity dispersion of the central galaxy are usually made from spectroscopic measurements. Obviously with increasing distance, these estimates become worse and for sufficiently distant objects no estimates are available. However, it is shown this in thesis that is also possible to make an independent estimate using the gravitational acceleration profile derived from the temperature and density of the ICM. The benefit of this method is that the gravitational acceleration can be extrapolated all the way to the cluster centre. The value of the stellar velocity dispersion can then be obtained. For systems where there are spectroscopic estimates, the agreement between the spectroscopic and the gravitational methods is better than a factor of two. However, the main use of this method is for systems that do not have a spectroscopic estimates.

Using the gravitational estimates of the stellar velocity dispersion means that one can estimate the mass of the black hole at the centre of the galaxy assuming that the standard relation holds. A simple analysis of galaxy-galaxy mergers suggests that the $M_{\rm bh} - \sigma_{\rm v}$ relation roughly holds if significant amounts of gravitational radiation are released during the merging of the black holes. It also appears possible that the $M_{\rm bh} - \sigma_{\rm v}$ relation is conserved if both the bulge and the black hole grow by accreting mass from the ICM. However, whether the black holes in BCGs really do adhere to this relation can only be answered if the masses can be measured using an independent method.

There are many questions highlighted in this thesis that are still to be answered. For example, the quantity of energy injected by AGNs and just how it is distributed. The issue of how the AGN is triggered is still to be answered. These questions will require the application of more detailed numerical models, ultimately including such effects as turbulence and magnetic fields while resolving distance scales down to the Bondi radius in 3-d simulations. However, there is little point attempting to re-create real life without first understanding the role of each individual process that is included.

Despite these unaswered question progress has been made. For example, it seems that the AGN power output is related to the Bondi accretion from a cooling flow. Other important points to note are that thermal conduction no longer seems viable as a dominant heating mechanism in galaxy clusters and lower-power AGN jets can generate cavities that resemble those observed in real clusters, without the need for magnetic fields.

Acknowledgements

Firstly, I wish to acknowledge the exceptionally helpful and enthusiastic support of my two supervisors: Christian Kaiser and Hans Fangohr. Also the friendship and huge amount of computational expertise provided by Georgi Pavlovski. I also wish to thank Phillip Best for his help.

On a personal note I would like to thank my wonderful parents - I hope you enjoy reading the thesis - my brother, Simon, my sister, Catherine, my grandparents, and Doreen.

It would take far too long to thank everyone who has given me encouragement over the last three years. However, I would like to thank the entire, ever changing, Southampton Astronomy group, but particularly my dear friends: the irreplaceable Jose Luis Galache (+ Karina!) and Vanessa McBride (+ Brent!), but also Colin Ferguson, Matt Dallimore, Grant Crossingham, Sebastian (Boris) Jester, Vito Sguera, Liz Barlow, Ralph (Tony Bird), my office mates, and a few people from outside astronomy: Doug Poole, Abi Pattenden, Richard (Beast) Sinden, Gareth (Krang) Thomas, and anyone else I've missed out!

I would like to say a special thankyou to everyone at the University of Southampton Academics cricket club who, thanks to Andy (Self-love) Hampshire, think that theoretical astrophysics isn't a proper subject! Special thanks go to my fellow cricketing astronomers: Andy (Andre B.) Barnes, Derek Moss and Andy (Withers) Witham, aswell as assorted others: Zak (Wylde) Hussain, Andy (Mullet) Rose, Paul (Fence) Douglas and Alistair (Steptoe) Fitt, and everyone else who came on the August 2006 tour of Kent (and also the previous one in 2005).

I must also thank my friends from my home town of Chelmsford: Ross MacKay, Craig Holliday, Gary Cansell, Julie King, Simon Springett, Geoff and Amanda Munday, (Andy) Currie, and Jamie Bennett who, despite my best efforts, still suspect I've really been doing astrology all these years!

I would like to thank my past office mates: Ross Collins, Aris Kypriotis, Julie-Ann Goodlet and Will Clarkson, for helping me settle in. My final thanks go to my current office mates: Katrine Rogers, Retha (Marge) Pretorius, Omar (O-dawg) Jamil and Stephen (I-Chun) Shih, for being excellent company, putting up with their nicknames, as well as providing a seemingly endless stream of highly dubious topics for debate. I will miss you all.

I must also thank the University of Southampton Escience Centre for funding my PhD.

Chapter 10

Appendix

10.1 Numerical Resolution Convergence

The numerical convergence of the simulations was tested by running simulation 0.01κ with varied spatial resolution. The objective is to compare the evolution of temperature and density profiles for otherwise identical simulations in which the minimum refinement, maximum refinement and region of increased initial resolution in the central region are all increased by one level of refinement. For the size of the computational box employed for these simulations, a refinement level of 9 corresponds to a resolution of 0.31 kpc; a refinement level of 10 corresponds to 0.15 kpc. The initial enhanced resolution of the central region (refinement of 6) corresponds to 2.53 kpc in the central $\sim$16 kpc. The effect of increasing this resolution by one level of refinement, to a resolution of 1.26 kpc, is also investigated. The resolution in the outer regions of the cluster is determined by the minimum refinement level. This is initially set to 3 (corresponding to roughly 20 kpc), but is also tested at level 4 (roughly 10 kpc). The refinement parameters corresponding to each simulation are summarised in table 10.1.

From figure 10.1 it is evident that only for a central resolution of refinement level 6, or lower, do the results differ significantly to any other simulation. In

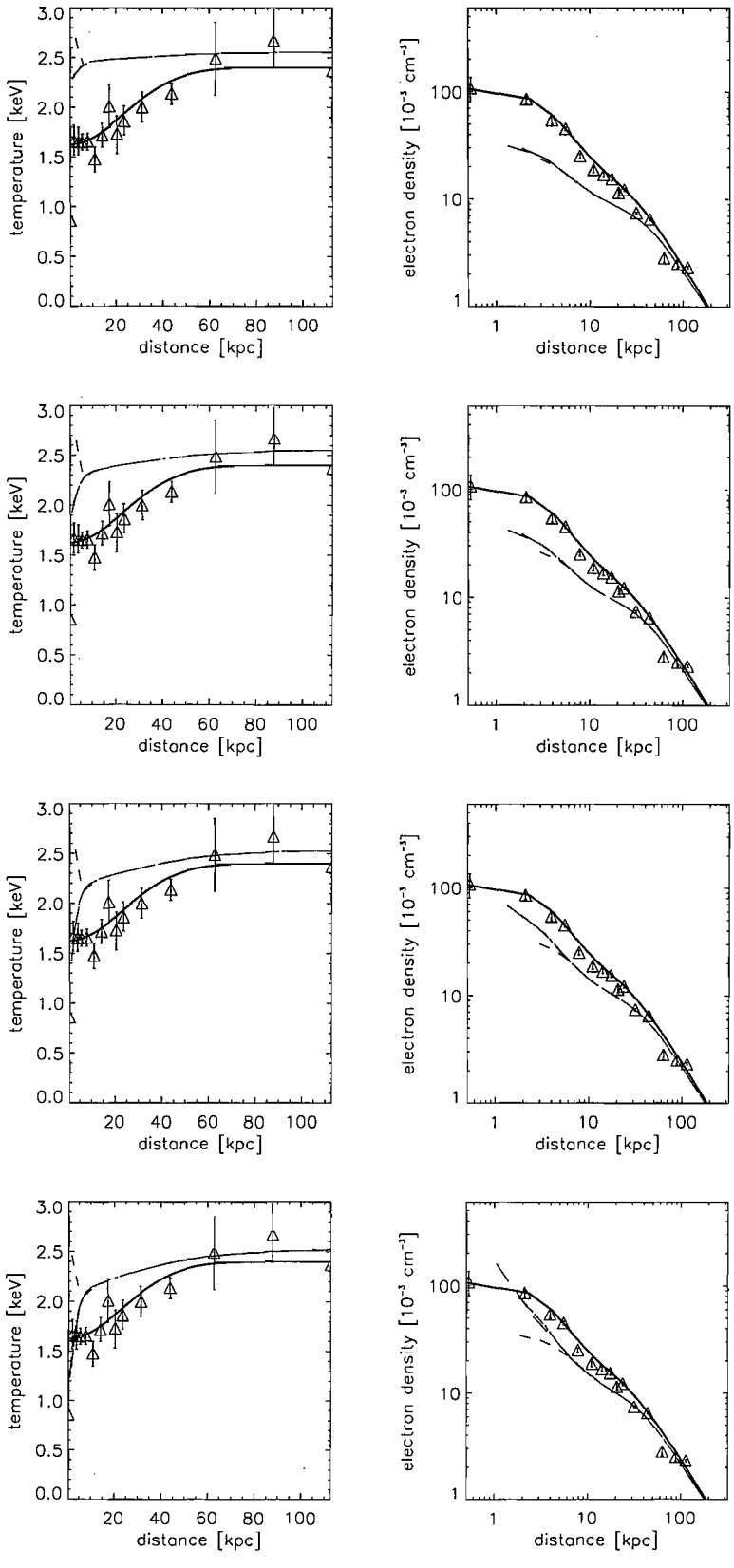

Figure 10.1: Comparison of simulation 0.01κ temperature and density profiles at each of the different numerical resolutions at intervals of 3.16×10^8 yrs starting at 3.16×10^8 yrs. The results for test 1 are shown by dot dashed lines, test 2: dashed, test 3: triple dot dash, test 4: long dash, test 5: dot

Table 10.1: Summary of the refinement parameters of the numerical resolution tests.

Test	Central Refinement	Maximum refinement	Minimum refinement
1	7	9	3
2	6	9	3
3	7	10	3
4	8	9	3
5	7	9	4

this particular case it appears that the central resolution is not sufficient for the inner regions to be in hydrostatic equilibrium when the simulation is initialised. This results in a slight collapse of material near the cluster centre and therefore significant compressional heating. For the other simulations the differences in the temperature and density plots are minimal. The central effective adiabatic index is also unchanged and in good agreement across the range of different resolutions. This series of tests demonstrates that for a central refinement of level 7, a maximum refinement of level 9 and a minimum refinement of level 3 the results are in close agreement with those achieved with higher resolutions.

10.2 Hydrodynamic differences between 3-d and 1-d coordinate systems

This section outlines the differences between a purely spherically symmetric geometry and a full 3-d geometry, for this problem, with the aid of the hydrodynamic equations and trial simulations of the Virgo cluster. For these purposes two of the simulations from the main study have been repeated with i) zero thermal conductivity and viscosity and ii) full Spitzer thermal conductivity and viscosity, in 1-d spherical coordinates, both at the same spatial resolution as the 3-d runs and at higher spatial resolutions. The minimum level of refinement for the 1-d simulation performed at the same spatial resolution as the 3-d runs was 7 corresponding to

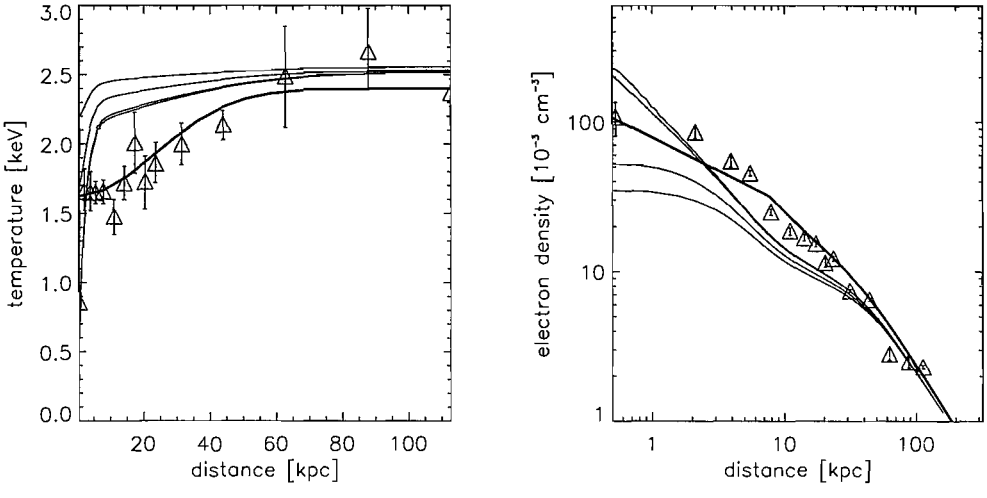

Figure 10.2: Temperature and density profiles evolving with time for simulation 0κ for a 1-d spherically symmetric geometry. The profiles are plotted for the same times as the equivalent temperature and density profiles in section 4.4.1, with the same spatial resolution, except for the final profile which is plotted at 1×10^9yrs.

roughly 1.27 kpc. For the higher spatial resolution 1-d test the minimum refinement was level 9, corresponding to a spatial scale of nearly 0.32 kpc. In both cases the maximum level of the refinement was 12 corresponding to approximately 0.04 kpc.

The results of these 1-d spherically symmetric simulations explicitly show that a cooling catastrophe always occurs in 1-d as well as 3-d. Furthermore, the cooling catastrophe takes less time to evolve in the 1-d spherically symmetric case than the 3-d case and increasing spatial resolution has almost no effect. For the simulation with zero thermal conductivity the cooling catastrophe occurs after approximately 1×10^9yrs-roughly 3×10^8 yrs before the occurance in 3-d. For the simulation with full Spitzer thermal conductivity the cooling catastrophe occurs after roughly 4.2×10^9yrs which is approximately 0.5×10^9yrs less than in the 3-d case (see figures 10.2 and 10.3).

If the differences for simulations using different geometries are real physical effects, rather than numerical errors, then one should also expect to see differences in the equations of hydrodynamics for the 1-d and 3-d cases. Since viscosity enters into

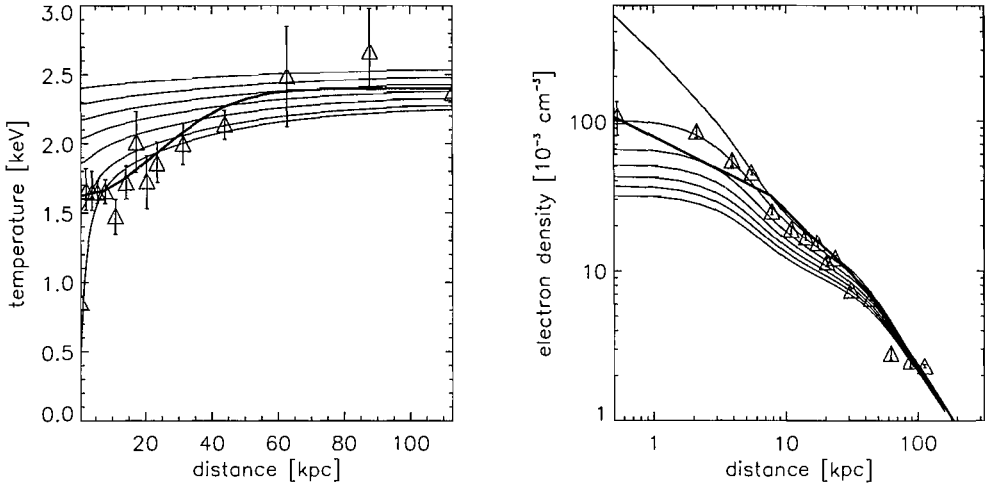

Figure 10.3: Temperature and density profiles evolving with time for simulation 1κ for a 1-d spherically symmetric geometry. The profiles are plotted for the same times as the equivalent temperature and density profiles in section 4.4.1, with the same spatial resolution, except for the final profile which is plotted at 4.2×10^9yrs.

the momentum equation it is an appropriate choice to investigate any differences which may arise due to dimensional effects.

The equation for the viscous force per unit volume is given by (e.g. Sarazin, 1986)

$$\boldsymbol{F}_{\rm vis} = \eta\left(\nabla^2\boldsymbol{v} + \frac{1}{3}\boldsymbol{\nabla}\boldsymbol{\nabla}.\boldsymbol{v}\right), \tag{10.1}$$

where η is the bulk viscosity and v is fluid velocity.

Using the standard vector identity we can substitute for the divergence term

$$\nabla^2\boldsymbol{v} = \boldsymbol{\nabla}(\boldsymbol{\nabla}.\boldsymbol{v}) - \boldsymbol{\nabla}\times(\boldsymbol{\nabla}\times\boldsymbol{v}) \tag{10.2}$$

so that equation (10.1) becomes

$$\boldsymbol{F}_{\rm vis} = \eta\left(\frac{4}{3}\nabla^2\boldsymbol{v} + \frac{1}{3}\boldsymbol{\nabla}\times(\boldsymbol{\nabla}\times\boldsymbol{v})\right). \tag{10.3}$$

Even without the evidence from simulations, from equation (10.3) alone it is evident that viscous processes are different in 3-d and 1-d cases due to shear effects.

In 3-dimensions the term involving the vector products constitutes a mechanism for the dissipation of momentum, whereas in 1-d all vector products are zero, by definition, and so this mechanism is suppressed.

It seems that equation (10.3) is able to account for some of the differences between the 1-d and 3-d simulations in which full Spitzer thermal conductivity and viscosity were present. However, there was also a significant difference in the time at which the cooling catastrophe occured in the simulations in which diffusion processes were not present. Studying the complete momentum equation allows us to investigate these differences.

$$\frac{\partial \boldsymbol{v}}{\partial t} + (\boldsymbol{v}.\boldsymbol{\nabla})\boldsymbol{v} = \boldsymbol{F} - \frac{1}{\rho}\boldsymbol{\nabla}P + \nu\left(\frac{4}{3}\nabla^2\boldsymbol{v} + \frac{1}{3}\boldsymbol{\nabla}\times(\boldsymbol{\nabla}\times\boldsymbol{v})\right), \tag{10.4}$$

where F is the force per unit mass, P is the fluid pressure and ν is the kinematic viscosity.

Using a second standard vector calculus identity for the second term on the left hand side of equation (10.4) gives

$$(\boldsymbol{v}.\boldsymbol{\nabla})\boldsymbol{v} = \frac{1}{2}\boldsymbol{\nabla}(\boldsymbol{v}.\boldsymbol{v}) - \boldsymbol{v}\times(\boldsymbol{\nabla}\times\boldsymbol{v}), \tag{10.5}$$

and substituting into equation (10.4), the total momentum equation is

$$\frac{\partial \boldsymbol{v}}{\partial t} + \frac{1}{2}\nabla(\boldsymbol{v}.\boldsymbol{v}) - \boldsymbol{v}\times(\boldsymbol{\nabla}\times\boldsymbol{v}) = \boldsymbol{F} - \frac{1}{\rho}\boldsymbol{\nabla}P + \nu\left(\frac{4}{3}\nabla^2\boldsymbol{v} + \frac{1}{3}\boldsymbol{\nabla}\times(\boldsymbol{\nabla}\times\boldsymbol{v})\right). \tag{10.6}$$

Since vector products are zero in 1-dimension, equation (10.6) reduces to

$$\frac{\partial v}{\partial t} + \frac{1}{2}\frac{\partial(v^2)}{\partial r} = F - \frac{1}{\rho}\frac{\partial P}{\partial r} + \nu\frac{4}{3}\frac{1}{r^2}\frac{\partial}{\partial r}\left(r^2\frac{\partial v}{\partial r}\right), \tag{10.7}$$

in 1-d spherically symmetric coordinates.

From equation (10.7) it is clear that there is an additional dissipation term in the 3-d case which is not present in 1-d, even in the absence of viscosity. Thus, in agreement with the simulations, it is reasonable to expect the behaviour of a fluid to be different in 1-d compared to 3-d, even in the absence of viscosity.

The overall properties of the simulations, e.g. the temperature and density profiles, remain roughly the same in 1-d spherically symmetric and 3-d coordinates. Therefore, for simulations such as these it seems possible to gain a reasonable estimate of the main properties and timescales for the given circumstances at a lower computational expense than for 3-d simulations. However, in order to gain a more complete understanding of the physical processes at work it is necessary to perform even these basic simulations in 3-d due to the non-spherically symmetric process which may occur in both viscous and inviscid fluid dynamics.

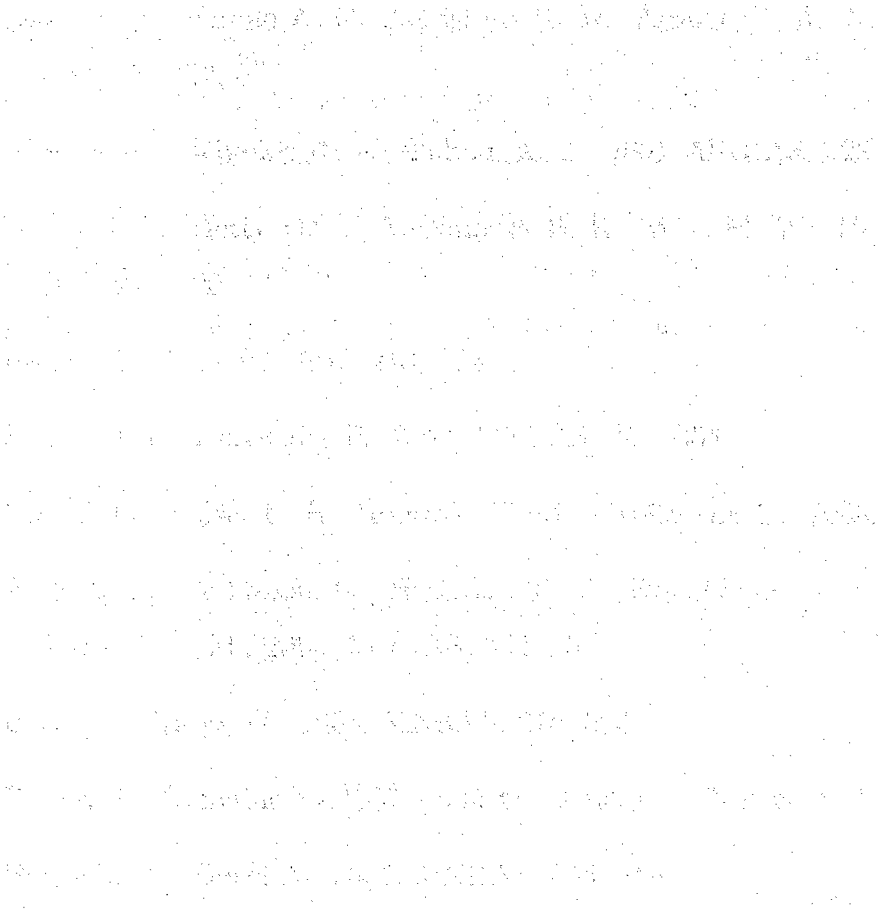

Bibliography

Alexander P., 2002, MNRAS, 335, 610

Allen S. W., Dunn R. J. H., Fabian A. C., Taylor G. B., Reynolds C. S., 2006, ArXiv Astrophysics e-prints

Allen S. W., Fabian A. C., Johnstone R. M., Arnaud K. A., Nulsen P. E. J., 2001, MNRAS, 322, 589

Allen S. W., Schmidt R. W., Fabian A. C., 2001, MNRAS, 328, L37

Bîrzan L., Rafferty D. A., McNamara B. R., Wise M. W., Nulsen P. E. J., 2004, ApJ, 607, 800

Bahcall N. A., 1977, ApJ, 218, L93

Basson J. F., Alexander P., 2003, MNRAS, 339, 353

Best P. N., Kaiser C. R., Heckman T. M., Kauffmann G., 2006, MNRAS, 368, L67

Best P. N., Kauffmann G., Heckman T. M., Brinchmann J., Charlot S., Ivezić Ž., White S. D. M., 2005, MNRAS, 362, 25

Binney J., Tabor G., 1995, MNRAS, 276, 663

Binney J., Tremaine S., 1987, Galactic Dynamics. Princeton University Press

Birnboim Y., Dekel A., 2003, MNRAS, 345, 349

Blanton E. L., 2004, in Reiprich T., Kempner J., Soker N., eds, The Riddle of Cooling Flows in Galaxies and Clusters of galaxies The Interaction of Radio Sources and X-Ray-Emitting Gas in Cooling Flows. pp 181–+

Brüggen M., 2003, ApJ, 593, 700

Brüggen M., Kaiser C. R., 2002, Nat., 418, 301

Brighenti F., Mathews W. G., 1997, ApJ, 486, L83+

Burns J. O., 1990, Bull. Am. Astron. Soc., 22, 821

Carilli C. L., Taylor G. B., 2002, ARA&A, 40, 319

Chandrasekhar S., 1942, Principles of Stellar Dynamics. University of Chicago

Cho J., Lazarian A., Honein A., Knaepen B., Kassinos S., Moin P., 2003, ApJ, 589, L77

Choudhuri A., 1998, The Physics of Fluids and Plasmas, an introduction for astrophyisicists. Cambridge University Press

Churazov E., Brüggen M., Kaiser C. R., Böhringer H., Forman W., 2001, ApJ, 554, 261

Churazov E., Forman W., Jones C., Böhringer H., 2003, ApJ, 590, 225

Churazov E., Forman W., Jones C., Böhringer H., 2003, ApJ, 590, 225

Churazov E., Sunyaev R., Forman W., Böhringer H., 2002, MNRAS, 332, 729

Ciotti L., Ostriker J. P., 2001, ApJ, 551, 131

Cowie L. L., Henriksen M., Mushotzky R., 1987, ApJ, 317, 593

Cowie L. L., McKee C. F., 1977, ApJ, 211, 135

Croton D. J., Springel V., White S. D. M., De Lucia G., Frenk C. S., Gao L., Jenkins A., Kauffmann G., Navarro J. F., Yoshida N., 2006, MNRAS, 365, 11

Dalla Vecchia C., Bower R. G., Theuns T., Balogh M. L., Mazzotta P., Frenk C. S., 2004, MNRAS, 355, 995

David L. P., Nulsen P. E. J., McNamara B. R., Forman W., Jones C., Ponman T., Robertson B., Wise M., 2001, ApJ, 557, 546

Davidsen A., Henry R., Snyder W., Shulman S., Fritz G., Friedman H., 1975, Bull. Am. Astron. Soc., 7, 506

De Young D. S., 2003, MNRAS, 343, 719

Dennis T. J., Chandran B. D. G., 2005, ApJ, 622, 205

Dolag K., Jubelgas M., Springel V., Borgani S., Rasia E., 2004, ApJ, 606, L97

Donahue M., Horner D. J., Cavagnolo K. W., Voit G. M., 2005, ArXiv Astrophysics e-prints

Edge A. C., 2001, MNRAS, 328, 762

Edge A. C., Stewart G. C., Fabian A. C., 1992, MNRAS, 258, 177

Elvis M., Wilkes B. J., McDowell J. C., Green R. F., Bechtold J., Willner S. P., Oey M. S., Polomski E., Cutri R., 1994, ApJ Supp., 95, 1

Ettori S., Fabian A. C., 2000, MNRAS, 317, L57

Ettori S., Fabian A. C., Allen S. W., Johnstone R. M., 2002, MNRAS, 331, 635

Faber S. M., Jackson R. E., 1976, ApJ, 204, 668

Fabian A. C., 1994, ARA&A, 32, 277

Fabian A. C., Allen S. W., Crawford C. S., Johnstone R. M., Morris R. G., Sanders J. S., Schmidt R. W., 2002, MNRAS, 332, L50

Fabian A. C., Celotti A., Blundell K. M., Kassim N. E., Perley R. A., 2002, MNRAS, 331, 369

Fabian A. C., Reynolds C. S., Taylor G. B., Dunn R. J. H., 2005, MNRAS, 363, 891

Falle S. A. E. G., 1991, MNRAS, 250, 581

Fanaroff B. L., Riley J. M., 1974, MNRAS, 167, 31P

Feller W., 1968, An introduction to probability theory and its applications. Wiley, New York

Fender R. P., Maccarone T. J., van Kesteren Z., 2005, MNRAS, 360, 1085

Forman W., Nulsen P., Heinz S., Owen F., Eilek J., Vikhlinin A., Markevitch M., Kraft R., Churazov E., Jones C., 2005, ApJ, 635, 894

Fryxell B., Olson K., Ricker P., Timmes F. X., Zingale M., Lamb D. Q., MacNeice P., Rosner R., Truran J. W., Tufo H., 2000, ApJ Supp., 131, 273

Fryxell B. A., Mller E., Arnett D., 1989

Fujita Y., Reiprich T. H., 2004, ApJ, 612, 797

Fujita Y., Suzuki T. K., Wada K., 2004, ApJ, 600, 650

Fukazawa Y., Botoya-Nonesa J. G., Pu J., Ohto A., Kawano N., 2006, ApJ, 636, 698

Gaetz T. J., 1989, ApJ, 345, 666

Gallo E., Fender R., Kaiser C., Russell D., Morganti R., Oosterloo T., Heinz S., 2005, Nat., 436, 819

Gebhardt K., Kormendy J., Ho L. C., Bender R., Bower G., Dressler A., Faber S. M., Filippenko A. V., Green R., Grillmair C., Lauer T. R., Magorrian J., Pinkney J., Richstone D., Tremaine S., 2000, ApJ, 543, L5

Ghizzardi S., Molendi S., Pizzolato F., De Grandi S., 2004, ApJ, 609, 638

Godunov S., 1959

Graham A. W., Driver S. P., 2006, ArXiv Astrophysics e-prints

Greene J. E., Ho L. C., 2006, ApJ, 641, 117

Heinz S., Brueggen M., Young A., Levesque E., 2006, ArXiv Astrophysics e-prints

Hoeft M., Brüggen M., 2004, ApJ, 617, 896

Johnstone R. M., Allen S. W., Fabian A. C., Sanders J. S., 2002, MNRAS, 336, 299

Kaastra J. S., Tamura T., Peterson J. R., Bleeker J. A. M., Ferrigno C., Kahn S. M., Paerels F. B. S., Piffaretti R., Branduardi-Raymont G., Böhringer H., 2004, A&A, 413, 415

Kaiser C. R., 2003, MNRAS, 343, 1319

Kaiser C. R., Alexander P., 1997, MNRAS, 286, 215

Kaiser C. R., Pavlovski G., Pope E. C. D., Fangohr H., 2005, MNRAS, 359, 493

Kaiser N., 1991, ApJ, 383, 104

Khosroshahi H. G., Jones L. R., Ponman T. J., 2004, MNRAS, 349, 1240

King I., 1962, AJ, 67, 274

Landau L., Lifschitz E., 1995, Fluid Mechanics. Butterworth-Heinemann Ltd

Lea S. M., Silk J., Kellogg E., Murray S., 1973, ApJ, 184, L105+

Loeb A., 2002, New Astronomy, 7, 279

Malyshkin L., Kulsrud R., 2001, ApJ, 549, 402

Markevitch M., Mazzotta P., Vikhlinin A., Burke D., Butt Y., David L., Donnelly H., Forman W. R., Harris D., Kim D.-W., Virani S., Vrtilek J., 2003, ApJ, 586, L19

Mathews W. G., Faltenbacher A., Brighenti F., 2006, ApJ, 638, 659

Matthews T. A., Morgan W. W., Schmidt M., 1964, ApJ, 140, 35

McElroy D. B., 1994, Bulletin of the American Astronomical Society, 26, 1498

McLure R. J., Willott C. J., Jarvis M. J., Rawlings S., Hill G. J., Mitchell E., Dunlop J. S., Wold M., 2004, MNRAS, 351, 347

McNamara B. R., Wise M. W., Nulsen P. E. J., David L. P., Carilli C. L., Sarazin C. L., O'Dea C. P., Houck J., Donahue M., Baum S., Voit M., O'Connell R. W., Koekemoer A., 2001, ApJ, 562, L149

Melnick J., Sargent W. L. W., 1977, ApJ, 215, 401

Mohr J. J., Mathiesen B., Evrard A. E., 1999, ApJ, 517, 627

Monin A. S., Yaglom A. A., 1975, Statistical Fluid Mechanics: Mechanics of Turbulence. Vol. 2, Cambridge: MIT Press

Narayan R., Medvedev M. V., 2001, ApJ, 562, L129

Navarro J. F., Frenk C. S., White S. D. M., 1995, MNRAS, 275, 56

Navarro J. F., Frenk C. S., White S. D. M., 1996, ApJ, 462, 563

Navarro J. F., Frenk C. S., White S. D. M., 1997, ApJ, 490, 493

Nipoti C., Binney J., 2004, MNRAS, 349, 1509

Nipoti C., Binney J., 2005, MNRAS, 361, 428

Nipoti C., Londrillo P., Ciotti L., 2003, MNRAS, 342, 501

Nulsen P. E. J., McNamara B. R., Wise M. W., David L. P., 2005, ApJ, 628, 629

Omma H., Binney J., Bryan G., Slyz A., 2004, MNRAS, 348, 1105

Onken C. A., Ferrarese L., Merritt D., Peterson B. M., Pogge R. W., Vestergaard M., Wandel A., 2004, ApJ, 615, 645

O'Sullivan E., Vrtilek J. M., 2003, ArXiv Astrophysics e-prints

Owen F. N., Eilek J. A., Kassim N. E., 1998, Bulletin of the American Astronomical Society, 30, 1303

Peterson B., 1997, An Introduction to Active Galactic Nuclei. Cambridge University Press

Peterson B. M., 1993, PASP, 105, 247

Pizzolato F., Soker N., 2006, ArXiv Astrophysics e-prints

Pope E. C. D., Pavlovski G., Kaiser C. R., Fangohr H., 2005, MNRAS, 364, 13

Pope E. C. D., Pavlovski G., Kaiser C. R., Fangohr H., 2006, MNRAS, 367, 1121

Press W. H., Flannery B. P., A. T. S., Vetterling W. T., 1992, Numerical Recipes in Fortran. Cambridge University Press

Raymond J. C., Smith B. W., 1977, ApJ Supp., 35, 419

Reynolds C. S., Heinz S., Begelman M. C., 2002, MNRAS, 332, 271

Reynolds C. S., McKernan B., Fabian A. C., Stone J. M., Vernaleo J. C., 2005, MNRAS, 357, 242

Robinson K., Dursi L. J., Ricker P. M., Rosner R., Calder A. C., Zingale M., Truran J. W., Linde T., Caceres A., Fryxell B., Olson K., Riley K., Siegel A., Vladimirova N., 2004, ApJ, 601, 621

Ruszkowski M., Begelman M. C., 2002, ApJ, 581, 223

Ruszkowski M., Brüggen M., Begelman M. C., 2004, ApJ, 611, 158

Rybicki G. B., Lightman A. P., 1979, Radiative Processes in Astrophysics. Wiley-Interscience

Sanders J. S., Fabian A. C., Allen S. W., Schmidt R. W., 2004a, MNRAS, 349, 952

Sanders J. S., Fabian A. C., Allen S. W., Schmidt R. W., 2004b, MNRAS, 349, 952

Sarazin C. L., 1986, X-ray Emission from Clusters of Galaxies. Reviews of Modern Physics

Sarazin C. L., 2002, The Physics of Cluster Mergers. ASSL Vol. 272: Merging Processes in Galaxy Clusters, pp 1–38

Scheepmaker A., Ricker G. R., Brecher K., Ryckman S. G., Ballintine J. E., Doty J. P., Downey P. M., Lewin W. H. G., 1976, ApJ, 205, L65

Sijacki D., Springel V., 2006, MNRAS, 366, 397

Soker N., 2004, A&A, 414, 943

Sparke L. W., Gallagher J. S., 2000, Galaxies in the Universe. Cambridge University Press

Spitzer L., 1962, Physics of Fully Ionized Gases. Wiley-Interscience, New York

Sun M., Jones C., Murray S. S., Allen S. W., Fabian A. C., Edge A. C., 2003, ApJ, 587, 619

Sutherland R., Dopita M., 1993, ApJ Supp., 88, 253

Tabor G., Binney J., 1993, MNRAS, 263, 323

Tremaine S., Gebhardt K., Bender R., Bower G., Dressler A., Faber S. M., Filippenko A. V., Green R., Grillmair C., Ho L. C., Kormendy J., Lauer T. R., Magorrian J., Pinkney J., Richstone D., 2002, ApJ, 574, 740

Tribble P. C., 1989, MNRAS, 238, 1247

Uttley P., McHardy I. M., Vaughan S., 2005, MNRAS, 359, 345

van Leer B., 1979, Journal of Computational Physics, 32, 101

Vernaleo J. C., Reynolds C. S., 2005, ArXiv Astrophysics e-prints

Vikhlinin A., Markevitch M., Forman W., Jones C., 2001, ApJ, 555, L87

Voigt L. M., Fabian A. C., 2004, MNRAS, 347, 1130

Voigt L. M., Schmidt R. W., Fabian A. C., Allen S. W., Johnstone R. M., 2002, MNRAS, 335, L7

Yaglom A. M., 1966, in , Vol. 166, Dokl. Akad. Nauk SSSR. Akademkniga, pp 49–52

Zakamska N. L., Narayan R., 2003, ApJ, 582, 162

Zanni C., Murante G., Bodo G., Massaglia S., Rossi P., Ferrari A., 2005, A&A, 429, 399

Zombeck M. V., 1990, Handbook of Astronomy and Astrophysics. Cambridge University Press